Computer-Assisted Planning and Robotics in Epilepsy Surgery

[redacted]

Thesis submission to University College London for the degree of

Doctor of Philosophy

February 2020

I, Vejay Niranjan Vakharia confirm that the work presented in this thesis is my own. Where information has been derived from other sources, I confirm that this has been indicated in the thesis.

[redacted]

Abstract

Epilepsy is a severe and devastating condition that affects ~1% of the population. Around 30% of these patients are drug-refractory. Epilepsy surgery may provide a cure in selected individuals with drug-resistant focal epilepsy if the epileptogenic zone can be identified and safely resected or ablated. Stereoelectroencephalography (SEEG) is a diagnostic procedure that is performed to aid in the delineation of the seizure onset zone when non-invasive investigations are not sufficiently informative or discordant.

Utilizing a multi-modal imaging platform, a novel computer-assisted planning (CAP) algorithm was adapted, applied and clinically validated for optimizing safe SEEG trajectory planning. In an initial retrospective validation study, 13 patients with 116 electrodes were enrolled and safety parameters between automated CAP trajectories and expert manual plans were compared. The automated CAP trajectories returned statistically significant improvements in all of the compared clinical metrics including overall risk score (CAP 0.57 +/- 0.39 (mean +/- SD) and manual 1.00 +/- 0.60, $p < 0.001$). Assessment of the inter-rater variability revealed there was no difference in external expert surgeon ratings. Both manual and CAP electrodes were rated as feasible in 42.8% (42/98) of cases. CAP was able to provide feasible electrodes in 19.4% (19/98), whereas manual planning was able to generate a feasible electrode in 26.5% (26/98) when the alternative generation method was not feasible.

Based on the encouraging results from the retrospective analysis a prospective validation study including an additional 125 electrodes in 13 patients was then undertaken to compare CAP to expert manual plans from two neurosurgeons. The manual plans were performed separately and blindly from the CAP. Computer-generated trajectories were found to carry lower risks scores (absolute difference of 0.04 mm (95% CI = -0.42-0.01), $p = 0.04$) and were subsequently implanted in all cases without complication. The pipeline has been fully integrated into the clinical service and has now replaced manual SEEG planning at our institution.

Further efforts were then focused on the distillation of optimal entry and target points for common SEEG trajectories and applying machine learning methods to develop an active learning algorithm to adapt to individual surgeon preferences. Thirty-two patients were prospectively enrolled in the study. The first 12 patients underwent prospective CAP planning and implantation following the pipeline outlined in the previous study. These patients were

used as a training set and all of the 108 electrodes after successful implantation were normalized to atlas space to generate 'spatial priors', using a K-Nearest Neighbour (K-NN) classifier. A subsequent test set of 20 patients (210 electrodes) were then used to prospectively validate the spatial priors. From the test set, 78% (123/157) of the implanted trajectories passed through both the entry and target spatial priors defined from the training set. To improve the generalizability of the spatial priors to other neurosurgical centres undertaking SEEG and to take into account the potential for changing institutional practices, an active learning algorithm was implemented. The K-NN classifier was shown to dynamically learn and refine the spatial priors. The progressive refinement of CAP SEEG planning outlined in this and previous studies has culminated in an algorithm that not only optimizes the surgical heuristics and risk scores related to SEEG planning but can also learn from previous experience. Overall, safe and feasible trajectory schema were returning in 30% of the time required for manual SEEG planning.

Computer-assisted planning was then applied to optimize laser interstitial thermal therapy (LITT) trajectory planning, which is a minimally invasive alternative to open mesial temporal resections, focal lesion ablation and anterior 2/3 corpus callosotomy. We describe and validate the first CAP algorithm for mesial temporal LITT ablations for epilepsy treatment. Twenty-five patients that had previously undergone LITT ablations at a single institution and with a median follow up of 2 years were included. Trajectory parameters for the CAP algorithm were derived from expert consensus to maximize distance from vasculature and ablation of the amygdalohippocampal complex, minimize collateral damage to adjacent brain structures whilst avoiding transgression of the ventricles and sulci. Trajectory parameters were also optimized to reduce the drilling angle to the skull and overall catheter length. Simulated cavities attributable to the CAP trajectories were calculated using a 5-15 mm ablation diameter. In comparison to manually planned and implemented LITT trajectories,CAP resulted in a significant increase in the percentage ablation of the amygdalohippocampal complex (manual 57.82 +/- 15.05% (mean +/- S.D.) and unablated medial hippocampal head depth (manual 4.45 +/- 1.58 mm (mean +/- S.D.), CAP 1.19 +/- 1.37 (mean +/- S.D.), p = 0.0001).

As LITT ablation of the mesial temporal structures is a novel procedure there are no established standards for trajectory planning. A data-driven machine learning approach was, therefore, applied to identify hitherto unknown CAP trajectory parameter combinations. All possible combinations of planning parameters were calculated culminating in 720 unique

combinations per patient. Linear regression and random forest machine learning algorithms were trained on half of the data set (3800 trajectories) and tested on the remaining unseen trajectories (3800 trajectories). The linear regression and random forest methods returned good predictive accuracies with both returning Pearson correlations of $\rho = 0.7$ and root mean squared errors of 0.13 and 0.12 respectively. The machine learning algorithm revealed that the optimal entry points were centred over the junction of the inferior occipital, middle temporal and middle occipital gyri. The optimal target points were anterior and medial translations of the centre of the amygdala.

A large multicenter external validation study of 95 patients was then undertaken comparing the manually planned and implemented trajectories, CAP trajectories targeting the centre of the amygdala, the CAP parameters derived from expert consensus and the CAP trajectories utilizing the machine learning derived parameters. Three external blinded expert surgeons were then selected to undertake feasibility ratings and preference rankings of the trajectories. CAP generated trajectories result in a significant improvement in many of the planning metrics, notably the risk score (manual 1.3 +/- 0.1 (mean +/- S.D.), CAP 1.1 +/- 0.2 (mean +/- S.D.), $p<0.000$) and overall ablation of the amygdala (manual 45.3 +/- 22.2 % (mean +/- S.D.), CAP 64.2 +/- 20 % (mean +/- S.D.), $p<0.000$). Blinded external feasibility ratings revealed that manual trajectories were less preferable than CAP planned trajectories with an estimated probability of being ranked 4^{th} (lowest) of 0.62.

Traditional open corpus callosotomy requires a midline craniotomy, interhemispheric dissection and disconnection of the rostrum, genu and body of the corpus callosum. In cases where drop attacks persist a completion corpus callosotomy to disrupt the remaining fibres in the splenium is then performed. The emergence of LITT technology has raised the possibility of being able to undertake this procedure in a minimally invasive fashion and without the need for a craniotomy using two or three individual trajectories. Early case series have shown LITT anterior two-thirds corpus callosotomy to be safe and efficacious. Whole-brain probabilistic tractography connectomes were generated utilizing 3-Tesla multi-shell imaging data and constrained spherical deconvolution (CSD). Two independent blinded expert neurosurgeons with experience of performing the procedure using LITT then planned the trajectories in each patient following their current clinical practice. Automated trajectories returned a significant reduction in the risk score (manual 1.3 +/- 0.1 (mean +/- S.D.), CAP 1.1 +/- 0.1 (mean +/- S.D.), $p<0.000$).

Finally, we investigate the different methods of surgical implantation for SEEG electrodes. As an initial study, a systematic review and meta-analysis of the literature to date were performed. This revealed a wide variety of implantation methods including traditional frame-based, frameless, robotic and custom-3D printed jigs were being used in clinical practice. Of concern, all comparative reports from institutions that had changed from one implantation method to another, such as following the introduction of robotic systems, did not undertake parallel-group comparisons. This suggests that patients may have been exposed to risks associated with learning curves and potential harms related to the new device until the efficacy was known. A pragmatic randomized control trial of a novel non-CE marked robotic trajectory guidance system (iSYS1) was then devised. Before clinical implantations began a series of pre-clinical investigations utilizing 3D printed phantom heads from previously implanted patients was performed to provide pilot data and also assess the surgical learning curve. The surgeons had comparatively little clinical experience with the new robotic device which replicates the introduction of such novel technologies to clinical practice. The study confirmed that the learning curve with the iSYS1 devices was minimal and the accuracies and workflow were similar to the conventional manual method.

The randomized control trial represents the first of its kind for stereotactic neurosurgical procedures. Thirty-two patients were enrolled with 16 patients randomized to the iSYS1 intervention arm and 16 patients to the manual implantation arm. The intervention allocation was concealed from the patients. The surgical and research team could be not blinded. Trial management, independent data monitoring and trial steering committees were convened at four points doing the trial (after every 8 patients implanted). Based on the high level of accuracy required for both methods, the main distinguishing factor would be the time to achieve the alignment to the prespecified trajectory. The primary outcome for comparison, therefore, was the time for individual SEEG electrode implantation. Secondary outcomes included the implantation accuracy derived from the post-operative CT scan, infection, intracranial haemorrhage and neurological deficit rates. Overall, 32 patients (328 electrodes) completed the trial (16 in each intervention arm) and the baseline demographics were broadly similar between the two groups. The time for individual electrode implantation was significantly less with the iSYS1 device (median of 3.36 (95% CI 5.72 to 7.07) than for the PAD group (median of 9.06 minutes (95% CI 8.16 to 10.06), p=0.0001). Target point accuracy was significantly greater with the PAD (median of 1.58 mm (95% CI 1.38 to 1.82) compared to the

iSYS1 (median of 1.16 mm (95% CI 1.01 to 1.33), p=0.004). The difference between the target point accuracies are not clinically significant for SEEG but may have implications for procedures such as deep brain stimulation that require higher placement accuracy. All of the electrodes achieved their respective intended anatomical targets. In 12 of 16 patients following robotic implantations, and 10 of 16 following manual PAD implantations a seizure onset zone was identified and resection recommended. The aforementioned systematic review and meta-analysis were updated to include additional studies published during the trial duration. In this context, the iSYS1 device entry and target point accuracies were similar to those reported in other published studies of robotic devices including the ROSA, Neuromate and iSYS1. The PAD accuracies, however, outperformed the previously published results for other frameless stereotaxy methods.

In conclusion, the presented studies report the integration and validation of a complex clinical decision support software into the clinical neurosurgical workflow for SEEG planning. The stereotactic planning platform was further refined by integrating machine learning techniques and also extended towards optimisation of LITT trajectories for ablation of mesial temporal structures and corpus callosotomy. The platform was then used to seamlessly integrate with a novel trajectory planning software to effectively and safely guide the implantation of the SEEG electrodes. Through a single-blinded randomised control trial, the ISYS1 device was shown to reduce the time taken for individual electrode insertion. Taken together, this work presents and validates the first fully integrated stereotactic trajectory planning platform that can be used for both SEEG and LITT trajectory planning followed by surgical implantation through the use of a novel trajectory guidance system.

Impact Statement

An estimated 60 million people globally have epilepsy, with one third failing to achieve seizure freedom despite two or more adequate anti-epileptic drug schedules. Surgery may provide a cure if the epileptogenic zone (EZ) can be identified and safely resected or ablated. The evaluation of patients with drug-refractory epilepsy is, therefore, focused on distinguishing the putative EZ from nearby critical structures. The EZ is approximated from inferences derived from a collection of investigations of the symptomatogenic zone, seizure onset zone, functional deficit zone, irritative zone and potential epileptogenic lesions. In complex cases, these investigations are non-concordant and intracranial investigations in the form or stereoelectroencephalography (SEEG) or grid and strip recordings are necessary. Representing these investigations in a single space as a 'multi-modal' collection is a prerequisite to establishing the brain structures that require evaluation.

Unlike grid and strip insertion, which necessitates a large craniotomy (removal of a section of the skull), SEEG insertion is minimally invasive. The technique entails the stereotactic insertion of 8-14 electrodes, each with contacts that sample a radius of 3-5 mm. The precise trajectory must, therefore, be meticulously planned and executed to ensure adequate sampling of the implicated brain regions and prevent conflict with intracranial vasculature. Manual trajectory planning is time-consuming and requires simultaneous optimisation of numerous parameters, many of which lack consensus.

Conventional frame-based methods of SEEG implantation are increasingly being replaced with robotic trajectory guidance systems. A pipeline combining computer-assisted planning with robotic implantation has the potential to provide a streamlined workflow that improves the speed, accuracy and safety of stereotactic neurosurgical procedures, but high-quality evidence and economic evaluations are required to prove benefit.

To address these issues, a novel stereotactic trajectory planning platform has been developed and validated for SEEG computer-assisted planning. Initially, the computer-derived plans were retrospectively compared to manual SEEG trajectory parameters and external blinded expert ratings of feasibility were sought. After improved vascular imaging, a prospective comparison was initiated and computer-assisted plans were found to confer lower risk scores in all patients. The computer derived trajectories were subsequently implanted without complication providing the first prospective validation of their utility. Further work

was then undertaken to identify common entry and target points for SEEG trajectories from prior implantations and the generation of an atlas toward standardising trajectory planning in an objective and systematic fashion. A machine learning algorithm was also deployed to learn trajectory planning practices actively and dynamically modify the priors to increase the generalisability of the work. Computer-assisted planning was also applied to the optimization of laser interstitial thermal therapy for mesial temporal lobe ablations and corpus callosotomy, representing the first of its kind.

Finally, computer-assisted planning was applied to provide objective and systematic trajectories for use in a pragmatic randomised control trial comparing the iSYS1 robotic trajectory guidance system with conventional frameless SEEG implantation. This trial provides the first Class 1 evidence for robotic use in stereotactic neurosurgery despite the growing adoption of the technology.

Publication List:

First author publications:

Vakharia, V., & Duncan, J. (2016). A Randomised Control Trial of SEEG Electrode Placement Methods. ISRCTN Registry. BMC. Springer Nature. https://doi.org/10.1186/ISRCTN17209025

Vakharia, V. N., Sparks, R., O'Keeffe, A. G., Rodionov, R., Miserocchi, A., McEvoy, A., … Duncan, J. (2017). Accuracy of intracranial electrode placement for stereoencephalography: A systematic review and meta-analysis. Epilepsia, 58(6), 1–12. http://doi.org/10.1111/epi.13713

Vakharia, V. N., Sparks, R., Rodionov, R., Vos, S., Dorfer, C., Miller, J., … Duncan, J. (2017). Computer Assisted Planning For The Insertion Of Stereoelectroencephalography Electrodes For The Investigation Of Drug Resistant Focal Epilepsy: An External Validation Study. Journal of Neurosurgery, JNS17-1826.

Vakharia, V. N., Duncan, J. S., Witt, J.-A. A., Elger, C. E., Staba, R., & Engel, J. J. (2018). Getting the best outcomes from epilepsy surgery. Annals of Neurology, 83(4), 676–690. http://doi.org/10.1002/ana.25205

Vakharia, V. N., Rodionov, R., McEvoy, A. W., Miserocchi, A., Sparks, R., O'Keeffe, A. G., … Duncan, J. S. (2018). Improving patient safety during introduction of novel medical devices through cumulative summation analysis. Journal of Neurosurgery, 130(1), 213–219. http://doi.org/10.3171/2017.8.JNS17936

Vakharia, V. N., Sparks, R., Li, K., O'Keeffe, A. G., Miserocchi, A., McEvoy, A. W., … Wu, C. (2018). Automated trajectory planning for laser interstitial thermal therapy in mesial temporal lobe epilepsy. Epilepsia, 59(4), 814–824. http://doi.org/10.1111/epi.14034

Vakharia, V.N., Sparks, R., Vos, S.B., McEvoy, A.W., Miserocchi, A., Ourselin, S., Duncan, J.S., (2019). The Effect of Vascular Segmentation Methods on Stereotactic Trajectory Planning for Drug-Resistant Focal Epilepsy: A Retrospective Cohort Study. World Neurosurg. X. https://doi.org/10.1016/j.wnsx.2019.100057

Vakharia, V.N., Sparks, R., Miserocchi, A., Vos, S.B., O'Keeffe, A., Rodionov, R., McEvoy, A.W., Ourselin, S., Duncan, J.S., (2019). Computer-Assisted Planning for Stereoelectroencephalography (SEEG). Neurotherapeutics EPub ahead, 1–15. https://doi.org/10.1007/s13311-019-00774-9

Vakharia, V. N., Sparks, R. E., Li, K., O'Keeffe, A. G., Pérez-García, F., França, L. G. S., …

Duncan, J. S. (2019). Multicenter validation of automated trajectories for selective laser amygdalohippocampectomy. Epilepsia, (May), epi.16307. http://doi.org/10.1111/epi.16307

Vakharia, V. N., Sparks, R. E., Vos, S. B., Bezchlibnyk, Y., Mehta, A. D., Willie, J. T., … Duncan, J. S. (2020). Computer-assisted planning for minimally invasive anterior two-thirds laser corpus callosotomy: A feasibility study with probabilistic tractography validation: Automated laser callosotomy trajectory planning. NeuroImage: Clinical, 25(December 2019), 102174. https://doi.org/10.1016/j.nicl.2020.102174

Published work I supervised:

Li, K., Vakharia, V. N., Sparks, R., França, L. G. S., Granados, A., McEvoy, A. W., … Duncan, J. S. (2019). Optimizing Trajectories for Cranial Laser Interstitial Thermal Therapy Using Computer-Assisted Planning: A Machine Learning Approach. Neurotherapeutics, Jan(16(1)), 182:191. http://doi.org/10.1007/s13311-018-00693-1

Marcus, H. J., Vakharia, V. N., Sparks, R., Rodionov, R., Kitchen, N., McEvoy, A. W., … Duncan, J. S. (2019). Computer-assisted versus manual planning for stereotactic brain biopsy: a retrospective comparative pilot study. Operative Neurosurgery, (ONS-D-18-00919R1). http://doi.org/10.1093/ons/opz177

Li, K., Vakharia, V. N., Sparks, R., Rodionov, R., Vos, S. B., McEvoy, A. W., … Duncan, J. S. (2019). Stereoelectroencephalography electrode placement: Detection of blood vessel conflicts. Epilepsia, (October 2018), epi.16294. http://doi.org/10.1111/epi.16294

Published work I co-authored:

Granados, A., Vakharia, V., Rodionov, R., Schweiger, M., Vos, S. B., O'Keeffe, A. G., … Ourselin, S. (2018). Automatic segmentation of stereoelectroencephalography (SEEG) electrodes post-implantation considering bending. International Journal of Computer Assisted Radiology and Surgery. http://doi.org/10.1007/s11548-018-1740-8

Kovac, S., Vakharia, V. N. V. N., Scott, C., & Diehl, B. (2017). Invasive epilepsy surgery evaluation. Seizure, 44, 125–136. http://doi.org/10.1016/j.seizure.2016.10.016

Mancini, M., Vos, S. B., Vakharia, V. N., O'Keeffe, A. G., Trimmel, K., Barkhof, F., …

Ourselin, S. (2019). Automated fiber tract reconstruction for surgery planning: Extensive validation in language-related white matter tracts. NeuroImage: Clinical, 101883. http://doi.org/https://doi.org/10.1016/j.nicl.2019.101883

Marcus, H. J., Vakharia, V. N., Ourselin, S., Duncan, J., Tisdall, M., & Aquilina, K. (2018). Robot-assisted stereotactic brain biopsy: systematic review and bibliometric analysis. Child's Nervous System. http://doi.org/10.1007/s00381-018-3821-y

Rodionov, R., O'Keeffe, A., Nowell, M., Rizzi, M., Vakharia, V. N., Wykes, V., … Duncan, J. S. (2019). Increasing the accuracy of 3D EEG implantations. Journal of Neurosurgery, EPub ahead, 1–8. http://doi.org/10.3171/2019.2.JNS183313

Sparks, R., Vakharia, V., Rodionov, R., Vos, S. B., Diehl, B., Wehner, T., … Ourselin, S. (2017). Anatomy-driven multiple trajectory planning (ADMTP) of intracranial electrodes for epilepsy surgery. International Journal of Computer Assisted Radiology and Surgery, 12(8), 1245–1255. http://doi.org/10.1007/s11548-017-1628-z.

Manuscripts under review at the time of thesis submission:

Vakharia, V., Sparks, R., Granados, A., Miserocchi, A. McEvoy, A., Ourselin, S., Duncan, J. S. (2020) Refining Planning For Stereoelectroencephalography: A Prospective Validation Of Spatial Priors For Computer-Assisted Planning

Vakharia, V., Rodionov, R., Miserocchi, A., McEvoy, A., O'Keeffe, A., Granados, A., … Duncan, J. S. (2020) Comparison of robotic and manual implantation of intracerebral electrodes: a single center, single blinded, randomised controlled trial.

Conference Attendance List:

1. Joint German / SBNS meeting (Magdeburg, Germany) 2017 – Oral presentation
2. American Epilepsy Society (Washington, USA) 2017 - Poster presentation
3. North American Neuromodulation Society (Las Vegas, USA) 2017 – Invited presentation
4. American Society Stereotactic Functional Neurosurgery (Denver, USA) 2018 – Invited oral presentation

5. SBNS Plymouth (Torquay, UK) 2018 – Oral presentation 'high scoring submission.'
6. SBNS London (London, UK) 2018 – Oral and Poster presentations
7. British ILAE meeting (Birmingham, UK) 2018 – Poster presentation
8. American Epilepsy Society (New Orleans, USA) 2018 – Poster presentation
9. American Epilepsy Society (Baltimore, USA) 2019 – Poster presentation
10. 14th European Congress on Epileptology 2020 (Geneva, Switzerland) 2020 – Invited oral presentations in two separate parallel sessions

Prizes:

Sir Hugh Cairns Prize: Machine learning for stereotactic neurosurgery: A prospective implementation and validation (based on Chapter 4)

Acknowledgements

I would like to thank my parents for their tireless pursuit of educating their three sons and pushing us to achieve our academic potential. Through their sacrifices, they have afforded us the opportunity to excel. I would not be the person I am, and could not have achieved all that I have, without them.

I have been very fortunate to be guided and supported by my friend and mentor Prof John S. Duncan. I owe a debt of gratitude to him for steering me into the wind and allowing me to take off to pursue research wherever it leads me. He has helped me to develop into a better scientist, clinician and person. I will always be grateful for his kindness, wisdom, generosity and friendship. I strive every day to follow his example.

I have been blessed to have a wife that has supported me throughout my career. Her enduring patience, humour and love have allowed me to overcome all obstacles. Even with the arrival of our first son, she has been the foundation from which I have been able to devote all of my time and effort to academia.

I would like to make mention of recently departed friends that have had a significant impact on my life. I am grateful that our orbits intersected. Without you, my path would not have led me here. It is with a heavy heart that I must continue my journey without you. You will always be in my thoughts.

Thank you to the patients that were gracious enough to give up their time and take part in the studies. Without them this work would have no purpose.

Finally, I would like to thank my friends and colleagues that I have worked closely with during the PhD: [redacted] It has been a privilege to work with you all.

बुद्धिहीन तनु जानिके सुमिरौं पवन-कुमार ।

बल बुधि बिद्या देहु मोहिं हरहु कलेस बिकार ॥

“Knowing myself to be ignorant, I humbly ask of you,
Bestow on me strength, wisdom and knowledge, and remove my blemishes.”

Goswami Tulsidas, Hanuman Chalisa

Contents

Tables:

Figures:

Equations:

Abbreviations:

AC-PC	ANTERIOR COMMISSURE – POSTERIOR COMMISSURE
ADC	APPARENT DIFFUSION COEFFICIENT
AF	ARCUATE FASCICULUS
AHC	AMYGDALOHIPPOCAMPAL COMPLEX
ANOVA	ANALYSIS OF VARIANCE
ATLR	ANTERIOR TEMPORAL LOBE RESECTION
BOLD	BLOOD OXYGEN LEVEL DEPENDENT
CAP	COMPUTER ASSISTED PLANNING
CDSS	CLINICAL DECISION SUPPORT SOFTWARE
CHARMED	COMBINED HINDERED AND RESTRICTED MODEL OF DIFFUSION
CSD	CONSTRAINED SPHERICAL DECONVOLUTION
CSF	CEREBROSPINAL FLUID
CTA	CT-ANGIOGRAPHY
CUSUM	CUMULATIVE SUMMATION ANALYSIS
CVLT	CALIFORNIA VERBAL LEARNING TEST
d.f.	DEGREES OF FREEDOM
DBS	DEEP BRAIN STIMULATION
DBS	DEEP BRAIN STIMULATION
DEC	DIFFUSION ENCODED COLOUR
DKI	DIFFUSION KURTOSIS IMAGING
dODF	DIFFUSION ORIENTATION DISTRIBUTION FUNCTION

DSA	DIGITAL SUBTRACTION CATHETER ANGIOGRAPHY
DTI	DIFFUSION TENSOR IMAGING
DVLA	DRIVING AND VEHICLE LICENSING AGENCY
EC	ENTORHINAL CORTEX
EEG	ELECTROENCEPHALOGRAPHY
ERSET	EARLY SURGERY THERAPY FOR DRUG-RESISTANT EPILEPSY TRIAL
ESI	ELECTRICAL SOURCE IMAGING
EZ	EPILEPTOGENIC ZONE
FA	FRACTIONAL ANISOTROPY
FACT	FIBRE ASSIGNMENT BY CONTINUOUS TRACKING
FCS	FOCAL CORTICAL DYSPLASIA
FDA	FOOD AND DRUG ADMINISTRATION
FLAIR	FLUID ATTENTUATED INVERSION RECOVERY
FLARE	FEASIBILITY STUDY ON LITT FOR MEDICAL REFRACTORY EPILEPSY
FLE	FRONTAL LOBE EPILEPSY
fMRI	FUNCTIONAL MRI
FOV	FIELD-OF-VIEW
GM-WM	GREY-WHITE MATTER
GRE	GRADIENT-RECALLED ECHO
HARDI	HIGH-ANGULAR RESOLUTION DIFFUSION IMAGING
HH	HYPOTHALAMIC HAMARTOMA
IFOF	INFERIOR FRONTO-OCCIPITAL FASCICULUS
ILF	INFERIOR LONGITUDINAL FASCICULUS

K-NN	K-NEAREST NEIGHBOR
LGN	LATERAL GENICULATE NUCLEUS
LITT	LASER INTERSTITIAL THERMAL THERAPY
MD	MEAN DIFFUSIVITY
MEG	MAGNETO-ENCEPHALOGRAPHY
MgLITT	MR GUIDED LASER INTERSTITIAL THERMAL THERAPY
MINORS	METHODOLOGICAL INDEX FOR NON-RANDOMIZED STUDIES
MPRAGE	MAGNETIZATION PREPARED RAPID ACQUISITION GRE
MRV/A	MR-VENOGRAPHY / -ANGIOGRAPHY
MTLE	MESIAL TEMPORAL LOBE EPILEPSY
PAD	PRECISION-AIMING DEVICE
PET	POSITRON EMISSION TOMOGRAPHY
PHG	PARAHIPPOCAMPAL GYRUS
PRISMA	PREFERRED REPORTING ITEMS FOR SYSTEMATIC REVIEWS AND META-ANALYSIS
PVH	PERIVENTRICULAR HETEROTOPIA
rCBF	RELATIVE CEREBRAL BLOOD FLOW
RNS	RESPONSIVE NEUROSTIMULATION
ROI	REGION OF INTEREST
ROSE	RADIOSURGERY OR OPEN SURGERY FOR EPILEPSY
SAH	SELECTIVE AMYGDALOHIPPOCAMPECTOMY
SEEG	STEREOELECTROENCEPHALOGRAPHY
SLAH	SELECTIVE LASER AMYGDALOHIPPOCAMPECTOMY

SLATE	STEREOTACTIC LASER ABLATION FOR TEMPORAL LOBE EPILEPSY
SLF	SUPERIOR LONGITUDINAL FASCICULUS
SMA	SUPPLEMENTARY MOTOR AREA
SOZ	SEIZURE ONSET ZONE
SPECT	SINGLE POSITRON EMISSION TOMOGRAPHY
SPGR	SPOILED GRADIENT-RECALLED ACQUISITION
SRS	STEREOTACTIC RADIOSURGERY
SWI	SUSCEPTIBILITY WEIGHTED IMAGES
TE / TR	ECHO-TIME / REPETITION-TIME
TLE	TEMPORAL LOBE EPILEPSY
TMS	TRANSCRANIAL MAGNETIC STIMULATION
TOF	TIME OF FLIGHT
TPR+AH	TEMPORAL POLE RESECTION AND AMYGDALOHIPPOCAMPECTOMY
TS	TUBEROUS SCLEROSIS
UF	UNCINATE FASCICULUS
VFD	VISUAL FIELD DEFICIT
VNS	VAGAL NERVE STIMULATION
WCSS	WITHIN-CLUSTER SUM OF SQUARES

Outline and statement of personal communication:

Chapter 1 provides an overview of the contemporary literature surrounding epilepsy surgery. The purpose of the presurgical evaluation of epilepsy is to estimate the epileptogenic zone. This is defined as the region of cortex that when resected, ablated or disconnected results in seizure freedom. The techniques and rationale for invasive electrophysiological monitoring are also described as well as the different surgical strategies and postoperative complications. An overview of the fundamental considerations for computer-assisted planning is also provided.

In Chapter 2, I describe a retrospective validation study to outline the potential impact of computer-assisted planning (CAP) on SEEG strategies and compare this to manual implantations. Building upon previous work developing EpiNav™ as a stereotactic trajectory planning platform, led by [redacted], an entirely anatomically driven approach to trajectory planning was developed and clinically validated in this study. Blinded external experts then validated both CAP and manually planned trajectories through ratings of individual electrode feasibility. I am grateful to [redacted] (Consultant Neurosurgeons) for their collaboration as external expert independent reviewers. Based on the encouraging results of the retrospective comparison study, a prospective validation was undertaken with surgical implantation of CAP derived SEEG plans. The GIF parcellation used in this and subsequent studies was developed by Dr George Cardoso (University College London).

Chapter 3 provides the first and only reported prospective application of a CAP algorithm to date that has been embedded within a clinical work-flow as a complex clinical decision support software. Based on the results of this study, manual planning has now been replaced by CAP at our institution. Dr Rachel Sparks was responsible for the technical enhancements of the EpiNav™ software to facilitate this study. [redacted] reviewed all of the automated trajectories before surgical implantation.

To further improve the external applicability and generalisability of the CAP algorithm, in Chapter 4, a series of spatial priors were developed to allow CAP to leverage knowledge and experience from previous SEEG implantations. The spatial priors were utilized and validated in a further large prospective series of SEEG implantations. To overcome the heterogeneity

between different institutional implantation practices a machine learning algorithm, in the form of a K-nearest neighbour classifier, was implemented to learn and dynamically adapt to evolving SEEG planning practices actively. This allows the CAP algorithm to optimise the trajectory planning metrics, whilst also conforming to the individual preferences of the user.

Following on from the application of CAP for SEEG in Chapters 2-4, Chapter 5 investigates whether the scope could be broadened to other stereotactic procedures in which predefined parameters, quantifiable on the pre- or post-operative imaging, could be optimised. Laser interstitial thermal therapy (LITT) is the prototypical example of an emerging therapeutic technology for which the trajectory parameters themselves have been suggested to determine prognostic factors such as seizure-free outcome and neuropsychological sequelae. Maximal ablation of the mesial hippocampal head is an independent predictor of seizure-free outcome, whilst sparing the surrounding cortical and subcortical structures are thought to mitigate the post-ablation neuropsychological decline. Due to the novel nature of the procedure experience is concentrated at high volume centres and there remains a wide variation in clinical practice. As the uptake of LITT increases, a systematic and objective method of trajectory planning based on the contemporary evidence-based literature would help to standardise care, allow multi-centre outcome data to be combined more efficiently and ensure maximal therapeutic benefit. To this end, I describe and validate a method for automating LITT trajectory planning based on expert consensus and available evidence base within the literature. By applying a conservative uniform ablation diameter of 5-15 mm to CAP generated trajectories ablation volumes of critical regions of interest were estimated. Through an external collaboration manually planned and implemented trajectories and were reconstructed. The estimated ablation volumes were compared with CAP generated trajectories in a series of patients that have previously undergone LITT at a high volume institution (Thomas Jefferson Univesity, PA, USA) and in whom 2-year outcome data were available. This suggested that CAP generated trajectories could have provided significantly greater ablation of the amygdalohippocampal complex, less mesial hippocampal head remnant and a reduced overall trajectory risk score. A 15 mm diameter ablation cavity estimation was also found to be an accurate estimation of the achieved ablation volume and was applied in all subsequent studies. I am grateful to [redacted] for their collaboration. [redacted] was responsible for the technical enhancements of the EpiNav™ software to facilitate this study.

Building from this, in Chapter 6, an entirely data-driven approach to identifying new trajectory parameters through the application of machine learning was pursued. For machine learning approaches, a large quantity of data is required to derive optimal trajectory planning parameters. To this end, all clinically acceptable entry, target and trajectory planning parameter permutations were applied to identify the optimal combinations to maximise ablation of the amygdalohippocampal complex and spare the parahippocampal gyrus. A novel composite score that could be objectively and systematically applied was developed for this purpose. This showed that optimal entry points were focused at the temporo-occipital junction (confluence of the inferior occipital, middle occipital and middle temporal gyrus). The optimal target point was found to be the anteromedial amygdala. I developed the initial study concept, derivation of the entry and target point combinations and interpretation of results. I supervised [redacted] (Visiting Neurosurgical Fellow) in the use of the EpiNav software, model generation and automated trajectory calculation. [redacted] (PhD student) trained the machine learning algorithms deployed in this study.

A multicenter collaborative study was then undertaken in Chapter 7, including 95 patients from three high volume epilepsy surgery services comparing expert planned (manual) trajectories against the computer-assisted planning algorithm incorporating the machine learning derived parameters from Chapter 6. Utilising these novel planning parameters the automated trajectories were able to improve amygdala ablation whilst sparing the collateral structures and reducing trajectory risk scores compared to expert plans. Furthermore, feasibility ratings revealed that external blinded experts were more likely to favour the computer-generated trajectories over that of manual expert trajectories suggesting that this may provide an acceptable means of standardizing LITT trajectories for the treatment of MTLE. Prospective application and validation of these trajectories are now required to determine if the machine learning derived parameters translate into improved clinical outcomes. I am grateful to [redacted] (Consultant Neurosurgeons) for their collaboration. The statistical analysis in this study was undertaken with guidance from Dr Aidan O'Keefe (University College London Biostatistician).

In Chapter 8, I describe a novel application of automated multi-LITT trajectory planning to undertake minimally invasive anterior two-thirds corpus callosotomy. Through the application of three distinct laser fibre trajectories, a fully automated multi-trajectory planning pipeline was developed in which the individual entry and target points were derived directly

from the whole brain parcellation. As part of the validation of this feasibility study, anterior two-thirds corpus callosotomy manual trajectory planning was undertaken by two blinded external experts and extent of interhemispheric disconnection, through probabilistic tractography, was compared with the computer-derived trajectories. The computer-assisted planning algorithm was able to provide feasible multi-trajectory plans in all cases and improved the overall risk scores associated with the plans. I am grateful to [redacted] (Consultant Neurosurgeons) for their collaboration.

In Chapters 9-11, I focus on the introduction of robotic medical devices into clinical neurosurgical practice, which has significantly increased over the last decade. Robotic systems provide a precise and reliable targeting platform which has popularized their use for brain biopsy, deep brain stimulation, SEEG, LITT, focal drug delivery, spinal screw placement and as instrument holders. Despite these benefits, robotic devices carry significant economic costs associated not only with the purchase of the device but also with consumables and service contracts. It is unclear, therefore, if the opportunity cost of these devices out-weighs the perceived incremental benefits. In chapter 9, I conduct a systematic review and meta-analysis of the different operative techniques used for SEEG implantation and quantify the accuracy associated with each of these from the published literature. [redacted] (University College London Biostatistician) performed the statistical analysis for the meta-analysis. All new devices or procedures are associated with a learning curve, both from the point of the operating surgeon and for the institution. When integrating these devices in clinical practice is essential that patient safety is maintained and early warning systems for performance assessment and preventative vigilance are put in place. Of the 15 studies included in the quantitative analysis, there were no prospective comparative studies of SEEG implantation methods. The most extensive series compared prospective robotic SEEG implantation accuracies with historical frame-based cohorts. Before and after studies such as these are not sensitive to learning curves and may inadvertently result in patient harm during the introduction of the new device.

To address this issue, in Chapter 10, I quantify the learning curve associated with the novel iSYS1 robotic trajectory guidance system using 3D printed phantoms in which SEEG implantation schema were reconstructed. I also implement cumulative summation analysis (CUSUM) as a quality assurance tool. Chapter 10 was undertaken as a pre-clinical validation of the device in preparation for undertaking a formal prospective clinical single-blinded parallel-group randomised control trial, comparing the current frameless method (Precision-aiming device,

Medtronic Inc.) employed at the study institution since 2012 with the iSYS1 robotic trajectory guidance device (Medizintechnik GmbH). [redacted] (Consultant Neurosurgeon) performed the simulated SEEG implantation on the 3D printed phantoms.

Chapter 11 provides the highest level of evidence to date and represents the only randomised control trial of a robotic trajectory guidance system for stereotactic neurosurgery. The automated computer planning algorithm described in Chapter 4 was used to prospectively generate the implemented trajectories. The results of this randomised control trial will be of particular benefit to clinicians undertaking stereotactic neurosurgical procedures as well as funding commissioners and national policymakers. Under the supervision of the Chief Investigator Prof. John Duncan, I developed the study protocol, secured ethics committee and MHRA approval and undertook the day to day management of the trial. I also convened and attended the Trial Management Group, the Independent Data Monitoring Committee and the Trial Steering Committee. [redacted] (Consultant Neurosurgeons) performed the implantation surgeries. [redacted] aided with the data acquisition. [redacted] (University College London Biostatistician) performed the statistical analysis. I would like to thank [redacted] for participation in the Independent Data Monitoring Committee and D[redacted] for participation in the Trial Steering Committee. I also thank the independent statistician, [redacted] and our colleagues in the NHNN video-EEG monitoring unit, [redacted] for their support of the trial. Medtronic Inc., provided loan of the robotic equipment, consumables and a neuronavigation system for use during the trial.

1 Literature Review

1.1 **Introduction to epilepsy surgery**

The International League against epilepsy have recently updated the definition of epilepsy to: ***"A disease of the brain defined by any of the following conditions: 1) At least two unprovoked (or reflex) seizures occurring >24 hours apart; 2) One unprovoked (or reflex) seizure and a probability of further seizures similar to the general recurrence risk (at least 60%) after two unprovoked seizures, occurring over the next ten years; 3) diagnosis of an epilepsy syndrome"***(Fisher et al., 2014)**.**

It is estimated to affect 60 million people worldwide with an incidence of over 50 new cases per 100,000 people per year in developed countries. The prevalence in low and middle-income countries is likely underestimated due to social stigmatization and reduced access to healthcare(de Boer et al., 2008). Currently, the societal and economic impact of epilepsy is higher than that of Parkinson's disease, multiple sclerosis, Alzheimer's disease and all other dementias together(Ventola, 2014). Epilepsy affects patients of all ages, genders and social classes. The prevalence of epilepsy, when stratified by age, follows a bimodal distribution with a high incidence in early childhood and after the age of 50 years. The incidence is lowest in patients aged 20-40 years. Consequently, it has wide-ranging impacts on patients, caregivers and society as a whole from seizure-related injuries, psychiatric and cognitive sequelae. Depression, anxiety, psychosis, suicide rates and sudden unexpected death rates are significantly greater than observed in the general population(Bujarski et al., 2011). Failure to control seizures, frequency and the age of seizure onset have detrimental consequences for memory, cognition and social integration resulting in social isolation, discrimination and low employment rates(Jobst et al., 2015).

Three out of four patients that experience two or more unprovoked seizures, occurring more than 24 hours apart, within 12 months will have a further unprovoked seizure within the next four years(Fisher et al., 2018). Based on this, it is recommended that patients undergo further investigation and commencement of drug therapies after a second seizure or after the first seizure if there remains an enduring predisposition for further seizures. Over the last 150 years, 40 clinically effective anti-seizure medications have been developed, yet an adequate trial

of up to two anti-epileptic drugs, either alone or in combination, fails to achieve seizure freedom in one-third of patients(Kwan et al., 2009). The addition, or trial, of further drug regimes, has LITTle incremental effect on seizure control. In the remaining two-thirds of patients where drug treatments can prevent disabling seizures, around half of patients experience moderate or severe drug-related side effects(Choi et al., 2016).

The appropriate selection of antiepileptic medications is based on the seizure type, epilepsy syndrome, clinical response, drug side effect profile and after consideration of co-morbidities and drug contra-indications(Löscher et al., 2013). Further attention must also be applied to women of childbearing age due to their potential teratogenic side effects. Tailored drug therapies, referred to as narrow-spectrum agents, carry the most substantial therapeutic benefit when a particular seizure type or syndrome can be identified. In the case of focal epilepsies, with or without secondarily generalised tonic-clonic seizures, carbamazepine, oxcarbazepine, gabapentin, pregabalin, eslicarbazepine, vigabatrin and tiagabine are useful but are likely to exacerbate generalized seizures. In particular myoclonic and absence, seizures are worse affected. A definitive diagnosis of a particular epilepsy syndrome, however, can only be made in around half of patients(Schmidt et al., 2014). In the remaining patients, broad-spectrum agents such as lamotrigine, levetiracetam, phenytoin, sodium valproate, benzodiazepines and zonisamide are preferred. Head to head comparative trials have shown similar efficacies between appropriate first-line agents, but second-generation drugs such as lamotrigine, levetiracetam, oxcarbazepine and zonisamide have improved tolerability and safety profiles(French, 2007). In patients with unclassified or idiopathic generalised epilepsies valproate is more efficacious than lamotrigine and has improved tolerability over topiramate(Marson et al., 2007). Polypharmacy with antiepileptic medications carries increasing risks of pharmacokinetic and pharmacodynamics interactions with certain drug combinations, such as phenytoin and carbamazepine, resulting in bidirectional induction of metabolism. The resulting consequence is drug toxicity, commonly manifesting as dizziness and diplopia. Additional considerations when combining enzyme-inducing drugs are that substantially higher drug doses are required due to increased drug clearances.

Large long-term observational studies in newly diagnosed drug-naive epilepsy patients revealed 47% achieved seizure control with the first medication. The addition of a second and third drug resulted in an additional 13% and 4% seizure freedom, respectively(French et al., 2013). In a landmark study by Wiebe et al., patients with drug-refractory temporal lobe epilepsy

achieved seizure freedom rate in 58% following anterior temporal lobectomy, compare to 8% in the medical group(Wiebe et al., 2001). The Early Surgery Therapy For Drug-Resistant Epilepsy Trial (ERSET) randomised patients with temporal lobe epilepsy immediately after the failure of two medications to early surgery or further antiepileptic drug use(Engel et al., 2012). The trial initially aimed to recruit 200 patients but was terminated following randomisation of 36 patients and having reached statistical significance for the primary outcome of seizure freedom rate. In the medical therapy group, 0% (0/23) patients achieved seizure freedom compared to 73% (11/ 15) in the surgical group at two years, whilst the number of serious adverse events were similar in the two groups. An additional benefit of epilepsy surgery is the possibility of reducing or in some cases, completely stopping drug therapy once seizure freedom is achieved. Despite over two decades of growing evidence for the benefits of epilepsy surgery in patients with drug-refractory epilepsy, many physicians are still hesitant to refer for surgical evaluation. Subsequent trials have shown the results are generalizable(De Tisi et al., 2011) and durable with long-term follow up as long as 25 years and acceptable complications rates(Bell et al., 2017; Gooneratne et al., 2017). Despite the significant improvements in seizure freedom rates and quality of life following neurosurgical intervention, epidemiological studies have shown that a large proportion of those eligible are not referred for consideration of surgery and there remains a delay of an average of 18 years from diagnosis to evaluation for surgery (Haneef et al., 2010).

The correct selection of patients for neurosurgical intervention is key to ensuring optimal outcomes(Abosch et al., 2002; Kovac et al., 2017; Lee et al., 2006). A large variety of histopathologically confirmed diagnoses have been shown to result in epilepsy(Blumcke et al., 2017), only a proportion of which are detectable using clinically available imaging modalities(Duncan et al., 2016; Feindel, 2013; Knake et al., 2005). When the clinical semiological features of the habitual seizures are concordant with the results of the neuro-imaging, neuropsychological assessment and scalp electroencephalography (EEG), surgery can be undertaken without the need for any further investigations(Diehl et al., 2000). In patients in whom the presurgical investigations are discordant, invasive EEG recordings may be needed in the form of stereoelectroencephalography (SEEG) or grid +/- depth electrode insertion, each of which has its benefits and complications(Enatsu et al., 2016; Mullin et al., 2016a; Reif et al., 2016).

There has been a significant increase in SEEG over grid +/- depth insertion over the last decade with multiple techniques, such as frame-based, frameless, custom-fixture and robotic

methods being used(Cardinale et al., 2013; Mullin et al., 2016a). Invasive EEG has the added benefit of allowing electrical activity to be recorded from multiple regions in the brain during (ictal) and between seizures (interictal) over an extended period. The individual contacts of the inserted electrodes can also be stimulated to facilitate extra-operative mapping and characterisation of the epileptogenic network(David et al., 2010; Serletis et al., 2014). Optimal planning of SEEG electrodes is vital to ensure safe and accurate targeting of anatomical structures. SEEG electrode insertion carries several risks including bleeding, infection and neurological deficit due to damage to the brain as a result of misplacement, with risk in large centres of 1.3% per patient (Mullin et al., 2016a). Electrode trajectories are therefore carefully planned to sample from the intended parts of the brain and to avoid blood vessels and important brain structures.

The seizure onset zone (SOZ) can then be determined based on the recorded electrophysiological characteristics, which is a distinct entity to the epileptogenic zone (EZ). The EZ is defined as the minimum amount of cortex that needs to be resected to result in seizure freedom(Kovac et al., 2017). The implication, therefore, is that patients who fail to achieve seizure freedom do so because the entirety of the EZ was not resected. This may include distant regions of the brain that may have been quiescent and, through some mechanism of epileptogenesis, have become involved in the epileptogenic network(Berg et al., 2003). In contrast, when patients achieve seizure freedom, one must consider if non-epileptogenic regions of the brain have also been resected, thereby potentially resulting in unnecessary neurological sequelae.

Multiple open and minimally invasive methods of surgical resection or ablation have been described(Niemeyer, 1958; Spencer et al., 1984b; Wieser et al., 1982). Theoretically, minimally invasive techniques and image-guided open procedures may result in improved neurological or neuropsychological outcomes through reduced collateral damage to surrounding structures such as the optic radiation(Winston et al., 2012) and adjacent neocortex respectively(Drane et al., 2015).

This chapter summarises the pipeline for the pre-surgical investigations of patients with drug-resistant focal epilepsy, indications for invasive EEG, contemporary techniques and outcomes of epilepsy surgery and the essential considerations for computer-assisted stereotactic trajectory planning.

1.2 **Brain Imaging**

The pre-surgical evaluation of epilepsy aims to estimate the EZ, through the integration of clinical seizure semiology, EEG, neuropsychological evaluation and multi-modal imaging(Kovac et al., 2017). Patients with an identified epileptogenic lesion have 2.5 times higher odds of achieving seizure freedom following surgery than those without(Téllez-Zenteno et al., 2010). In this context, the EZ is a working hypothesis which is empirically derived by seizure outcome after surgery. If the patient is not seizure-free, a portion of the actual EZ may have been missed from the resection, or a secondary ictal network exists. If, however, the patient achieves seizure freedom, it is unclear if the extent of the resection could have been more selective while achieving the same level of success. Smaller resections may ultimately lead to less neurological and neuropsychological sequelae from surgery. Estimations of the EZ are derived from investigations of the symptomatogenic zone, functional deficit zone, irritative zone, seizure onset zone and epileptogenic lesions. Information pertaining to the symptomatogenic zone is derived from the clinical history, physical examination and seizure semiology. The seizure semiology includes descriptions or physical manifestations of auras, which precede the clinical onset of seizure activity, as well as the clinical manifestations of the seizure itself(Foldvary-Schaefer et al., 2011). Stereotyped ictal features allow inferences to be drawn regarding the underlying cortical regions from which they arise. It should be noted that seizures arising in so-called 'silent regions' of the brain, such as the parietal lobe, do not result in any clinical features until the abnormal electrical activity spreads to surrounding cortical regions(Balestrini et al., 2015). Information related to the functional deficit zone is deduced from abnormalities between seizures. In the immediate post-ictal phase this may be transient and include post-ictal limb paresis and aphasia, implicating the contralateral hemisphere and language-dominant hemisphere, respectively. Persistent inter-ictal deficits may be detected by under-functioning on neuropsychological testing or a reduction in glucose metabolism as detected using positron emission tomography (PET)(Willmann et al., 2007). The irritative zone relates to regions of the brain from which epileptic discharges occur between seizures. Detection of epileptic discharges can be through EEG, magneto-encephalography (MEG)(Englot et al., 2015) and EEG-fMRI(van Houdt et al., 2013). The seizure onset zone is surmised from EEG recordings at the start of the seizure. Ictal-interictal subtraction single positron emission tomography (SPECT) also provides information regarding the seizure onset zone if the injection of the tracer is optimally timed(la Fougère et al., 2009). Advances in MRI techniques and sequences improve the identification and delineation of epileptogenic lesions. The spectrum of

lesions that result in epilepsy that may be surgically remediable includes developmental abnormalities, infections, neoplasia, stroke, trauma, vascular malformations(Blümcke, 2009). Optimized imaging protocols and interpretation of images by neuroradiologists with experience in epilepsy imaging have been shown to increase the detection of epileptogenic lesions(von Oertzen, 2002). The range of investigations performed in individual units is likely to be constrained by the local availability of specific imaging modalities (see Table 1)

1.2.1 MRI-based imaging

Basic requirements for Epilepsy imaging protocols have been suggested by the ILAE(International League Against Epilepsy, 1997) and optimal MRI protocols defined(Wellmer et al., 2013). The mainstay of imaging is based on a high-quality structural 3T MRI scan. This provides a better signal to noise ratio with improved spatial and contrast resolution, compared to 1.5T scans, and is enhanced with the use of surface coils. Knake et al. compared 1.5T to 3T acquisitions and showed that in 65% (15/23) of cases epileptogenic lesions could be detected following 3T scans that were not visible on the 1.5T imaging(Knake et al., 2005). The majority of these lesions were subtle focal cortical dysplasias.

1.2.1.1 Structural MRI

Volumetric T1-weighted gradient-recalled echo (GRE) images including sequences such as MPRAGE (magnetization prepared rapid acquisition GRE) or SPGR (spoiled gradient-recalled acquisition) provide sharp grey/white matter distinction for detection of subtle malformations of cortical development. Images are routinely acquired with 1-mm isotropic voxels to allow reformatting in additional planes and segmentation of the hippocampus for volumetric measurements. Hippocampal volumes are first corrected for the whole brain volume and those that have an absolute volume or asymmetry index of 2 S.D. less than the normal population are considered atrophic(Woermann et al., 1998). Whole-brain parcellations derived from these sequences are also increasingly being employed to allow automated anatomical region labelling and assessment(Keihaninejad et al., 2012). Gadolinium-enhancement is recommended in patients in which tumours, infection or neurocutaneous syndromes are suspected(Friedman, 2014).

High resolution T2-weighted coronal images are acquired in a plane perpendicular to the long axis of the hippocampus in addition to a traditional orthogonal plane. The coronal

sequences through the frontal and temporal cranial fossa additionally allow for the detection of small encephaloceles, which are an underestimated and surgically remediable cause of epilepsy(Panov et al., 2016). T2* sequences such as GRE or SWI (susceptibility-weighted images) improve the detection of calcified or hemorrhagic lesions.

Hippocampal sclerosis is the most commonly identified pathology in surgical series and is characterized by hippocampal atrophy and increased T2 signal intensity. Visual inspection of the hippocampus can miss subtle, focal or bilateral hippocampal sclerosis. T2 relaxometry allows for quantification of the T2 relaxation time along the length of the hippocampus. When the hippocampal volume and T2 relaxometry are considered in combination, this can lead to an increased rate of hippocampal sclerosis detection of up to 28% compared to expert qualitative assessment alone(Coan et al., 2014). T2 relaxometry is more sensitive and specific than normalized FLAIR imaging in detecting hippocampal sclerosis(Rodionov et al., 2015).

3D T2-weighted FLAIR (fluid-attenuated inversion recovery) sequences aid in the detection of focal cortical dysplasias which are often located at the bottom of a sulcus, may blur the grey-white boundary and have dyslamination extending into the white matter.

Post-acquisition processing of MRI data may increase the detection of subtle abnormalities, but with the caution of reduced specificity being the price of increased sensitivity (Ahmed et al., 2015; Besson et al., 2008; Focke et al., 2009; Hong et al., 2014; Huppertz et al., 2005; Wagner et al., 2011). If a lesion has been detected and this is concordant with the clinical semiology, prolonged interictal and ictal scalp video EEG, neuropsychology and neuropsychiatric assessments then no further investigation may be required prior to definitive surgical management. In individuals in whom the planned resection margins are close to eloquent cortex, functional mapping techniques such as language and motor fMRI and transcranial magnetic stimulation (TMS) have been used to help to delineate the boundaries of a safe resection(Bauer et al., 2014; Gaillard et al., 1997; Helmstaedter et al., 2015).

Table 1: Imaging sequences commonly employed for presurgical evaluation.

MRI	3D volumetric T1-weighted imaging (1mm isotropic voxels) in AC-PC angulation
	T2-weighted axial and coronal images (< 3mm slice thickness) angulated perpendicular to hippocampal axis
	3D volumetric FLAIR (1 mm isotropic voxels) or axial and coronal images (< 3mm slice thickness) angulated perpendicular to hippocampal axis
	T2* gradient echo or susceptibility-weighted axial imaging angulated perpendicular to hippocampal axis
a) Confirmation of epileptogenic zone	^{18}F-FDG PET
	Ictal inter-ictal subtraction SPECT
	MEG
	Electrical source imaging (ESI)
	EEG-fMRI
b) Eloquent function mapping	Language and motor functional MRI
	Tractography
	Transcranial magnetic stimulation

Figure 1: Magnetic resonance imaging of common pathologies underlying drug-resistant focal epilepsy:

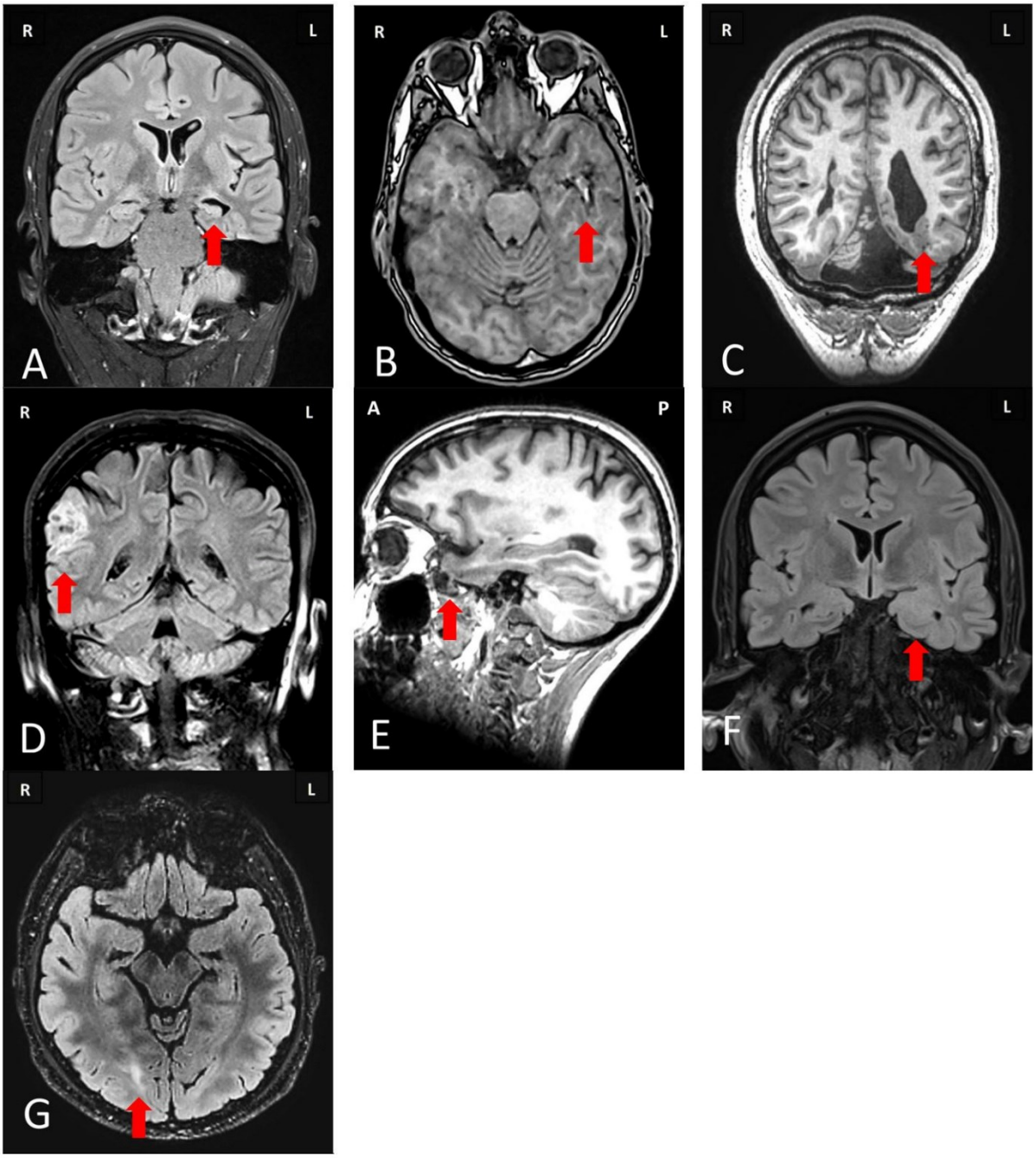

Figure 1 Legend: Magnetic resonance imaging of common pathologies underlying drug-resistant focal epilepsy that are amenable to surgical treatment. (A) Coronal fluid-attenuated inversion recovery (FLAIR) image showing increased T2 signal in the left hippocampus associated with volume loss and compensatory dilatation of the left temporal horn consistent with left hippocampal sclerosis. (B) Nonenhanced axial T1-weighted image of a patient with a

lesion in the left temporal lobe that has a "popcorn" appearance due to a hemosiderin ring and mixed intensity blood products consistent with a cavernoma. (C) Nonenhanced coronal T1-weighted image of a patient with multiple bilateral well-demarcated periventricular lesions that have imaging characteristics matching grey matter consistent with nodular periventricular heterotopia. This is associated with polymicrogyria-like overlying cortex. A note is also made of a posterior fossa arachnoid cyst and ventricular asymmetry. (D) Coronal FLAIR image of a patient with a sharply demarcated cortically based "pseudocystic" lesion in the right supramarginal gyrus that returns a hyperintense signal, consistent with a dysembryoplastic neuroepithelial tumour. There is associated with overlying calvarial remodelling. (E) Sagittal T1-weighted image through the left temporal lobe revealing herniation of the temporal pole through the floor of the middle cranial fossa consistent with a meningoencephalocele. (F) Coronal FLAIR image with increased signal and expansion of the left amygdala. Contrast-enhanced imaging did not reveal any enhancement, consistent with a diffusely infiltrating low-grade glioma. (G) Axial FLAIR image revealing increased signal in the right occipital lobe with the blurring of the cortical-subcortical margin consistent with type 2B focal cortical dysplasia.

1.2.1.2 fMRI

fMRI is based on the detection of increased blood flow and brain tissue oxygenation in specific regions during specially designed cerebral tasks. This is referred to as the blood oxygen level-dependent (BOLD) signal (Cordes et al., 2000). Commonly used fMRI language paradigms, verbal fluency and verb generation, are used to lateralize, rather than precisely localize, language functions (Doucet et al., 2015). The sensitivity and specificity of fMRI for language lateralization is between 80-90% and has replaced Wada testing (intracarotid sodium amobarbital procedure) in most cases(Bauer et al., 2014).

1.2.1.3 Diffusion tractography

Fibre tractography is used to localize major white matter tracts such as corticospinal tract and optic radiation. Tractography is derived from diffusion-weighted MRI sequences in which the anisotropic movement of water molecules within a voxel provides information regarding the most likely direction of white matter tracts between user-specified regions of interest(Mukherjee et al., 2008). The theoretical underpinnings of diffusion imaging have been

comprehensively reviewed in other texts(Chung et al., 2011; Mukherjee et al., 2008). I will not, therefore, repeat these details here, but when considering the use of diffusion-weighted imaging in an academic or clinical context, three important concepts should be borne in mind. The first is that diffusion imaging is a structural imaging modality pertaining to in-vivo water movement, which indirectly allows inferences to be drawn regarding the cytoarchitecture of white matter(Jellison et al., 2004b). The second is that an algorithm must subsequently be applied to calculate the diffusion orientation distribution function (dODF) for each voxel. The accuracy of the dODF and the ability to resolve multiple different fibre populations within a voxel is dependent on the number of diffusion gradients and directions applied. Finally, streamline propagation through different tracking algorithms provide a mathematical estimate of water movement between adjacent voxels. The streamline density is, therefore, a reflection of the probability of water diffusion in a particular direction and not a quantification of the number of axons.

The simplest and earliest representation of water movement within a voxel is the diffusion tensor. The tensor is composed of three orthogonal directions assigned as eigenvectors, which can be visualised together as an ellipsoid. If we consider the movement of water as unhindered, i.e. 'isotropic', the eigenvalues (λ1, λ2 and λ3) are equal in all axes. As water movement becomes progressively more 'anisotropic' the ellipsoid becomes elongated and by convention, the largest 'principle' eigenvalue is assigned λ1. The λ1 value, therefore, represents the longitudinal diffusivity. The remaining λ2 and λ3 values are perpendicular to λ1 and the average of the two is referred to as the radial diffusivity. For visualisation purposes and through convention, this is represented as a diffusion encoded colour (DEC) map (see Figure 2). Voxels in which the longitudinal diffusivity is in the craniocaudal axis are coloured blue, anterior-posterior axis green and left-right axis red. A six-dimensional representation is provided with each three-dimensional voxel in the brain, encoding a three-dimensional map of water displacement. If the voxel size is sufficiently small enough or only includes axon bundles running precisely in parallel, then the tensor will be a true and accurate reflection of the actual axonal direction. If, on the other hand, the voxel size is large, or there are crossing axon populations, then the tensor will misleadingly reflect the average fibre direction. Alternative methods such as q-space approaches are based on high-angular resolution diffusion imaging (HARDI) and allowing multiple axon directions within a single voxel to be differentiated within an acceptable time-frame. One such method is q-Ball imaging and is based on a dense sampling of directions (defined by the number of

gradients, typically >60) on a sphere (also termed a shell) with a constant radius (defined by a high b-value, typically >4000 sec/mm2) allowing the derivation of a dODF. Depending on the number q-values (directions applied) the dODF allows complex internal architecture within a voxel to be modelled such as crossing, kissing and fanning fibres. Although lower q-values result in shorter scanning times, they also inherently increase blurring of the dODF as the approximation is based on interpolations between fewer sampling points on the shell. Other methods such as combined hindered and restricted model of diffusion (CHARMED) are based on the fitting multiple different tensor models comprising of one extra-axonal compartment and a number of intra-axonal compartments, each allowing distinct fibre population modelling. Spherical deconvolution is a further extension of multiple tensor modelling in which the potential number of different fibre populations are considered infinite. Spherical deconvolution, however, can result in negative values within the dODF, which is physically implausible. Constrained spherical deconvolution (CSD), therefore, constrains the presence of negative values and significantly reduces noise.

Figure 2: Diffusion-weighted imaging acquisitions and fibre tractography

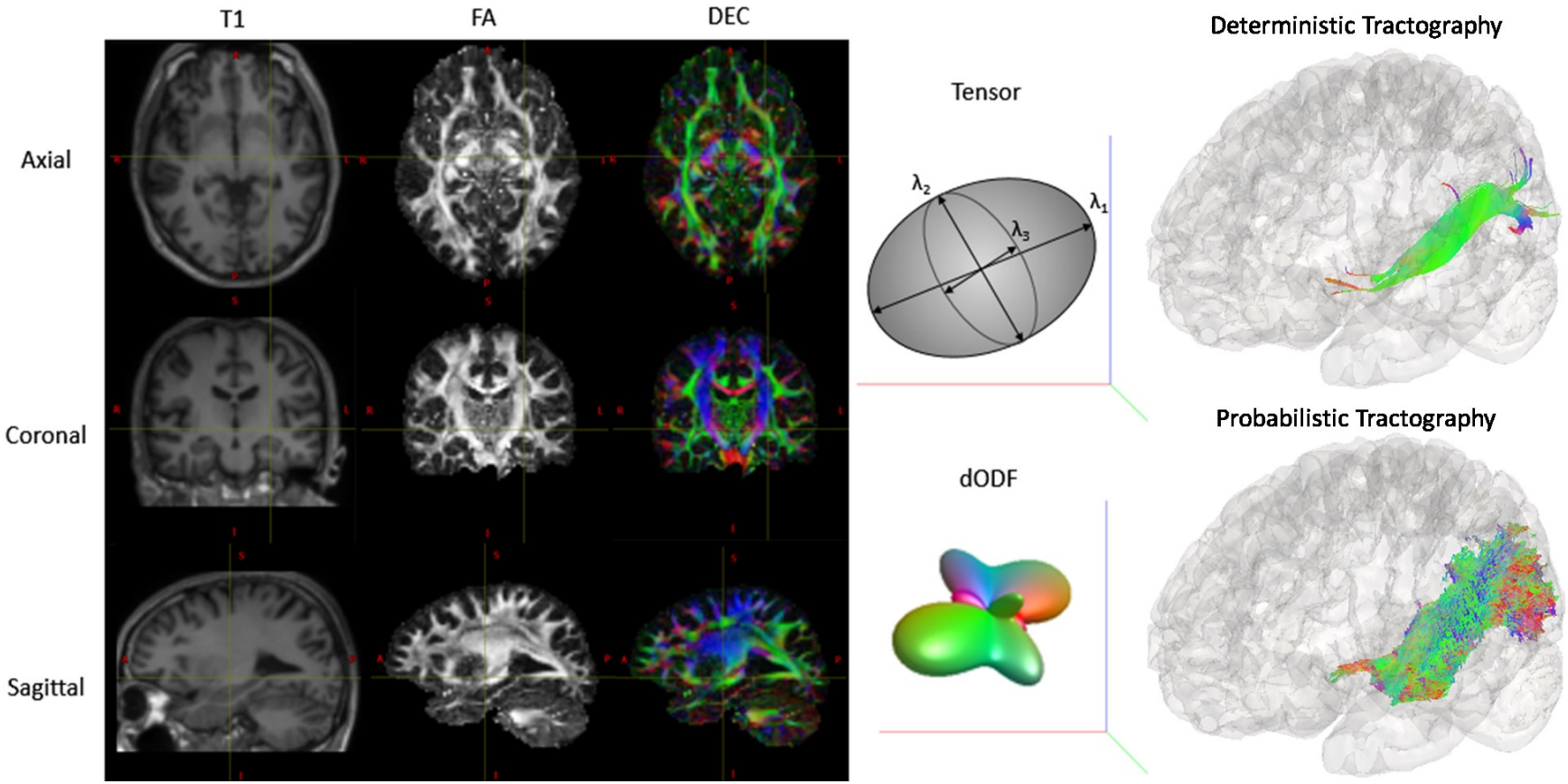

Figure 2 Legend: Axial, coronal and sagittal images from the T1, Fractional anisotropy (FA) and Diffusion encoded colour (DEC) map are shown. Tensor and diffusion orientation distribution function (dODF) representations at the site of the crosshair (left lateral geniculate nucleus). The dODF shown was calculated using a constrained spherical deconvolution technique. Corresponding results of tractography of the left optic tract and radiation reconstructed with a seed voxels placed in the left lateral geniculate nucleus, inclusion region in the left sagittal stratum and exclusion regions placed in the ipsilateral frontal lobe and contralateral hemisphere. Left anterolateral view of fibre tractography performed using algorithms for deterministic and probabilistic tracking(Tournier et al., 2010; Willats et al., 2014)*. The anterior projection of the optic radiation (Meyer's loop) is poorly reconstructed in the deterministic tractography, i.e. more false-negative streamlines, whilst the probabilistic tractography likely over-represents the tract, i.e. more false-positive streamlines (see* (Maier-Hein et al., 2017) *for further discussion regarding this).*

Within epilepsy surgery, diffusion-weighted imaging has been applied to detect white matter structural abnormalities, reconstruct fibre tracts for intra-operative guidance and identify changes in whole-brain structural network connectivity. Studies of diffusion-weighted imaging in temporal lobe epilepsy (TLE) have utilised quantitative measures of water movement such as fractional anisotropy (FA) and mean diffusivity (MD) to infer white fibre architecture and microstructure. Mean diffusivity measures within the ipsilateral parahippocampal white matter and fimbria-fornix, as well as the uncinate fasciculus bilaterally, have been shown to be significantly higher in patients with TLE compared to controls(Keller et al., 2017). The MD of the fimbria-fornix was also found to be a predictor of postoperative seizure freedom with patients that exhibit raised MD within the fimbria-fornix outside of the resection cavity were less likely to achieve seizure-free (ILAE 1(Wieser et al., 2001)) outcome. Additionally, MD changes in the contralateral parahippocampal gyrus were also found to predict failure of surgery and may reflect a bitemporal seizure onset. Accordingly, the MD measures from the ipsilateral dorsal fimbria-fornix as well as the contralateral parahippocampal gyrus were able to predict a seizure-free outcome with a sensitivity of 84% and a specificity of 89%.

Tractography requires the user to define a seed region from which streamlines are propagated to adjacent voxels governed by the tracking algorithm. A series of constraints are then applied to allow anatomical fibre tracts to be reconstructed. Taking the example of optic radiation tractography, a seed region is typically placed within the lateral geniculate nucleus and inclusion and exclusion zones are applied based on the known anatomical course of the tract. The optic radiation is known to travel posteriorly to the occipital cortices via the sagittal striatum, a region of white matter lateral to the atrium of the lateral ventricle(Ebeling et al., 1988). Placing an inclusion region in this area, therefore, allows the results of the tracking algorithm to be refined by rejecting tracts that do no pass through the predefined inclusion zone. Similarly, the optic radiation does not propagate to the frontal lobe or the contralateral hemisphere. Exclusion zones placed within the frontal white matter and at the midline, therefore, prevent anatomically inaccurate streamline generation. The resulting fibre tract reconstruction is highly dependent on the user-defined seed, inclusion and exclusion zones(Ciccarelli et al., 2003). Furthermore, diffusion-weighted images are subject to distortions compared with anatomical scans and must be corrected prior to their use(Andersson et al., 2003). The reliability of the tract reconstruction is judged based on an estimation of the known anatomical course as there is no in-vivo gold-standard for comparison. Efforts to standardise tractography through the implementation of automatically derived regions of interest have shown this to be comparable to expert human reconstructions(Keller et al., 2017; Mancini et al., 2019), but caution is required when utilising tract reconstructions intra-operatively as it does not provide information regarding the function of the reconstructed tracts(Duffau, 2014a, 2014b). A study utilising simulated human brain data, where the ground truth tract morphology information was known, evaluated 96 tractography pipelines submitted from 20 different research groups(Maier-Hein et al., 2017). DTI-based deterministic and HARDI-based probabilistic algorithms were found to reconstruct approximately 50% and 90%, respectively, of the fibres within the superior longitudinal fasciculus, uncinated fasciculus and inferior longitudinal fasciculus. This fell to 20% and 83%, respectively, when considering the corticospinal tract. The HARDI-based probabilistic reconstructions, therefore, were more sensitive than the DTI-based deterministic algorithms, but comparatively less specific as they over-represented the size of the fibre tracts and contained more invalid streamlines. Confirmative direct electrical stimulation is recommended when employing either method as this represents the gold-standard for intraoperative functional mapping (Borchers et al., 2011).

Prevention of damage to the major white matter tracts is more critical than cortical grey matter as unlike the cortex, white matter tracts cannot exhibit plasticity and therefore functional recovery following damage is not possible(Jellison et al., 2004a). The white matter tracts that are susceptible to injury during surgical resection of epileptogenic lesions are dependent on the location and approach taken by the surgeon. In cases of mesial TLE, amygdalohippocampectomy can be undertaken through a variety of approaches. Selective amygdalohippocampectomy approaches include transcortical, trans-sylvian and subtemporal routes. Additionally, anterior temporal lobe resection involves a variable amount of resection of the lateral neocortex. Trans-sylvian and subtemporal approaches are less likely to result in visual field deficit through disruption of the temporal projection of the optic radiation (Meyer's loop) but cause damage to the temporal stem and inferior longitudinal fasciculus respectively(Hori et al., 1993, 2002; Lutz et al., 2004; von Rhein et al., 2012). Tractographic and white matter fibre dissection studies have shown considerable variability in the anterior extent of Meyer's loop ranging from 20 – 50mm from the temporal pole(Ebeling et al., 1988; Nowell et al., 2015b). The anterior extent has been shown to be significantly related to hemispheric language dominance(Nowell et al., 2015b). Both anterior temporal lobe resection and SAH have reported rates of significant visual field deficits that preclude patients from driving even if they have achieved seizure freedom in up to 50%(Beisse et al., 2014; Pathak-Ray et al., 2002; Yeni et al., 2008). Presentation of the tractographic representation of the optic radiation into the oculars of the surgical microscope during temporal lobe resection successfully averted visual field defects when surgery was performed within an interventional MRI suite(Winston et al., 2014). Tractography of the corticospinal tract and optic radiation may be of particular benefit in the pediatric population where both fMRI and awake neurosurgical resection with functional mapping is not possible. Tractography of the corticospinal tract using deterministic algorithms fails to adequately reconstruct streamlines projecting to the lateral precentral gyrus representing the hand and face motor regions(Maier-Hein et al., 2017) Probabilistic CSD tractography has been shown to generate more accurate reconstructions and is, therefore, recommended for clinical use(Kupper et al., 2015). The corticospinal tract can be reconstructed using seeds derived from fMRI data, such as during finger tapping and lip-puckering tasks, or from anatomically placed seeds. Within epilepsy surgery, the epileptogenic zone may be larger than the visualized lesion or area of recorded electrographic seizure onset following invasive recordings. Tract reconstructions can be used to plan maximal resection volumes whilst also preserving function (see Figure 3).

Figure 3: SEEG guided tailored resection of focal cortical dysplasia with utilisation of corticospinal tract tractography

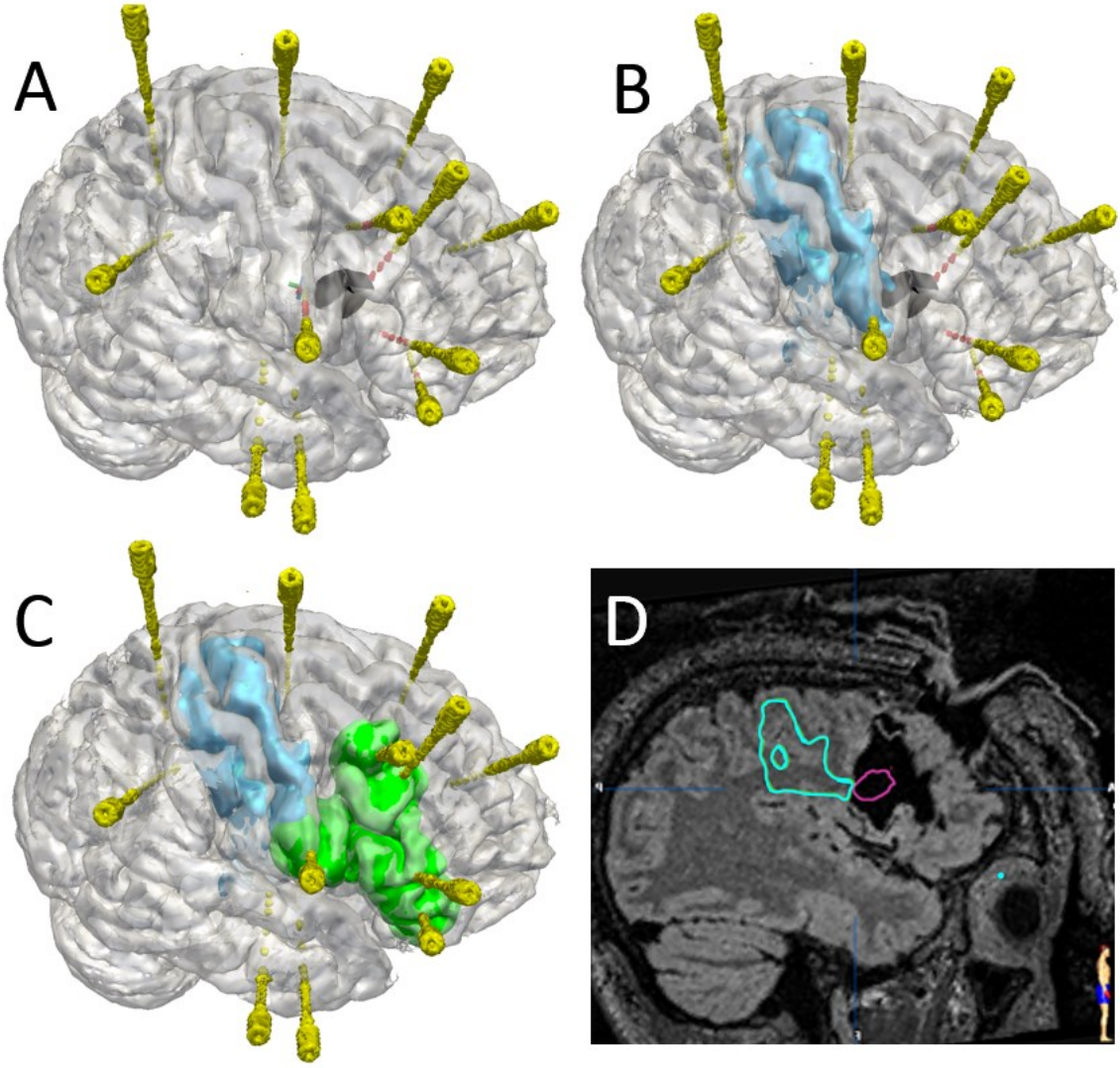

Figure 3 Legend: A) Right hemispheric implantation with a region of the thickened grey matter deep to the pars opercularis of the inferior frontal gyrus (black). SEEG implantation with electrode contacts active at the seizure onset shown in red. B) Addition of the corticospinal tract tractography in cyan. C) Proposed resection volume (green) based on active electrode contacts and constrained by corticospinal tract tractography. D) Intraoperative MRI scan showing resection of the thickened grey matter (magenta) and preservation of the corticospinal tract (cyan).

Global tractography or tractography-based whole-brain connectivity is based on individually propagating streamlines from all of the regions of interest derived from a brain atlas (nodes) sequentially and quantifying the number of streamlines (edges) that terminate in all of the other regions in the brain. In conjunction, a whole-brain connectome can be generated that represents the structural networks of the brain. Network analysis can then be performed at local and global scales through the application of graph theory metrics(He et al., 2010; Rubinov et al., 2010), to explore the structural connectivity relationships and potential perturbations within disease states(Gleichgerrcht et al., 2017). Tractography-based connectivity is weighted, based on the number of propagated streamlines, but is not directionally encoded. Comparison of whole-brain connectivity in patients with TLE compared to control subjects revealed a marked reduction in connectivity which lateralised to the side of hippocampal sclerosis. Whilst both right and left TLE were associated with diffuse global and interhemispheric connectivity reduction, left TLE connectivity changes were comparatively more pronounced in the perisylvian language circuitry(Besson et al., 2014). Correlation with histopathological findings revealed that hippocampal sclerosis results in marked remodelling of the structural connectome correlating with CA1-3 cell loss when compared to isolated gliosis(Bernhardt et al., 2019). Combination of diffusion and resting-state fMRI connectivity data has also revealed a decoupling between the structural and functional networks within the regions of the brain that are typically active at rest, known as the default mode network. Greater structural-functional connectivity decoupling has also been associated with idiopathic generalized epilepsies(Zhang et al., 2011), left temporal lobe epilepsy and higher seizure burden(Wirsich et al., 2016). Furthermore, restoration of the default mode network has been shown to correlate with better memory preservation in patients following temporal lobe surgery(McCormick et al., 2013). Studies utilising intracranial EEG recordings with structural and functional imaging data report that structural and functional connections are highly stereotyped for each patient and that seizures utilize the underlying structural connectome for non-contiguous propagation(Shah et al., 2019). Structural connectivity has also been combined with cortico-cortical evoked potentials stimulated during intracranial implantations over the electrographically confirmed seizure-onset zone. Compared to adjacent regions outside of the epileptogenic focus the seizure onset zone was significantly more hyperexcitable and highly outwardly connected(Parker et al., 2018). This opens the potential for minimally invasive techniques, such as radiofrequency ablation and laser interstitial thermal therapy to disrupt the seizure network and prevent seizures from spreading.

1.2.1.4 Novel MR contrasts

Novel MRI contrasts offer the possibility of identifying covert lesions. Current diffusion algorithms are based on an unhindered (Gaussian) model of diffusion. Diffusion kurtosis imaging (DKI) is an extension with an assumption of hindered diffusion characterized by the cell membranes of the tissue or structure under investigation. As such, the kurtosis metrics convey information regarding tissue microstructure that is no longer restricted to apparent diffusion coefficient (ADC) alone. In conventional diffusion imaging, grey matter is isotropic and LITTle information regarding the microstructure of the cortex is provided. DKI provides improved grey-white matter (GM-WM) contrast and may act as a biomarker for severity, treatment efficacy and disease subtypes(Bonilha et al., 2015).

1.2.1.5 MRI Negative cases

Concordance of neurophysiological and imaging data provides the highest chance of success following resective surgery(Téllez-Zenteno et al., 2010). It is estimated that 20-30% of patients with focal epilepsy have no identifiable lesion on clinical strength (up to 3-Tesla) MRI examinations(Duncan et al., 2016). As a result, surgical resections are less likely to be offered to such patients without additional confirmatory imaging modalities and invasive EEG investigation. Despite this, the resected volumes tend to be larger in MRI negative patients as incomplete resection of the epileptogenic focus is not infrequent. A review of the histopathological findings following resections in MRI negative patients revealed that the majority were secondary to focal cortical dysplasias with gliosis, hamartomas, hippocampal sclerosis and nodular heterotopias being less frequent(Wang et al., 2013). Ultra-high field MRI scanners, such as those at 7-Tesla, improve the signal to noise ratio and provide higher resolution images. Early results from institutions employing T2* sequences at 7-Tesla have shown promise at identifying regions of focal cortical dysplasia that were not apparent on 3-Tesla imaging(Veersema et al., 2016). Another approach to identifying subtle lesions is to deploy machine learning classifiers to multi-modal MRI sequences (T1, T2 and FLAIR). The ability to compare multiple MRI sequences at the same time allowed for ‘junction’ maps to be created at the grey-white matter interface and identification of focal cortical dysplasias that were not distinguishable by expert radiologists from the sequences individually(Bennett et al., 2019).

1.2.2 Nuclear medicine

If MRI sequences do not identify a lesion, or one that is not concordant with clinical and EEG data, functional imaging with PET or SPECT may be useful. PET imaging in epilepsy is performed interictally, due to the long uptake period and short unpredictable nature of spontaneous seizures, defining regions of cortical dysfunction through hypometabolism. Ictal and post-ictal ^{18}F-FDG PET are challenging to interpret as there may be an intricate pattern of increased and decreased uptake. Once acquired PET images are then co-registered with structural images in the form of either CT or MRI. PET-MRI provides better anatomical and functional information than PET-CT without inferior localization accuracy(Paldino et al., 2017). Interictal PET has a sensitivity of up to 90% in cases of temporal and 50% in extra-temporal lobe epilepsy(Willmann et al., 2007). The region of hypometabolism detected by ^{18}F-FDG PET is generally more extensive than the epileptogenic zone and cannot be used to outline a surgical resection plan. The role of ^{18}F-FDG PET is, therefore, to aid in hemispheric lateralization and general lobar localization in cases with discordant scalp EEG and MRI. The overall positive predictive value of achieving an Engel 1 post-surgical outcome following ^{18}F-FDG PET in temporal lobe epilepsy was 77.5% when MRI, EEG or both were non-concordant. PET provides limited additional value in cases where the MRI and scalp EEG are concordant and is even associated with a false positive rate of 6.9%(Willmann et al., 2007). Specific PET ligands for GABA-A, NMDA, opioid and serotonin receptors have research applications and the potential for clinical use to localize the EZ, but are not yet in widespread use(Duncan et al., 2016).

SPECT imaging utilizes technetium-99m-labelled ligands to measure regional cerebral blood flow. Due to the very short brain uptake time (2 minutes) the tracer can be administered at the time of seizure onset and will be distributed in the brain as a reflection of the relative cerebral blood flow (rCBF) at the time of injection. The tracer shows LITTle redistribution for at least 2 hours and coupled with the long half-life of ^{99m}Technetium (6 hours) provides an acceptable timescale for clinical use. The timing of tracer administration as early into the seizure onset as possible is critical for the identification of the hyperperfusion associated with the seizure onset zone. Delayed administration will result in a 'false positive' involvement of areas that show hyperperfusion due to early seizure propagation. Studies comparing ictal SPECT to interictal ^{18}F-FDG PET have shown a sensitivity of 70.3% and 77.7%, respectively(la Fougère et al., 2009). When ictal and interictal SPECT are normalized and subtracted, the sensitivity of SPECT reached 87% surpassing interictal PET(Desai et al., 2013).

1.2.3 Other functional imaging methods

Simultaneous scalp EEG-fMRI recordings can show hemodynamic alterations associated with interictal epileptic discharges, with a sensitivity of 30-40%(Grouiller et al., 2011) and may be useful for planning intracranial implantations,(van Houdt et al., 2013) with widespread abnormalities warning of poor outcome from resection(Thornton et al., 2011). Ictal EEG-fMRI often shows focal or widespread hemodynamic changes before the onset of the seizure on scalp EEG(Chaudhary et al., 2012), highlighting the low sensitivity of scalp EEG(Federico et al., 2005). The current clinical place of scalp EEG-fMRI is that localization of ictal and interictal networks revealed can be useful during the presurgical assessment, helping to design intracranial EEG sampling strategies and indicating if there is likely to be a poor outcome, which may justify stopping further investigation.

MEG is a non-invasive technique that measures the magnetic field generated by synchronized post-synaptic currents in dendrites of pyramidal cells in the cortex. Magnetic source imaging is a process in which current dipole maps of interictal spikes measured from MEG are co-registered and overlaid onto an MRI scan. The acquisition of MEG is susceptible to environmental noise, but unlike EEG is not attenuated by the skull and scalp. The spatial and temporal resolution of MEG is superior to scalp EEG, but is limited to current dipoles on the cortical surface and less sensitive to deeper sources. In a retrospective study of 132 patients, dipole source modelling of interictal spikes was possible in 78%(Englot et al., 2015). Of these patients, MEG was concordant with the lobe of resection in 66%. Comparison of long-term seizure outcomes (mean 3.6 years) in patients in which the MEG signal was concordant with the resection revealed an Engel 1 outcome in 85% compared to 37% in which the MEG signal was lateralized only, non-specific or discordant.

In clinical practice, EEG-fMRI, magnetic and electrical source imaging are used to map interictal epileptic discharges, with a small chance of recording seizures, this chance being greater with electrical source imaging as more prolonged recordings are possible. The patient group who stand to benefit from these investigations are those in whom there is not a clear surgical solution and who would require intracranial EEG to define the EZ. The data may help to generate a hypothesis that can be tested with intracranial EEG and to identify patients with widespread abnormalities, in whom invasive studies should not be carried out. Prospective studies to evaluate these issues will be very challenging and a multi-centre study with at least 12 months

postoperative follow-up would be required. It seems likely that each method would show some benefit, and with each individual technique being uniquely helpful in a subset of patients.

1.3 **Invasive EEG**

Invasive EEG methods include subdural grid and strip insertion with optional depth electrode placement through the grid or SEEG. Historically the methods used for invasive EEG have fallen into the Anglo-American and French-Italian schools of thought.

1.3.1 Grids, strips and depth electrodes

The Anglo-American method consisted of subdural grid and strip insertion. This is a procedure that involves a large craniotomy over the region of the brain of interest and upon which a silastic sheet is placed. Within the silastic sheet are a number of electrical contacts that, when placed on the cortex, record the electrical activity of the underlying brain. The main advantage of this method is that it allows for extra-operative cortical functional mapping through grid contact stimulation. This is particularly useful for lesions close to language and motor function allowing accurate delineation of the cortical function. Large 8cm x 8cm grids coupled with strip electrodes can provide robust sampling over larger areas of the lateral neocortex. The main disadvantage, however, is that deep and mesial structures are relatively under-sampled due to their inaccessibility and patient recovery is prolonged. Depending on the venous anatomy of the cortical veins entering the superior sagittal sinus it may be possible to place small grid or strip electrodes on the mesial hemispheric surfaces, such as over the supplementary motor area (SMA). Furthermore, sampling of deeper structures can be undertaken through the freehand placement of depth electrodes through the silastic sheet. Conversely, SEEG involves the stereotactic placement of electrodes along predefined trajectories. The electrodes have a variable number of contacts and spacing to allow denser sampling at the target or entry regions. Contact stimulation can still be performed for extra-operative mapping, but due to technical limitations during SEEG electrode placement a minimum distance of 1 cm is maintained at the entry point from other electrodes. This, therefore, reduces the resolution of the cortical sampling. Nevertheless, SEEG procedures have significantly increased in popularity over the last decade as they allow the epileptogenic network to be mapped and have reduced complication rates with rapid patient recovery.

Figure 4: Grid and SEEG electrode sampling methods

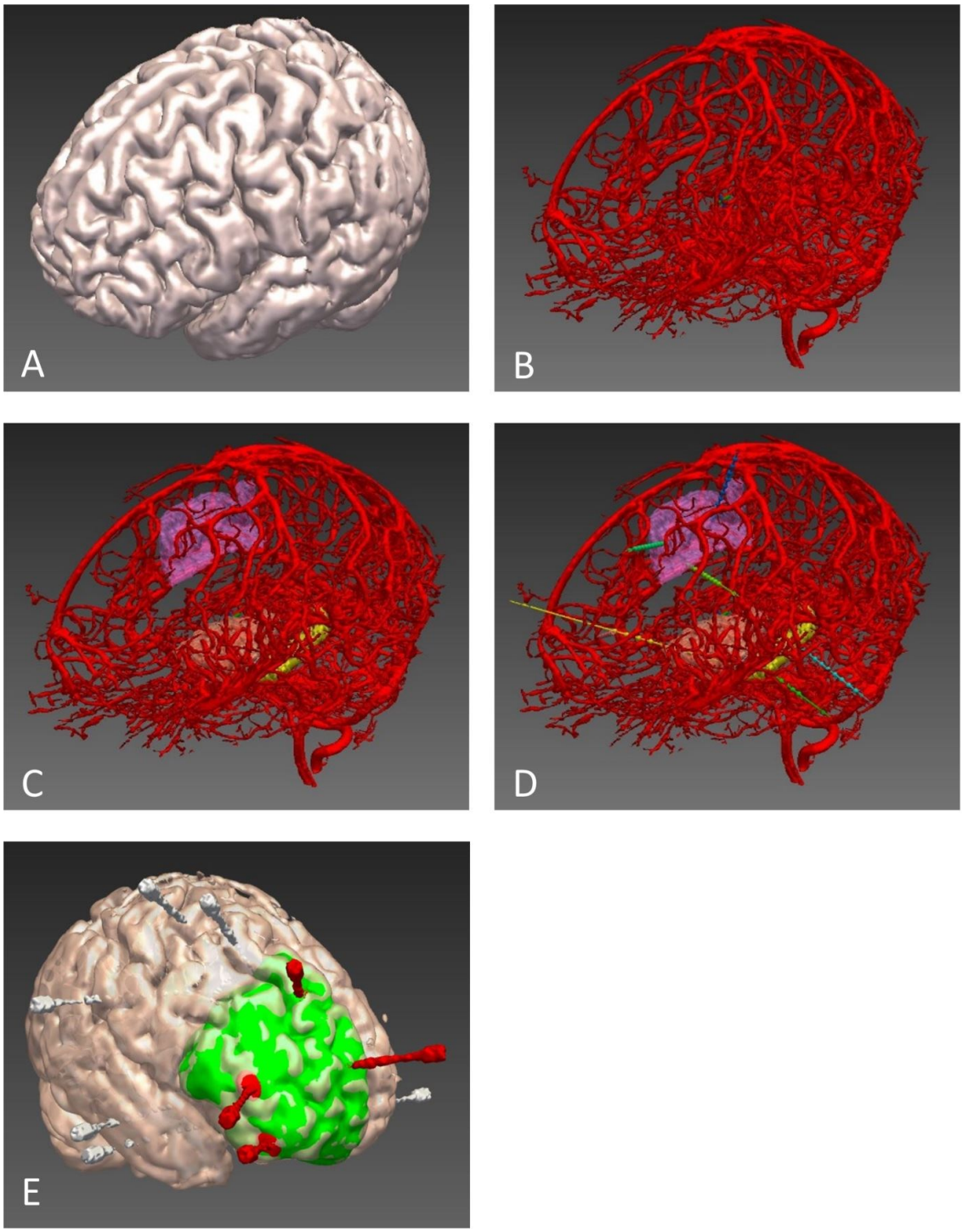

F

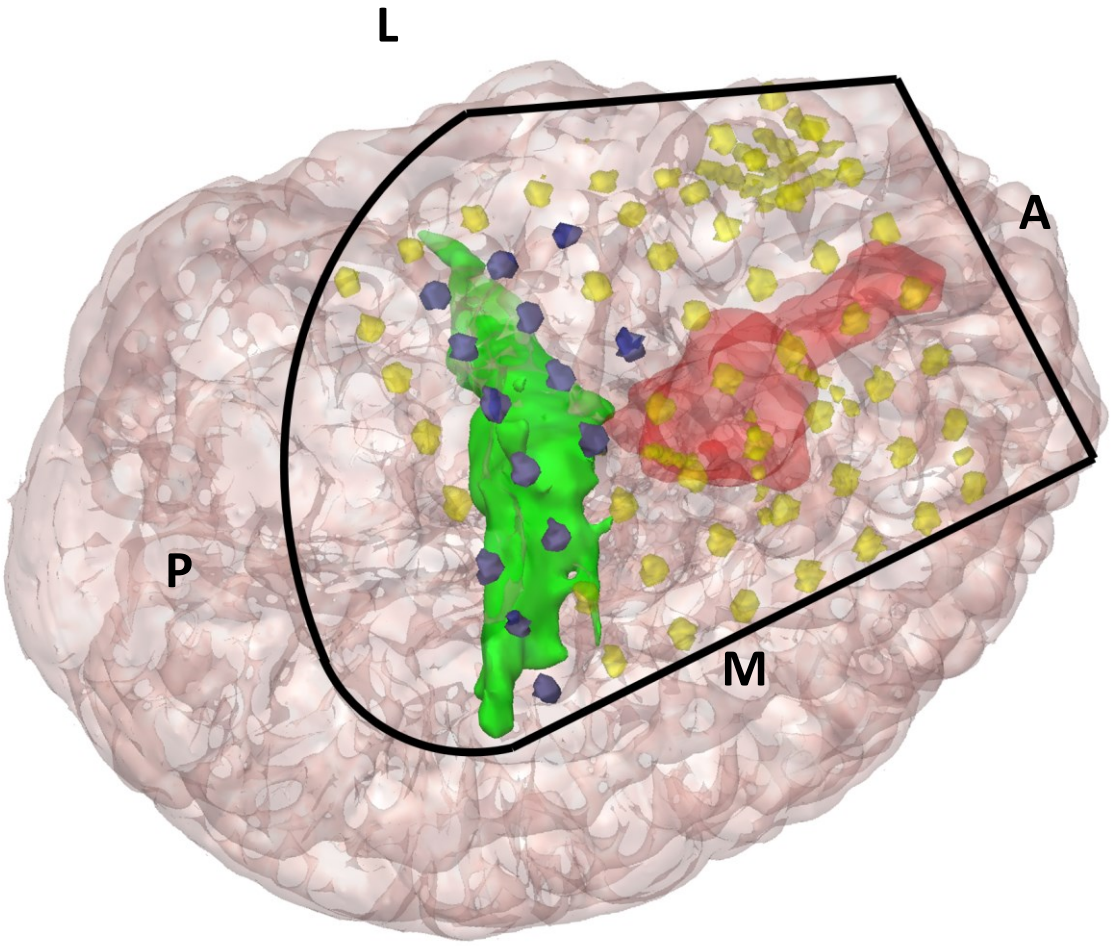

G

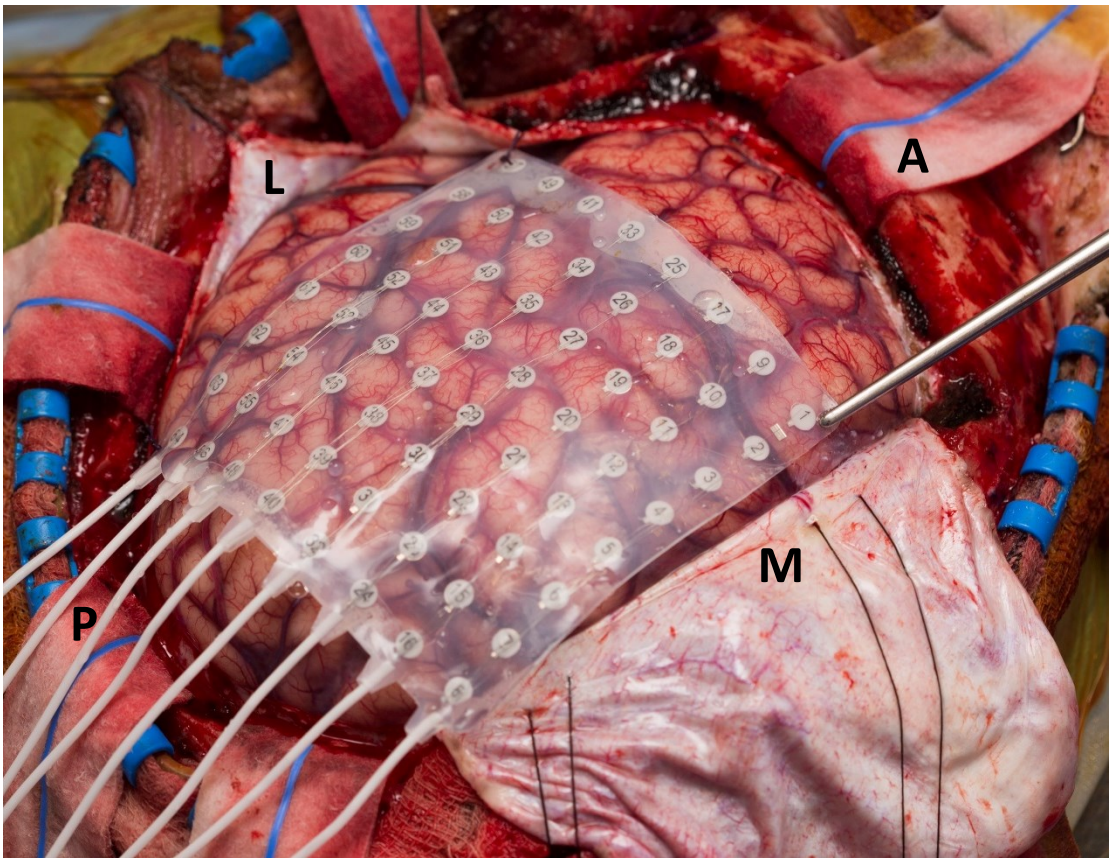

Figure 4 Legend: Left hemispheric SEEG implantation for hypothesized mesial posterior frontal seizure onset. A) View of the 3D cortical model. B) Vascular segmentation derived from DSA. C) Vascular imaging with rendering for the regions of interest for SEEG sampling. D) SEEG trajectory plans with coverage including the orbitofrontal, superior and medial frontal regions as well as motor cortex and posterior temporal regions. E) Right frontal view of another patient following implantation with bolts for electrodes with contacts active at seizure onset shown in red. F) Left hemispheric grid sampling for hypothesized frontal lobe onset. Suspected focal cortical dysplasia (red). Tractography of the underlying white matter fibre tracts reveals the position of the corticospinal tract (green) and the grid contacts eliciting motor responses following cortical stimulation (blue). Black lines delineate margins of the planned craniotomy. G) Corresponding intra-operative picture of grid placement following large fronto-temporoparietal craniotomy and dural reflection over the superior sagittal sinus. Picture orientation: A – Anterior, P – Posterior, M – Medial and L – Lateral.

1.3.2 Stereoelectroencephalography

The overall rate of complication associated with SEEG has been reported as 1.3% per patient, equating to a risk of 1 in 287 electrodes. The main complication reported was haemorrhage, occurring in 1% of patients(Mullin et al., 2016a). Haemorrhage occurs when a planned electrode conflicts with a cortical or subcortical vessel or when the method of implantation is inaccurate. The detection of vasculature within the brain for the purpose of stereotactic implantation planning is varied. Some centres prefer the use of gadolinium-enhanced or phase-contrast MR sequences (MR venography and angiography) whilst other units elect to perform CT-angiography or digital subtraction catheter angiography (DSA) pre-operatively. DSA is considered the 'gold-standard' but is invasive and in pediatric populations necessitates a general anaesthetic(Cardinale et al., 2015). Proponents of MR venography, however, do not consider the new vasculature visualized with DSA to be clinically relevant, and do not report increased haemorrhage rates(Cardinale et al., 2016b).

Planning of SEEG electrode placement is time-consuming and requires a multi-disciplinary approach to ensure that the electrodes are sampling regions that are consistent with the electrophysiological hypothesis. In general terms, SEEG electrodes are planned to enter the brain at the crown of a gyrus, maximize distance from cerebral vasculature, not to transgress

pial boundaries (sulci), not come within 10 mm of other implanted electrodes, limit the angle to which the bolt crosses the skull, avoid critical neurological structures, have the shortest feasible intracranial length and maximize grey-matter contact.

Cardinale et al. suggested a safety margin from cerebral vasculature based on the diameter of the electrode, mean implantation accuracy plus three standard deviations to ensure more than 1% of electrodes do not deviate from this(Cardinale et al., 2013). Based on their data, they implement a 3 mm safety margin. Optimizing electrodes for each of the aforementioned parameters whilst ensuring a sufficient safety margin for each electrode is challenging to plan manually. Computer-assisted planning algorithms have been described that achieve better and more consistent adherence to these parameters while significantly reducing the time for planning (De Momi et al., 2013b; Nowell et al., 2016b; Sparks et al., 2016).

Reported implantation methods for SEEG include frame-based, frameless and robotic systems. The original method of stereoencephalography used the Talairach frame(Talairach et al., 1962). Since then, several different frame-based systems have been used including the Leksell, CRW, Vogele-Bale-Honen and Fischer-Leibinger frames(V. N. Vakharia et al. 2017). These systems require the placement of a stereotactic frame on the patient before acquiring a volumetric navigation image. Automatic patient registration can be achieved through the use of an intraoperative CT scanner such as the O-arm (Medtronic Inc.). Due to the inconvenience and time associated with placing a stereotactic frame, frameless systems were developed based on the use of a neuronavigation system and adjustable arm. The patient is placed in a rigid clamp fixator, such as the Mayfield clamp and neuroanatomical targets or pre-placed markers (fiducials) are used as registration points. Bone-anchored fiducials are more accurate than scalp based fiducials or surface tracing. Most neuronavigation systems are based on the emission of infrared light from a source attached to an infrared camera. The infrared light then reflects against a series of small spheres to allow the neuronavigation system to detect instruments with known geometry in space in relation to the spheres. The instruments are then aligned to the pre-planned trajectories and fixed in place using an adjustable arm. The arm then acts as a working channel through which drilling and electrode bolt placement can be performed. Frameless techniques offer a more convenient and quicker alternative to frame-based systems, especially when 8-14 SEEG electrodes are typically inserted, at the relative cost of accuracy. Robotic systems have been introduced to allow highly accurate electrode placement with shorter implantation times compared to both frame-based and frameless systems. To date,

accuracy results have been published for Neuromate (Renishaw), ROSA (Zimmer Biomet) and iSYS1 (iSYS Medizintechnik GmbH). A recent meta-analysis of the reported accuracies of the different implantation methods revealed significant heterogeneity between the studies precluding any direct comparisons, mainly due to different accuracy measures(Vakharia et al., 2017b). In the most extensive comparative study by Cardinale et al., 1050 electrodes placed in 81 patients achieved a median 0.78 mm entry point and 1.77 mm target point error, compared to a historical cohort of 517 electrodes in 37 patients using the Talairach frame where a median 1.43 mm entry point and 2.69 mm target point error was found(Cardinale et al., 2013). It remains controversial whether the average improvement in target point accuracy between the implantation methods by an order of 1 mm is clinically significant as the electrode contacts are likely to measure electrophysiological activity within a region of interest of at least 3-5 mm and target brain structures are significantly larger. To date, no studies have delineated the size of vasculature that is critical for consideration during SEEG or the optimal method of vascular imaging and whether these factors affect haemorrhage rates.

1.4 **Surgical Treatments For Epilepsy**

1.4.1 Types of surgical procedures

A variety of surgical procedures are offered to treat different types of epilepsy. Resective surgeries can be divided into standardized and tailored procedures. Standardized resections are performed when it is clear that the EZ, defined as the volume of the brain necessary and sufficient for the generation of spontaneous seizures(Luders et al., 1993), is included within the standardized boundaries. Common standardized procedures are anteromesial temporal resections for mesial temporal lobe epilepsy and hemispherectomies for diffuse lesions that are limited to one hemisphere. Tailored resections require not only localization of the EZ, but a more precise delineation of its boundaries and consideration of the nearby critical tracts and eloquent cortex. Neocortical resections are usually tailored based on electrophysiological, imaging, and neuropsychological testing, unless the lesion lies in essential cortex, such as language or motor areas, when lesionectomies, sparing adjacent neocortex, can be performed. When a small ablation would be sufficient, this can be achieved with radiosurgery,(Chang et al., 2010) and there has been recent interest in laser thermoablation(Lagman et al., 2017). Disconnection procedures include corpus callosotomy, performed specifically for disabling drop attacks,

multiple subpial transections, which might eliminate seizures in essential cortex while sparing function, and hemispherotomy, which disconnects rather than removes one hemisphere. Palliative neuromodulation, include vagus nerve stimulation (VNS) and deep brain stimulation (DBS) (Fisher et al., 2010). Responsive neurostimulation (RNS) is a new procedure for patients with more than one epileptogenic zone or an epileptogenic zone in a cortical area that cannot be removed(Morrell, 2011). This is an innovative approach involving the implantation of a small computer in the skull, connected by electrodes to one or more EZs, which records EEG continuously, detects seizure onset, and stimulates to abort it. DBS and RNS can be useful in reducing the frequency and severity of seizures, but rarely render patients seizure-free(Duncan et al., 2015).

1.4.1.1 Mesial temporal resections

Anterior temporal lobe resection (ATLR) has undergone various modifications since its inception and involves resection of the temporal pole amygdala, hippocampal head and body and a variable amount of lateral neocortex. The most common anterior temporal resection procedure performed today is based on the technique described by Spencer et al. (Spencer et al., 1984b). The resection of the lateral neocortex was limited to a maximum of 4.5 cm measured from the temporal pole to minimize visual and speech deficits and an en bloc resection of the amygdala, hippocampus, parahippocampus, uncus and fusiform gyrus was performed through an intraventricular approach via the temporal horn. At a similar time, Wieser and Yasargil described a trans-sylvian SAH that spared the lateral neocortex in its entirety. Niemeyer et al. had previously established a transcortical SAH approach through a 2.5 cm corticotomy in the middle temporal gyrus(Niemeyer, 1958; Wieser et al., 1982). Further modifications to the Spencer anterior temporal lobectomy have been described such as ‘keyhole’ anterior temporal lobe resections that aim to further limit the lateral neocortical resection to the temporal pole (<3 cm)(Schmeiser et al., 2017). Numerous studies have aimed to compare operative approaches with regards to seizure freedom and neuropsychological outcomes. In a meta-analysis, anterior temporal lobectomy resulted in improved seizure outcome compared to transcortical SAH with an absolute risk difference of 8%, which equates to the need to treat 13 patients for an additional patient to achieve an Engel 1 outcome(Josephson et al., 2013). A randomized controlled trial of trans-sylvian and transcortical SAH in patients with MTLE gave similar seizure freedom rates at seven months follow up(Lutz et al., 2004). Transcortical SAH resulted in significantly better verbal fluency post-operatively whilst all other

neuropsychological outcomes were not affected by approach. Helmstaedter et al. prospectively compared temporal pole resection and amygdalohippocampectomy (TPR+AH) with trans-sylvian SAH and found improved post-operative figural (visually encoded) memory following right-sided trans-sylvian SAH and verbal memory following left TPR+AH(Helmstaedter et al., 2008). This suggests the importance of the temporal stem, which includes the uncinate and inferior fronto-occipital fasciculi, in dominant hemisphere verbal memory and the non-dominant lateral neocortex in non-verbal memory. Visual field deficits are common following anterior mesial temporal resections due to the proximity of Meyer's loop, which is the temporal portion of the optic radiation, to the temporal horn of the lateral ventricle. In early series, where 4 cm and 6 cm of the dominant and non-dominant temporal lateral neocortex, respectively, were routinely resected as part of the mesial temporal resection, visual field deficits occurred almost universally and were expected complications. As resections became more refined, a great emphasis was placed on preserving the optic radiation and hence reducing visual field deficit rates. In contemporary series, however, visual field deficit rates are still reported in up to 50% of patients(Nilsson et al., 2004). A randomised control trial comparing visual field deficit rates between trans-sylvian SAH and TPR+AH revealed rates of 87% and 54%, respectively(Delev et al., 2016). The method of locating the temporal horn through a basal approach using the collateral sulcus as a landmark, therefore, prevents excessive damage to the optic radiation during the temporal pole resection phase of TPR+AH. In contrast, the trans-sylvian approach identifies and enters the superior aspect of the temporal horn and therefore carries a greater risk of damage to the optic radiation. DVLA requirements for holding a Group 1 (car and motorcycle) driving licence in the United Kingdom are based on the binocular Estermann test and necessitates a field of view of at least 120^{o} on the horizontal meridian and no significant deficit within 20^{o} of the vertical meridian. The application of a standardised resection protocol implementing a maximum lateral neocortical resection of 3 cm as measured from temporal pole, still resulted in 13% of patients being disqualified from driving due to the extent of the visual field deficit. Promising results from the incorporation of optic radiation tractography overlaid in the operative microscope, within an interventional MRI setting, has revealed a significant reduction in the overall size of visual field deficits and no patients were precluded from driving(Winston et al., 2014). Retrospective studies have not found any difference in seizure freedom rates between ATLR and trans-sylvian SAH, but worse neuropsychological outcomes have been reported with ATLR (Clusmann et al., 2002; Wendling et al., 2013). Hermann et al. prospectively randomized patients to left ATLR with resection or sparing of the superior

temporal gyrus(Hermann et al., 1999). No significant difference in seizure freedom rate or neuropsychological outcome was detected. Similarly, Schramm et al. performed a multicenter randomized control trial of 2.5 cm versus 3.5 cm extent of hippocampal resection between patients with hippocampal sclerosis and found no significant difference(Schramm et al., 2011b).

1.4.1.2 Neocortical resection and extratemporal lobe epilepsies

1.4.1.2.1 Frontal lobe resection

Frontal lobe epilepsy (FLE) is the most common refractory focal epilepsy after TLE and accounts for up to 30% of cases. It is more difficult to localize the EZ in FLE than in TLE, reflecting great size, complex organization and connectivity of the frontal lobes. Frontal lobe resections carry a one-year seizure remission rate of approximately 45% (ranging from 21-61%) and less durable long term outcomes(Englot et al., 2012). Long term observational studies have shown that 90% of cases that relapse following FLE surgery do so within the first year, due to incomplete resection of the EZ(Bonini et al., 2017). Even in individuals with MRI defined lesions, the EZ frequently extends beyond this and the extent of surgical resection may need to be tailored according to the invasive EEG findings. Invasive EEG has, therefore, been recommended in both lesional and non-lesional cases of FLE and has been found to be an independent predictor of improved seizure outcome(Bonini et al., 2017). Histological analysis of most FLE resections that had normal pre-operative MRI shows focal cortical dysplasia. The most favourable postoperative outcome is associated with type 2B, with less good results associated with less discrete pathologies, which along with having a focal seizure onset, and total resection of the EZ are independent predictors of favourable post-surgical outcome(Bonini et al., 2017; Englot et al., 2012).

1.4.1.2.2 Insula resections

Insular seizure semiology often presents with a sensation of throat tightening and widespread somatic dysesthesia before developing dysphagia, dysarthria and focal motor symptoms(Foldvary-Schaefer et al., 2011). It may be difficult to determine whether seizure onset is in the insula with propagation to the temporal and/or frontal lobes or vice-versa(Barba et al., 2016). Due to its deep location, scalp EEG has limited sensitivity in localizing insular seizure onset and SEEG studies are most commonly performed through oblique, orthogonal or a

combination of approaches(Alomar et al., 2017). Insular tumour resections can be safely undertaken through trans-sylvian or transopercular approaches(Benet et al., 2016), but there are no studies comparing seizure freedom rates between operative approaches. In an initial series of insular tumours resected through a transsylvian approach, Yasargil et al. reported a seizure freedom rate of 84% (Yasargil et al., 1992). Further studies have reported seizure-free outcomes ranging from 60-70%(Laoprasert et al., 2017). It should be noted that in some series, almost 50% of patients following insular tumour resections develop transient hemiparesis with no permanent long term deficits(Malak et al., 2009). Insula resections, without a well-defined lesion on MRI, require a careful analysis of the risk-benefit ratio, especially in the language-dominant hemisphere.

1.4.1.2.3 Parietal lobe resections

Parietal lobe epilepsies account for 2-6% of patients undergoing epilepsy surgery(Asadollahi et al., 2017; Salanova, 2012). Due to the widespread connectivity of the parietal lobe, patients have few localizing semiological features and can present with somatosensory disturbances, vertigo, psychic symptoms and language dysfunction(Balestrini et al., 2015). Propagation to the frontal lobes results in hyperkinetic manifestations whilst automatisms and auditory hallucinations can develop with spread to the temporal lobe. Parietal lobe epilepsies may, therefore, be misdiagnosed as frontal or temporal in origin. Scalp EEG findings are also often poorly localizing with a single study finding that ictal onset could be detected in one-third of cases(Salanova, 2012). In the remaining cases, EEG findings were either non-localising or normal. As such positive MRI findings were most predictive of a parietal epileptogenic source. Post-surgical outcomes vary widely between 45%-78% achieving Engel 1 outcomes. Of note, in reported series with the best surgical outcomes, almost all patients had a focal MRI lesion(Asadollahi et al., 2017).

1.4.1.2.4 Occipital lobe resections

Occipital lobe seizures are uncommon. Semiological manifestations include visual auras and disturbances such as hallucinations, blindness, nystagmus and blinking as well as altered mental state and secondary generalization(Foldvary-Schaefer et al., 2011). Scalp EEG is often misleading with interictal spikes being most prominent over the temporal lobe. In patients with known epileptogenic sites in the occipital lobe, scalp EEG demonstrated occipital inter-ictal spikes in only 17%(Salanova et al., 1992). Compared to other forms of epilepsy, occipital lobe

epilepsies are more often multifocal, thus complicating the diagnosis and surgical management. In a recent meta-analysis surgical resection had an average of an Engel 1 outcome in 65% of cases (range 20-100%)(Harward et al., 2018). Detection of pathology on histological analysis, abnormal MRI features and age <18 years were all found to be predictive of successful surgical outcome. Due to the proximity of the optic radiation and primary visual cortices occipital lobe epilepsy surgery carries a significant risk of postoperative visual dysfunction, occurring in in two-thirds of patients. Language deficits and visual neglect may also be associated.

1.4.1.2.5 Multi-lobar resections and Hemispherotomy

Multilobar resections are usually undertaken in individuals with extratemporal seizure onset. The most common cause is a focal cortical dysplasia that is associated with a widespread epileptogenic network. Such resections are usually extensive to achieve seizure freedom and may need to be guided by intraoperative electrocorticography. The presence of functional eloquent cortex usually limits the extent of the cortical resection and may necessitate subtotal resection of the epileptogenic zone. Depending on the extent of the surgical resection and the completeness of the resection, seizure freedom rates of 60-70% may be achieved(Sarkis et al., 2012). When the EZ is too large for a multilobar resection but is confined to one hemisphere, hemispherotomy, or functional hemispherectomy, may be considered. In general, this is restricted to patients who have already developed a significant hemiparesis with a useless hand. The most common indications are Rasmussen's encephalitis, hemimegancephaly, perinatal stroke, hemispheric malformations of cortical development, Sturge-Weber syndrome and hemiconvulsion-hemiplegia-epilepsy(Marras et al., 2010). The initial description of hemispherectomy was in 1928 as a treatment for malignant gliomas(WE, 1928). The first use for the treatment of epilepsy was in 1938(Bahuleyan et al., 2013). The term 'anatomical hemispherectomy' involved total anatomical resection of a single hemisphere with or without the inclusion of the basal ganglia. This was a very morbid procedure with numerous complications including significant blood loss, post-operative hydrocephalus and superficial cerebral hemosiderosis. Superficial cerebral hemosiderosis is a delayed complication that resulted from recurrent haemorrhages into the subdural cavity. Connection with the ventricular system was thought to be the cause of the postoperative hydrocephalus. The anatomical hemispherectomy was therefore abandoned in favour of a functional hemispherectomy or hemispherotomy.

Functional hemispherectomy comprises resection of the temporal lobe and central regions with disconnection of the remaining structures from the contralateral hemisphere and brainstem(Rasmussen, 1973). Further modifications of the technique have focused on disconnection, as opposed to resection, of the affected hemisphere and have been termed 'hemispherotomy'. The distinction between functional hemispherectomy and hemispherotomy is dependent on the extent of cortical resection that is performed. Transventricular and transsylvian, as well as open and endoscopic approaches, have also been described(Schramm, 2002; Schramm et al., 2001). Functional hemispherectomy / hemispherotomy has one of the highest rates of seizure freedom with some series reporting rates of up to 90% Engel 1 outcome(Di Rocco et al., 2000). A recent meta-analysis found a pooled seizure freedom rate of 73%(Hu et al., 2016). Failure of hemispherectomy / functional hemispherotomy may be a result of the presence or development of a new EZ within the contralateral hemisphere or inadequate disconnection. Due to the low incidence of performing the procedure, even within highly specialized centres, there is unlikely ever to be a prospective comparison of operative techniques. A single Canadian series retrospectively compared peri-insular hemispherotomies to hemidecortication and reported a doubling in seizure freedom rates with the former approach(Kwan et al., 2010). Pre-operative factors suggestive of a poor postoperative seizure freedom rate include older patient age, bilateral imaging abnormalities and malformations of cortical development(Marras et al., 2010).

Post-operatively homonymous hemianopia and some degree of motor and somatosensory deficits are expected. Most patients who are ambulatory prior to surgery remain so afterwards with the aid of orthoses. As expected, there is the loss of fine motor skills in the contralateral upper and lower limbs whilst cognitive outcomes are usually stable after functional hemispherectomy / hemispherotomy, with language functions having developed in the contralateral hemisphere (Hu et al., 2016).

1.4.1.2.6 Corpus callosotomy

Corpus callosotomy is a palliative procedure performed in patients with epilepsy of generalized, diffuse bilateral or unilateral origin with rapid propagation to the contralateral hemisphere. Disconnection of the cerebral hemispheres is particularly successful at preventing secondary seizure generalization and drop attacks. Corpus callosotomy is performed through a midline interhemispheric microsurgical approach, although endoscopic approaches have also

been described(Smyth et al., 2017a). Corpus callosotomy can be either anterior, posterior or total(Graham et al., 2016). Anterior corpus callosotomy involves transection of the commissural fibres between the prefrontal and paracentral regions passing through the rostrum, genu and body, whilst posterior corpus callosotomy is restricted to the splenium and isthmus(Paglioli et al., 2016). In some cases, anterior corpus callosotomy is performed as an initial stage and converted to a total corpus callosotomy if patients do not have sufficient improvement in seizure outcomes. No cases of disconnection syndrome were described following anterior compared to 12% following total corpus callosotomy. Other sequelae include akinetic mutism and sphincter dysfunction that are usually transient. Meta-analyses have shown a worthwhile (>50%) reduction in seizures in 58.6% of anterior compared to 88.2% of total corpus callosotomy cases(Graham et al., 2016). Posterior corpus callosotomy as an initial procedure has been suggested in order to preserve prefrontal connectivity due to similar outcomes between posterior and total corpus callosotomy(Paglioli et al., 2016). Rathmore et al. reported a satisfactory seizure reduction in 33% of cases following anterior two-thirds corpus callosotomy and 82% following total corpus callosotomy in paediatric patients(Rathore et al., 2007). 80% of the patients who underwent anterior corpus callosotomy became seizure-free when a second-stage procedure to disconnect the splenium was undertaken(Bower et al., 2013). Eighty-three percent of patients had complete resolution and 90% had a worthwhile improvement in drop attacks with selective posterior corpus callosotomy alone(Paglioli et al., 2016). Current practice favours a partial callosotomy as the initial procedure, with an anterior two-thirds transection if EEG abnormalities show frontal predominance. Completion of the transection may be performed if drop attacks continue, although some groups advocate total callosotomy upfront. Open corpus callosotomy involves a bicoronal incision and midline craniotomy to expose the superior sagittal sinus. The dural reflection is made towards the midline to protect the superior sagittal sinus and an interhemispheric dissection is performed. The cingulate gyri are parted and the callosomarginal and pericallosal arteries identified and protected. The corpus callosum is then encountered and transection is performed through microsuction and sharp dissection until the ependyma overlying the lateral ventricles and forming the septum pellucidum is encountered.

Novel minimally invasive alternatives to open corpus callosotomy include stereotactic radiosurgery(Barbaro et al., 2018) and laser interstitial thermal therapy(Hoppe et al., 2017). Due to the therapeutic latency and cerebral oedema associated with stereotactic radiosurgery, it is

rarely performed as first-line therapy(McGonigal et al., 2017; Pendl et al., 1999). Laser interstitial thermal therapy (see Chapters 1.4.3) is a novel stereotactic procedure that is capable of performing thermal ablations. The thermal ablations are dependent on the stereotactic placement of a small laser fibre and its associated cooling catheter within the structure of interest. Laser anterior two-thirds corpus callosotomy(Palma et al., 2018), completion posterior corpus callosotomy(Ho et al., 2016) and total callosotomy(Lehner et al., 2018; Pruitt et al., 2017) (one- and two-stage) have all been described in small single-centre case series. Due to the curved shape of the corpus callosum and linear laser fibre placement, disconnection usually requires three independent trajectories(Karsy et al., 2018). This is achieved through two frontal trajectories and a non-dominant parietal trajectory. One of the frontal trajectories passes through the superior or middle frontal gyrus to target the rostrum of the corpus callosum. The second frontal trajectory passes through the superior or middle frontal gyrus to target the posterior body of the corpus callosum. The non-dominant parietal trajectory usually enters through the superior parietal lobule, or angular gyrus, due to presence of veins and lacunae draining into the superior sagittal sinus and targets the genu of the corpus callosum. To achieve disconnection through thermal ablation, the target points need not cross the midline. The complex 3-dimensional nature of the trajectory planning to ensure complete disconnection and optimisation of safety metrics makes this procedure ideally suited to computer-assisted planning (see Chapter 8).

1.4.2 Stereotactic radiosurgery

Stereotactic radiosurgery (SRS) comprises the precise convergence of gamma rays to regions of the brain that results in a lesion. It is associated with a mean delay of 10-24 months to render patients seizure-free. Seizure free outcomes range from 0-86% with a pooled estimated mean Engel 1 outcome of 51%(Feng et al., 2016). Complications similar to open surgical resection include visual field deficit and cognitive and psychiatric impairments. Headache and cerebral oedema are not uncommon, and frequently there is a transient increase in focal seizures in the months following treatment, and there is the possibility of radionecrosis(Usami et al., 2012). The ROSE (Radiosurgery or Open Surgery for Epilepsy) randomised control trial was recently completed evaluating the efficacy of gamma knife as a potential first-line alternative to surgery for the treatment of mesial temporal lobe

epilepsy(Barbaro et al., 2018; Rolston et al., 2011). This comprised a multicentre study of 14 epilepsy centres in the USA, UK and India, but was stopped early due to poor recruitment. In total, 58 patients were recruited, of which 31 were randomised to the SRS arm and 27 to the open surgery arm. Due to the delayed therapeutic effect associated with radiosurgery, the primary end-point of seizure remission rate was assessed between 25-36 months post-intervention. Open surgery provided a significantly higher seizure freedom rate of 78% compared to 52% following SRS. Additional secondary outcomes included verbal memory and quality of life indices. Of interest, the gradual reduction in seizure frequency associated with SRS meant that within the first three months following therapy, 94% of patients continued to have seizures compared to 19% following open surgery. Similarly, the quality of life indices mirrored seizure freedom rates and unlike open surgery were therefore delayed until after 24 months in the SRS group. Adverse events were significantly more frequent following SRS compared with open surgery. Complications associated with SRS were delayed and presented between 11-27 months, whilst all complications associated with open surgery occurred within the first 3 months. Two patients developed significant intracranial infections following open surgery, whilst headache, cerebral oedema, new neurological deficits, seizure exacerbation and pin-site infections were reported as serious adverse events related to SRS. Two-thirds of patients following SRS required steroid treatment as a result of post-operative oedema. Expected visual field deficits consisted of superior quadrantanopsia and occurred in 34% of SRS and 42% of open surgery patients. Verbal memory was assessed using the California Verbal Learning Test (CVLT) and revealed no significant difference at last study follow up. Overall, the ROSE study has shown that SRS is inferior to open surgery in terms of seizure remission rate, but the authors conclude that it may still be a valid alternative in patients that are not be candidates for open surgery. Further uses of stereotactic radiosurgery for epilepsy include corpus callosotomy and treatment of hypothalamic hamartomas(Celis et al., 2007; Regis et al., 2017).

1.4.3 MR-guided laser interstitial thermal therapy

MR guided Laser Interstitial Thermal Therapy (LITT) is a novel minimally invasive treatment which can result in a focal ablation zone between 5-20 mm in diameter. The heating induced by the laser is monitored using MR thermography which is acquired in real-time and allows precise control of the ablation zone. Two commercial systems have currently been used

in neurosurgery, Visualase (Medtronic Inc.) and NeuroBlate (Monteris Medical). The Visualase system has mostly been for epilepsy ablation procedures in patients with hypothalamic hamartoma (HH), focal cortical dysplasia (FCD) (Ellis et al., 2016; Lewis et al., 2015), tuberous sclerosis (TS)(Lewis et al., 2015), periventricular heterotopia (PVH)(Esquenazi et al., 2014) and mesial temporal lobe epilepsy (Wicks et al., 2016). Two industry-funded uncontrolled prospective open-label studies are currently on-going. The Feasibility Study on LITT for Medical Refractory Epilepsy (FLARE) study (NIH Clinical Trials.gov NCT02820740, 2016), sponsored by Monteris Medical is aiming to enrol 30 patients from 6 institutions, whilst the SLATE study (NIH Clinical Trials.gov NCT02844465, 2016), sponsored by Medtronic Inc., lists a recruitment target of 150 patients from 16 participating centres. Both studies are restricting enrolment centres within the USA.

MTLE represents the largest cohort of patients in which LITT has been performed. Jermakowicz et al. reported 23 patients in whom 65% achieved an Engel 1 outcome at a minimum of one year follow up(Jermakowicz et al., 2017b). Laser trajectories and ablation volumes in patients that achieved Engel 1 outcome were compared with Engel 2-4 and revealed a lateral position of the laser within the head of the hippocampus resulted in a lack of ablation of the mesial hippocampal head and persistent seizures. Wu et al. implemented a standardized protocol to improve laser trajectories and found this increased total, hippocampal and amygdala ablation volumes(Wu et al., 2015). Similar to the placement of SEEG electrodes, laser trajectories should avoid cerebral vasculature and pial boundaries, circumvent the atrium of the lateral ventricle and maximize ablation volume of the hippocampus and amygdala. Drane et al. reported a prospective non-randomized comparison of 19 patients that had LITT compared with 39 patients following tailored resection, selective amygdalohippocampectomy and standard anterior temporal lobectomy (Drane et al., 2015). Engel 1 postoperative outcomes at six months were 58% in the LITT and 62% in the surgical cohorts. This study also demonstrated that cognitive outcomes with regards to the naming of common objects and famous face recognition were better preserved following LITT. Given that LITT may result in less adverse cognitive effects, can be repeated if necessary and does not preclude open surgical resection if optimal seizure outcome is not achieved, it may represent a minimally invasive first-line treatment in patients with MTLE.

In a series of 14 pediatric patients with HH, laser ablation resulted in 86% seizure freedom and no permanent surgical complication following a nine-month mean follow

up(Wilfong et al., 2013). In a smaller study, LITT has also been shown to be feasible as salvage therapy in patients who had previously undergone unsuccessful stereotactic radiosurgery or partial surgical resection of HH(Burrows et al., 2016). Lewis et al. reported a pediatric series of 19 patients in whom 11 had FCD and achieved an Engel 1 seizure outcome in 45%(Lewis et al., 2015). It should be noted that most of the patients had previous unsuccessful surgery prior to LITT and were discharged within one day of surgery. Inaccurate laser placement in a single FCD patient, however, resulted in an intraventricular haemorrhage, aseptic meningitis and required CSF diversion. In the whole series, including patients with tuberous sclerosis, HH and Rasmussen's encephalitis, the authors reported complications in 24% of patients including one case of device malfunction in which the laser tip could not be retrieved and was retained within the brain. LITT has also been used in a staged fashion to ablate surgically inaccessible portions of FCD prior to open surgical resection of the remaining lesion. This resulted in complete eradication of the otherwise unresectable FCD acting as an adjunct to open surgery and resulted in seizure freedom at 12 months follow up(Ellis et al., 2016).

A single centre case series has reported the complications associated with early experience of LITT for a variety of indications including MTLE, corpus callosotomy, intracerebral lung metastases, myxopapillary ependymoma of the cauda equina, glioblastoma, radiation necrosis and hypothalamic hamartoma(Pruitt et al., 2017). This reports a complication rate of 22.4% (11/49) including intracerebral haemorrhage, cranial neuropathy, device malfunction and malposition and persistent neurological deficit. Persistent neurological morbidity was secondary to direct thermal injury in 6% (3/49). Malposition of the laser fibre was reported in 4 cases and the authors attributed this to the use of the precision aiming device compared to a frame-based method of stereotaxy. Additional factors attributing to improved accuracy of implantation was the addition of metal skull anchors and stylets for long trajectories.

Figure 5: Laser interstitial thermal therapy for MTLE

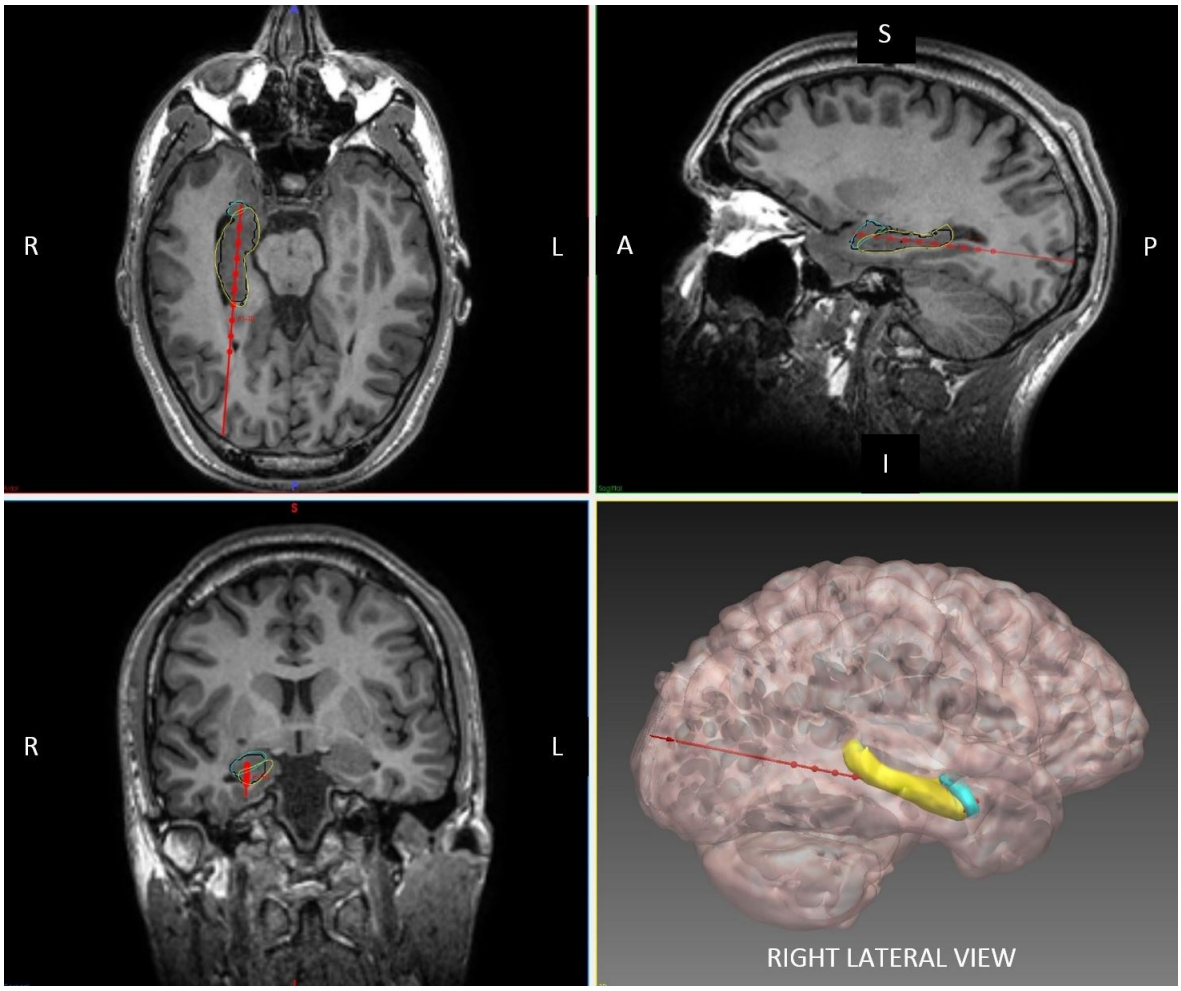

FIGURE 5 Legend: Axial, sagittal, coronal, and 3-dimensional reconstruction of planned laser ablation trajectory (red) with an outline of the hippocampus (yellow), amygdala (cyan), and modelled ablation cavity (black). Other structures, such as the entorhinal cortex and parahippocampal gyrus, have been excluded for clarity. The entry point of the trajectory is centred over the crown of a gyrus, parallel to the superficial sulci. The ideal trajectory should maximize distance from vasculature, avoid crossing sulci or the lateral ventricle. In this example, the entry point is within the inferior occipital gyrus and the target point is on the anterior border of the amygdala. The Visualase (Medtronic) system is capable of performing an

ablation diameter of between 5 and 20mm. The modelled ablation cavity shown above is based on a conservative estimate of 15mm.

1.4.4 MR-guided focused ultrasound

MR guided focused ultrasound (MRgFUS) ablation is a minimally invasive method of creating focused lesion ablations that have multiple proven applications throughout the body including breast, liver, prostate and uterine tumours(Jolesz et al., 2005). The confluence of highly concentrated ultrasound waves, at a discrete location, causes a thermal injury that results in necrosis. The extent of the lesion can be monitored in real-time(Jolesz et al., 2005) and precisely controlled using MR thermography. Until recently, the main obstacle to targeting intracranial lesions was the significant attenuation of the ultrasound waves and resultant heating of the overlying skull. The development of US transducers with over 1000 array elements, active scalp cooling and improved focusing has seen a resurgence in interest in transcranial MRgFUS for the treatment of brain tumours, epilepsy and functional neurosurgery(Jenne, 2015). All clinical studies to date have used the commercially available ExAblate system (In-Sightec Ltd, Israel). Studies have been performed for the treatment of chronic pain and drug-resistant essential tremor through focal lesioning of thalamic nuclei(Jeanmonod et al., 2012; Lipsman et al., 2013). Monteith et al. reported a feasibility study in which MRgFUS was used to perform 'virtual' anterior temporal lobectomies on gel-filled cadaveric skulls(Monteith et al., 2013). Cavity volumes of 5 cm^3 could be achieved with minimal heating of the skull base. Given that longer sonication times would be required to generate permanent lesions in vivo, blocking algorithms have been suggested to prevent potential complications such as cranial neuropathies. MRgFUS remains an exciting potential therapy that may have utility for minimally invasive ablation or disconnection procedures, especially with lesions in eloquent or deep-seated locations.

1.5 **Neurological and Surgical Complications of Epilepsy Surgery**

Neurological complications of epilepsy surgery depend on the extent and location of the surgical resection and any pre-existing functional deficits. Neurological complications of temporal and extra-temporal lobe resections are governed by hemispheric language dominance, the potential for vascular injury and proximity to critical white matter tracts and eloquent cortex. The white matter tracts at risk during temporal lobe surgery include the temporal portion of the optic radiation (Meyer's loop), uncinate fasciculus (UF), inferior fronto-occipital fasciculus (IFOF), superior longitudinal fasciculus (SLF), arcuate fasciculus (AF) and the inferior longitudinal fasciculus (ILF)(Duffau et al., 2008; Mancini et al., 2019).

In a recent Cochrane review of epilepsy surgery outcomes, less than half of the included studies provided data on surgical complications and procedure-related deaths(West et al., 2015a). The reported overall complication rate was 7.3% from the eligible studies. Few studies, however, reported pre- and post-operative neuropsychological assessment of cognition, language, memory, social function, formal visual field testing and psychiatric sequelae. A review spanning 25 years and almost one thousand patients following epilepsy surgery at a single institution found that the overall incidence of complications was 17.2%(Gooneratne et al., 2017). The most common complication was a permanent visual field deficit, significant enough to prevent retaining a driving license, in 9.4% following temporal lobe resection. Other neurological deficits included hemiparesis (1%), dysphasia (1%), frontalis muscle weakness (0.2%) and oculomotor nerve paresis (0.1%). Incidence of severe infection requiring bone flap removal was 2.6% whilst intracranial infection was 0.9%. The risk of infection was 4-fold higher in those that underwent subdural EEG grid placement prior to resection. Other rarer complications included postoperative haematoma (0.3%), hydrocephalus (0.3%) and CSF leak (1.2%). Reported complication rates are higher in patients older than 50 years undergoing surgery and range from 6-25% in different series(Grivas et al., 2006).

1.5.1 Neuropsychological function

Neuropsychological function in epilepsy patients can be influenced by a number of factors including brain injury, developmental malformations, seizure frequency, interictal spike discharges, psychiatric history and medication side-effects(Baxendale et al., 2019). The impact of a neurosurgical intervention on the neuropsychological function is, therefore, dependent on the pre-operative level of function and hence the 'cognitive reserve' in the unaffected regions

of the brain. Release phenomena may result in patients having improved neuropsychological function once seizure control is achieved. Broadly speaking, long-term memory can be categorised into declarative and non-declarative memory(Hoppe et al., 2007). Declarative memory describes the ability to recall facts and events consciously and can be further subdivided into the episodic and semantic memory. Episodic memory specifically relates to the recall of personal experiences and is also known as 'autobiographical memory', whilst semantic memory applies to the general knowledge of concepts, words and their meaning. Patients with temporal lobe epilepsy have impairments of declarative memory whilst non-declarative (e.g. the memory of procedural tasks) memory remains unaffected(Skirrow et al., 2015). In addition, the corresponding decline can be further categorized into verbal and non-verbal depending on whether the seizure-onset is within the speech-dominant or non-speech dominant temporal lobe, respectively(Tanriverdi et al., 2008). Further anatomical distinctions can be made based on whether the seizures arise from the temporal neocortex, which predominantly affects the ability to acquire new information (learning), or the mesial temporal lobe structures, such as the amygdala, hippocampus and parahippocampal gyrus, concerned with consolidation, retention and delayed recall (long-term memory)(JonesGotman et al., 1997; Joo et al., 2005). The effect of antiepileptic drugs may also have significant implications on neuropsychological testing, but these may be masked by the confounding effects of improved seizure control and must, therefore, be accounted for when investigating neuropsychological outcomes. Furthermore, poor performance on task-specific neuropsychological tests may be secondary to generalised medication effects on alertness, attention and psychomotor functions as well as behavioural side-effects. An added complexity is the synergistic effect of polytherapy on neuropsychological function.

Overall, adverse cognitive effects are reported in between 30-40% of patients following epilepsy surgery. Comparisons between different surgical approaches suggest that a standard anterior temporal lobe resection, including the lateral neocortex, temporal pole and mesial structures causes impaired acquisition (learning) and delayed recall (long term memory), whilst a selective amygdalohippocampectomy sparing the lateral neocortex causes decline in delayed recall only. This would suggest that the mesial temporal structures are critical for memory retention, whilst the lateral neocortex is vital for learning new information(Tanriverdi et al., 2008). Confusingly, however, patients undergoing resections of the lateral neocortex alone do not show isolated impairments in the acquisitions of new memories suggesting a more complex

interplay between mesial and lateral neocortical structures(Helmstaedter et al., 2008). Patients with poor cognitive reserve prior to surgery are at risk of the greatest decline following epilepsy surgery. In carefully selected patients that achieve good seizure-free outcomes, around 25% will experience a decline in memory post-operatively. In contrast, two-thirds of patients that have a poor seizure-free outcome following epilepsy surgery go on to have significant memory decline. The discrepancy is likely to be secondary to a combination of a release phenomenon, from better seizure control, as well as the reduction or cessation of anti-epileptic drugs following surgery. A meta-analysis comparing studies reporting standard anterior temporal lobe resection with selective amygdalohippocampectomy suggested that seizure-freedom rates were significantly greater following standard anterior temporal lobe resection such that a number needed to treat of 13 would result in one additional patient achieving seizure-freedom(Josephson et al., 2013). Additional studies focusing specifically on post-operative neuropsychological sequelae in hippocampal sclerosis have suggested that different operative approaches have disproportionate effects on the right and left temporal lobe epilepsy(Helmstaedter et al., 2008; Joo et al., 2005; Lee et al., 1997). Patients that underwent a dominant hemisphere selective transsylvian amygdalohippocampectomy had a greater decline in verbal memory, whilst non-dominant hemisphere anterior temporal lobe resections resulted in worsening non-verbal memory(Helmstaedter et al., 2008). The implication, therefore, is that patients with speech dominant temporal lobe epilepsy should undergo anterior temporal lobe resections and those with non-speech dominant temporal lobe epilepsy should undergo selective amygdalohippocampectomy. One possible explanation for this is that the transsylvian amygdalohippocampectomy results in transgression of the temporal stem, which results in damage to both the IFOF and the UF (see Figure 6: Probabilistic fibre tractography of language-related tracts). Studies employing direct electrical stimulation during awake temporal lobe resections for low-grade glioma have suggested a parallel semantic language stream subserved by (i) the IFOF as a direct connection and (ii) a combination of the ILF and the UF as an indirect connection between the posterior temporal regions and the orbitofrontal cortices(Duffau et al., 2014; Mandonnet et al., 2007). Damage to one of the streams may result in preserved language function as a result of compensation through the parallel stream. A transsylvian SAH potentially causes damage to both the IFOF and UF, whilst transcortical SAH and ATLR leave the IFOF intact (Duffau et al., 2008; Schmeiser et al., 2017)(see Figure).

Figure 6: Probabilistic fibre tractography of language-related tracts

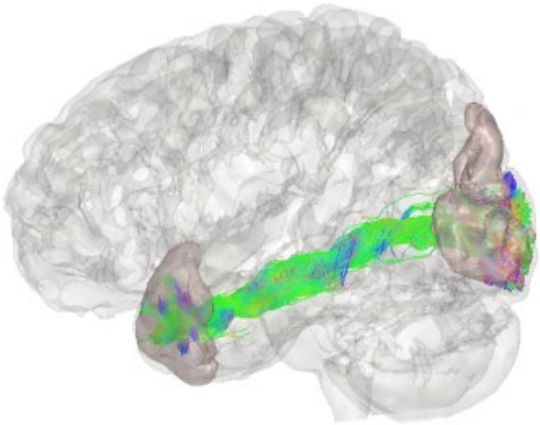

Inferior Longitudinal Fasciculus

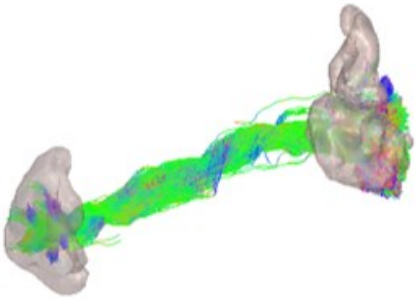

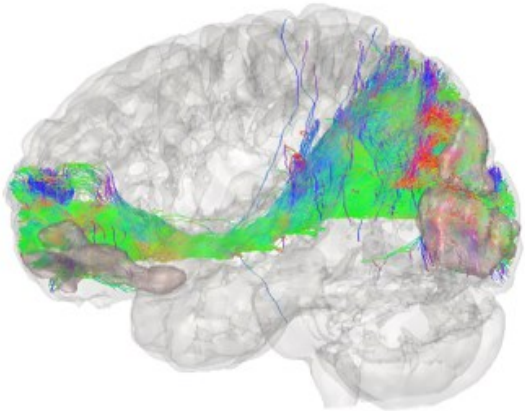

Inferior Fronto-Occipital Fasciculus

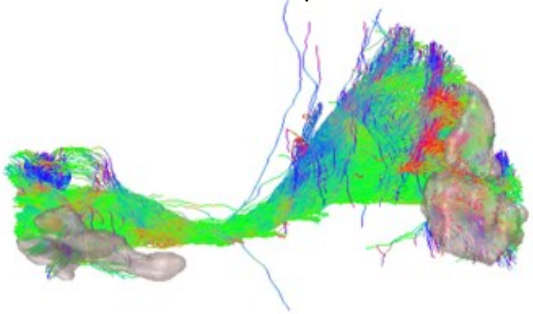

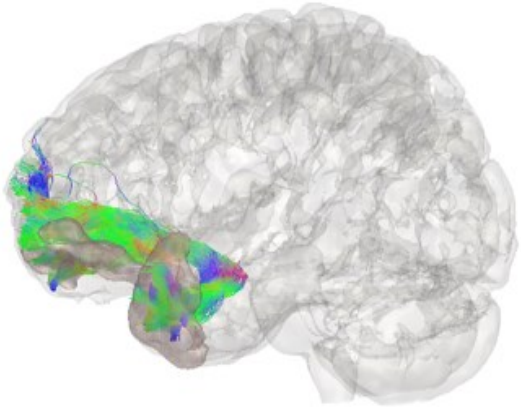

Uncinate Fasciculus

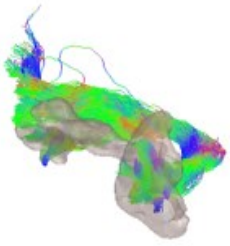

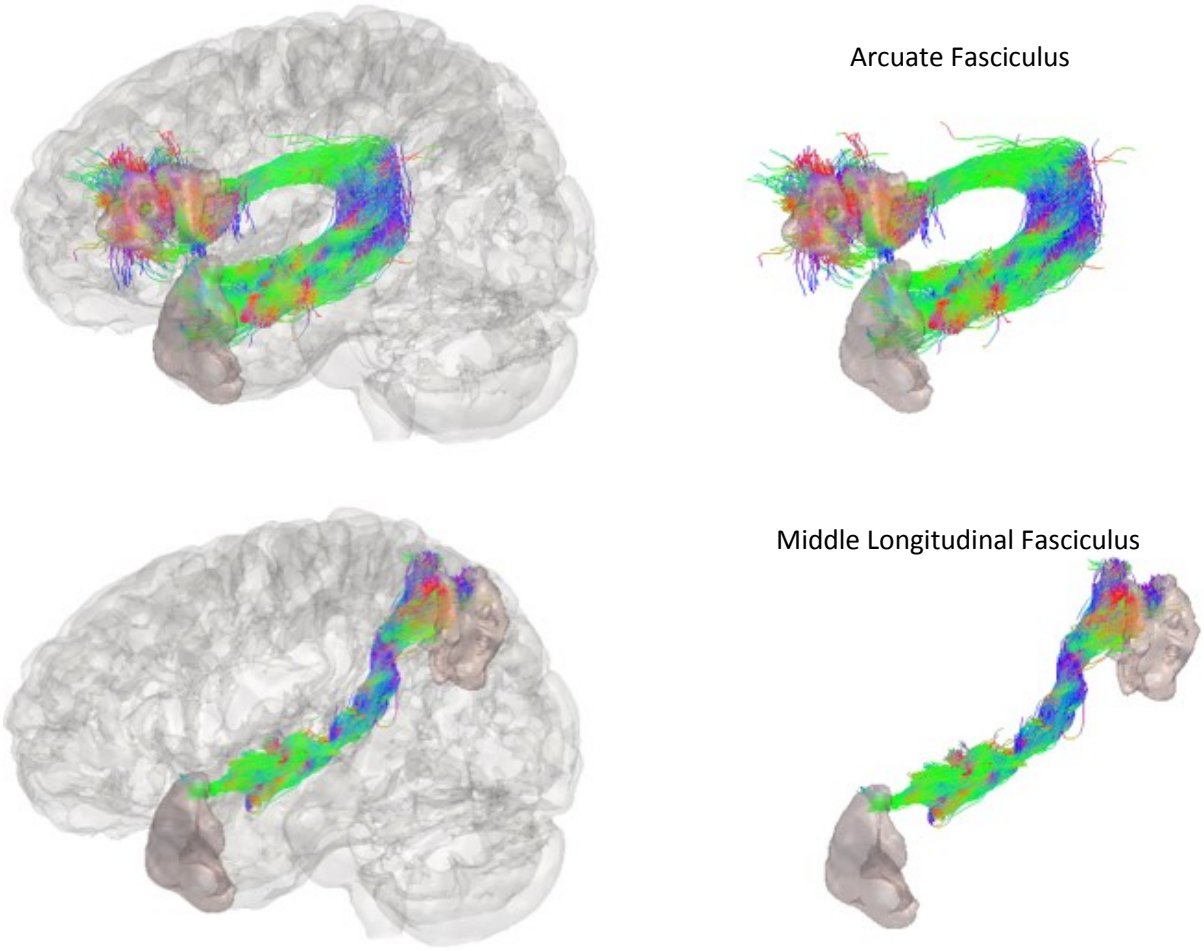

Figure 6 Legend: Left Column – Constrained spherical deconvolution derived probabilistic fibre tractography with 5000 streamlines in descending order of the inferior longitudinal fasciculus, inferior fronto-occipital fasciculus, uncinate fasciculus, arcuate fasciculus and middle longitudinal fasciculus with the overlying cortex (transparent grey) and regions of cortical connectivity (pink). Right Column – Respective fibre tractography without overlying cortex.

Figure 7: Probabilistic fibre tractography of language-related tracts and surgical footprint

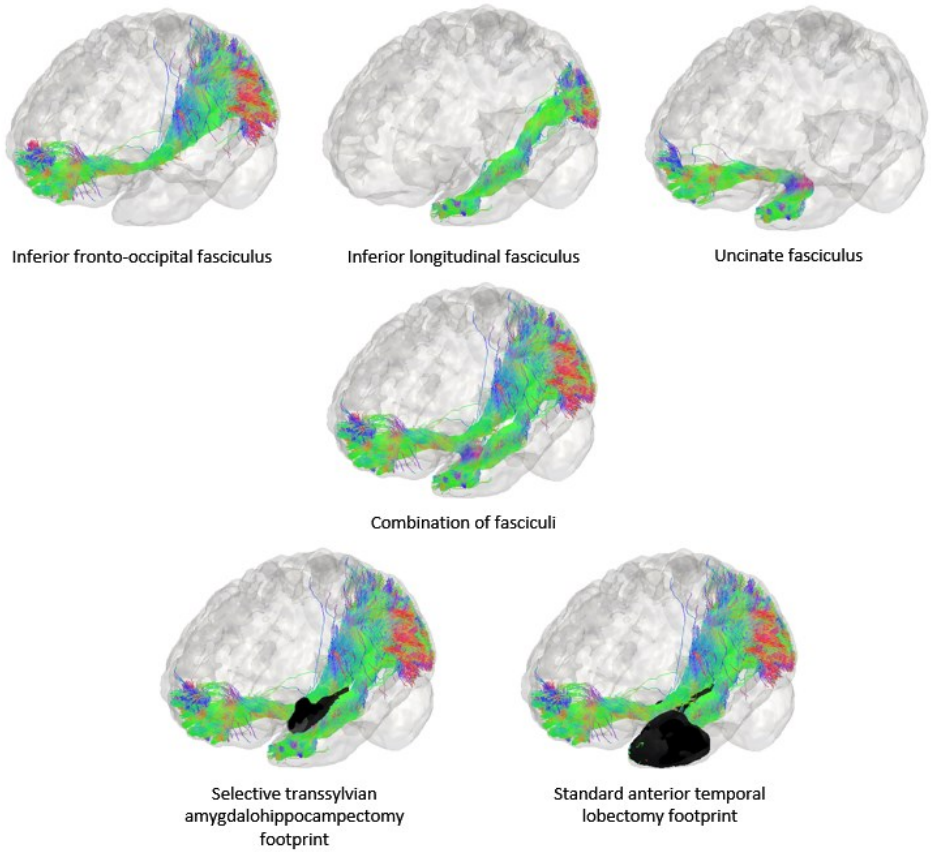

Figure 7: The inferior fronto-occipital fasciculus, inferior longitudinal fasciculus and uncinated fasciculus have each been reconstructed using probabilistic tracking of HARDI data with fibre orientation distributions derived using constrained spherical deconvolution. The inferior fronto-occipital fasciculus connects the orbitofrontal regions to the posterior temporal and occipital regions (direct pathway). The same connectivity is also subserved by the unicate fasciculus between the orbitofrontal cortices to the temporal pole and the inferior longitudinal fasciculus connecting the temporal pole to the posterior temporal and occipital regions. The surgical footprint of the selective transsylvian amygdalohippocampectomy and standard anterior temporal lobectomy approaches are depicted as black regions. The selective transsylvian amygdalohippocampectomy, which involves dissection through the inferior limiting sulcus of the insula, causes disruption of both the uncinate fasciculus and the inferior longitudinal fasciculus thereby causing a structural disconnection in both the direct and indirect pathways. The standard anterior temporal lobectomy approach has a larger surgical footprint in terms of resection volume but spares the inferior fronto-occipital fasciculus. Knowledge of the white matter fibre tracts as a hodotopical map may also be beneficial when planning extratemporal tailored resections.

1.5.2 Neuropsychiatric evaluation.

Around 50% of patients with epilepsy develop psychiatric disturbances which most commonly include depression, anxiety and psychosis(Marsh et al., 2002). Psychiatric manifestations may also be linked to the seizure semiology and appear in the prodromal, inter-ictal or post-ictal stages. During the prodromal stages, patients may demonstrate behavioural alterations, such as emotional lability, irritability, anxiety and even aggression. Fear is reported during an epileptic aura in up to one-third of patients and implicates ictal activity within the medial temporal structures, classically the amygdala, as well as the temporal neocortex and mesial frontal regions(Foldvary-Schaefer et al., 2011). Post-ictal confusion is common following dialeptic seizures and is associated with diffuse EEG slowing. Psychiatric disturbances are more common following clusters of seizures or status epilepticus. Post-ictal psychosis, which closes resembles chronic schizophrenia, is estimated to occur in 6% of patients and is most commonly associated with temporal lobe epilepsies. There is commonly a lucid interval ranging from 6-72

hours following the termination of the seizure and the onset of the psychosis(Kanner et al., 1996). Delusions, hallucinations and mania are the most common presentations.

Following resective epilepsy surgery, transient mood disturbances are reported in 45% of patients at six weeks(Ring et al., 1998). In 10% of patients, the symptoms, most commonly depression, may be persistent and warrant treatment. A single study comparing the long–term psychiatric outcomes between trans-cortical middle temporal gyrus selective amygdalohippocampectomy versus standard anterior temporal lobectomy revealed post-surgical paranoia was significantly more frequent in the standard anterior temporal lobectomy group(Bujarski et al., 2011). Outside of epilepsy, the uncinate fasciculus has been implicated in a number of psychiatric disorders including anxiety, schizophrenia, psychopathy and personality disorders(Kubicki et al., 2002; Olson et al., 2015). The hodotopical substrate underlying this potential link has been suggested to be disruption between the temporal association regions and modification of behaviour through the lateral orbitofrontal cortex(Von Der Heide et al., 2013).

1.6 EpiNav: A Computer-Assisted Planning Platform

Due to the multitude of imaging investigations performed in the presurgical evaluation of epilepsy, a method to accurately co-register the images into a common space is critical to interpreting the results and guiding further management(Cardinale et al., 2015; Zombori et al., 2011). The introduction of 3D multi-modal imaging has been shown to change clinical practice in 81% of all individuals undergoing presurgical evaluation of epilepsy and in 100% of patients specifically undergoing SEEG(Nowell et al., 2015a). SEEG is increasingly becoming more common and is essential for identifying the seizure onset zone, identifying function and hence tailoring surgical resection margins. SEEG electrodes are inserted blindly through bolts placed within the skull that dictate the electrode trajectory. Meticulous planning and accurate implementation of the plan is required as this is a diagnostic procedure that carries a significant risk of intracranial haemorrhage when the electrode is passed through the brain(Mullin et al., 2016a). Accurate vascular imaging registration and segmentation are paramount to ensuring that intracranial vascular is visualised and avoided. Coupled with this, the results of other imaging modalities that comprise the presurgical evaluation of epilepsy, such as the PET and SPECT images, can be co-registered and used as targets for SEEG electrode planning. The generation of 3D multimodal images is, therefore, the foundation upon which computer-assisted planning is based. As such, novel computer algorithms are utilised to optimise surgical parameters that are implemented by human experts, such as drilling angle to the skull and grey matter sampling, as well as safety metrics such as intracerebral electrode length, minimum distance to critical structures and overall trajectory risk.

In order to automate SEEG planning, parameter ranges for each of the above factors must be identified and applied in a systematic and hierarchical manner to find the optimal solution for all electrodes in the implantation and not on an individual electrode basis. To be prospectively integrated within the SEEG pathway, the image acquisitions and pre-processing should be standardized, performed in advance of the SEEG implantation and be automated as far as possible to maximize efficiency and consistency. The selection of the anatomical structures for sampling should be available for input in a user-friendly manner and the output of the algorithm be returned within a clinically acceptable timeframe that allows the neurosurgeon and multi-disciplinary team to review and modify the trajectories as needed. Finally, a method for seamlessly transferring the plan to the operating room for implantation is required. Here we

provide an overview of the considerations, controversies and practicalities of implementing an automated computer-assisted planning solution for SEEG planning.

1.6.1 Model generation

The minimum requirements for performing computer-assisted planning for SEEG are a volumetric T1 MRI of the head, with and without Gadolinium-enhancement and an appropriate vascular image. The Gadolinium-enhanced T1 acquisition serves as the reference image and defines the coordinate planning space to which all other images are registered. The non-enhanced T1 sequence should allow differentiation between the grey and white matter, such as MPRAGE acquisitions so that whole-brain parcellations can be derived(Vakharia et al., 2019b). The whole-brain parcellation serves as an automatic means of labelling anatomical structures within the brain. The two whole-brain parcellations that are most frequently applied to automated SEEG planning are FreeSurfer(Dale et al., 1999; Fischl, 2012) and GIF (Cardoso et al., 2015b) and each has their unique advantages and disadvantages. The whole-brain parcellations allow automatic generation of three-dimensional models of the cortex, ventricular system, sulci and grey matter (see Figure 8). The main disadvantage of a whole-brain parcellation is the time required to generate such imaging, which can between 2 and 6 hours for GIF and 10-15 hours for FreeSurfer, depending on computing power. Deep learning methods, however, have been successfully developed that could reduce this time to ~5 minutes(Gibson et al., 2018; McClure et al., 2019), but clinical validation of such techniques are still on-going. The aforementioned whole-brain parcellation methods were developed from structurally normal 'healthy' brains. It is likely therefore that images with gross structural abnormalities, such as previous resection cavities or neonatal ischaemic injuries, maybe incorrectly labelled.

Trajectory distance and drilling angle metrics are measured from the external surface of the skull model. Scalp models are derived directly from the T1 MRI, whilst skull models require either a pseudo-CT to be generated from the T1 MRI or from a CT scan, which may have been acquired as part of previous investigations, such as PET or SPECT.

Figure 8: Model generation from GIF parcellation

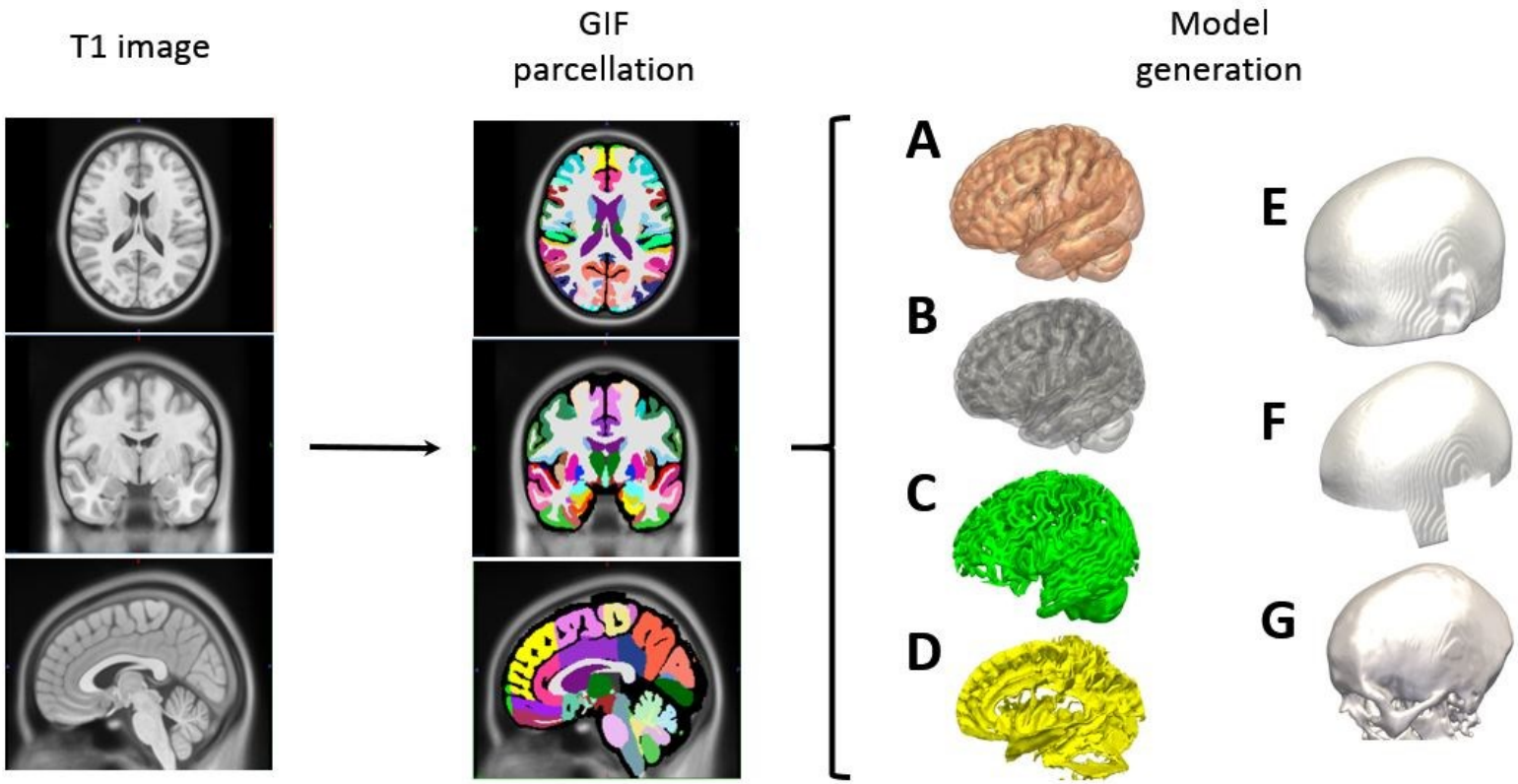

Figure 8 Legend: Input T1 image (axial, coronal and sagittal slices shown) used to generate GIF parcellation. Models generated from the GIF parcellation in an automated fashion include A) Cortex, B), Grey matter, C) Grey matter-derived sulcal model and D) CSF-derived sulcal model. The scalp model (E), derived directly from the T1 image through smoothing and thresholding, is modified to generate a scalp mask (F) that prevents entry through critical regions such as the orbit, face, ear and skull base. The skull model (G) is derived from a pseudoCT image (not shown).

The user can select entry and target points for automated planning based on the labelled structures provided by the whole brain parcellation. The extent to which anatomical structures are subdivided is therefore crucial, as this defines the precision with which the computer-assisted plans conform to the required implantation strategy. In the example outlined in Figure 9, as part of a frontotemporal implantation strategy, we see that the hippocampus is not subdivided into its anatomical subcomponents or head, body and tail as part of the GIF parcellation. If two electrodes are therefore required within the hippocampus, such as one in the head and the other in the body, a means of ensuring this required. One solution that has been successfully applied when two or more trajectories are within the same entry or target structure is to maximize their geometric spacing to ensure uniform spatial sampling.

1.6.2 Automated Trajectory planning considerations

1.6.2.1 Maximising distance from vasculature

The greatest risk associated with SEEG trajectory planning is intracranial haemorrhage and meta-analytic data of the published literature suggests a pooled prevalence rate of 1%, with the most common type being intracerebral followed by subdural and extradural haemorrhages(Mullin et al., 2016a). Intracerebral haemorrhages most likely arise from sulcal vessels, subdural haemorrhages from cortical veins and extradural haemorrhages from branches of the middle meningeal artery within the dura. For automated trajectory planning to avoid such haemorrhages, it is imperative that the vascular imaging modality employed accurately delineates the vasculature with sufficient contrast to noise ratio to allow segmentation(Zuluaga et al., 2015). Segmentation is the process through which the individual vessels are extracted from the source imaging. Once segmented 3-dimensional representations of the vascular trees can be generated and considered as structures during automated trajectory planning(Li et al.,

2019b). This highlights the critical difference between vessels that can be seen by the naked eye on the source imaging by the surgeon, compared to those that can be considered and avoided by the automated planning software.

The optimal vascular imaging modality for SEEG is still controversial(Cardinale et al., 2013, 2016a; Isnard et al., 2018). Digital subtraction angiography (DSA) is accepted as the gold-standard method of visualizing intracranial vasculature and is undertaken by approximately half of the large volume centres currently performing SEEG(Cardinale et al., 2015). DSA, however, is an invasive procedure that involves radiation exposure and carries the risk of stroke, arterial wall dissection and puncture site morbidity(Zuckerman et al., 2015). This has led to the development and use of less invasive methods such as CT-angiography (CTA) as well as MR-based methods(Barros et al., 2017; Vakharia et al., 2019c; Zuluaga et al., 2015). Unlike DSA, in which contrast media is injected into the internal carotid or vertebral arteries, CTA involves the injection of the contrast medium into a peripheral vein thereby circumventing the morbidity associated with groin puncture and potential intimal vessel wall injury. The compromise, however, is that the contrast medium is diluted throughout the total circulating volume resulting in a reduced contrast-to-noise ratio compared to DSA. MR-based methods, which include MR-venography and MR-angiography (MRV/A), do not involve radiation exposure and phase-contrast methods exist which do not require the use of contrast agent administration(Wahlin et al., 2012). This is particularly important in patients with contraindications to contrast-administration such as renal dysfunction or, rarely, allergic reactions.

Figure 9: Pipeline for automated SEEG trajectory planning

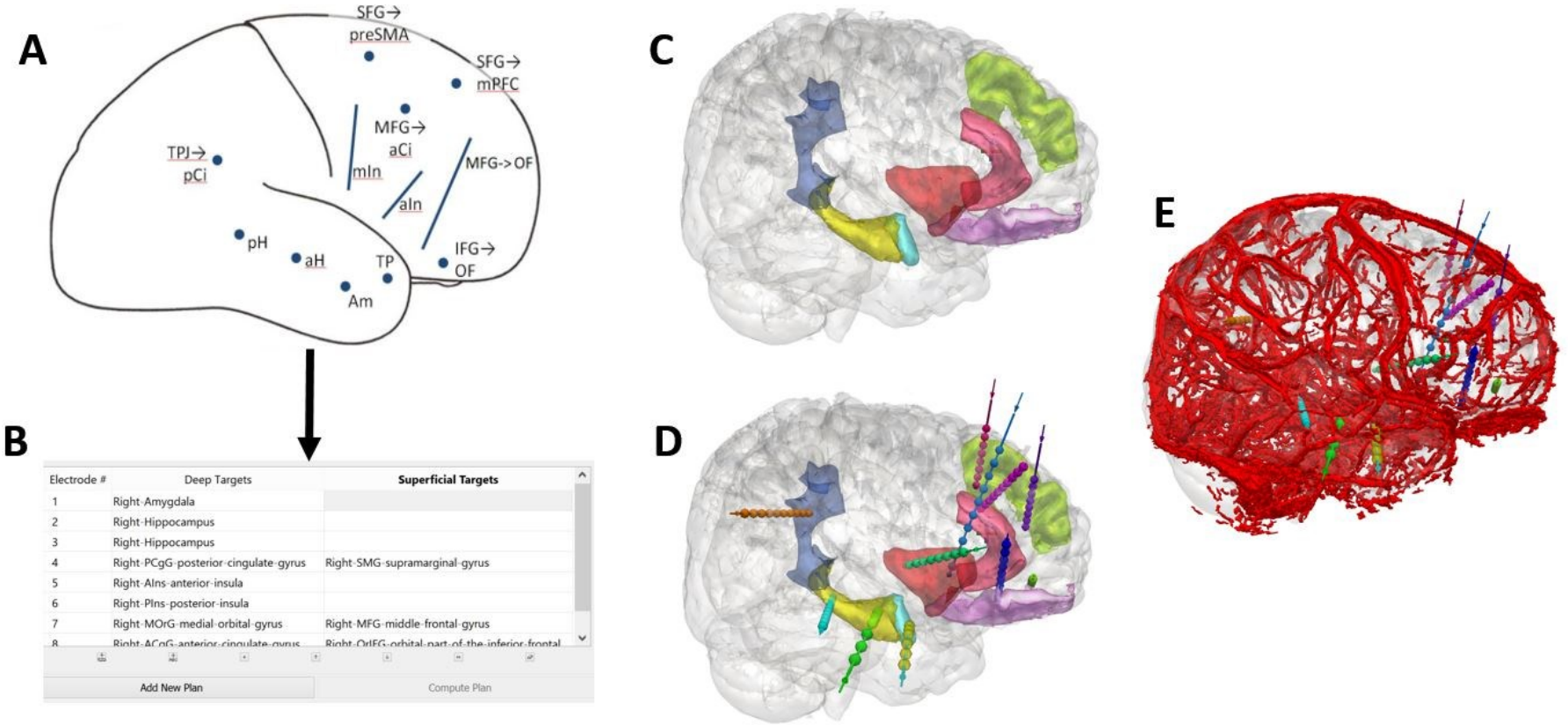

Figure 9 Legend: SEEG implantation strategy (A) from multi-disciplinary team meeting of a patient with a suspected right frontotemporal seizure-onset zone and corresponding input into computer-assisted planning software (B) based on the anatomically defined regions in the GIF parcellation. Automatic segmentation and 3-dimensional model generation of the anatomical structures (C) defined as part of the implantation strategy. The corresponding computer planned trajectories shown without (D) and with the vascular model (E).

Due to the low incidence of haemorrhage during SEEG it is unlikely a comparative study between vessel imaging modalities will be performed, as prohibitively large sample sizes would be required(Vakharia et al., 2019c). Another essential factor that is rarely considered in the literature is the geometric distortions that are introduced through MR-based methods. Unlike with DSA / CTA, the vessels imaged through MR-based methods may not appear to be in precisely the same location due to magnetic field inhomogeneities, although distortion correction methods can be applied(Guo et al., 2018)

Another controversial topic is the diameter of vessels that are considered to be significant for SEEG. DSA allows vessels <1mm in diameter to be reliably segmented, whilst MR-based modalities are reported to be between 2-4 mm in diameter(Vakharia et al., 2019c). Some studies have shown electrode-vessel conflicts with median vessel diameters <1.5 mm do not result in any radiological haemorrhage(Barros et al., 2017; Li et al., 2019b), suggesting that they may be clinically insignificant. The implication of considering clinically non-significant vasculature is that this may over-restrict SEEG electrode trajectory planning and unnecessarily limit the intracranial sampling.

Based on the vascular imaging method provided, the automated planning software must then calculate an optimal trajectory accounting for the location and distance from the vasculature. This is undertaken through the calculation of the minimum distance (mm) from the vasculature at any point along the trajectory and the risk score, which is an approximation of the size of the avascular corridor along the entire trajectory. A number of different risk scores have been applied(De Momi et al., 2013b; Essert et al., 2012; Shamir et al., 2012; Trope et al., 2015; Zombori et al., 2011) and are automatically calculated by the software by placing nodes (~128) along the entire trajectory. At each one of these nodal points, the closest segmented

vessel is identified and the distance is measured. The closer the vessels are to the electrode the greater the risk score. The cumulative sum of the scores for all the nodal points, therefore, provides a total risk score for the entire trajectory. In addition, the user defines a safety margin, which is the minimum distance from vasculature that is clinically acceptable and is derived from the implantation accuracy achieved at that centre. In general, a 3-5 mm safety margin is employed(Cardinale et al., 2013). Trajectories that return nodal points less than the pre-specified safety margin are discarded. The remaining trajectories are then returned based on the lowest risk score for the entire plan(Sparks et al., 2017b). The risk score is solely based on the segmentation of the vessels from the vascular imaging provided. As described above, a poor segmentation will result in fewer vessels for consideration during automated trajectory planning and falsely low apparent risk scores being returned to the surgeon(Vakharia et al., 2019c). The majority of computer-assisted plans that are deemed as infeasible by expert human raters are because of electrode vessel conflicts with non-segmented vasculature(Nowell et al., 2016b; Scorza et al., 2017; Sparks et al., 2017a).

1.6.2.2 Sulcal avoidance

Anatomical dissections of the brain reveal that vessels are present within sulci, even if they cannot be visualized with the vascular imaging method employed, and data from DBS electrode implantation suggests that crossing such pial and ependymal boundaries increase the intracranial haemorrhage rates more than ten-fold(Elias et al., 2009). Within the SEEG literature, however crossing sulci improves the yield of grey matter sampling and increased haemorrhage rates have not been described(Alomar et al., 2017). Sulcal models can be derived from the whole brain parcellation in one of two ways. The first is to extract the intracranial CSF spaces below the crown of the gyrus. This is dependent on CSF being present within the sulci and being correctly labelled by the whole brain parcellation. The majority of patients undergoing SEEG are young without visible CSF in the sulci making this method less sensitive. A second method is to derive a grey matter model from the whole brain parcellation and sequentially shrink this until it overlies the sulci (see Figure 8). The sulcal models are considered as ‘no-go‘ zones by some computer planning algorithms(De Momi et al., 2013b; Sparks et al., 2017a). No-go zones are applied in a subtly different way compared to the risk scores when considering vascular models. Here, the trajectories are permitted to run close to the sulci, in order to permit grey matter sampling, but cannot cross through them.

To date, only two studies have analyzed the effect of implementing sulcal models on computer-generated trajectories. In the first study(Li et al., 2019b), patients that had undergone SEEG implantation and also pre-operative T1+Gad, MRV/A and DSA imaging were retrospectively selected. The postoperative CT scan of the implanted electrodes was then overlaid on the pre-operative vascular imaging. The total number of vascular conflicts between the implanted electrodes and the raw imaging were then counted. This represents the number of 'true' conflicts. This was also compared to the number of conflicts with segmented vessels from the corresponding imaging modality. Given that computer-assisted planning algorithms can only consider segmented vasculature, and the segmentation yield is dependent on the vascular imaging modality applied, this represents the 'apparent' number of conflicts. Of 354 electrodes implanted in 33 patients, 166 electrode vessel conflicts were found on the raw DSA imaging with a median vessel size of 1.3 mm. Taking this to be the number of 'true' conflicts (ground truth), it was found that 26.5% (44/166) of the conflicts were within the grey matter derived sulcal models, suggesting that these could have been avoided if a sulcal model was implemented during the planning. It should be noted, however, that despite there being 166 electrode vessel conflicts there were no radiological haemorrhages, suggesting vessels <1.3 mm may be discounted during SEEG planning. In the second study(Vakharia et al., 2019c), the impact of sulcal models on different vascular modalities at the planning stage was considered. Here, computer-assisted planning was performed based on providing the algorithm with DSA, MRV/A and T1+Gad segmentations. In each of these cases, the plans were recomputed with and without the use of a sulcal model as no-go zones. In these cases, the use of sulcal models did not significantly improve the risk scores as the majority of the vessels within the sulci were not segmented. Overall, these studies suggest that sulcal vessels are too small to be segmented from the raw imaging and are unlikely to result in radiological or clinically significant haemorrhage. Nevertheless, further research is required before definitive conclusions can be drawn, as these studies were underpowered to detect small differences in haemorrhage rates.

Figure 10: Different vessel imaging techniques for SEEG:

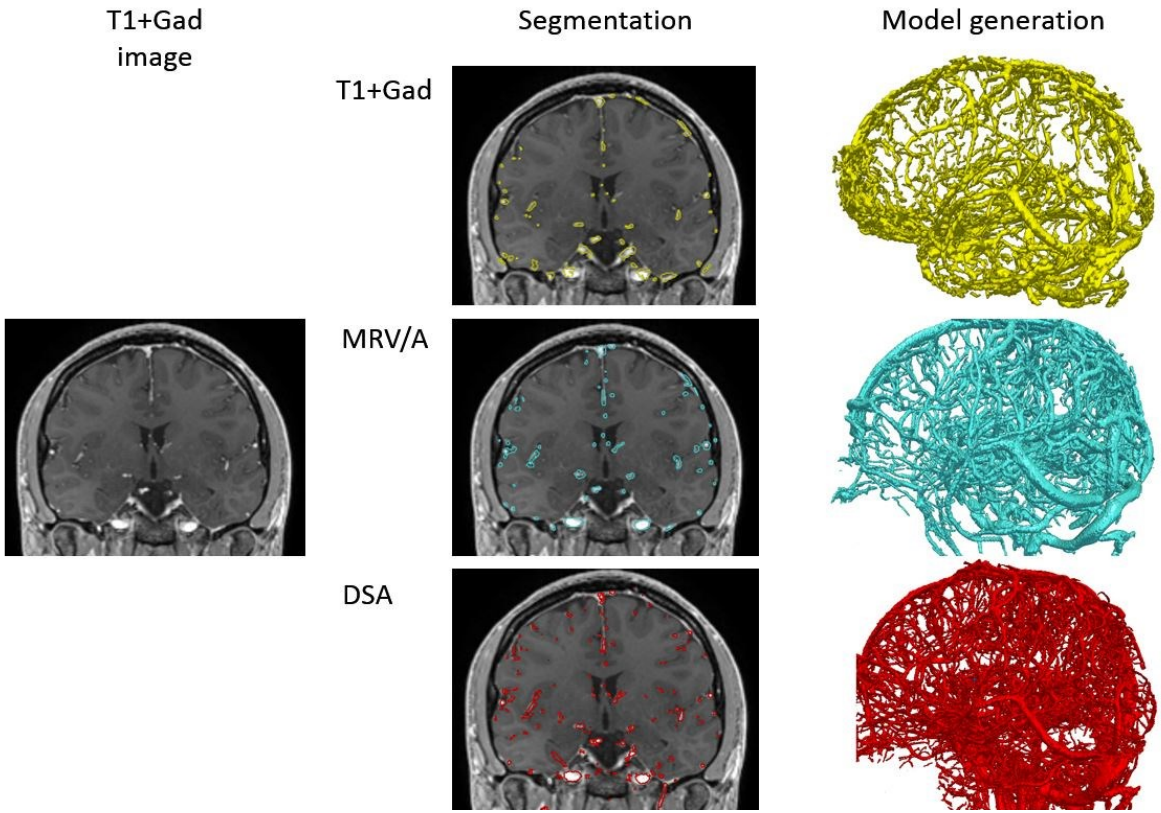

Figure 10 Legend: Examples of vessel segmentations from T1+Gad, MRVA/A and DSA shown in 2D coronal planes and corresponding 3D vascular model. The optimal vessel imaging technique for automated planning is based on the minimum vessel diameter considered significant by the surgeon.

1.6.2.3 Maximize grey matter sampling

Seizures arise within the grey matter. It is, therefore, an essential requirement of efficient SEEG sampling that the maximum possible number of electrode contacts record from grey matter. The grey matter (cortical ribbon) can be extracted directly from the whole brain parcellation by segmentation of all cortical labels. Computer-assisted planning algorithms, therefore, calculate the proportion of the electrode that lies within the grey matter model. With prior knowledge of the electrode specification from the manufacturer the optimal electrode, based on the active length and contact spacing, can be automatically assigned to each trajectory to maximize sampling efficiency. An example of this is shown in Figure 11, where electrodes were assigned to position contacts at grey matter interfaces and have fewer contacts in the white matter. It is necessary to have some contacts in white matter to act as reference electrodes.

1.6.2.4 Minimize drilling angle to the skull

The skull is most reliably segmented from a plain CT scan of the head. In practice, this is usually already acquired as part of other investigations such as PET, SPECT or DSA imaging and does not require additional radiation exposure. In cases where CT imaging is not available, a pseudoCT can be generated from a T1 MRI sequence. The skull model can then be extracted from either the CT or pseudoCT image by thresholding. The skull model is used to measure the angle of electrode insertion through the skull as this determines the drilling angle. Drilling angles perpendicular to the bone are considered to be more accurate as they prevent the drill from sliding along the bone, a phenomenon known as 'skiving'. As far as possible, drilling angles are limited to <30 degrees to the orthogonal, although improved drill bit designs and robotic drilling platforms with increased stability are likely to overcome this limitation.

Figure 11: EpiNav™ automated planning software user interface:

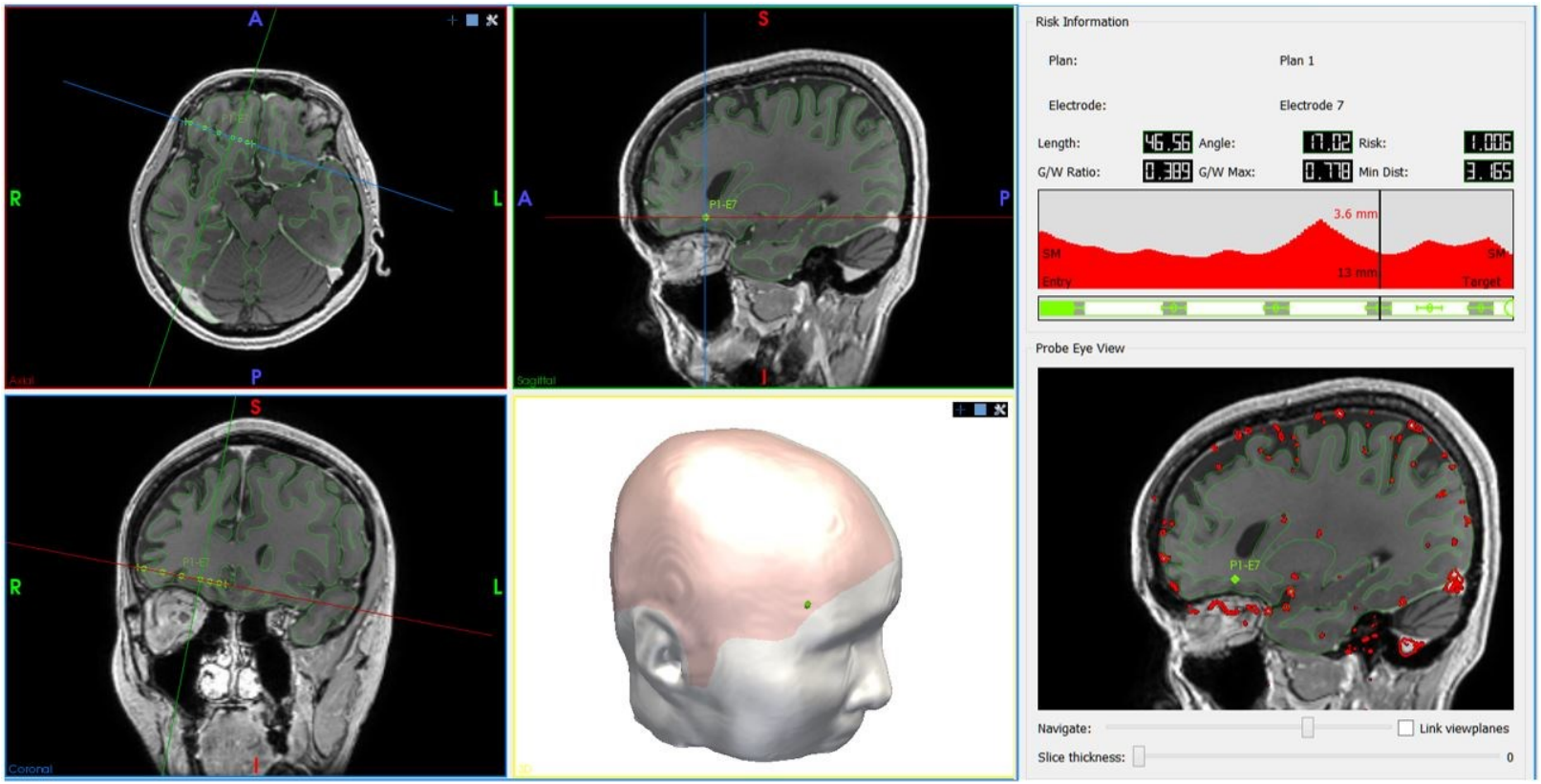

Figure 11 Legend: Automated right orbitofrontal electrode trajectory shown with axial (top left), coronal (bottom left) and sagittal (top middle) with planes adjusted to be orthogonal to the trajectory. Grey matter sulcal model is shown in green. Scalp model derived from the T1 image (bottom middle) shown with a scalp mask (pink overlay) to prevent entry through the face, orbit, ear and skull base. The right panel shows trajectory metrics including length, drilling angle to the bone, risk score, grey-white matter sampling ratio and minimum distance from vasculature (mm). Graphical display (red) shows the distance from vasculature at varying distances from the target point, i.e. at 13 mm from the target point the closest segmented blood vessel is 3.6 mm away. Beneath the graphical display is a pictographic representation of the electrode (green) and the corresponding contract position of the automatically segmented electrode that maximizes grey matter sampling. Electrode contacts that are sampling grey matter are coloured grey and those in white matter are not coloured. Probe eye view of the electrode along its length can be navigated using the slider to check the safety and feasibility of the trajectory.

1.6.2.5 Minimize Intracerebral length

The total intracerebral length of the electrode is minimized to provide the most direct trajectory to the target structures and also minimize cerebral transgression. In practice, this also prevents the algorithm from considering contralateral entry points and returning bilateral target sampling in the cases of paramedian structures such as the cingulate cortices or the supplementary motor areas. The intracerebral length is measured from the surface of the cortical model to the target point.

1.6.2.6 Avoidance of critical structures

In addition to vasculature, other critical structures that must be considered as part of automated SEEG trajectory planning include the orbit, face, skull base, posterior fossa, ears, ventricles and basal ganglia. The skull or scalp models can be modified, either manually or by using a predefined mask, to remove the face, orbit, ears, posterior fossa and contralateral hemisphere in the case of unilateral implantations (see Figure 8 F and Figure 11). The mask is then be used to constrain entry points for trajectory planning. The ventricular system and basal ganglia can be extracted from the whole brain parcellation and, similar to sulcal models,

designated as no-go regions. Typically, only the frontal horns, body and occipital horns of the lateral ventricles are segmented and considered as no-go zones as lateral trajectories to the hippocampus typically require transgression of the temporal horns.

1.6.2.7 Avoiding other electrodes

Unlike DBS implantations, where usually only one electrode is implanted into a single hemisphere, SEEG typically requires consideration of multiple trajectories (typically 8-14 electrodes). To prevent electrode conflict within the brain or clashing of the bolts on the scalp surface, it is common for algorithms to implement a minimum distance constraint between the trajectories. Based on the user's preference, a distance of 10 mm is usually employed. This adds another layer of computational complexity, as the optimal electrode for a single target point may therefore not be the optimal solution for the entire implantation strategy. A slightly higher risk score for a single trajectory may therefore ultimately translate to a lower overall risk score for the entire implantation. A potential advantage of this is that if an electrode trajectory is then modified or added at a later time by the user, the remaining trajectories can then be automatically recalculated and optimized without the need to laboriously manually adjust each of the other electrodes.

1.6.3 Post-implantation functionality

Following SEEG implantation patients will usually have CT imaging to check for any immediate post-implantation complications, such as haemorrhage, and to segment the electrodes. An MRI scan may also be performed to provide accurate data regarding the anatomical regions that have been sampled, although the artefact from the electrode contacts may be significant. From the post-operative implantation data, automated systems are available to automatically segment the individual contacts and assign them to the corresponding electrode(Granados et al., 2018b). The purpose of this is to: a) improve understanding of which regions of the brain are being sampled, b) allow implantation accuracy measures to be automated, c) assess electrode bending and d) allow linking of the recorded EEG data to identify the relevant brain region/structure from which seizures arise.

There is a lack of uniformity in the published literature regarding how post-operative SEEG accuracy is measured and reported(Vakharia et al., 2017b). Approximately half of the studies reporting post-SEEG implantation accuracy report the Euclidean distance between the

planned and implemented target points, whilst the remaining half report lateral deviation. Automated systems provide a means of objectively standardizing implantation accuracy reporting.

1.6.4 Clinical applications of computer-assisted planning

The first reported clinical use of computer-assisted planning software was to aid the calculation of frame-based coordinates for paediatric brain biopsy (Davis et al., 1988). In this study, the surgeon manually planned trajectories in 30 patients and the software was used to calculate the frame-based stereotactic coordinates of the target point. This was improved by the addition of multimodal imaging to allow co-registration of CT, MRI and digital angiography (Giorgi et al., 1989a). The next notable advance was the addition of 3-dimensional models to trajectory planning. These early prototypes laid the foundation for computer-assisted planning, but due to the lack of computing power were time-consuming and impractical. A resurgence in computer-assisted planning was marked by the development of digital brain atlases(Nowinski et al., 1998; Otsuki et al., 1994) which were initially registered to the patient's MRI scans and used to plan lesioning procedures for movement disorders. This was particularly useful for target structures that could not be visualized on the MRI, such as the ventral intermediate (VIM) nucleus of the thalamus.

The NeuroPlanner software allowed image co-registration, integration of multiple brain atlases, 3-dimensional model generation, manual stereotactic trajectory planning and simulation of therapeutic lesioning and stimulation(Nowinski et al., 2000) resulting in reduced operative time, cost and complication rates but with increased flexibility. In a path-planning algorithm that attributed cost-functions to critical structures, after manual selection of a target point, the algorithm individually selected and calculated trajectories arising from entry points on the scalp model. The proximity to a critical structure, such as vasculature, incurred a cost and an overall score was attributed to each of the potential trajectories. A display of the lowest cost paths gave a 'risk map' to aid in the selection of the optimal entry point(Vaillant et al., 1997). Systems integrating probabilistic functional targeting atlases(Guo et al., 2007) and increasingly complex weighting systems applied to the critical structures marked further advancements in deep brain stimulation planning(Beriault et al., 2011; Bériault et al., 2012; Essert et al., 2012; Liu et al., 2014). Table 2 provides an overview of the different planning platforms and their respective functionality as related to automated trajectory planning.

Table 2: Summary of currently available trajectory planning platforms

Platform	**EpiNav™**	**SEEG assistant - 3D Slicer extension**	**MINC Tool Kit (ITK & Matlab)**	**Curry**
Group	UCL / Kings College London	Politecnico di Milano	Montreal Neurological Institute	CompuMedics NeuroScan
Licensing	Academic Use	Academic Use	Academic Use	Commercial
Primary use	SEEG planning	SEEG planning	SEEG planning (Amygdala and hippocampus only)	Grid & Strip planning
Image registration	Rigid Affine Non-linear	Rigid Affine Non-linear	Rigid Affine Non-linear	Rigid Affine Non-linear
Multi-modal imaging	Yes	Yes	No	Yes
Vessel segmentation	Yes	Yes	Yes	No
Target structure segmentation	Yes	Yes	Yes	No

Surface / Target Risk map	Yes	Yes	Yes	No
Sulcal model extraction	Yes	Yes	Yes	No
Grey matter maximisation	Yes	Yes	Yes	Yes
Electrode selection optimisation	Yes	Yes	No	No
Single trajectory planning	Yes	Yes	Yes	No
Multi-trajectory planning	Yes	Yes	Yes	No
Automated contact segmentation	Yes	No	No	Yes
Automated implantation accuracy measurement	Yes	No	No	No
Linking of intracranial EEG data to contacts	Yes	No	No	Yes

Signal processing and source reconstruction	Yes	No	No	Yes
Automated Resection planning	Yes	No	No	No
Retrospective validation data	Yes – external and multicentre	Yes – internal and single centre	Yes – internal and single centre	N/A
Prospective validation data	Yes	No	No	N/A
Extended uses	LITT – MTLELITT – Corpus callosotomy Brain biopsy	Not specified	Not specified	Spike detection and clustering

Early studies reporting automated SEEG planning software incorporated many of the planning features that had been developed for single trajectory deep brain stimulation planning. These systems additionally integrated 3D multimodal imaging allowing co-registration of different imaging modalities, such as FLAIR, PET and SPECT to aid the inference of the epileptogenic zone(Cardinale et al., 2013; Lüders et al., 2006; Perry et al., 2017). The desired target points were then selected manually by the surgeon, based on the implantation strategy, and the automated planning algorithm returned the trajectory with the lowest risk based upon the user-defined angle and length constraints(Nowell et al., 2015a; Rodionov et al., 2013; Zombori et al., 2014). Based on a fixed target point the trajectory risk was then be represented to the user as a heat map on the scalp surface(Navkar et al., 2010; Zombori et al., 2014).

Unlike DBS procedures where the target points are stereotyped, during SEEG the target points vary significantly between electrodes and between patients. If the manually selected target points were close to a blood vessel or critical structure, this subsequently restricted the number of potential trajectory options(Nowell et al., 2016b). To mitigate this, some algorithms allowed the entry and target points to be 'roughly' selected and the algorithm would expand the potential search radius by 0.5 mm(De Momi et al., 2013a). In this manner, the software was able to return the optimal solution that was most closely in keeping with the preferences of the surgeon. Using DSA derived vasculature, this algorithm was retrospectively validated on 15 patients that underwent implantation of 199 electrodes. The automated trajectories took ~1 minute per electrode to be generated and when compared to the manually planned trajectories returned significantly improved distance from vasculature and insertion angles. Feasibility was also rated by three blinded internal neurosurgeons and the automatically generated trajectories were rated as preferable to the manual trajectories in between 50-73% of cases. This highlights the difference in planning practices, even between neurosurgeons at the same institution. In a similar study utilizing MRV/A based vasculature, the EpiNav™ software considered all points on the skull surface as potential entry points thereby obviating the need for the surgeon to select a rough entry region manually. A total of 166 electrodes were retrospectively recreated in 18 patients and external validation from blinded neurosurgeons rated 79% of these as feasible(Nowell et al., 2016b). This method took on average 8 minutes to generate the entire implantation strategy. In these studies, however, reasons for rejecting computer-generated trajectories included conflict with non-segmented vasculature, restrictions placed by the use of the implantation method (i.e. the stereotactic frame) and potential conflict with other electrodes.

The next level of complexity introduced to automated SEEG trajectory planning was the consideration of multiple trajectories(De Momi et al., 2014a; Scorza et al., 2017; Sparks et al., 2017b) to find the global optimum solution, that is the lowest overall risk for the implantation strategy as a whole, as opposed to the lowest risk for the individual trajectory. One such method utilized a serial approach in which the optimal first electrode was planned and any electrode in conflict with this was subsequently removed followed by the selection of the best next trajectory from the remaining pool(De Momi et al., 2014a). This was then repeated for all of the electrodes in the plan. Expert feasibility ratings of retrospectively reconstructed plans revealed that 30-40% of the automated trajectories were preferred over the manually planned trajectories. As this

method was based on the order of the trajectories considered, it could return different solutions according to the order of target regions chosen. To remove the limitation of a serial constraint and to improve computational efficiency, a dynamic programming strategy was included in the EpiNav™ software that was able to find combinations without limitations on the number or order of trajectories and was able to return a whole implantation strategy in less than an average of 20 seconds (Sparks et al., 2017b).

Original Work

2 Computer Assisted Planning For The Insertion Of Stereoelectroencephalography Electrodes For The Investigation Of Drug Resistant Focal Epilepsy: A Retrospective External Validation Study: Based on (Vakharia et al., 2018e)

2.1 **Abstract**

2.1.1 Objective

One-third of patients with focal epilepsy are drug-refractory and surgery may provide a cure. Seizure free outcome following surgery is dependent on the correct identification and resection of the epileptogenic zone. In patients with no visible MRI abnormality, or when pre-surgical evaluation yields discordant data, invasive EEG recordings may be necessary. SEEG is a procedure in which multiple electrodes are stereotactically placed in key targets within the brain to record interictal and ictal electrophysiological activity. Correlating this activity with the seizure semiology allows identification of the seizure onset zone and crucial structures within the ictal network. The main risk of SEEG electrode placement is haemorrhage, which occurs in 1% of patients. Planning safe SEEG electrodes requires meticulous adherence to the following constraints: 1) maximise distance from cerebral vasculature, 2) avoid crossing sulcal pial boundaries (sulci), 3) maximize grey matter sampling, 4) minimise electrode length, 5) drilling angle orthogonal to the skull and 6) avoid critical neurological structures. We provide validation of EpiNav^{TM}, a multimodal platform that allows automated computer-assisted planning CAP of SEEG electrodes by user-defined regions of interest.

2.1.2 Methods

Thirteen consecutive patients who underwent implantation of a total 116 electrodes over a 15-month period were studied retrospectively. Models of the cortex, gray matter, and sulci were generated from patient-specific whole-brain parcellation, and vascular segmentation was performed on the basis of preoperative MR venography. Then, the multidisciplinary implantation strategy and precise trajectory planning were reconstructed using CAP and compared with the implemented manually determined plans. Paired results for safety metric comparisons were available for 104 electrodes. External validity of the suitability and safety of electrode entry points, trajectories, and target-point feasibility was sought from 5 independent, blinded experts from outside institutions.

2.1.3 Results

CAP-generated electrode trajectories resulted in a statistically significant improvement in electrode length, drilling angle, gray matter–sampling ratio, minimum distance from segmented vasculature, and risk ($p < 0.05$). The blinded external raters had various opinions of trajectory feasibility that were not statistically significant, and they considered a mean of 69.4% of manually determined trajectories and 62.2% of CAP-generated trajectories feasible; 19.4% of the CAP-generated electrode-placement plans were deemed feasible when the manually determined plans were not, whereas 26.5% of the manually determined electrode-placement plans were rated feasible when CAP-determined plans were not (no significant difference).

2.1.4 Conclusions

CAP generates clinically feasible electrode-placement plans and results in statistically improved safety metrics. CAP is a useful tool for automating the placement of electrodes for SEEG; however, it requires the operating surgeon to review the results before implantation, because only 62% of electrode-placement plans were rated feasible, compared with 69% of the manually determined placement plans, mainly because of proximity of the electrodes to unsegmented vasculature. Improved vascular segmentation and sulcal modeling could lead to further improvements in the feasibility of CAP-generated trajectories.

2.2 Introduction

Epilepsy has been defined as "a disorder of the brain characterized by an enduring predisposition to generate epileptic seizures." Epilepsy can have wide-ranging effects on a patient's quality of life and can result in physical injury, psychosocial dysfunction, cognitive decline, and risk of death. One-third of patients with epilepsy continue to have seizures despite their use of 2 or more appropriately prescribed antiepileptic drug schedules. These patients are defined as having drug-resistant epilepsy. Surgical intervention can potentially cure drug-resistant epilepsy if the region from which the seizures arise, known as the epileptogenic zone (EZ), can be identified and removed safely. In a proportion of patients, results of the noninvasive presurgical evaluation are not clear or discordant, and invasive intracranial EEG recordings, in the form of either grid/strip implantation or stereoelectroencephalography (SEEG), are required. SEEG involves the stereotactic placement of multiple (8–16) electrodes at predefined regions of the brain to help delineate the EZ and the spatial and temporal seizure-network spread within the brain. Electrode trajectories currently are planned manually to sample the regions of interest (ROIs) while maximizing gray matter contact and distance from blood vessels. This task is time-consuming and requires significant multidisciplinary input. We previously described the benefits of multimodal 3D imaging for manual electrode planning and an early version of computer-assisted planning (CAP).[17,18] In the initial study, manually planned electrode-implantation schemes for 18 patients (166 electrodes) were recreated retrospectively using EpiNav software. An earlier version of the software required the target points for the electrodes to be placed manually on the MR image, and the software then would calculate the safest electrode trajectory based on the cumulative distance from segmented blood vessels along the whole trajectory.[18] The computer-generated and manually determined trajectories then were rated by 3 independent, blinded neurosurgeons as to whether they were feasible for implantation. Overall, the computer-generated electrodes resulted in significantly shorter intracranial length, increased distance from blood vessels, greater gray matter sampling, and improved drilling angles ($p < 0.05$ for all parameters). Of the computer-generated electrodes, 78.9% were deemed feasible for implantation by at least 2 of the 3 independent neurosurgeons.

Further development of the EpiNav software implemented its ability to define entry and target zones constrained by anatomical structures.[24]Users can now define an ROI by typing or clicking on an anatomical location (e.g., right amygdala) and allowing the computer algorithm to define the safest entry and target points within the anatomical structure as a whole. Furthermore, multiple trajectories can be placed within the same anatomical structure, and

electrodes will be spread evenly within safe zones to maximize region sampling. This ability is of particular benefit for large anatomical targets, such as the cingulate cortex, and when high-density sampling of a structure such as the insula or hippocampus is required. We confirmed external validity of the generated electrodes from 5 independent, blinded epilepsy neurosurgeons, from outside institutions, who had expertise in implanting electrodes for SEEG and none of whom were involved in the generation of the initial manually determined plans. To gauge surgeon variability and preferences, we assessed why surgeons rated trajectories as infeasible. The implantation methods used by the external raters included frame-based (J.M.), frameless (D.N.), iSYS1 (S.W. and C.D.), and Neuromate (M.T.) robotic implantation methods.

2.3 **Methods**

2.3.1 Subjects

We included thirteen consecutive patients who underwent manual planning of electrodes and surgical implantation between July 2015 and October 2016. Informed consent was taken from each patient prior to inclusion in the study. National Research Ethics Service Committee London approval reference: 12/LO/0377.

2.3.2 Patient demographics

Table 3: Patient demographics:

Patient	Age	Sex	Hemisphere implanted	Hemispheric language dominance (fMRI)	EZ hypothesis	No. of electrodes
1	37	M	Left	Left	Frontal (non-lesional)	11
2	27	M	Right	Left	Frontal (non-lesional)	8
3	45	F	Right	Bilateral	Frontal (non-lesional)	13
4	35	F	Left	Left	Temporal (lesional)	3
5	31	M	Right	Left	Temporal (lesional)	8
6	42	M	Right	Left	Frontal (non-lesional)	10
7	49	F	Right	Left	Left temporal (non-lesional)	10
8	61	M	Right	Left	Frontal (non-lesional)	11
9	24	M	Right	Left	Frontal (non-lesional)	8
10	42	M	Left	Left	Frontal (non-lesional)	6
11	31	M	Bilateral	Left	Right Temporal (non-lesional)	12
12	48	F	Right	Left	Right Temporal (non-lesional)	8
13	27	M	Right	Left	Right Occipital (lesional)	8

2.3.3 Determination of target points

All patients had been discussed in a multidisciplinary team (MDT) setting consisting of epileptologists, neurosurgeons, neuropsychologists, neuropsychiatrists and neuroradiologists. From the non-invasive presurgical evaluation, the hypothesized epileptogenic zone was agreed and the requirement for invasive EEG recording was determined. Patients requiring subdural grid implantation were excluded from the study. Regions for SEEG sampling were agreed

between the multidisciplinary team and a list of brain regions requiring sampling were generated. The manual plans were then performed by a Consultant Neurosurgeon with subspecialty expertise in epilepsy surgery prior to final approval by the MDT.

2.3.4 Multimodal imaging

MR imaging was performed on a GE 3T MR750 scanner with a 32-channel head coil. A coronal 3D T1-weighted MPRAGE scan was performed with a field-of-view (FOV) of 224×256×256 mm (AP´LR´IS) with an acquisition matrix of 224×256×256 for a voxel size of 1 mm isotropic (TE/TR/TI = 3.1/7.4/400 ms; flip angle 11°; parallel imaging acceleration factor 2). 3D-FLAIR scans were acquired with a 3D fast spin-echo sequence with variable flip-angle readout with the same FOV and acquisition matrix for a 1 mm isotropic resolution (TR/TI/TE = 6200/1882/137 ms; echo train length of 150; parallel imaging acceleration 2 along both the in-plane and through-plane phase-encoding axes). Vascular imaging comprises a post-gadolinium T1, and phase-contrast MR angiography and venography scans. The axial post-gadolinium T1-weighted scan was acquired with an FSPGR sequence with a FOV of 256×256×224 mm and acquisition and reconstruction matrix of 256×256×224 (TE/TR = 3.1/7.4 ms; flip angle 11°). MRA and MRV were performed using a 3D phase-contrast sequence with a FOV of 220×220×148.8 mm with an acquisition matrix of 384×256×124 for a reconstructed voxel size of 0.43×0.43×0.60 mm (flip angle 8°; parallel imaging acceleration factor 2). To highlight the arteries, the MRA was scanned with a velocity-encoding of 80 cm/s (TE/TR = 4.0/9.3 ms). For sensitivity to the venous circulation, the MRV was scanned with a velocity-encoding of 15 cm/s (TE/TR = 4.8/26.4 ms), fat suppression, and a saturation band inferior to the FOV.

2.3.5 Manual planning

Manual plans were generated using volumetric T1 gadolinium-enhanced images as the reference image upon which MRV images were co-registered and vessels were extracted using a previously described tensor voting framework algorithm(Zuluaga et al., 2015). Entry and target points were manually placed using axial, coronal and sagittal reconstructions and trajectories were checked using the 'probe's eye' function. A 3D model of the cortical surface was used to ensure entry points were on the crown of gyri.

2.3.6 Computer-assisted planning

Data processing and model generation: EpiNav™ is a software platform that allows multimodal image co-registration, vessel segmentation, 3D model generation, manual and automated electrode planning. T1 MPRAGE sequences were submitted for whole-brain parcellation (GIF) from which cortical, grey matter and sulcal models were generated(Cardoso et al., 2015b; Ferran Prados, M. Jorge Cardoso, Ninon Burgos, Claudia AM Wheeler-Kingshott, 2016). Pre-operative CT scans were used to generate skull models, which were then modified to prevent entry through the contralateral hemisphere, face, ear, posterior fossa and skull base.

The technical aspects of the CAP algorithm used in this study have been previously described(Sparks et al., 2017a). In brief, the user defines target points as a region of interest (ROI) for electrode sampling. This can be through typing the name of the structure (e.g. right amygdala) or clicking on the ROI of the brain parcellation image. The entry ROI can be specified if a superficial target is also required (e.g. entry through the motor cortex to target the supplementary motor area), but is not obligatory. In this study, the same target points, and if specified the entry points, were selected based on the requirements of the SEEG MDT planning meeting. The user defines a maximum electrode length (90 mm was applied for all electrodes), as well as a maximum drilling angle (25 degrees from orthogonal to skull). The CAP algorithm will then remove any potential electrode trajectories that do not adhere to length and angle constraints before ensuring the trajectories pass through the skull model to the target ROI. If an entry ROI is defined, trajectories not passing through this ROI will also be removed. The remaining trajectories are then checked to ensure they do not collide with a critical structure such as blood vessel or sulcus. A minimum distance from vessels can be set as a safety margin by the user (3 mm was used for all electrodes in this study). The electrode trajectories that satisfy the requirements are then stratified based on risk, which is calculated as a function of the cumulative distance from vessels along the whole trajectory, optimised for grey matter contact and adjusted to avoid conflicts with other electrode trajectories. The electrode trajectories are then presented for review by using the 'probe's eye' function linked to the orthogonal planes. The resulting electrode trajectories were then iterated through using either the 'Next Entry' and 'Next Target' buttons until a feasible electrode trajectory is chosen by the user. (See Figure 12 8).

2.3.7 External validation

Five independent external raters who were neurosurgeons with expertise in performing SEEG implantations performed the external validation. The external raters have a range of experience with different implantation techniques, including frame-based (Jonathan Miller), frameless (Daniel Nielsson), iSYS1 (Stefan Wolfsberger / Christian Dorfer) and Neuromate (Martin Tisdall) robotic implantation methods. A prospective power calculation based on a pilot study in which 14 electrodes from two patients were rated by a single surgeon (Martin Tisdall) revealed 24 electrodes were required to detect an absolute difference in risk of 0.2 assuming a standard deviation of 0.3 and a power of 0.90 to achieve a significance level $p = 0.05$, two-tailed. To account for a potential clustering effect, a total of 13 patients were recruited. All raters appraised the same two pairs of plans (n = 32 electrodes) to assess inter-rater variability and a further 3-4 sets of paired plans (n = 34-41 electrodes) independently. All raters were blinded to the electrode trajectory generation method and were asked to provide ratings of the entry, trajectory and target feasibility for paired manual and CAP electrodes. Raters were asked to rate the feasibility of each trajectory based on their current implantation practice. Given that the sampling region suitability had previously been approved by the multi-disciplinary team based on the non-invasive presurgical evaluation, the raters were only asked to comment on the surgical feasibility of electrode implantation.

2.3.8 Statistical evaluation:

Risk metrics for manual and CAP electrodes were confirmed to have a normal distribution through the Shapiro-Wilks test ($p>0.05$). A paired Students t-test was performed for manual and CAP electrode comparisons. Clustering of electrodes within patients was assessed using a patient-specific random effects model (model 1) and the possible difference between surgeons using a fixed-effect model (model 2). A generalised likelihood ratio test comparing models 1 and 2 was performed, with a resulting p-value of 0.151, indicating that there is insufficient evidence to suggest a significant difference between surgeons with regard to feasibility ratings. Feasibility ratings of electrodes generated from manual and CAP methods were compared using McNemar's test and an odds ratio calculated.

Figure 12: Computer-assisted trajectory generation workflow

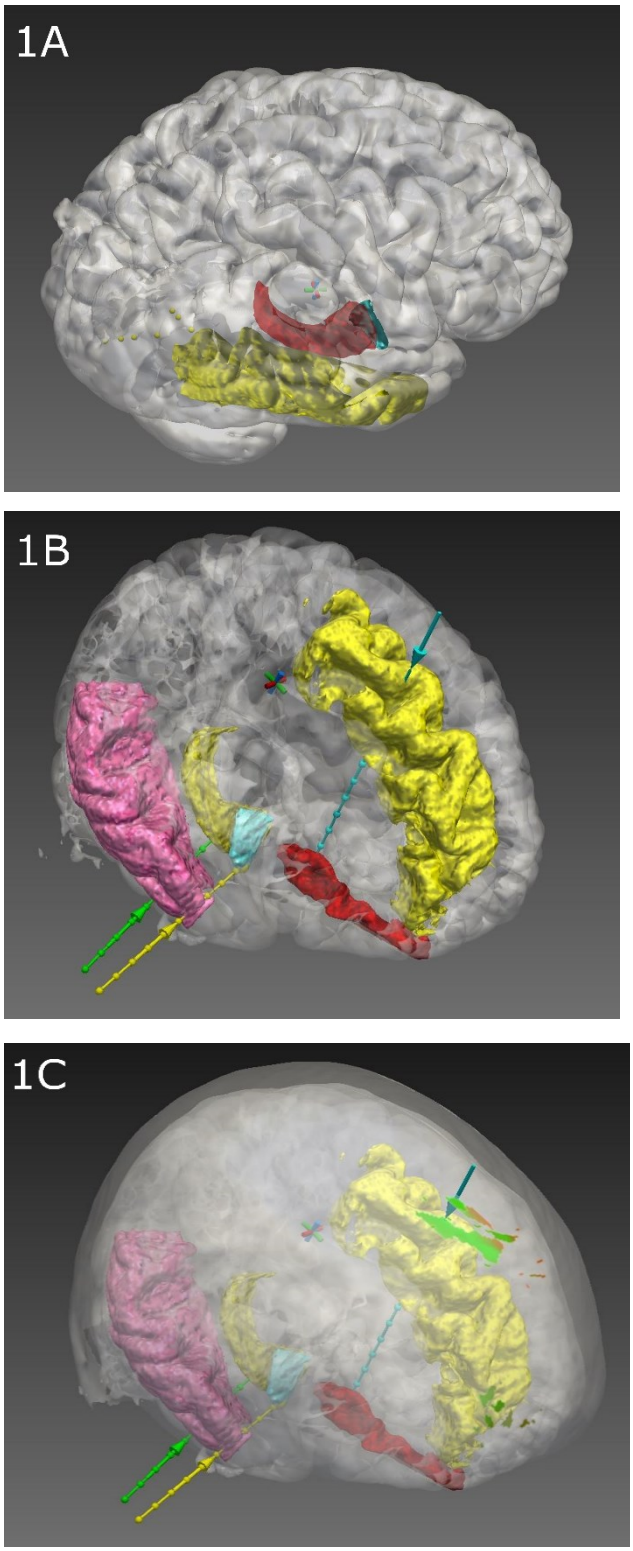

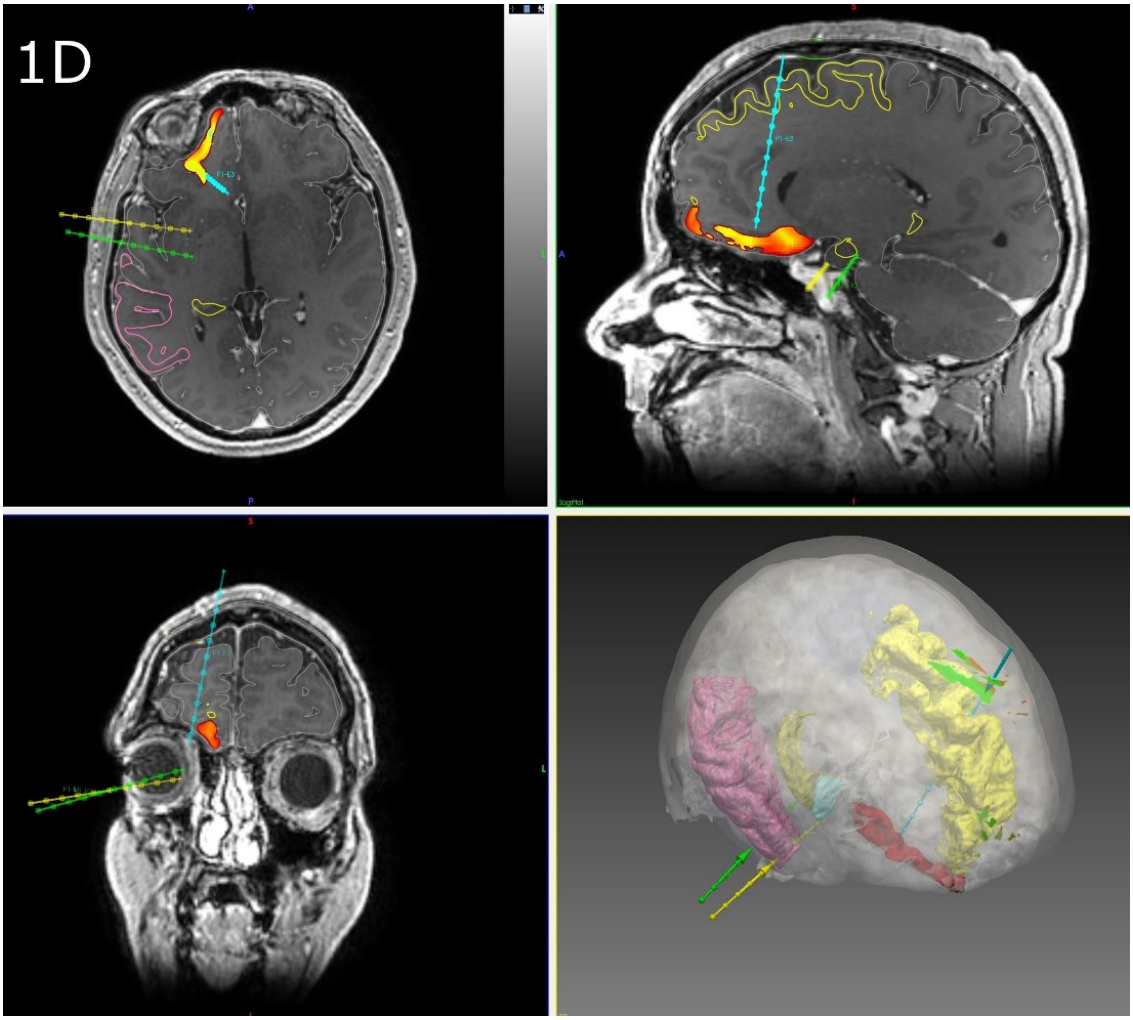

Figure 12 Legend: A) Using the EpiNav Strategy™ module ROIs are automatically segmented from the parcellation image. In this example, the cortex (white) is semi-transparent to allow visualisation of the underlying middle temporal gyrus (yellow), amygdala (blue) and hippocampus (red). B) Entry points and target points for the electrodes within the strategy are generated automatically based on the safety metrics defined by the user. Electrode colours are shown as the right amygdala (yellow), right anterior hippocampus (green) and right posterior medial orbitofrontal (blue). C) A surface risk 'heat map' on the scalp has been generated for the mesial orbitofrontal electrode, as an example, representing the safety of potential trajectory entry points. D) Orthogonal and 3D views showing the target risk 'heat map' has been generated for the mesial orbitofrontal electrode, as an example, showing safe trajectory target points in orthogonal planes. Please note, in Figures 8.a.1 B-D, only three electrode trajectories are shown for clarity.

2.4 **Results**

Thirteen consecutive patients who underwent SEEG implantation of 116 electrodes were included in the study. Manual plans were not provided for 12 electrodes due to safety concerns of reaching specified targets; however, CAP was able to generate trajectories for these electrodes. As such, paired results for safety metric comparison were available for 104 electrodes Table 4 and Figure 13: Comparison of CAP and manual electrode risk metrics.).

Table 4: Risk metric comparison between CAP and Manual plans:

Metric	CAP plan (mean +/- SD)	Manual plan (mean +/- SD)	Student's t-test
Mean length (mm)	39.8 +/- 14.9	54.0 +/- 14.7	p = 0.001
Drilling angle (deg)	14.8 +/- 5.8	18.9 +/- 9.0	p = 0.001
Grey matter sampling ratio	0.35 +/- 0.2	0.30 +/- 0.16	p = 0.007
Minimum distance from vessel (mm)	5.4 +/- 3.0 mm	2.8 +/- 1.9 mm	p < 0.001
Risk	0.57 +/- 0.39	1.00 +/- 0.60	p = 0.001

Figure 13: Comparison of CAP and manual electrode risk metrics.

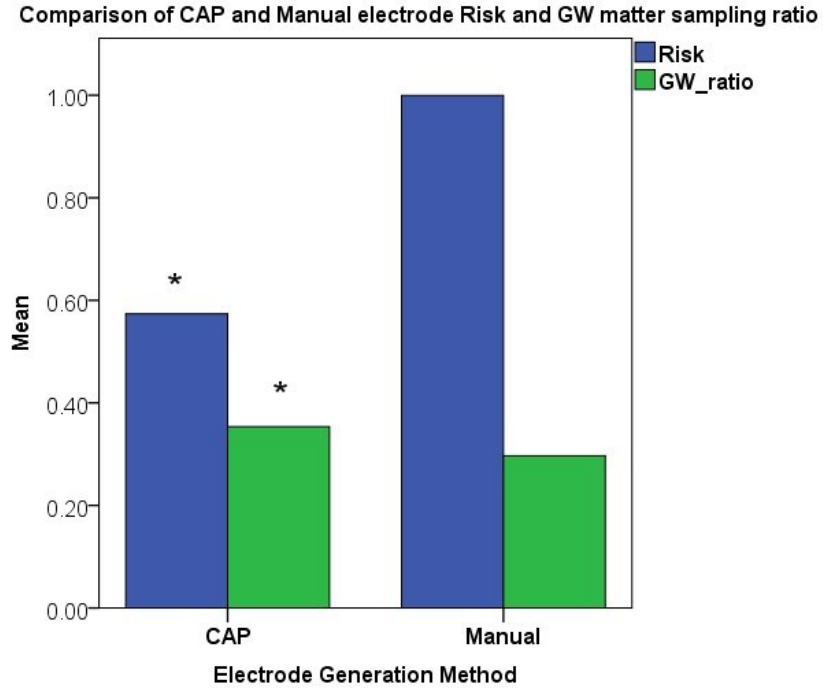

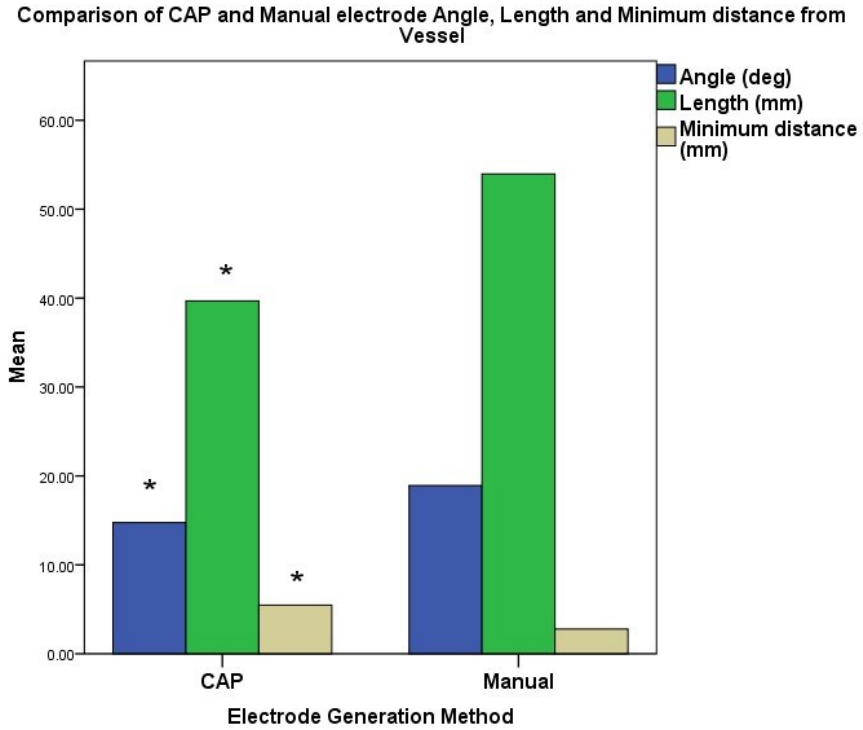

Figure 13 Legend: A) Comparison of Risk and GM sampling ratio between CAP and manually generated electrodes showing a statistically significant reduction in Risk and improvement in GM sampling ratios. B) Comparison of trajectory angle, length and minimum distance from segmented vessels showing a statistically significant reduction in electrode trajectory length, drilling angle and increase in minimum distance from vasculature using CAP compared to manually generated electrodes. (p<0.01)*

2.4.1 Inter-rater variability

Surgeons rated each electrode for the feasibility of the entry point, trajectory and target point. If all three ratings were deemed feasible, the electrode was deemed feasible as a whole. All surgeons initially rated the same two pairs of plans (5 x 18 CAP and 5 x 14 manual electrode ratings) to assess inter-rater variability. A generalised likelihood ratio produced a test statistic of 6.72. When compared to the quantiles of Chi-squared distribution with 4 degrees of freedom, a p-value of 0.11 was obtained, implying that there is insufficient evidence to suggest a difference in surgeon ratings. The remaining 98 electrode ratings pairs were then pooled.

2.4.2 Feasibility of electrode trajectories

Based on independent external ratings, both manual and CAP electrodes were rated as feasible in 42.8% of cases. CAP was able to provide feasible electrodes in 19.4%, whereas manual planning was able to generate a feasible electrode in 26.5% when the alternative generation method was not feasible. In 11.2% of cases, both the CAP and manual electrode plans were both rated as not feasible (see Table 5)

Table 5: External blinding ratings of electrode feasibility:

	Manual feasible		
CAP feasible	Yes	No	Total
Yes	42.8% (42/98)	19.4% (19/98)	62.2% (62/98)
No	26.5% (26/98)	11.2% (11/98)	37.8% (37/98)
Total	69.4% (68/98)	30.6% (30/98)	100% (98/98)

2.4.3 Time to generate plans

Both CAP and manual electrodes were generated using EpiNav^{TM,} which requires multimodal images to be co-registered and segmentation of vascular, sulcal and grey matter models prior to electrode planning. This time was common to both methods and depending on the number of images can take up to 60 minutes. Both CAP and manual planning require generated electrodes to be checked using the probe's eye and orthogonal views to ensure the electrodes are suitable and take approximately 2 minutes per trajectory. Time for the generation of the plans using the manual method ranged from 2-4 hours whilst computational time for CAP varied from 34-120 seconds. EpiNav computation times are based on the use of a commercially available laptop (Intel® Xeon™ i7-6820HK CPU @ 2.70 GHz, 16 Gb RAM and NVIDIA GeForce GTX 980M 4GB).

2.5 **Discussion**

CAP for surgical interventions provides the potential to automate time-consuming tasks and optimise clinically significant parameters to improve the safety and efficacy of surgical interventions. Unlike human users, CAP systems provide reliable and reproducible results regardless of the institution or team providing the intervention. CAP algorithms, however, are only as good as the information provided to them. As a result, rigorous quality assurance is

required for the imaging acquisition, post-processing and model segmentation used to generate CAP electrodes. The success of epilepsy surgery is dependent on the detection and safe resection of the epileptogenic zone. This is defined as the minimum region of the brain that is required to be resected or ablated to result in sustained seizure freedom. In cases in whom the presumed seizure onset zone cannot be accurately defined due to discrepancy or lack of clarity in the non-invasive presurgical evaluation (imaging studies, scalp EEG and neuropsychological investigations), invasive EEG in the form of SEEG or subdural grid/strip implantation is indicated. SEEG investigations involve the stereotactic placement of electrodes within predefined brain structures to allow for the spatial and temporal evolution of interictal and ictal activity to be recorded. This is subsequently used to guide surgical resection margins as well as functional cortical mapping. Here we describe a multimodal imaging platform for automated SEEG electrode implantation that allows for multiple electrode trajectories to be planned into anatomically defined structures, whilst avoiding conflicts with other electrodes, maintaining a user-defined safety margin from cerebral vasculature, increasing cumulative distance from vessels, prevents crossing of sulcal pial boundaries and maximising grey matter sampling whilst reducing intracerebral electrode length and drilling angles.

2.5.1 Previous studies evaluating computer-assisted planning

Initial studies of CAP in neurosurgery were described in the 1980s for stereotactic intracranial biopsies(Davis et al., 1988; Giorgi et al., 1989b). The system described by Davies et al. allowed the co-registration of pre-operative MRI scans with digital subtraction angiography and a CT scan performed once patients were placed in stereotactic frames(Davis et al., 1988). The target points for the biopsies were manually placed by the surgeon and the computer system automatically calculated the stereotactic coordinates. Potential trajectories could then be simulated on anterior-posterior and lateral projections. Davies et al. provided results from 447 biopsies performed in 439 patients for both supratentorial and infratentorial targets over a five year period in which a histological diagnosis was achieved in 99% and a clinically significant haemorrhage occurred in <1% (3/439). The next significant advance in CAP was through the introduction of 3D reconstructions of the cortex to allow the surgeon to choose the most appropriate surgical trajectory for the resection of supratentorial mass lesions(Giorgi et al., 1989a). Giorgi et al. utilised this to plan a transfrontal approach as an alternative to a transcallosal approach for intraventricular lesions thereby preventing the neuropsychological complications related to partial corpus callosotomy(Giorgi et al., 1989b). A further iteration of

this system was also used to allow manual segmentation of lesions and improve the distinction between normal brain structures. Zamorano et al. described the 'Wayne State University hardware and software configuration' which in addition to pre-planning surgical approaches could also be used intra-operatively with a neuronavigation system to track instruments in real-time relative to the patients head(Zamorano et al., 1994). The NeuroPlanner software also integrated multiple brain atlases within a computer-assisted planning system for functional neurosurgical procedures such as thalamotomy, pallidotomy and deep brain stimulation (DBS) procedures(Nowinski et al., 2000). This system resulted in a reduction in surgical operative time, improved targeting accuracy, reduced surgical complications and lower overall procedure cost. The prior use of clinical information to build upon and guide further surgery was described by Guo et al. who developed probabilistic functional maps to guide the targeting of the subthalamic nucleus for DBS(Guo et al., 2007). Here the CAP automated targets and trajectories in 10 patients were compared to those developed by an experienced stereotactic neurosurgeon. The average distance between the CAP and manually planned target points was on average <2 mm. The incorporation of trajectory risk was used by Vaillant et al. based on whether a particular trajectory intersected a critical brain structure and the relative weighting given to the importance of that structure(Vaillant et al., 1997). Given that the major complications of stereotactic electrode placement include haemorrhage and inaccuracy of targeting a structure the inaccuracy of the implantation method also requires consideration(Mullin et al., 2016a; Vakharia et al., 2017b). It is not sufficient therefore to calculate whether an electrode conflicts with a critical structure (such as an intracerebral vessel) but also how close the electrode passes to it along its trajectory. Cardinale et al. introduced the concept of a minimum safety margin when planning SEEG electrodes based on the accuracy of the implantation method being used calculated by the following equation(Cardinale et al., 2013):

Equation 1: Planning Safety Margin

$$Planning\ safety\ margin = Electrode\ radius + \frac{\Sigma \parallel i - \hat{\imath} \parallel}{n} + 3\sigma$$

where, $\frac{\Sigma \parallel i - \hat{\imath} \parallel}{n}$ *represented the mean implantation error and σ the standard deviation of the implantation error.*

Based on this, a minimum distance of 3 mm was recommended so that 99% of electrodes will fall within this safety margin. Once a minimum planning distance is set, the risk score for candidate trajectories can be calculated and represented as a heat map on the cortical surface (Beriault et al., 2011; Nowell et al., 2016a; Shamir et al., 2010). The calculation of risk, however, is based on the accuracy and completeness of segmentation of critical structures. In the case of cerebral vasculature, a number of different vessel segmentation methods have been utilised including gadolinium-enhanced MR, MR venography, MR angiography, time of flight (TOF) and DSA(Cardinale et al., 2015). The gold-standard method is DSA, but this entails an invasive procedure and radiation exposure. Non-invasive techniques visualize fewer segmented vessels, but it is unclear whether this is clinically significant and whether there is a minimum vessel size that needs to be avoided. A simple weighting based on vessel size may not be appropriate as multiple factors such as stylet design, vessel tethering and vessel wall (arteries versus veins) also impact upon the likelihood of haemorrhage(Brunenberg et al., 2007). Whilst reviewing complications associated with the placement of DBS electrodes Elias et al. described a haemorrhagic complication rate of 10% in cases when electrodes crossed a sulcus and an intraventricular haemorrhage rate of 5% with ventricular penetration(Elias et al., 2009). Beriault et al. described a CAP algorithm that avoided segmented vasculature, critical neurological structures, ventricles, sulci and did not allow crossing of the midline providing qualitative safety metrics for each trajectory(Bériault et al., 2012). Trope et al. added additional tractography and fMRI data and found that presentation of multi-modal information to the surgeon resulted in a change in trajectory for intracranial biopsies in 85% of cases(Trope et al., 2015). Shenai et al. described the use of CAP for the stereotactic placement of depth electrodes within the amygdalohippocampal complex in patients with epilepsy(Shenai et al., 2007). The system resulted in one additional electrode contact being inserted within the target structure. De Momi et al. described an automated system for the placement of multiple SEEG electrodes in which entry and target points are “roughly” selected and drilling angle to the skull as well as the distance from other electrodes are additionally considered when calculating optimal trajectories(De Momi et al., 2014b). Clinical validation of 26 electrodes in three patients was assessed by four blinded neurosurgeons and feasible electrodes were planned in 86% of cases and in 30% of cases, these were preferred to manually planned electrodes. Of note, CAP resulted in a significantly greater distance from vessels within the first 25 mm of the trajectory compared to the manual plans.

2.5.2 Improvements from previous work

We have previously described the EpiNav™ software platform for the automated placement of SEEG electrodes based on a user-defined target and the aforementioned constraints(Nowell et al., 2016b). We have subsequently improved upon this work by allowing entire anatomical structures to be selected as the target point based on a whole-brain parcellation. This, therefore, allows the safest target within the anatomical structure of interest to be selected as manually placed targets may not represent the optimal solution. Furthermore, to improve the feasibility of electrodes and to account for different surgical preferences, we have allowed the user to iterate through risk-stratified CAP generated electrodes. The development of a 'Next Target' or 'Next Entry' function allows the user to iterate through computed trajectories until they are satisfied with the trajectory. In line with our previous work, we have shown that targeting whole structures, as opposed to specific target points, results in improved safety metrics when compared to manually generated plans.

2.5.3 External validation of computer-assisted planning

To provide external validation of the CAP planned trajectories 116 paired manual and CAP electrode plans for 13 patients were rated by neurosurgeons with expertise in SEEG from external institutions. The manual plans presented to the raters had already been implanted and no haemorrhages (clinically or non-clinically significant) occurred so by definition can be considered feasible. Of interest, 69.4% of manual implantations were rated as feasible by the external raters reflecting the variation in individual surgeon practices and preferences depending on the implantation method used. Raters were asked to rate the feasibility of the trajectories based on their individual practices and whether they would be prepared to implant the trajectories themselves. It would be expected, therefore that raters use different safety margins and heuristics, such as the crossing of sulci, when assessing trajectories. CAP trajectories were deemed feasible in 62.2% and were able to generate feasible electrodes in 19.2% of cases where manual plans were considered infeasible. CAP is able to generate clinically feasible electrodes which are no less feasible than manually planned electrodes when externally rated. To our knowledge, this is the first study in which both manual and CAP electrodes have been rated by blinded external raters to provide a more methodologically robust comparison between the implantation methods.

2.5.4 Limitations of the study

Methodologically the main limitation of the study is that it is retrospective in nature. Retrospective comparisons provide the potential for bias when generating the comparison dataset. Given that CAP data were generated in an automated fashion many months after the manual plans, the impact of bias is likely to be minimal but cannot be excluded entirely. A prospective validation study is currently underway.

MRV vessel segmentations were used to generate both the CAP and the manual electrode trajectories. The Gadolinium-enhanced T1 sequences were used as the reference image against which raters assessed feasibility. Gadolinium-enhanced T1 sequences highlight a number of vessels that are not possible to segment from the MRV. As such, one would expect this to favour manual planning over the CAP generated electrodes. There is significant heterogeneity between the vessel segmentation methods used within European and North American epilepsy surgery centres. Although DSA is regarded by many as the gold standard, it in itself is an invasive investigation that carries risk and radiation exposure. Given that DSA was not the standard of care in our institution at the time of manual electrode implantation, we were unable to assess the impact of DSA on CAP trajectories. A potential future improvement of CAP would be to plan using DSA or multi-modal MR vessel segmentations.

Sulcal models used for CAP electrode generation are based on the whole brain parcellation and subsequent ability to segment CSF. The presence of CSF below the level of the gyrus is then taken to be within a sulcus and this is used as a region for exclusion during CAP electrode generation. CSF based sulcal models are not optimal in young patients, as the majority of sulci do not have visible CSF within them and the sulci are 'potential' as opposed to actual spaces. Further improvements in the sulcal model generation are likely to lead to improved CAP electrode safety.

EpiNav™ has an integrated export function to allow planned trajectories to be seamlessly exported to the S7 stealth station (Medtronic Inc). Currently, the software does not seamlessly export to other neuronavigation systems and this could potentially reduce the number of potential users of the software, especially in the developing world.

2.6 **Conclusion**

Here we provide a retrospective validation study of CAP for the placement of SEEG electrodes in patients with drug-resistant focal epilepsy. CAP electrodes overall had an improved risk profile, increased minimum distance from vessels, shorter intracranial length, increased GM sampling, and lower drilling angles to the skull. CAP electrodes were assessed by blinded external raters as feasible in 62.2% of cases compared to 69.4% of manually generated trajectories and were also found to be feasible when manually planned electrodes were infeasible in 19.4% of cases. CAP electrode planning is a valuable tool that can be used as a first-line method of electrode trajectory generation. The electrodes can then be reviewed by the operating surgeon with the ability to iterate through CAP-generated alternative trajectories or to re-plan electrodes manually when CAP electrodes are deemed infeasible. Given that CAP electrodes can be generated in a fraction of the time compared to manual electrodes, this is likely to reduce the planning burden whilst ensuring improved safety metrics.

3 A Prospective validation study of computer-assisted planning for stereoelectroencephalography. Based on (Vakharia et al., 2019b)

3.1 **Abstract**

3.1.1 Objective

Stereoelectroencephalography (SEEG) is a diagnostic procedure in which multiple electrodes are stereotactically implanted within pre-defined areas of the brain to identify the seizure onset zone, which needs to be removed to achieve remission of focal epilepsy. Computer-assisted planning (CAP) has been shown to improve trajectory safety metrics and generate clinically feasible trajectories in a fraction of the time needed for manual planning. We report a prospective validation study of the use of EpiNav^{TM} as a clinical decision support software for SEEG.

3.1.2 Methods

Thirteen consecutive patients (125 electrodes) undergoing SEEG were prospectively recruited. EpiNav^{TM} was used to generate 3D models of critical structures (including vasculature) and other important regions of interest. Manual planning utilising the same 3D models was performed in advance of CAP. CAP was subsequently employed to automatically generate a plan for each patient. The treating neurosurgeon was able to modify CAP generated plans based on their preference. The plan with the lowest risk score metric was stereotactically implanted.

3.1.3 Results

In all cases (13/13) the final CAP generated plan returned a lower mean risk score and was stereotactically implanted. No complication or adverse event occurred. CAP trajectories were generated in 30% of the time with significantly lower risk scores compared to manually generated.

3.1.4 Conclusions

EpiNav™ has successfully been integrated as a CDSS into the clinical pathway for SEEG implantations at our institution. To our knowledge, this is the first prospective study of a complex CDSS in stereotactic neurosurgery and provides the highest level of evidence to date.

3.2 **Introduction**

Surgery can result in sustained seizure freedom in patients with drug-resistant focal epilepsy if the seizure onset zone can be resected(De Tisi et al., 2011). Invasive EEG recordings are needed to identify the SOZ when non-invasive pre-surgical investigations are discordant when a tailored resection is required and for mapping adjacent eloquent cortex(Isnard et al., 2018; Kovac et al., 2016). Over the last two decades, there has been a significant shift toward SEEG from subdural grid placement in most epilepsy surgery centres(Vakharia et al., 2018a). SEEG is a procedure in which electrodes are stereotactically inserted into 10-16 predefined brain regions and affords a comparatively favourable safety profile(Bourdillon et al., 2017; Schmidt et al., 2016) with rapid patient recovery time. Trajectory planning follows the formulation of an intracranial EEG sampling strategy, derived from consideration of seizure semiology, scalp EEG and imaging data. Precise SEEG trajectory planning requires a number of parameters to be optimised, including accurate targeting of the anatomical structures of interest through an avascular corridor, drilling angle to the skull, intracerebral length, grey matter sampling and avoidance of other SEEG electrodes. Planning is, therefore, a time-consuming process that requires multi-disciplinary input. The risk of morbidity from SEEG in a recent meta-analysis was 1 per 287 electrodes, which equates to 1 in every 29 patients implanted(Mullin et al., 2016a). The greatest risk associated with SEEG is haemorrhage and it is imperative that all possible measures to mitigate this are employed.

Computer-assisted planning enables parameters, which are thought to be most useful during pre-operative planning, to be optimised in a systematic and time-saving manner. Such software has been classified by the FDA as 'Clinical Decision Support Software' (CDSS) and legislation differentiates this from medical devices(Gottlieb, 2017). A working definition of CDSS is a system that "provides clinicians or patients with computer-generated clinical knowledge and patient-related information, intelligently filtered or presented at appropriate times, to enhance patient care"(O'Sullivan. et al., 2014). To be classified as a CDSS the software must: (1) be intended to display, analyse or print medical information about a patient or (2) be intended to support or provide recommendations to a health care professional about prevention, diagnosis or treatment of a disease but (3) not be intended to acquire, process or analyse medical images or signals and (4) the healthcare professional must be able to review the basis for such recommendations(Gottlieb, 2017). Most current CDSSs provide clinicians with alerts or reminders, such as drug allergy status and are embedded within hospital electronic systems.

More sophisticated CDSSs include disease-related scoring systems or utilise artificial intelligence to aid diagnosis or management.

We utilise EpiNav™ as a CDSS that is able to automatically generate multi-trajectory SEEG plans in a fraction of the time required for manual planning. Previous studies of SEEG CDSSs have been retrospective comparisons with previously implanted manually planned trajectories(De Momi et al., 2014a; Nowell et al., 2016b; Sparks et al., 2017b; Vakharia et al., 2018e). These showed reduced risk scores with the use of CAP. Blinded neurosurgeons rated the feasibility of planned trajectories, with no difference between the acceptability of manual and CAP trajectories. Ratings for implanted manually planned trajectories were ~70%, highlighting the variability in surgical practice (Vakharia et al., 2018e).

We report a prospective comparative study between CAP and manually planned SEEG trajectories in which the plan with the lowest mean risk score was stereotactically implanted.

3.3 **Methods**

3.3.1 Patient demographics

Thirteen consecutive patients (7 male) with drug-resistant focal epilepsy undergoing SEEG as part of their routine clinical care at The National Hospital for Neurology and Neurosurgery, London, UK, were enrolled between July 2017 and January 2018. This study was granted by the National Research Ethics Service Committee London, approval reference: 12/LO/0377. Written consent was obtained from all patients prior to inclusion in the study. Patient age at the time of SEEG implantation was 33.5±6.5 years (mean±S.D.). Target regions for SEEG sampling were determined following a multi-disciplinary team meeting in which the clinical history, semiology, video telemetry, imaging, neuropsychological, and neuropsychiatric assessments were reviewed (see Table 6). Following this, the EpiNav™ software was then utilized to assist the surgeon with the precise planning of the electrode trajectories, after the acquisition of vascular imaging.

Table 6: Patient demographics

No.	Age (years)	Onset of epilepsy (years)	Hemispheric language dominance (fMRI)	Semiology	Scalp EEG (contact names based on EEG 33 system)	Neuroimaging findings	Primary hypothesis of EZ
1	42	3	Left	Psychic aura Automotor seizure Dystonic posturing of the left arm Post-ictal nose-wiping with the right hand	Interictal: Intermittent right temporal slowing and right temporal sharp waves. Ictal: Fast activity in the posterior parietal region.	Right mesial temporal sclerosis; Hippocampal volumes: Right 2.34 cm^3 Left 2.94 cm^3 Ratio:79% FDG PET inconclusive	Neocortical posterior quadrant onset with early temporal involvement

2	43	14	Left	Psychic aura Complex motor / hyperkinetic seizure Loss of awareness Post-ictal speech difficulties	Interictal: Intermittent slow left and right temporal regions. Sharp waves left anterior temporal (F7>LSPh>F11>F3, ~50%) and right frontotemporal (F8>RSPh>F12>T4, ~50%). Ictal: Left temporal discharges at the onset of the seizure.	Normal structural imaging FDG PET left frontal and temporal hypometabolism Ictal SPECT inconclusive	Left frontal (Neuropsychological testing implicates the dominant frontotemporal region)
3	26	6	Left	Autonomic aura Automotor seizure – vomiting	Interictal: Polyspikes and sharp waves (F8>FC6>F4) in runs	Normal structural imaging	Right hemispheric ?insula

				followed by outstretched arms and clenched fists Dialeptic – behavioural arrest with loss of awareness followed by oral automatisms Secondarily generalised tonic/clonic seizure	without clinical change. Ictal: Right inferior frontal > right frontocentral onset with prominent ictal tachycardia.	FDG PET – mildly reduced tracer activity in both temporal lobes	(Neuropsychological testing implicates the non-dominant temporal region)
4	34	1	Left	Psychic/autonomic aura Hyperkinetic seizure (bicycling	Interictal: No abnormalities.	Left temporal hippocampal sclerosis FDG PET - Reduced metabolic activity	Left frontotemporal (Neuropsychological testing unable to distinguish left frontal from temporal

				movements in both legs)	Ictal: Left temporal lobe onset.	in the left temporal lobe	dysfunction due to language barrier) Possible non-epileptic attacks
5	25	9	Not performed	Unspecified aura Dialeptic seizure Left-arm and leg tonic seizure Axial tonic seizure	Interictal: Intermittent slow over the vertex (Cz) and right frontocentral (F4 and C4) regions. Ictal: Right frontocentral onset.	Haemosiderin staining in the left superior frontal gyrus suggestive of cavernoma FDG PET – minimal hypometabolism in the left superior frontal region Ictal SPECT – hyperperfusion in the left superior	Right mesial frontal lobe (Neuropsychological testing suggests frontal lobe dysfunction)

						frontal and right frontal regions	
6	37	7	Bilateral	Unspecified aura Asymmetric tonic seizure (left arm extended) Dialeptic seizure	Interictal: Very rare sharp waves anterior frontal region. Ictal: Rhythmic activity (3-5 Hz) frontocentral region.	Normal structural imaging FDG PET – subtle reduction in metabolic activity in the right frontal lobe Ictal SPECT – hyperperfusion in the right frontal lobe	Right fronto-central (Neuropsychological testing suggests dominant hemisphere dysfunction)
7	31	3	Right	Right arm somatosensory aura	Interictal: Sharp waves left frontotemporal (max F7/T7) with polyspikes and left	Extensive damage to left hemisphere lined by gliotic rim involving temporal,	Left centro-parietal (Neuropsychological testing suggests widespread cerebral

				Asymmetric tonic seizure (right arm) Post-ictal right arm weakness Dialeptic / Automotor seizure	posterior temporoparietal (max P7). Ictal: Attenuation and low amplitude fast in the left temporoparietal region. Repetitive left temporoparietal sharp waves.	parietal and insula lobes.	dysfunction maximally implicating the non-dominant frontoparietal region)
8	36	4	Left	Dialeptic seizure Automotor seizure Secondarily generalised tonic/clonic seizure	Interictal: Sharp waves right temporal (max T4) 80% and sharp waves left anterior temporal (max F7) 20%.	Normal structural imaging FDG PET – Reduced metabolic activity in temporal lobes	Right frontotemporal (Neuropsychological testing did not provide any consistent lateralising or localising signs)

					Ictal: Onset non-localisable. Evolution was more prominent over the right hemisphere.	bilaterally, right more than left.	
9	33	7	Left	Left-arm and leg somatosensory aura Autonomic aura Automotor seizure Secondarily generalised tonic/clonic seizure	Interictal: Intermittent right temporal slowing Ictal: Right temporal onset with wider right-hemispheric onset recorded in some seizures	Right hippocampal sclerosis Hippocampal volumes: Right 2.08 cm^3 Left 2.53 cm^3 Ratio: 82%	Right temporal plus (Neuropsychological testing suggests dominant frontotemporal dysfunction)

10	19	15	Left	Bilateral visual/auditory aura Automotor seizure Secondarily generalised tonic/clonic seizure	Interictal: Sharp wave left temporal (LSph and T7) and left frontal (Fp1>F3>Fz) Ictal: Spike and slow waves left hemisphere, maximal in the fronto-centrotemporal region with spread to the right	Normal structural imaging FDG PET – Mild reduction in metabolic activity in the left temporal lobe	Left frontotemporal (Neuropsychological testing suggests left temporal lobe dysfunction)
11	29	22	Left	Psychic aura Automotor seizure – left hand and oral automatisms	Interictal: Sharp waves right temporal maximal (F12 and T8). Rare left temporal sharp waves (F11)	Right hippocampal sclerosis Hippocampal volumes:	Right frontotemporal (Neuropsychological testing suggests right frontal lobe dysfunction)

				Secondarily generalised tonic/clonic seizure	Ictal: Regional right inferior temporal onset which evolves to rhythmic theta and propagation to the right parasagittal and left temporal regions	Right 2.14 cm^3 Left 2.76 cm^3 Ratio: 77.6% FDG PET – Reduced metabolic activity in the right temporal lobe	
12	32	22	Right	Bilateral somatosensory aura Asymmetric tonic seizure - head turn to left with bilateral arm extension	Interictal: Sharp waves left frontocentral region (F3/FC1>FC5) Ictal: Left fronto-central onset	Subtle left hippocampal sclerosis Hippocampal volumes: Right 3.02 cm^3	Left fronto-central (Neuropsychological testing suggests dominant temporal lobe dysfunction)

				Secondarily generalised tonic/clonic seizure		Left 2.93 cm^3 Ratio: 97% FDG PET – Reduced hypometabolism over the left hemisphere most prominent in the left inferior frontal region	
13	36	27	Left	Dialeptic seizure Automotor seizure Secondarily generalised tonic/clonic seizure	Interictal: Sharp waves right anterior temporal (50%), left anterior temporal (30%), right frontopolar (10%) and left frontopolar (5%)	Widening of the sulci over the right cerebral hemisphere suggestive of a perinatal right-hemispheric insult	Right frontotemporal (Neuropsychological testing did not provide any consistent lateralising or localising signs)

					Right frontocentral paroxysmal fast activity Ictal: Right hemispheric activity at the onset, maximal centroparietal regions followed by temporal spread	FDG PET – Reduced metabolic activity in the right frontal and temporal lobes	

Figure 14: CAP Image Processing Pipeline

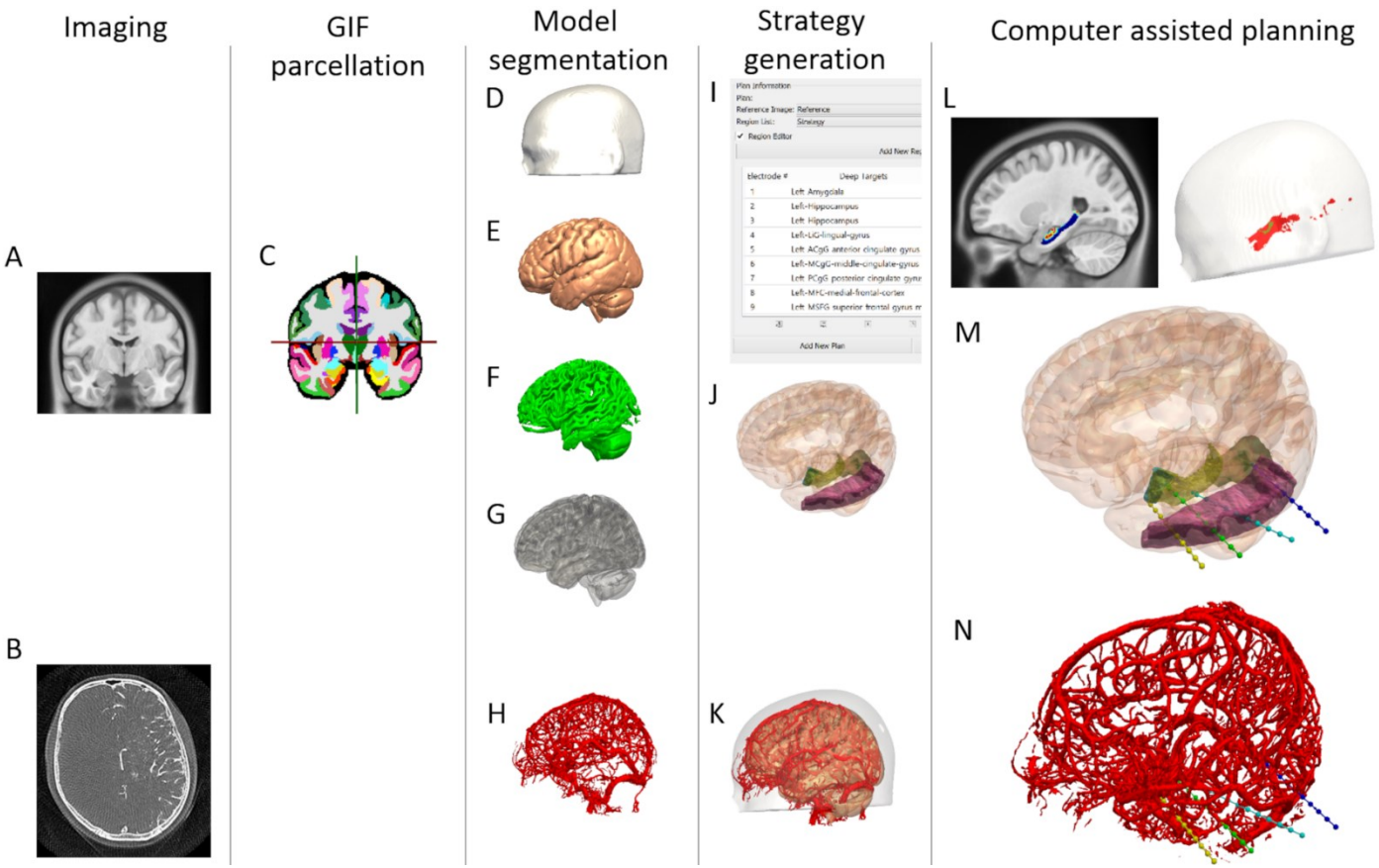

Figure 14 Legend: Imaging modalities required for CAP include a reference image (A), preferably a gadolinium-enhanced T1 image, and a vascular imaging modality (B). A whole-brain parcellation (C) is generated from the T1 image. A model of the scalp (D) is generated from the reference image whilst models of the cortex (E), sulci (F) and grey matter (G) are automatically extracted. Vascular models (H) are derived from the vascular imaging following filter application and mesh cleaning. The implantation schema entry and target points are then selected from the whole brain parcellation (I) and brain ROIs are automatically segmented (J). In this case amygdala, hippocampus and lingual gyrus target regions are shown with the middle temporal gyrus as the entry region. A composite image of the scalp, brain and vasculature is shown (K). Trajectories that exceed the length, angle and critical structure restrictions are removed from consideration. Risk maps for the target structures (only the hippocampus is shown) and corresponding entry zones are generated (L). CAP trajectories with shortest intracerebral length, orthogonal drilling angles, maximal grey matter sampling and lowest trajectory risk score are provided (M). Generated trajectories also shown with the vascular model (N). Region of interest (ROI). Note: for clarity, only temporal electrodes are shown.

3.3.2 Trajectory Planning

Experienced neurosurgeons undertook manual planning in all patients with 3D models of the cortex and vascular segmentation before CAP (see below for description). Entry points on the scalp surface and target points within the structure of interest were manually determined and iterated to achieve a satisfactory solution that was labelled *Plan 1*.

CAP was undertaken using EpiNav™ (CMIC, UCL). EpiNav™ is a multi-modal imaging platform that allows manual as well as advanced multi-trajectory automated trajectory planning(Sparks et al., 2017a), invasive EEG grid/electrode contact localisation(Granados et al., 2018b), SEEG signal visualisation, source localisation and resection planning(Nowell et al., 2017). CAP was performed with a gadolinium-enhanced T1 MRI reference image and vascular segmentation (see Figure 14). Patients also underwent digital subtraction catheter angiography with an intra-arterial contrast injection of the ipsilateral internal carotid artery and vertebral artery depending on the implantation strategy. A vessel extraction filter(Zuluaga et al., 2015) was applied to the raw bone subtracted DSA images before manual threshold setting, 3D model generation and mesh cleaning. Rigid registration of the bone-inclusive DSA image to the reference image was then performed. A visual check of the vessel segmentation suitability and

registration accuracy was performed before commencing planning. Whole-brain parcellations and Pseudo-CT images were generated from T1 MPRAGE sequences with a field-of-view of 224×256×256 mm (Antero-posterior, left-right, inferior-superior) an acquisition matrix of 224×256×256 for a voxel size of 1 mm isotropic (TE/TR/TI = 3.1/7.4/400 ms; flip angle 11°; parallel imaging acceleration factor 2) using geodesic information flows (Cardoso et al., 2015a). Patient-specific 3D models of the cortex, sulci, GM, scalp and SEEG entry and target regions were then generated from the GIF parcellations. The same models were utilised during manual planning as were required for CAP to ensure parity between the two planning methods. For a detailed description of the CAP, algorithm see Sparks et al. (Sparks et al., 2017b). In brief, the DSA vascular segmentation was used as a critical structure and the algorithm plans trajectories to remain as far from the vessel as possible, up to a distance of 1 cm. A minimum vessel distance of 3 mm was set based on previous accuracy data(Cardinale et al., 2013), whereby only 1% of implanted electrodes would exceed this distance from the planned trajectory. A risk score(Sparks et al., 2017b; Zombori et al., 2011), based on the cumulative distance of the planned trajectory from the vessel segmentation, was calculated using the following equation:

Equation 2: Risk Score

$$R = \begin{cases} \sum_{i}^{N} \frac{10 - Dist(i)}{N(10-3)}, & Dist(i) > 3 \\ 1 + \sum_{i}^{N} \frac{3 - Dist(i)}{3N}, & Dist(i) \leq 3 \end{cases}$$

Where N = 128, the total number of sampling nodes along the length of the trajectory and i denotes the indices of the individual node being computed. The risk score (R) is expressed as a value between 0-2, with values >1 indicating at least one node is within 3 mm of a segmented blood vessel.

Sulcal models were derived from the whole brain parcellation and were set as no-entry zones to prevent electrodes from passing through the sulci pial boundary where vessels are known to be present. The grey matter at the bottom of sulci is sampled by contacts on electrodes passed down the adjacent gyrus. GM was weighted so that trajectories with increased GM sampling were preferentially selected in order to maximise the efficiency of detecting epileptic activity. Coupled with the sulcal model, this preferentially places electrodes within grey matter

at a depth of sulci. Angle crossing the skull and length restrictions were applied at <30 degrees from orthogonal and <90 mm, respectively, based on previous work showing that these parameters generated clinically feasible trajectories when assessed by blinded external experts(Vakharia et al., 2018e). Planned trajectories were prevented from being within 10 mm of other trajectories to satisfy local post-SEEG MRI safety guidelines.

Trajectories generated by CAP were labelled as *Plan 2* and represent the output of CAP without any human review. Following this '*Next Entry'* and '*Next Target'* buttons were used to iterate through the CAP planned trajectories in a risk-stratified manner until the most feasible trajectory was found and labelled as *Plan 3*. This represents the most feasible trajectory that could be provided with CAP after human review but without precise adjustments. If precise adjustments were required, these were applied and labelled as *Plan 4*. The mean risk score of all trajectories in Plan 1 was compared to Plan 4 and the plan with the lowest risk score was implemented surgically. The plans were then exported to the S7 Stealth station (Medtronic Inc.) for stereotactic implantation. Following implantation, patients underwent both CT and MRI scans within 48 hours, which were then co-registered to the generated plans. Any haemorrhage (clinical or asymptomatic) present on the images was reviewed and noted. Repeat CT scans were not routinely performed after removal of the electrodes to prevent unnecessary irradiation unless there was a clinical indication. All other surgical complications were stratified according to the Clavien-Dindo classification(Clavien et al., 2009).

3.3.3 Statistical analysis

A prospective sample size calculation revealed that 42 electrode comparisons (~5 patients) would be required to detect a 0.1 reduction in risk score assuming a standard deviation (S.D.) of 0.1 and a power 0.9 ($\beta = 0.1$) and significance level $\alpha = 0.05$, two-tailed. To account for the potential of clustering, we required ≥118 electrodes (~13 patients), assuming a cluster size of 10 electrodes per plan and an intracluster correlation coefficient of 0.2.

Statistical analysis was performed using Stata (Version 15). Comparison of paired trajectory metrics between Plan 1 and 4 was undertaken using mixed-effects linear regression models, with patient-level random effects to account for the clustering of electrodes within patients. Difference estimates, together with associated 95% confidence intervals and P-values for a test of the null hypothesis that the true difference is zero, are reported. Comparison between the different phases of CAP (Plans 2-4) was also performed using mixed-effects linear

regression models with patient-level random effects to account for the clustering of electrodes within patients. Estimates for each metric are reported for each plan type (with 95% confidence intervals). In each case, a likelihood ratio test was used to obtain a P-value for tests of the null hypothesis of no difference in the corresponding metric between plans 2-4.

3.4 **Results**

A total of 125 electrodes (mean of 9.62 electrodes per patient) were implanted (See Table 7), of which seven were in the left hemisphere.

At an individual patient level plans derived following CAP with human review and adjustment (Plan 4) had a lower mean risk score compared to the manual plans (Plan 1) and were stereotactically implanted in all 13 cases (see Table 8). An example of CAP implantation is shown in Figure 15 and Figure 16. There were no haemorrhages or adverse events following the implementation of the plans (125 electrodes) and the target structures were successfully sampled in all cases.

Table 7: Summary of electrode sampling regions

		Subject Number [Implanted Hemisphere]												
		1 [R]	2 [L]	3 [R]	4 [L]	5 [R]	6 [R]	7 [L]	8 [L]	9 [R]	10 [L]	11 [R]	12 [L]	13 [L]
Temporal	Amygdala	✓	✓	✓	✓		✓	✓	✓	✓	✓	✓		✓
	Anterior hippocampus	✓	✓	✓	✓		✓	✓	✓	✓	✓	✓	✓	✓
	Posterior hippocampus	✓	✓		✓			✓	✓	✓	✓	✓		✓
	Temporo-occipital junction	✓								✓	✓			✓
	Superior temporal gyrus							✓						
	Middle temporal gyrus	✓	✓	✓	✓		✓	✓	✓	✓	✓	✓	✓	✓
Cingulum	Anterior cingulum	✓		✓	✓	✓	✓		✓	✓	✓	✓		✓

	Middle cingulum		✓	✓	✓		✓			✓			✓	
	Posterior cingulum	✓							✓		✓	✓		✓
Frontal	Mesial orbitofrontal cortex	✓	✓	✓	✓	✓	✓		✓	✓	✓	✓	✓	✓
	Lateral orbitofrontal cortex	✓	✓	✓	✓	✓	✓		✓	✓	✓	✓	✓	✓
	Superior frontal gyrus		✓	✓	✓	✓	✓	✓			✓	✓	✓	✓
	Middle frontal gyrus	✓	✓	✓					✓	✓	✓	✓	✓	
	Inferior frontal gyrus			✓	✓	✓			✓	✓	✓	✓	✓	✓
	Mesial prefrontal cortex	✓	✓	✓	✓	✓	✓		✓			✓	✓	✓
	Pre-SMA												✓	
	Anterior SMA		✓			✓	✓						✓	

	Posterior SMA		✓			✓	✓						✓	✓
	Precentral gyrus		✓								✓			
Parietal	Postcentral gyrus		✓			✓								✓
	Superior parietal lobule	✓		✓		✓	✓	✓	✓	✓			✓	✓
	Supramarginal gyrus	✓							✓		✓	✓		✓
	Angular gyrus	✓												
Insula	Anterior Insula	✓	✓	✓	✓	✓		✓	✓	✓	✓			
	Posterior Insula	✓	✓			✓		✓	✓	✓				

**Anatomic brain regions sampled by SEEG. Note: The same region may be sampled by more than one electrode and one electrode may sample multiple brain region, e.g. an orbitofrontal electrode implanted using an orthogonal trajectory may enter through the pars orbitalis of the inferior frontal gyrus, sample the lateral orbitofrontal gyrus, medial orbitofrontal gyrus and terminate in the medial prefrontal region. Occasionally, the anterior insula may also be sampled using this trajectory.*

Figure 15: EpiNav™ generated electrode trajectories implemented in patient 13:

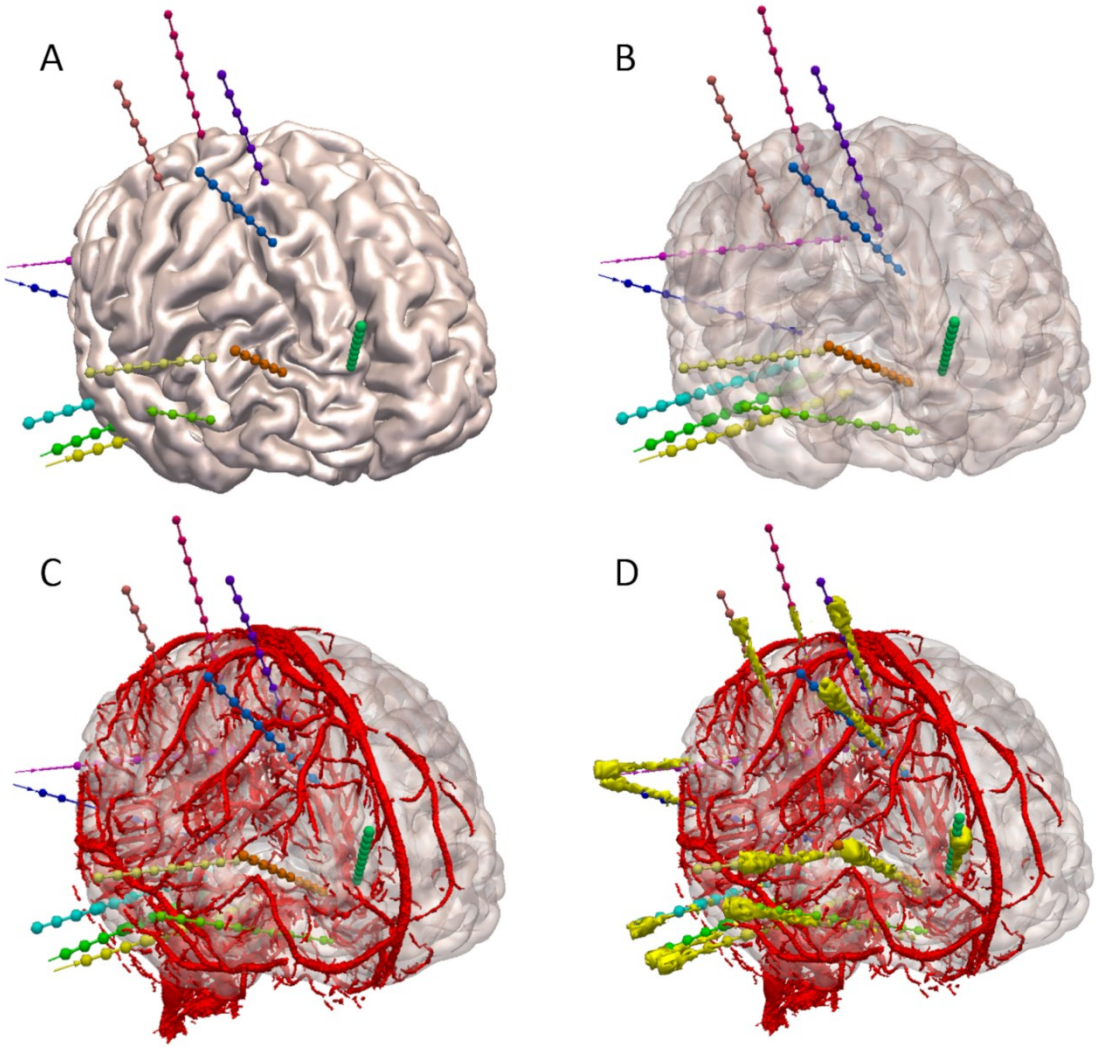

Figure 15 Legend: Example EpiNav™ generated implantation from patient 13 with suspected right frontotemporal onset. A) Right fronto-lateral view of 3D model of the cortex with the EpiNav™ generated implantation plan of 13 electrodes. B) Transparent cortex to allow visualisation of the intracerebral course of the planned electrodes. C) Superimposed vessel segmentation from a right internal carotid artery use for precise planning. D) Superimposed post-implantation bolt and actual electrode contact segmentation (yellow).

Figure 16: Detailed post-implantation view of active contacts:

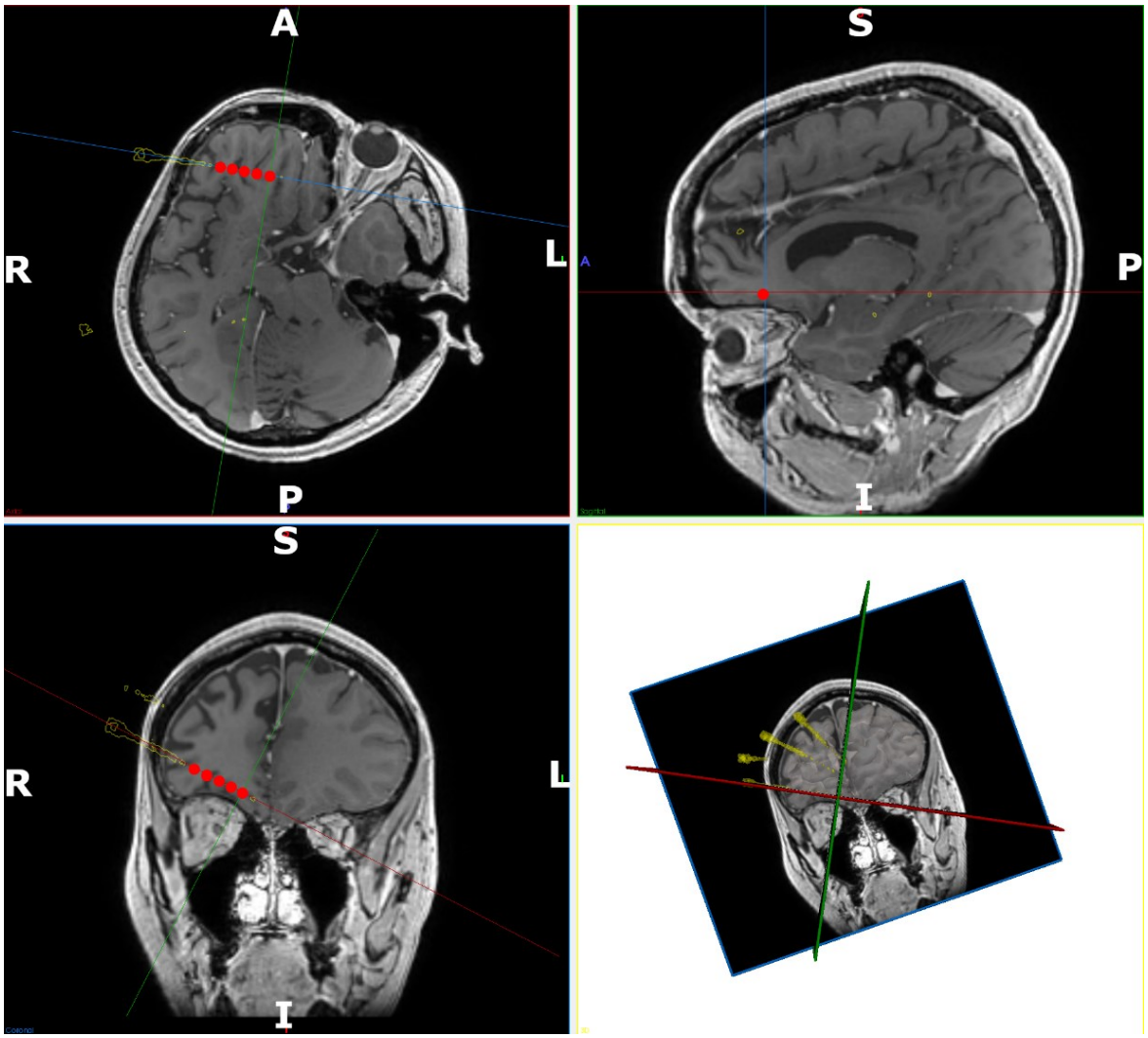

Figure 16 Legend: Detailed views of the contacts that were active on the right orbitofrontal electrode at the onset of the seizure. Implemented electrode trajectories segmented from the post-operative CT are shown (yellow) and fused with the pre-operative MRI. The electrode contacts active at the onset of the seizure are shown in Red. These have been accentuated for clarity. In-line trajectory views (top left and bottom left), as well as probes eye view (top right) and 3D model (bottom right), are shown. Note: The orbitofrontal trajectory passes through the grey matter at the depths of the sulci along the orbitofrontal cortex before terminating in the mesial prefrontal cortex. Electrode conflicts with vessels in the sulcus are averted by preventing the trajectory from crossing sulcal pial boundaries.

Table 8: Metric comparison between Manual (Plan 1) and final CAP (Plan 4):

Metric	Estimate (Plan 1 – Plan 4 difference)	95% Confidence Interval	p-value
Length (mm)	0.54	(-2.94, 4.02)	0.762
Drilling angle (deg.)	1.11	(-1.88, 4.10)	0.467
GM sampling ratio	-0.02	(-0.05, 0.00)	0.098
Risk score	0.05	(0.02, 0.08)	0.003
Minimum distance from critical structure (mm)	0.04	(-0.43, -0.01)	0.040

**Estimates for differences between Plan 1 and Plan 4, for each metric, together with associated 95% confidence intervals and P-values for a test of the null hypothesis that the true difference = 0. The estimates have been obtained from mixed-effects regression models that include within-patients random effects to account for within-patient clustering of electrodes.*

Table 9: Metric comparison between different phases of CAP (Plans 2-4):

Metric	Estimate (95% Confidence Interval)			P-value*
	Plan 2	Plan 3	Plan 4	
Length (mm)	43.65 (39.39, 47.92)	44.41 (40.15, 48.68)	43.16 (38.90, 47.44)	0.772
Drilling angle (deg)	18.85 (16.53, 21.18)	19.36 (17.04, 21.68)	18.84 (16.52, 21.16)	0.885
GM sampling ratio	0.37 (0.30, 0.45)	0.39 (0.31, 0.46)	0.37 (0.30, 0.45)	0.704
Risk score	0.90 (0.84, 0.96)	0.96 (0.90, 1.02)	1.01 (0.95, 1.07)	0.00023
Minimum distance from critical structure (mm)	2.76 (2.45, 3.07)	2.36 (2.05, 2.67)	2.23 (1.92, 2.54)	0.001

**Estimates for each metric by group from mixed-effects ANOVA models that include patient-level random effects to account for within-patient clustering of electrodes. *P-values are shown for likelihood ratio tests of the null hypothesis of no difference in the corresponding outcome variable between Plans 2-4*

Comparison of trajectory metrics between Plan 1 and 4 revealed a significant reduction in risk score ($p = 0.003$) and minimum distance from critical structures ($p = 0.04$), but not intracerebral trajectory length ($p = 0.76$), drilling angle ($p = 0.47$) or grey matter sampling ratio ($p = 0.10$). Subgroup analysis of the trajectory parameters between Plan 2-4 revealed that risk score and minimum distance following the immediate output of CAP (Plan 2) was significantly lower than following the subsequent human interaction (Plan 3 and Plan 4) $p = 0.00023$ and $p = 0.001$, respectively. (see

Table 9).

Computation times for CAP (generation of Plan 2) ranged from 34-89 seconds. Review of the trajectories and iteration through the risk-stratified trajectories (Plan 3) required an additional 15-20 minutes. Final precise adjustments (Plan 4) and review of all trajectories took an additional 20-40 minutes depending on the complexity of the implantation. Using CAP, the total time for plan generation, individual trajectory review and precise adjustment took 62 ± 17 minutes (mean ± S.D.). Manual planning took an average of 221 ± 39 minutes (mean ± S.D.). Due to the long manual planning duration, this was usually spread over two separate sessions. Overall CAP (Plan 2-4) was significantly quicker than manual planning ($p = 6.4 \times 10^{-8}$).

3.5 **Discussion**

Before CDSSs can be integrated into the clinical pathway, they must be rigorously tested and externally validated to ensure that they perform optimally across a representative range of patients and institutions. See Table 10 for a summary of the published literature to date along with methodological index for non-randomized studies (MINORS) scores for study design appraisal (see Supplementary for an itemisation of MINORS scores).

Table 10: Summary of published literature of clinical studies utilising CAP for SEEG:

Publication	CAP platform	MINORS	Type	Number of patients (electrodes)	Parameters optimised	Comments
De Momi et al. (2013)	3D Slicer	16/24	Retrospective	15 (199)	Vessel distance Skull drilling angle Sulci	Single electrode planning Entry and target points manually selected by surgeon and 4.38 mm and 4.27 mm search radius applied respectively. No external validation
Zombori (et al. 2014)	EpiNav	12/24	Retrospective	6 (30)	Vessel distance Skull drilling angle Electrode length Risk score	Single electrode planning Overall electrode risk score, length and drilling angle was improved with CAP
De Momi et al. (2014)	3D Slicer	16/24	Retrospective	3 (24)	Vessel distance Skull drilling angle Adherence to planned entry and target structure Cortex curvature value	Multi-electrode planning 1.6 mm safety margin from vasculature within 2.5 cm of skull entry point and 1 mm safety margin thereafter. Maximum drilling angle 40^{o}. Minimum distance from a vessel was significantly improved with multi-electrode planning. No external validation
Zelmann et al. (2014)	MINC toolkit	14/24	Retrospective	6 (27)	Vessel distance Sulci Ventricles	Multi-electrode planning Only amygdala and hippocampus targeted.

					Grey matter sampling Target volume sampling	Automated trajectories improved target volume sampling, distance from vasculature and grey matter contact. 25/27 trajectories were rated feasible
Zelmann et al. (2015)	MINC toolkit	14/24	Retrospective	20 (116)	Risk score ROI recording volume Grey matter sampling Skull drilling angle	Multi-electrode planning Only three electrodes (amygdala, anterior hippocampus and posterior hippocampus) planned with target structures defined as ROIs. A single neurosurgeon did a feasibility assessment on all patients. A second neurosurgeon scored 12 patients. No external validation Automated trajectories were statistically safer overall and rated more feasible than those that were manually planned. Insertion angle was higher with automated trajectories
Nowell et al. (2016)	EpiNav	16/24	Retrospective	18 (166)	Electrode length Skull drilling angle Risk score Vessel distance Grey matter sampling Sulci	Multi-electrode planning 3 mm safety margin from vasculature along the entire length of trajectory with risk profile graphic. The surgeon manually selects the target point. Able to generate 98.2% of the required trajectories. The external blinded evaluation revealed 79% were feasible for implantation without further adjustment.
Scorza et al. (2017)	3D Slicer	14/24	Retrospective	20 (253)	Vessel distance Sulcal avoidance Skull drilling angle	Multi-electrode planning 4 mm safety margin from vasculature within 1 cm of skull entry point and 1 mm safety margin thereafter.

					Electrode conflicts	Entry and target points manually selected by a surgeon and 7 mm and 3 mm search radius applied respectively. Improvement in optimisation parameters in 98% of electrodes. No feasibility ratings of trajectories or external validation undertaken.
Sparks et al. (2017)a	EpiNav	16/24	Retrospective	18 (165)	Electrode length Skull drilling angle Risk score Vessel distance Grey matter sampling Sulci	Multi-electrode planning 3 mm safety margin from vasculature along the entire length of trajectory with risk profile graphic. Surgeon manually selects the target point. Entry structure risk map generation Improvement in risk, grey matter sampling, intracerebral length and drilling angle with CAP. Skull template to remove infeasible entry points
Sparks et al. (2017)b	EpiNav	16/24	Retrospective	20 (190)	Electrode length Skull drilling angle Risk score Vessel distance Grey matter sampling Sulci	Multi-electrode planning 3 mm safety margin from vasculature along the entire length of trajectory with risk profile graphic. Entry and target regions defined as anatomic ROIs, allowing the algorithm to define optimal entry and target points. Entry and target structure risk map generation Iterative relaxation of hard constraints if suitable trajectories cannot be found. External blinded feasibility ratings were 97% for manual, and 90% for CAP generated trajectories

Vakharia et al. (2017)	EpiNav	20/24	Retrospective	13 (116)	Electrode length Skull drilling angle Risk score Vessel distance Grey matter sampling Sulci	Multi-electrode planning 3 mm safety margin from vasculature along the entire length of trajectory with risk profile graphic. Entry and target regions defined as anatomic ROIs, allowing the algorithm to define optimal entry and target points. External review of manual and CAP trajectories in blinded fashion revealed no difference in feasibility. Improvement in risk, grey matter sampling, intracerebral length and drilling angle with CAP.
Vakharia et al. (2018) *	EpiNav	24/24	Prospective	13 (125)	Electrode length Skull drilling angle Risk score Vessel distance Grey matter sampling Sulci	Multi-electrode planning First prospective CAP study in which CAP trajectories were implemented with no adverse events. Significant improvement in the risk score.

* Current Study

Over the last five years, CAP algorithms have significantly advanced. Initial studies implemented many of the single trajectory planning features(De Momi et al., 2013a; Zombori et al., 2014) that had been developed previously for deep brain stimulation(Bériault et al., 2012). As SEEG schema contain many more electrodes and the target points are anatomically more varied, multi-trajectory planning was required(De Momi et al., 2014a; Sparks et al., 2017b; Zelmann et al., 2015). This added an additional level of complexity to CAP planning as not only did individual electrodes need to be optimised with regards to planning parameters, but they could not come within a user-defined distance of each other. Various parameters for minimum vascular distance, sulcal avoidance, risk calculation and drilling angle through the skull have been implemented and these studies have shown significant improvements in planning time. With the addition of patient-specific whole-brain parcellations, entry and target structures no longer need to be manually selected, but whole-brain anatomical regions can now be specified. This helps to automate the process further and increase the potential number and safety of generated trajectories(Sparks et al., 2017a; Vakharia et al., 2018e). To date, all previous studies have been retrospective comparisons in which previous manually planned and implemented trajectories were re-planned utilising CAP and metrics compared back to the manual plans. Due to the low incidence of intracranial haemorrhage associated with SEEG most CAP studies have adopted a surrogate metric in the form of a risk score(Bériault et al., 2012; De Momi et al., 2014b; Essert et al., 2012; Shamir et al., 2012; Sparks et al., 2017b), which is the cumulative distance from the vasculature, for comparison. To validate the clinical feasibility of the trajectories, these were rated by expert neurosurgeons(De Momi et al., 2014a; Nowell et al., 2016b; Scorza et al., 2017; Sparks et al., 2017a).

We have previously undertaken a retrospective clinical assessment of SEEG planning with EpiNav™ (Vakharia et al., 2018e). Consecutive patients that had undergone manual planning and electrode implantation were selected from a prospectively maintained database and the implantation schema were re-planned using CAP. The resulting trajectory metrics revealed that CAP trajectories significantly improved trajectory length, drilling angle, grey matter sampling ratio, risk and minimum distance from vasculature. The trajectories were also externally validated by five expert neurosurgeons that were blinded to the trajectory generation method. There was no significant difference in feasibility between manual and CAP generated electrodes. The implication of this was that CAP could generate SEEG trajectories that are potentially safer and more efficient than those planned manually in a fraction of the time. This

study also instituted a sulcal model that prevents electrodes from crossing the sulcal pial boundaries in order to reflect the current surgical practise at our institution. We acknowledge that there is variability in surgical practice with regards to crossing sulcal pial boundaries and accordingly, this constraint can be turned on or off at the surgeon's discretion. The intent of the sulcal model is to prevent trajectories passing through sulcal pial boundaries where vasculature is known to reside. Our practice to sample grey matter at the bottom of sulci, that is a common site for focal cortical dysplasia, is to direct trajectories obliquely through the adjacent gyrus. The preferential GM sampling feature facilitates efficient sampling of all selected grey matter targets. The current prospective study builds upon our retrospective experience with CAP for SEEG, validating this as a CDSS for trajectory planning.

During the generation of CAP trajectories, we assessed metrics at each stage to replicate the expected 'real world' clinical application. As a CDSS it is intended that the recommended output of CAP (Plan 2) be reviewed by the operating neurosurgeon and any potential modifications be made by iterating through the CAP trajectories in a risk-stratified manner (Plan 3). This allows the neurosurgeon to customise trajectories to fit their usual practice whilst also utilising CAP to ensure that the trajectory carries the lowest risk. If required further modifications can be made by the neurosurgeon setting precise entry and target points (Plan 4) prior to implantation. For the purpose of this prospective validation study, we compared the manual plan (Plan 1), made in advance of CAP, with the final CAP-assisted plan ready for implantation (Plan 4). In all cases, plans carrying the lowest mean risk score were stereotactically implanted. No patients had an adverse event related to the planning or implantation of the CAP generated trajectories. Unlike in previous studies(Nowell et al., 2016b; Vakharia et al., 2018e), there was no significant difference in intracerebral length, drilling angle to the skull or GM sampling ratio between manual and implemented CAP trajectories. This is most likely due to the evolving nature in which manual planning was performed, whereby the pre-operative 3D models generated for use with CAP were also available to the neurosurgeon.

It should be noted that there is a significant distinction between computer-assisted and computer-autonomous planning. The former requires an expert neurosurgeon to review and modify the suggested plans as necessary prior to stereotactic implantation. Due to the complexity of SEEG planning and variability in implantation methods as well as surgeon planning practices, it is unlikely that computer-autonomous algorithms will be available in the near future. We have previously found that manually planned and implemented trajectories rated by

external blinded neurosurgeons were deemed feasible in only 70%. In each of these cases, the manually planned trajectories were by definition feasible as they had already been implanted without complication. This highlights the lack of consensus between stereotactic neurosurgeons regarding planning parameters and is likely to be a hurdle to widespread adoption of computer-autonomous planning. Furthermore, the variability in acquisition parameters for pre-operative MRI and methods for vascular imaging mean the results of CAP will vary between institutions. In this study, we employ DSA to provide the greatest segmentation of intracranial vasculature, although not all institutions acquire this(Cardinale et al., 2015). It still remains unclear what is the critical vessel size for visualisation for safe SEEG. The ability for the neurosurgeon to be able to modify CAP output is key to customising trajectories based on individual surgeon preferences and building user confidence in the algorithms.

There are limitations to this study. It would have been methodologically superior to perform a prospective, randomised controlled trial of CAP versus manual trajectory planning. As there have not been any prospective studies of CAP to date, we decided it would be safer to independently generate CAP and manual plans for comparison and implant those with the lowest risk score. As the position of individual trajectories impacts upon other trajectories in the plan, we compared the mean risk score for the overall plan and not at an individual electrode level. Furthermore, all patients and implantations were performed at a single institution where uniform imaging protocols were performed on all patients. It is unclear whether the same results would be achieved by other institutions employing different imaging strategies. We have suggested parameters for suitable image acquisition protocols using different MRI scanners (Supplementary), so this can be replicated at other centres. We acknowledge the small sample size of the study (n = 125 electrodes in 13 patients) but emphasize that even when controlling for clustering within patients the study was well powered to detect the study primary end-point (power = 0.9 to a difference in risk score of ≥0.1). A further limitation of this study, and one that is ubiquitous in all CAP algorithms, is the reliance on a risk score(Bériault et al., 2012; De Momi et al., 2013a; Essert et al., 2012; Shamir et al., 2012). Due to the low incidence of haemorrhage from SEEG, a prohibitively large sample size would be required to undertake a study in which reduction in haemorrhage rate was the primary outcome. Given that haemorrhage must occur from conflict with a blood vessel (visualised or not by modern imaging techniques) and that exploitation of avascular channels during trajectory planning is the primary goal of the surgeon, we apply the pragmatic tenet that haemorrhage is less likely to occur the further an electrode is

placed from an intracranial vessel. The risk score is, therefore, an objective means of quantifying the size of the avascular corridor. Future studies should aim to be multi-centre in nature to assess the external robustness of the algorithm and feasibility in the hands of different neurosurgeons. It would also be methodologically optimal if the neurosurgeon was blinded to the generation method but still retained the ability to modify the plans prior to implantation. In reality, surgeon blinding is challenging to implement as the surgeon performing the implantation would have to be different to the surgeon performing the manual planning.

Currently, EpiNav™ supports the direct export of CAP plans to the S7 Stealth Station (Medtronic Inc.) for implantation. Future developments may include export formats that are compatible with other devices, e.g. Leksell frame. We will also aim to improve the feasibility of the immediate CAP output (Plan 2) and reducing the modifications required by the surgeon (Plans 3 and 4). Given the significant variability in surgeons' preference for trajectory planning, this will require customisation of CAP to the individual surgeon's practice. To this end, we propose the generation of spatial priors for specific trajectories that will define commonly used entry and target zones.

3.6 **Conclusion**

CAP provides clinically feasible SEEG trajectory plans with improved safety metrics in one-third of the time required for manual planning. Incorporating automated SEEG planning into the clinical workflow is possible with the use of EpiNav™ as a CDSS. We have itemised each stage of the trajectory generation pathway and highlighted the ability of the surgeon to modify the trajectories based on their individual planning preferences in a risk-stratified manner. When the final CAP trajectories were directly compared with manual plans, they returned lower mean risk scores in all cases and were prospectively stereotactically implanted without complication. EpiNav™ is a significant advance in the planning of SEEG trajectories and has application for other stereotactic neurosurgical procedures including planning cranial LITT, DBS, focal therapy delivery, brain biopsies and shunt catheter placement.

3.7 **Supplementary materials**

Supplementary Table 11: Derivation of MINORS scores (Slim et al., 2003)

Publication	Aims clearly stated	Consecutive patients	Prospective data collection	Appropriate endpoints	Blinded evaluation	Appropriate follow-up period	Loss to follow up <5%	Prospective power calculation	Adequate control group	Prospective control	Baseline equivalence	Adequate statistics	Total
De momi et al. (2013)	2	0	0	2	2	2	2	0	2	0	2	2	16/24
De momi et al. (2014)	2	0	0	2	0	2	2	0	2	0	2	2	14/24
Zombori et al. (2014)	2	0	0	2	2	2	2	0	2	0	2	2	16/24
Zelmann et al. (2014)	2	0	0	2	0	2	2	0	2	0	2	2	14/24
Zelmann et al. (2015)	2	0	0	2	0	2	2	0	2	0	2	2	14/24
Nowell et al. (2016)	2	0	0	2	2	2	2	0	2	0	2	2	16/24

Scorza et al. (2017)	2	0	0	2	0	2	2	0	2	0	2	2	14/24
Sparks et al. (2017)a	2	0	0	2	2	2	2	0	2	0	2	2	16/24
Sparks et al. (2017)b	2	0	0	2	2	2	2	0	2	0	2	2	16/24
Vakharia et al. (2017)	2	2	0	2	2	2	2	2	2	0	2	2	20/24
Vakharia et al. - (2018) *	2	2	2	2	2	2	2	2	2	2	2	2	24/24

* Current Study

SupplementaryTable 12: Suggested MRI scanner parameters for CAP planning (Courtesy of Dr S. Vos).

a) 3T Siemens Prisma (software version VE11C)

Sequence	3D T1 MPRAGE (Acquisition time: 5m19s) Inversion-prepared gradient echo	MR Venography (Acquisition time: 16m05s) 3D Phase-contrast	MR Angiography (Acquisition time: 9m03s) 3D Phase contrast
Geometry	Orientation: Coronal In-plane FOV of 25.6x25.6 cm with an acquisition matrix 256x256 (GRAPPA factor 2) 240 slice locations of 1.0 mm thickness Reconstructed voxel size: 1.0x1.0x1.0 mm	Orientation: Axial In-plane FOV of 22x22 cm with an acquisition matrix 512x512 (GRAPPA factor 3) Phase FOV: 75% Phase-encoding direction R>>L 208 slice locations of 0.6 mm thickness with slice resolution 50% Phase partial Fourier: off Reconstructed voxel size: 0.43x0.43x0.60 mm	Orientation: Axial In-plane FOV of 22x22 cm with an acquisition matrix 512x512 (GRAPPA factor 3) Phase FOV: 75% Phase-encoding direction R>>L 208 slice locations of 0.6 mm thickness with slice resolution 50% Phase partial Fourier: off Reconstructed voxel size: 0.43x0.43x0.60 mm
Sequence details	TR/TE/TI = 7.4 / 2.7 / 909 ms Segment time (time between inversion pulses): 2300 ms	TR/TE = 76.55 / 8.31 ms Flip angle: 8 degrees BW: 425 Hz/pix	TR/TE = 46.45 / 6.76 ms Flip angle: 15 degrees BW: 425 Hz/pix

	Flip angle: 8 degrees BW: 200 Hz/pix		
Vascular		Velocity encoding: 15 cm/s	Velocity encoding: 80 cm/s
Other	Distortion Corr. (3D) Pre-scan Normalize	Suppression slab inferior to FOV	

b) 3T GE MR750 (software version DV24_R02)

Sequence	3D T1 MPRAGE (Acq time: 4m17s) Scan type: 3D Gradient Echo Fast SPGR Imaging Options: IR Prepared, ASSET, EDR	MR Venography (Acq time: 13m7s) Scan type: 3D Vascular Inhance Velocity Imaging Options: ASSET, ZIP2	MR Angiography (Acq time: 5m49s) Scan type: 3D Vascular Inhance Velocity Imaging Options: ASSET, ZIP2
Geometry	Orientation: Coronal In-plane FOV of 25.6x25.6 cm with an acquisition matrix 256x256 (ASSET acceleration 2) Phase FOV 0.8 224 slice locations of 1.0 mm thickness Reconstructed voxel size: 1.0x1.0x1.0 mm	Orientation: Axial In-plane FOV of 22x22 cm with an acquisition matrix 384x256 (ASSET acceleration 2) Phase FOV 0.9 124 slice locations of 1.2 mm thickness Reconstructed voxel size: 0.43x0.43x0.60 mm	Orientation: Axial In-plane FOV of 22x22 cm with an acquisition matrix 384x256 (ASSET acceleration 2) Phase FOV 0.9 124 slice locations of 1.2 mm thickness Reconstructed voxel size: 0.43x0.43x0.60 mm

Sequence details	TR/TE/TI = 7.4 ms / Min Full / 400 ms Flip angle: 11 degrees BW: 31.25	TR/TE = Minimum Flip angle: 8 degrees BW: 31.25	TR/TE = Minimum Flip angle: 8 degrees BW: 31.25
Vascular		Flow analysis off Velocity encoding: 15 cm/s Flow recon type complex difference Acquisition flow direction images: all add flow images, magnitude	Flow analysis off Velocity encoding: 80 cm/s Flow recon type complex difference Acquisition flow direction images: all add flow images, magnitude
Other	3D Geometry correction: on Intensity inhomogeneity correction: PURE	3D Geometry correction: on Intensity inhomogeneity: PURE Advanced: 80% pfkr Suppression slab inferior to FOV Chemical fat saturation	3D Geometry correction: on Intensity inhomogeneity: PURE Advanced: 80% pfkr

c) 3T Philips Achieva

Sequence	3D T1 MPRAGE (Acq time: 6m32s)	MR Venography (Acq time: 8m58s)	MR Angiography (Acq time: 5m30s)

	Inversion-recovery 3D TFE	3D T1 Fast Field echo, phase contrast	3D T1 Fast Field echo, phase contrast
Geometry	Orientation: Sagittal In-plane FOV of 25.6x25.6 cm with an acquisition matrix 256x256 (SENSE factor 2)180 slice locations of 1.0 mm thickness Reconstructed voxel size: 1.0x1.0x1.0 mm	Orientation: Axial In-plane FOV of 23x18 cm with an acquisition matrix 384x212 (SENSE factors: RL=3, IS=2) Scan percentage: 70.87% 248 slice locations of 1.2 mm thickness (overcontiguous slices) Reconstructed voxel size: 0.45x0.45x0.60 mm	Orientation: Axial In-plane FOV of 23x18 cm with an acquisition matrix 384x212 (SENSE factors: RL=3, IS=2) Scan percentage: 70.87% 248 slice locations of 1.2 mm thickness (overcontiguous slices) Reconstructed voxel size: 0.45x0.45x0.60 mm
Sequence details	TR/TE/TI = 6.9 / 3.1/ 867 ms Segment time (time between inversion pulses): 3000 ms Flip angle: 8 degrees	TR/TE (both set to shortest) = 21 / 8.3 ms Flip angle: 8 degrees Halfscan: yes water-fat shift: maximum BW: 114.6 Hz	TR/TE (both set to shortest) = 13 / 6.7 ms Flip angle: 8 degrees Halfscan: yes water-fat shift: maximum BW: 114.6 Hz
Vascular		Velocity encoding: 15 cm/s	Velocity encoding: 80 cm/s

Other	3D Geometry correction: on	fold-over direction: RL fat shift direction: P NSA: 2 REST slab: type=parallel, thickness=60 mm, position=feet, gap=default, power=1	fold-over direction: RL fat shift direction: P NSA: 2

Note: Parameters may have to be altered on different models.

4 Refining Computer Assisted Planning For SEEG: A Prospective Validation Of Spatial Priors.

4.1 **Abstract**

4.1.1 Objective

Stereoelectroencephalography (SEEG) is a procedure in which many electrodes are stereotactically implanted within different regions of the brain to estimate the epileptogenic zone in patients with drug-refractory focal epilepsy. Computer-assisted planning (CAP) improves risk scores, grey matter sampling, orthogonal drilling angles to the skull and intracerebral length in a fraction of the time required for manual planning. Due to differences in planning practices, such algorithms may not be generalizable between institutions. We provide a prospective validation of clinically feasible trajectories using 'spatial priors' derived from previous implantations and implement a machine learning classifier to adapt to evolving planning practices.

4.1.2 Methods

Thirty-two patients underwent consecutive SEEG implantations utilising computer-assisted planning over two years. Implanted electrodes from the first 12 patients (108 electrodes) were used as a training set from which entry and target point spatial priors were generated. CAP was then prospectively performed using the spatial priors in a further test set of 20 patients (210 electrodes). A K-nearest neighbour (K-NN) machine learning classifier was implemented as an adaptive learning method to modify the spatial priors dynamically.

4.1.3 Results

All of the 318 prospective computer-assisted planned electrodes were implanted without complication. Spatial priors developed from the training set generated clinically feasible trajectories in 79% of the test set. The remaining 21% required entry or target points outside of the spatial priors. The K-NN classifier was able to dynamically model real-time changes in the spatial priors in order to adapt to the evolving planning requirements.

4.1.4 Conclusions

We provide spatial priors for common SEEG trajectories that prospectively integrate clinically feasible trajectory planning practices from previous SEEG implantations. This allows institutional SEEG experience to be incorporated and used to guide future implantations. The deployment of a K-NN classifier may improve the generalisability of the algorithm by dynamically modifying the spatial priors in real-time as further implantations are performed.

4.2 Introduction

Stereotactic neurosurgery requires precise pre-operative trajectory planning and accurate implementation to ensure safety and efficacy. The greatest risk of this procedure is intracerebral haemorrhage, which can result in significant morbidity in 2-3% of cases(Mullin et al., 2016a). Various surgical techniques are employed for insertion of SEEG electrodes including frame-based, frameless and robotic methods with mean target point accuracies of around 2-3 mm(Vakharia et al., 2017b). To maximise safety surgeons plan SEEG trajectories to maximise distance from vasculature. Other important considerations include accurate targeting of the regions of interest (ROIs), avoidance of critical structures, maximising grey-matter sampling, orthogonal drilling angles to the skull, avoidance of other electrodes, optimal spatial sampling with ROIs and minimising intracerebral trajectory length. Various computer-assisted planning (CAP) algorithms have been employed to optimise these factors. EpiNav™ is one such stereotactic planning platform that has been applied to SEEG(Sparks et al., 2017a; Vakharia et al., 2018e), laser interstitial thermal therapy (LITT)(Li et al., 2019a; Vakharia et al., 2018d) and tumour biopsy. External feasibility ratings of CAP generated trajectories were not significantly different from manually planned trajectories, yet due to the wide variation in individual surgeon's planning preferences, these were 62% and 69%, respectively(Vakharia et al., 2018e). Another reason for this is the reliance on whole-brain parcellations to constrain the entry and target points, which in many cases are large structures that require multiple electrodes to pass through them. Furthermore, the algorithms are static without the ability to adapt or learn from previous trajectory planning experience.

Here we present an extensive series of patients that have undergone prospective SEEG planning with CAP. We provide spatial priors that have been generated from the first 12 patients and used these plans to subsequently constrain the entry and target points during the prospective planning of a further 20 patients. To aid in the generalisability of the spatial priors, we deploy an active learning algorithm that can dynamically modify the spatial priors based on individual surgeon's planning preferences.

4.3 Methods

4.3.1 Patient Inclusion

A total of 32 patients (17 male) with drug-resistant focal epilepsy, in whom SEEG was performed as part of their routine care at The National Hospital for Neurology and

Neurosurgery, London, U.K., were included in this prospective validation study. Patients underwent SEEG implantation between February 2017 and March 2019.

All patients underwent a standardized multi-disciplinary assessment consisting of specialist input from neurologists, neurosurgeons, neurophysiologists, neuropsychologists and psychiatrists. SEEG trajectory target selection was based on an estimation of the seizure onset zone derived from a review of the non-invasive pre-surgical investigations undertaken at the study institution. This includes the clinical history and semiology, scalp EEG / video telemetry, neuropsychological and neuropsychiatric evaluations, structural and functional MRI, PET and SPECT imaging. Entry regions were also specified for SEEG trajectories when the lateral neocortex was also of electrophysiological interest.

4.3.2 Ethical Approval

Ethical approval for this study was provided by the National Research Ethics Service Committee London, approval reference: 12/LO/0377. Written consent was obtained from all patients prior to inclusion in the study.

4.3.3 Computer-assisted planning

Pre-operative SEEG planning was performed within the EpiNav™ platform (CMIC, UCL / KCL), which has been described previously(Sparks et al., 2017a; Vakharia et al., 2018e). In brief, a single gadolinium-enhanced T1 acquisition is used as a reference image to which all other imaging modalities are registered. A whole-brain parcellation was generated, using Geodesic Information Flow (GIF)(Cardoso et al., 2015a), from which models of the cortex, grey matter and sulci are extracted in an automated fashion. Vascular segmentations were performed following application of a Sato filter to the pre-operative digital subtraction angiography and manual thresholding(Zuluaga et al., 2015). Depending on the spatial distribution of the SEEG implantation and the patient's individual anatomy, injections of the ipsilateral internal carotid artery and a vertebral artery were performed. The EpiNav™ algorithm generates SEEG trajectories based on optimisation of user-defined parameters, which include intracerebral length, drilling angle to the skull, grey matter sampling ratio, minimum distance from vasculature, risk score and avoidance of critical structures(Nowell et al., 2016b). The user-defined parameters applied during this study are shown in Table 13:

Table 13: User defined parameters for prospective computer-assisted planning

Parameter	Value
Intracerebral length (mm)	<90
Drilling angle to the skull (deg)	<30 to orthogonal
Grey matter sampling ratio	Maximise
Minimum distance from vasculature (mm)	>3
Risk score	<1
Avoidance of critical structures	Sulcal model
Distance between electrodes (mm)	>10

The risk score is a mathematical representation of the avascular corridor through which the planned trajectory passes in order to reach the target (see Equation 2). It is calculated by fitting 128 nodes along the planned trajectory and measuring the distance between the trajectory and vasculature at each node(Sparks et al., 2016, 2017a). A cumulative score is then provided scaled by the minimum distance defined by the user. In this study, a 3 mm minimum distance from vasculature was applied to result in trajectories that pass within 3 mm of a vessel returning a risk score >1.

The user inputs the implantation strategy by typing or selecting the anatomical region of interest. The entry and target regions are based on the segmentation provided by the GIF parcellation. An example of a typical strategy and plan generated from the GIF parcellation is shown in Figure 17. The automated planning algorithm first removes trajectories that do not

adhere to the length and angle constraints. Next, trajectories that do not pass through the entry region, if specified, or conflict with critical structures are also removed. The remaining trajectories are then optimised for grey matter sampling and returned to the user in a risk-stratified manner, i.e. lowest risk score first.

Following CAP, the user reviews each trajectory to ensure clinical feasibility and safety. The potential trajectories generated for a specific target (or entry-target pair) can be iterated through using the 'Next Entry' or 'Next Target' functions. Manual changes to the entry and target points can also be performed by the user if no suitable CAP generated trajectory is found.

4.3.4 Cluster generation

Following prospective SEEG planning and surgical implantation in the first 12 cases (108 electrodes), each patient's reference image was normalised to the MNI-152 (ICBM 2009a Nonlinear Asymmetric) group template(Fonov et al., 2011). The parameters for transformation were then applied to the electrode trajectories and coordinate points for the entry and target points were extracted. Right and left side trajectories were combined through flipping. Entry point coordinates were taken at the intersection of the planned trajectory and the cortical surface. The cluster centroids for trajectories were calculated from the coordinates in cases in whom the region of interest was targeted five or more times to form the training set. Trajectories targeting patient-specific abnormalities, such as lesions or PET / SPECT abnormalities, were excluded. A total of 11 entry and 14 target regions of interest were included. Within-cluster sum of squares (WCSS) was calculated to quantify the extent of variance. Based on the normalised trajectories, spatial priors were then generated to constrain the entry and target points and applied prospectively to a further 20 patients (210 electrodes).

Figure 17: EpiNav Strategy from GIF parcellations

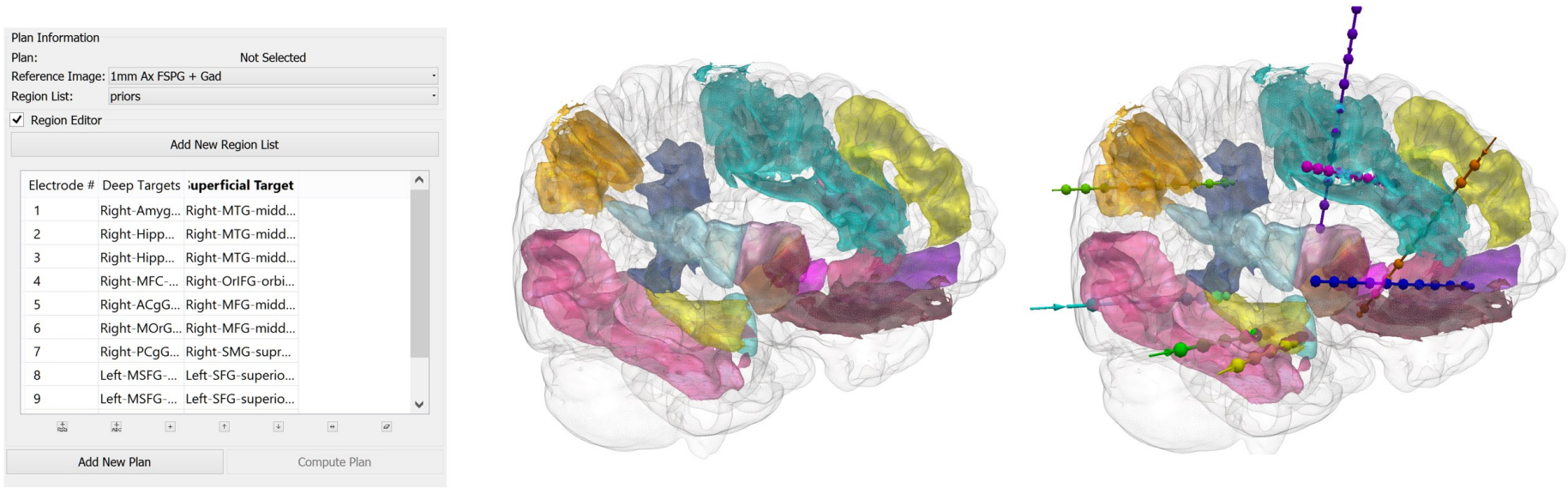

Figure 17 Legend: A) A typical example of an anatomy-driven multiple trajectory planning strategy (Sparks et al., 2017a)*, with the target and entry points for the trajectory specified by the user. B) The 3D segmentation of the whole brain structures outlined in the strategy and C) the corresponding CAP trajectories optimising for the user-defined parameters.*

4.3.5 Prospective Validation

Prospective planning was performed with spatial priors derived from the training set. Here binary masks were generated to include the previous trajectory entry and target points for each trajectory. The binary masks were then converted to meshes and used to subsequently guide implantation in a further 20 cases within the test set. The predictive accuracy of the spatial priors was determined by the proportion of trajectories that passed through both the entry and target spatial priors. In addition, the Euclidean distances between the cluster centroids from the prospective trajectories (test set) and those derived from the first 12 cases (training set) were calculated to quantify the prediction accuracy.

4.3.6 Active learning

As a further implementation, we sought to incorporate a system whereby the spatial priors could adapt to evolving SEEG planning practices. The added flexibility would allow the spatial priors to adapt and potentially incorporate new entry or target points outside of the original spatial priors. This would permit external institutions to use the above spatial priors and, with subsequent SEEG implantations, enable it to adapt to the individual surgeon's preferences. This was accomplished through the implementation of a K-Nearest Neighbor (K-NN) classifier to data from the prospective validation dataset, which was added in five-folds. The K-NN was deployed using Euclidean distance from 5 uniformly weighted neighbours to determine the classifier assignments. Computational analysis was performed with custom scripts utilising functions from the following python libraries: Pandas, Numpy and SciKit learn. The Matplotlib library was used for data visualisation.

4.4 **Results**

4.4.1 Cluster generation

In total, 11 entry and 14 target point clusters were included in the training set derived from the first 12 patients (See Figure 18). Entry spatial priors for the anterior insula, posterior insula and medial parietal regions were not generated due to the large dispersion indicating a lack of consistency during planning. An overview of colour coded spatial priors derived from the entry and target regions of the training set are showed in Figure 19

Figure 18: MNI coordinate space entry and target points for training set electrodes

a) Entry clusters from the training set:

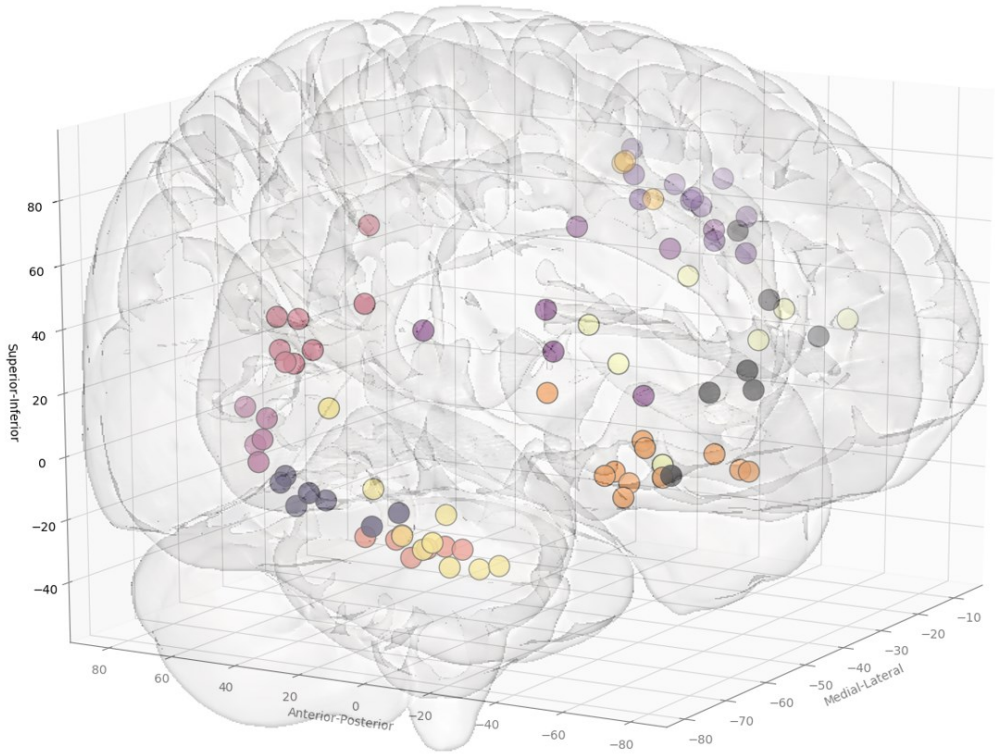

b) Target clusters from the training set:

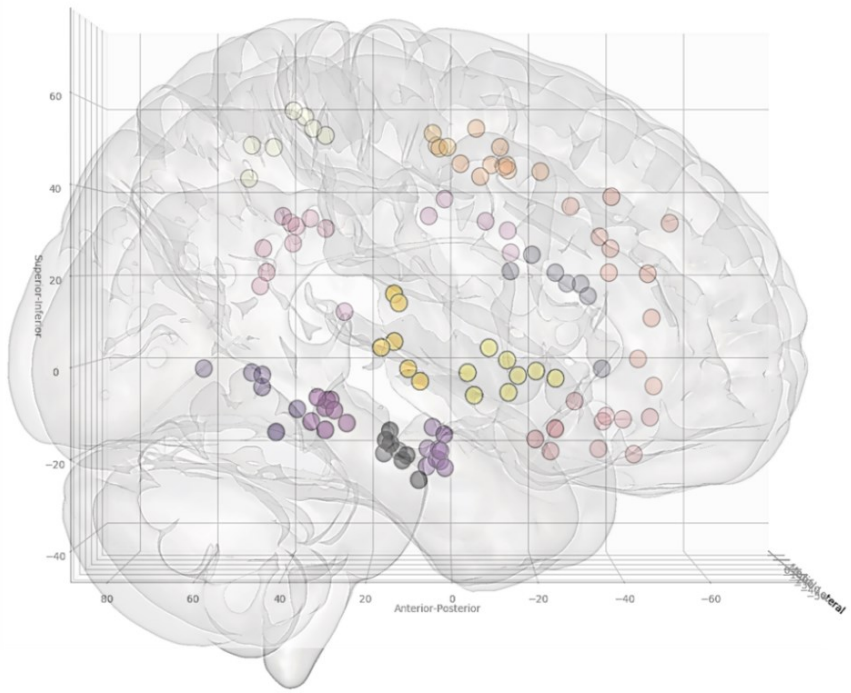

Figure 18 Legend: Coordinates of the a) entry, shown from a right anterolateral projection, and b) target points, shown from a right lateral projection, for electrode trajectories within the training set (n=12 patients). Greater transparency represents trajectory points closer to the midline.

Figure 19: Spatial Priors

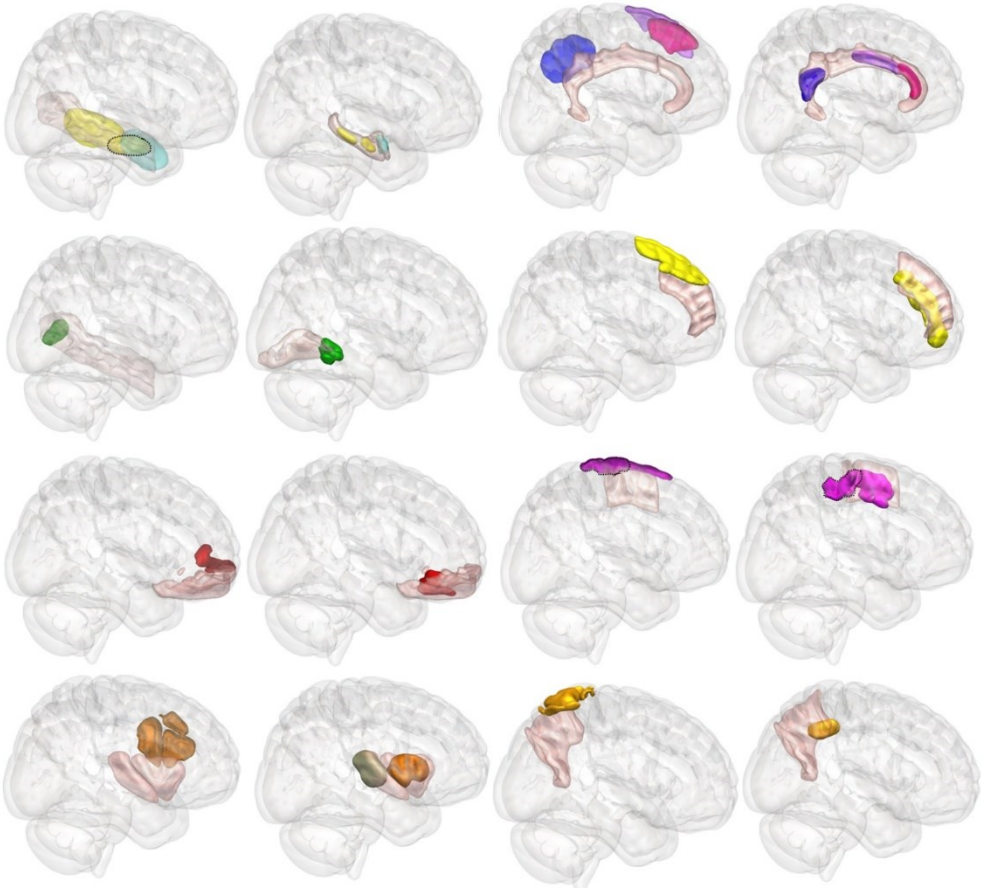

Figure 19 *Legend: Panel of 3D images shown from right lateral projection with colour-coded entry (columns 1 and 3) and target (columns 2 and 4) spatial priors within GIF defined anatomical regions (pink). Colour scheme: Amygdala: Cyan, Hippocampus: Yellow, Temporo-occipital junction: Green, Orbitofrontal cortex: Red, Anterior Insula: Copper, Posterior Insula: Grey, Anterior Cingulum: Dark pink, Middle Cingulum: Purple, Posterior Cingulum: Blue, Mesial prefrontal cortex: Yellow, Supplementary sensory-motor area: Magenta, Precuneus: Orange.*

Table 14: Summary of Test Set Trajectories in Relation to Training Set Priors

	No. trajectories	Through prior	Outside prior
Orbitofrontal	15	13 (87%)	2 (13%)
Amygdala	17	16 (94%)	1 (6%)
Anterior Hippocampus	11	8 (73%)	3 (27%)
Posterior Hippocampus	13	10 (77%)	3 (23%)
Anterior Cingulum	10	10 (100%)	0 (0%)
Middle Cingulum	13	7 (54%)	6 (46%)
Posterior Cingulum	15	12 (80%)	3(20%)
Mesial pre-frontal cortex	9	8 (89%)	1 (11%)
Anterior SSMA	12	11 (92%)	1 (8%)
Posterior SSMA	8	4 (50%)	4 (50%)
Precuneus	7	4 (57%)	3 (43%)
Anterior Insula	17	10 (59%)	7 (41%)
Posterior Insula	10	10 (100%)	0 (0%)
Total	157	123 (78%)	34 (22%)

Figure 20: Test set implanted electrodes

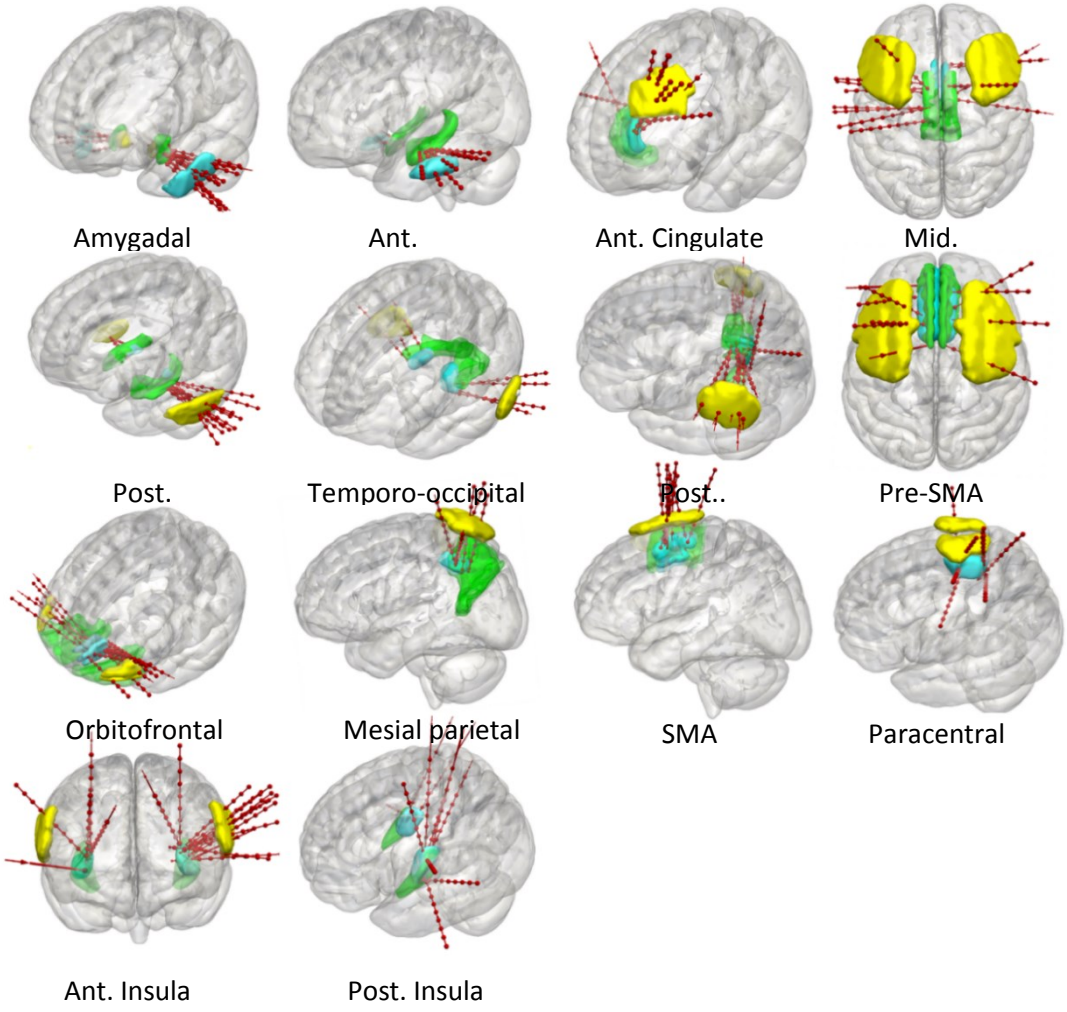

Figure 20 Legend: Panel of 3D cortical images shown from various projections with implanted electrode trajectories from the test set (red) passing through the entry spatial priors (yellow) to the target spatial priors (blue) with the GIF defined anatomical structure shown in green.

4.4.2 Prospective validation

A further 20 patients were then prospectively planned and implanted using the spatial priors derived from the previously implanted trajectories within the training set. Of the prospectively planned trajectories, 78% (123/157) were able to be planned and implanted using the spatial priors to restrict the entry and target regions (see Table 14 and Figure 20). The remaining 22% of prospectively implanted trajectories required entry or target pointed outside of the spatial priors. Coordinates for the entry and target point cluster centroids from the training set with Euclidean distance to the cluster centroid from the prospective group are shown in Table 15. There were no radiological or clinically significant haemorrhages as a result of electrode implantations in either the training or test set patients.

4.4.3 Active learning

As a further implementation, a K-NN classifier was applied to allow the spatial priors to adapt to on-going and evolving planning practices. To mimic the real-world workflow of an external institution, we first defined the boundaries of the entry and target spatial priors based on the data in the training set. Subsequent implantations from the test set validation group were then added to the training set in five folds (random selection of 42 new trajectories with each fold). The K-NN classifier was iteratively applied and the changes in the target spatial priors are shown in Figure 21. After the addition of the third fold, corresponding to 192 electrodes (roughly 20 patients), there was LITTle further change in the priors suggesting this was sufficient to learn the planning preferences of the surgeon.

Table 15: Entry and Target Cluster Centroid Coordinates for Training and Test Sets in MNI space

		Entry				Target			
		Cluster Centroid Coordinates			Test set error	Cluster Centroid Coordinates			Test set error
ROI	Method	X	Y	Z	Euclidean (mm)	X	Y	Z	Euclidean (mm)
Amygdala	Training	-62.63	9.47	-22.41	10.16	-14.29	3.55	-21.05	2.49
	Test	-57.40	2.24	-27.27	-	-15.06	5.53	-19.74	-
Anterior Hippocampus	Training	-66.20	8.00	-26.07	13.59	-20.44	13.33	-20.66	4.25
	Test	-69.07	18.68	-18.19	-	-21.16	14.75	-16.73	-
Posterior Hippocampus	Training	-69.12	36.34	-11.19	6.53	-23.53	30.35	-11.13	4.29
	Test	-69.87	36.35	-9.50	-	-25.17	26.46	-11.89	-
Temporo-occipital junction	Training	-67.41	55.60	3.71	10.29	-13.59	47.81	-6.84	9.09
	Test	-61.63	51.20	-3.57	-	-14.58	40.97	-12.73	-
Orbitofrontal cortex	Training	-51.96	-46.41	0.08	6.52	-2.05	-35.08	-16.66	5.23
	Test	-48.19	-43.82	4.72	-	-5.77	-34.26	-13.08	-
Anterior Cingulum	Training	-38.87	-47.14	32.07	18.08	-3.02	-28.10	16.48	3.64
	Test	-46.12	-31.09	36.19	-	-2.49	-26.58	13.22	-
Middle Cingulum	Training	-46.65	-20.74	46.22	8.57	-1.62	5.49	29.48	9.75
	Test	-45.40	-14.19	51.59	-	-2.34	-3.52	33.15	-

Posterior Cingulum	Training	-65.10	41.82	39.26	9.27	-1.95	41.16	27.60	3.37
	Test	-60.53	33.91	37.63	-	-2.49	38.44	25.67	-
Mesial prefrontal cortex	Training	-35.38	-54.05	26.89	28.80	-2.91	-44.27	20.73	15.90
	Test	-24.59	-38.85	48.83	-	-2.65	-31.24	29.84	-
Anterior SSMA	Training	-20.87	-19.80	66.95	18.65	-3.36	-9.94	47.31	10.76
	Test	-33.90	-6.46	66.90	-	-3.49	0.18	50.94	-
Posterior SSMA	Training	-23.90	-5.70	74.89	19.48	-3.58	2.80	51.37	11.41
	Test	-35.67	9.07	70.12	-	-4.02	14.20	51.12	-
Mesial parietal	Training	±35.50	52.00	71.26	8.37	-3.70	41.29	52.61	15.31
	Test	±41.96	50.50	66.15	-	-2.92	49.34	39.62	-
Anterior Insula	Training	±58.26	-16.00	24.83	12.07	-34.75	-13.33	-2.17	7.72
	Test	±48.50	-22.97	26.17	-	-31.64	-12.98	4.88	-
Posterior Insula	Training	-	-	-	-	-36.87	12.47	5.72	4.93
	Test	-	-	-	-	-32.23	13.82	4.76	-

**Please note, all coordinates provided in MNI-152 template space. Regarding the X-axis positive values denote the right hemisphere and negative values the left. Regarding the Z-axis negative values refer to coordinated inferior to the origin (centre of image).*

4.6 **Discussion**

We present the results of a prospective validation study utilising spatial priors to refine computer-assisted planning of SEEG electrode trajectories. Based on a training set of 12 patients (108 electrodes) in which the EpiNav™ platform was used for CAP based on the GIF parcellation, we generated entry and target spatial priors for common regions of interest (targeted five or more times). The spatial priors were then used to restrict the entry and target points within the regions of the interest for CAP in a further 20 prospective patients (210 electrodes). The spatial priors were able to return feasible trajectories for 78% of electrodes. Each of these was subsequently implanted without complication. For the remaining 22%, the entry or target points were outside of the spatial priors suggesting anatomical constraints necessitated changes in the planning strategy. We provide the spatial priors in template space for use by other institutions during CAP and as a potential starting point for standardisation of SEEG trajectories.

This is the first prospective study, specifically assessing the utility of spatial priors to refine computer-assisted SEEG trajectory planning. Two main methods for SEEG CAP have been implemented in the literature. The first is where the user defines a target point and the algorithm returns a trajectory with the lowest risk score(Nowell et al., 2016b). This has the benefit of ensuring that the precise region of interest within the anatomical structure is targeted, but this limits the algorithm to return the local, but not global, minimum risk score. It may also lead to a failure of the CAP algorithm to return a feasible trajectory, especially if the chosen target point is adjacent to a critical structure and therefore contravenes a 'hard constraint' within the planning algorithm. Due to this, some groups have suggested 'roughly' selecting the entry and target point(De Momi et al., 2013a, 2014b; Scorza et al., 2017). The algorithm then returns trajectories within a 1 cm radius allowing for slightly more variation in the entry and target points. This method still requires manual user interaction for rough placement.

Figure 21: K-Nearest Neighbour classifier

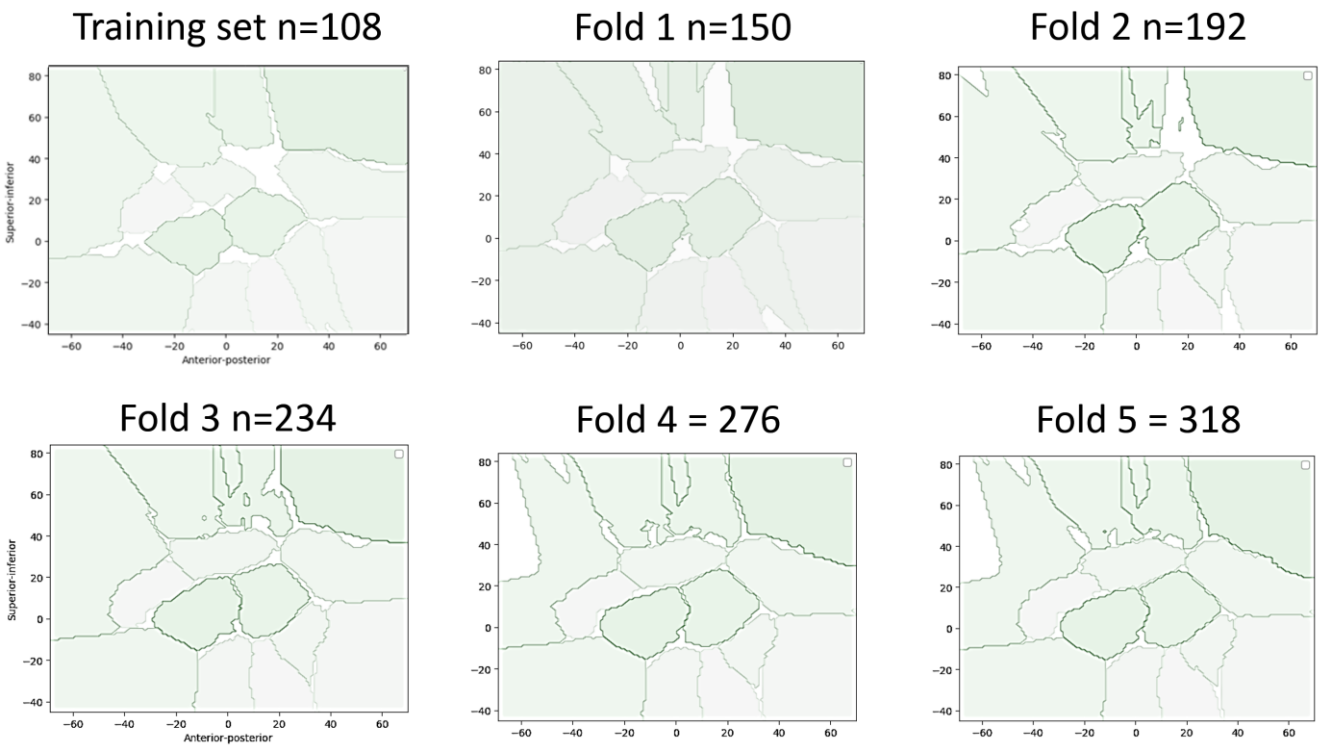

Figure 21 Legend: K-NN classifier in MNI coordinate system used to define spatial prior boundaries for target points based on the training set and subsequent addition of five folds of data from the test set. Dynamic refinement of the spatial priors can be seen with the addition of subsequent implantation information.

Another method that has been implemented is to allow the algorithm to define the entry and target points automatically within predefined anatomical structures(Sparks et al., 2017a). This is reliant on the anatomical segmentation provided by whole-brain parcellations such as Freesurfer(Dale et al., 1999) or GIF(Cardoso et al., 2015a). In general, whole-brain parcellations are developed from healthy controls and the accuracy of the segmentation may fail in patients with gross anatomical abnormalities or following previous surgery. A further limitation is that in some cases the anatomically defined entry and target regions may be very large such as electrodes targeting the anterior cingulum, which typically enter through the middle frontal gyrus. The computer planning algorithm then returns the global minimum risk score, but this may not be practical or feasible. Algorithms have been able to counter this problem to some extent through maximising spatial distribution, but only when multiple electrodes pass through a single region of interest(Sparks et al., 2017a). One example of this can be seen with temporal implantations. In such a scenario sampling the temporal pole, amygdala, anterior hippocampus, posterior hippocampus and temporo-occipital junction may be required. Unless the clinical scenario dictates otherwise, it is likely that that entry points for all of these electrode trajectories will pass through the middle temporal gyrus. It is beneficial, therefore for the lateral neocortical sampling to be spatially distributed along the anteroposterior axis to prevent electrode conflicts and also aid in the delineation of the lateral neocortical resection margin. More advanced systems also enable the user to iterate through the proposed trajectories in a risk-stratified manner until a feasible trajectory with the lowest risk score is identified. Spatial priors are able to overcome this limitation as the entry and target points are confined to previously implemented trajectories. This removes the reliance on whole-brain parcellations for the entry and target point constraints and ensures reliable spatial sampling. Another benefit is that the risk-stratified trajectories returned to the user are more likely to be feasible, reducing the need to iterate through the options. In generating these spatial priors, we purposefully excluded trajectories that targeted unique patient-specific abnormalities, such as focal cortical dysplasias, as these would not be generalizable when considering trajectory planning in other patients.

As a further analysis, we implemented a K-NN classifier as part of an adaptive learning algorithm. In order to mimic the real-world use of the algorithm for a new centre adopting the spatial priors, the K-NN classifier first generated the boundaries that define the spatial priors for the entry and target points of the electrodes in the training set. Further electrode entry and

target points were then iteratively added in five-folds, each with 42 randomly selected trajectories. The K-NN classifier then adjusted the spatial priors based on the additional implanted electrode information. The unique benefit of this active learning technique is the ability to dynamically adapt to different planning practices and learn individual surgeon preferences with time. In this implementation, the weighting was uniformly distributed, that is to say, that each of the entry and target points contributes to the classifier equally. When surgeons prefer entry or target regions within a specific prior, weightings could then also be applied to favour the distribution. Further work could also implement reinforcement learning algorithms to potentially improve the speed of learning.

4.7 **Conclusion**

Spatial priors are a valuable contribution to CAP, allowing future implantations to be guided by previous planning experience. Through the prospective application of spatial priors, we show that feasible trajectories can be planned and implanted in test cases enabling CAP to be performed without the need for whole-brain parcellations. In addition, experience from SEEG trajectory planning can be continually refined and used to personalise the spatial priors in a dynamic fashion, through the implementation of a K-NN classifier. We have made our institutional priors for commonly used SEEG trajectories publically available as a starting point for those wishing to embark upon computer-assisted planning or as motivation for manual planning

5 Automated trajectory planning for LITT in mesial temporal lobe epilepsy: Based on (Vejay N. Vakharia et al., 2018a)

5.1 **Abstract**

5.1.1 Objective

Surgical resection of the mesial temporal structures brings seizure remission in 65% of individuals with drug-resistant mesial temporal lobe epilepsy (MTLE). LITT is a novel therapy which may provide a minimally invasive means of ablating the mesial temporal structures with similar outcomes, whilst minimizing damage to the neocortex. Systematic trajectory planning helps ensure safety and optimal seizure freedom through adequate ablation of the amygdalohippocampal complex (AHC). Previous studies have highlighted the relationship between the residual unablated mesial hippocampal head and failure to achieve seizure freedom. We aim to implement computer-assisted planning (CAP) to improve the ablation volume and safety of LITT trajectories.

5.1.2 Methods

Twenty-five patients that had previously undergone LITT for MTLE were retrospectively studied. The EpiNav^{TM} platform was used to automatically generate an optimal ablation trajectory, which was compared with the previous manually planned and implemented trajectory. Expected ablation volumes and safety profiles of each trajectory were modelled. The implemented laser trajectory and achieved ablation of mesial temporal lobe structures were quantified and correlated with seizure outcome.

5.1.3 Results

CAP automatically generated feasible trajectories with reduced overall risk metrics ($p<0.001$) and intracerebral length ($p = 0.007$). There was a significant correlation between the actual and retrospective CAP anticipated ablation volumes supporting a 15 mm diameter ablation zone model ($p < 0.001$). CAP trajectories would have provided significantly greater ablation of the amygdala ($p = 0.0004$) and AHC ($p = 0.008$), result in less residual unablated mesial hippocampal head ($p = 0.001$), and also reducing ablation of the parahippocampal gyrus ($p = 0.02$).

5.1.4 Conclusion

Compared to manually planned trajectories CAP provides a better safety profile, with a potentially improved seizure-free outcome and reduced neuropsychological deficits, following LITT for MTLE.

5.2 **Introduction**

Numerous operative techniques have been described to treat mesial temporal lobe epilepsy (MTLE) including anterior temporal lobe resection (ATLR) and selective amygdalohippocampectomy (SAH). The most common form of ATLR, based on the technique described by Spencer et al(Spencer et al., 1984a), involves resection of the lateral neocortex, temporal pole and amygdala prior to intraventricular resection of the hippocampal head and body to the level of the tectal plate. More selective approaches, including transsylvian(Wieser et al., 1982), transcortical(Olivier, 2000) and subtemporal(Hori et al., 1993) SAH, have not given better seizure freedom rates or neuropsychological outcomes(Englot et al., 2014; Morino et al., 2006; West et al., 2015b). As the fear of the operation is cited as a major factor preventing patients from undergoing surgery, a less invasive means of ablation may be more acceptable to patients and potentially increase surgical uptake. Thermal ablation is a lesioning technique that has been used in neurosurgery for many years with variable success(Cossu et al., 2015; Malikova et al., 2014; Parrent et al., 1999). The main limitation of earlier methods was the unpredictable nature of thermal lesioning and the lack of real-time monitoring. The combination of MR thermography techniques with laser technology has allowed precise intracerebral lesioning to be performed using laser interstitial thermal therapy (LITT)(Curry et al., 2012). The majority of the clinical experience surrounding LITT in epilepsy uses the Visualase system (Medtronic Inc.). The extent of the thermal ablation volume is monitored with real-time with MR thermography(Hoppe et al., 2017). A critical part to the process, both in terms of safety and efficacy, involves the planning of the laser trajectory as this determines ablation safety, location and volume. Previous studies have not shown ablation volume to be a predictive factor for the post-LITT outcome, but have suggested anatomical height of the amygdala and volume of residual unablated mesial hippocampal head as important factors(Gross et al., 2016; Jermakowicz et al., 2017b; Kang et al., 2016; Willie et al., 2014; Wu et al., 2015).

Limiting collateral damage to the lateral temporal neocortex, parahippocampal gyrus (PHG) and subcortical white matter fibre tracts has been suggested to improve neuropsychological outcomes compared to ATLR (Drane et al., 2015). Our aim is to validate the use of computer assisted planning (CAP) to maximise ablation of the amygdalohippocampal complex (AHC) whilst improving the safety profile when compared to previously implemented manually planned laser trajectories.Surgical resection of the mesial temporal structures brings

seizure remission in 65% of individuals with drug-resistant mesial temporal lobe epilepsy (MTLE). LITT is a novel therapy which may provide a minimally invasive means of ablating the mesial temporal structures with similar outcomes, whilst minimizing damage to the neocortex. Systematic trajectory planning helps ensure safety and optimal seizure freedom through adequate ablation of the amygdalohippocampal complex (AHC). Previous studies have highlighted the relationship between the residual unablated mesial hippocampal head and failure to achieve seizure freedom. Our objectives were to implement computer-assisted planning (CAP) to improve the ablation volume and risk score of LITT trajectories.

5.3 **Methods**

5.3.1 Patient inclusion

Twenty-five patients with mesial temporal sclerosis that had previously undergone selective laser amygdalohippocampectomy (SLAH) at the Comprehensive Epilepsy Centre at Thomas Jefferson University between 2012 and 2016 were included in the study. Patients underwent manual trajectory planning and SLAH ablation using the Visualase system (Medtronic Inc.). All patients underwent a comprehensive pre-surgical evaluation and post-operative follow-up. Hemispheric language dominance was determined by functional MRI. The outcome was assessed based on a modified Engel scale in which we compared patients that were seizure-free with or without auras for one year or more (class 1) compared to all other outcomes (class 2-4)(Sperling et al., 2008).

5.3.2 EpiNav™

EpiNav™ (Centre for medical imaging computing, University College London) is a multimodal imaging platform that has been described in previous chapters to undertake multi-trajectory automated SEEG electrode planning optimised to maximise contact with grey matter and distance from segmented vasculature whilst reducing intracerebral trajectory length, drilling angle to the skull and overall risk(Nowell et al., 2016b; Sparks et al., 2016, 2017a; Vakharia et al., 2018e). We have now further developed EpiNav™ to plan automated selective amygdalohippocampal laser ablations.

5.3.3 Model generation:

Figure 22: Pipeline for automated LITT trajectories

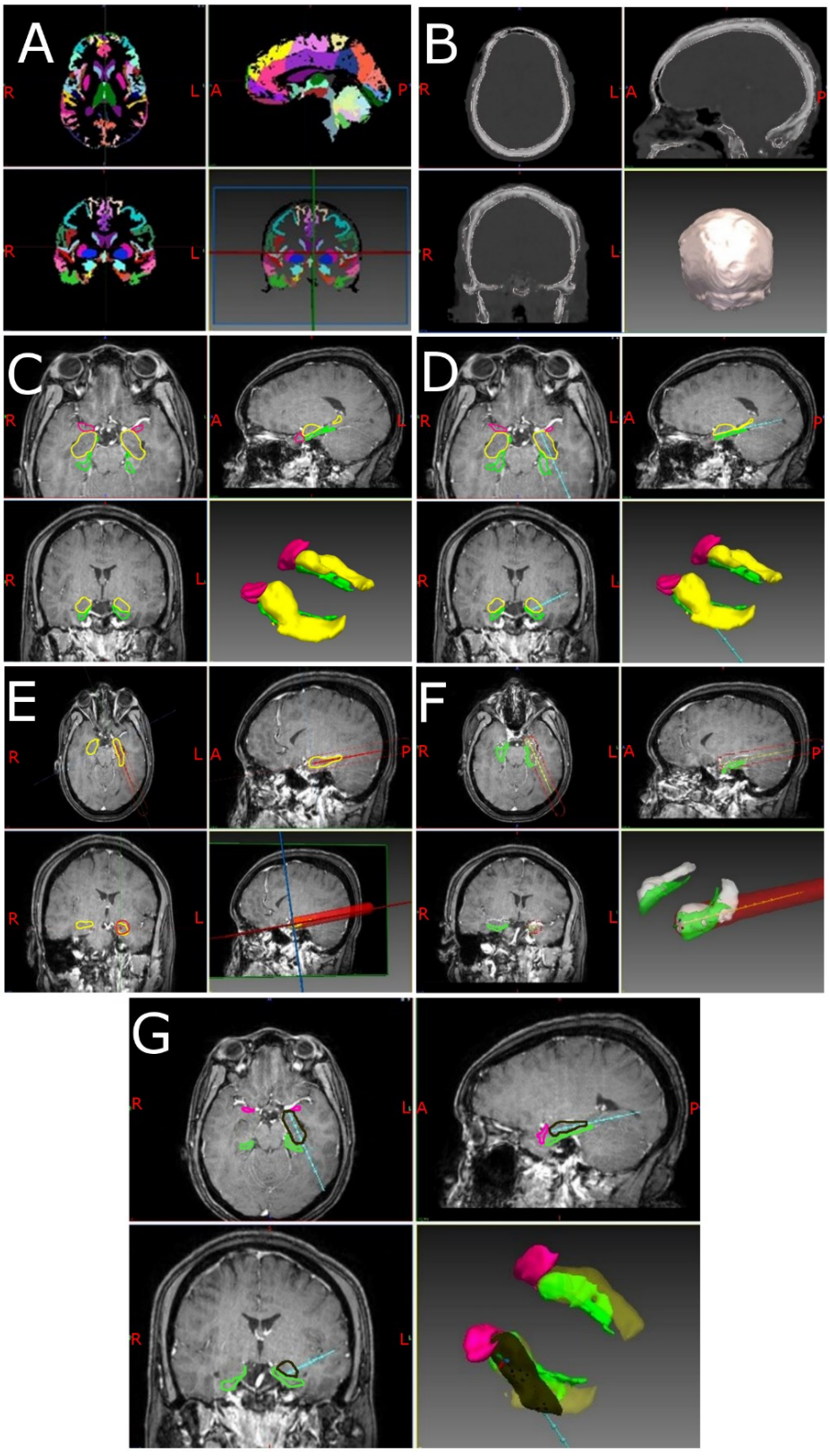
A
B
C
D
E
F
G

Figure 22 Legend: a) T1 weighted MRI scans for each patient were used to generate geodesic information flow (GIF) brain parcellations. The whole brain is segmented into 140 separate anatomical structures that can be used to guide trajectory planning and model generation.

b) Pseudo-CT images were generated from the same T1 weighted MRI scans to provide an image from which a model of the skull can be extracted. The external surface of the skull model is used to calculate the trajectory drilling angle and the inner surface is used to calculate intracranial trajectory length.

c) Models of the cortex, lateral ventricle, amygdala, hippocampus, entorhinal cortex, parahippocampal gyrus, grey matter ribbon, inferior occipital gyrus, middle occipital gyrus, inferior temporal gyrus, middle temporal gyrus, intracranial mask and sulci are extracted from the GIF parcellation and combined with the skull model. In the image shown, the amygdalohippocampal complex is coloured in yellow, entorhinal cortex in pink and parahippocampal gyrus in green. The remaining models have been excluded for clarity.

d) Based on the generated models the optimal trajectory is calculated to target the amygdala whilst preventing entry to the lateral ventricle, maximising contact with the hippocampus, distance from sulci and vasculature, minimising intracranial trajectory length and drilling angle to the skull. The calculated laser trajectory is shown in blue.

e) A region of ablation is then modelled along the model laser trajectory. The visualase system is able to ablate a diameter between 5-20 mm. A conservative maximum ablation diameter of 15 mm was applied to the model (red cylinder).

f) Areas of overlap between the modelled laser ablation zone and the anatomical regions of interest were then extracted so that an estimation of the modelled ablation cavity could be calculated. The volume of each of the regions of interest within the modelled ablation cavity was calculated individually and as a whole. The amygdalohippocampal complex is shown in white and parahippocampal gyrus in green.

(g) Expected ablation cavity within the ROIs (black) showing the extent of mesial hippocampal head ablation. The amygdalohippocampal complex is shown in yellow, parahippocampal gyrus in green and entorhinal cortex in pink.

Utilising a single T1-weighted MRI scan a whole-brain parcellation and pseudo-CT images were generated using geodesic information flow (GIF)(Cardoso et al., 2015b; Ferran Prados, M. Jorge Cardoso, Ninon Burgos, Claudia AM Wheeler-Kingshott, 2016). From the whole brain parcellation, anatomical regions of interest (ROIs) were extracted in an automated fashion including the lateral ventricles, hippocampus, amygdala, entorhinal cortex (ECx) and parahippocampal gyrus (PHG). ROIs were then manually inspected to confirm anatomical accuracy. Potential trajectories were risk-stratified based on cumulative distance from the sulci. The ventricular system was marked as an exclusion zone. Using CAP, target regions for LITT were defined as the amygdala in which the central point was transformed by 3 mm medial, 3mm anterior and 3mm inferior. The medial and inferior transformation was based on preliminary data to improve the ablation of the mesial hippocampal head and avoid heat transfer to the temporal stem and globus pallidus, respectively. The anterior transformation ensured that the trajectory target was situated on the anterior surface of the amygdala(Wu et al., 2015). The CAP algorithm selectively weights trajectories that maximise contact with the centre of the AHC and provides a quantitative measure of this as a proportion of the entire structure. To facilitate cannulation of the long axis of the AHC, the entry point for CAP was assigned as the inferior occipital gyrus. Post-ablation MRI scans were assessed after generation of CAP trajectories in all patients. Manual trajectory planning was undertaken utilizing the 'posteroinferior corridor' (Wu et al., 2015). Here, an initial target point is placed in the centre of the amygdala and a waypoint is placed between the occipital horn of the lateral ventricle and collateral sulcus. The trajectory is then extrapolated posteriorly to the cortical surface with medio-lateral adjustments to avoid vasculature, lateral ventricle and sulci. Finally, the target point is extrapolated forward to the anterior surface of the amygdala.

5.3.4 Safety metric calculation:

Each of the CAP generated trajectories were reviewed by a neurosurgeon for feasibility. For both CAP and manually planned trajectories, length, drilling angle to the skull, minimum distance from critical structures, overall risk (cumulative distance from critical structures) and minimum distance of trajectory from brainstem were automatically calculated(Sparks et al., 2016). Due to a lack of dedicated vascular imaging, it was not possible to segment vascular models for the majority of cases in the study. To prevent potential conflict with cerebral vasculature, sulcal models were used as critical structures as blood vessels are most likely to be present within sulci. The risk score was measured as a cumulative distance from critical structures along the entire trajectory. Derivation of safety margins for stereotactic implantations

was based on the sum of the diameter of the probe, average target inaccuracy and three standard deviations of the inaccuracy(Cardinale et al., 2013). Average target accuracy was based on the method of implantation used(Vakharia et al., 2017b). As a result, a 3 mm planning safety margin was applied. Distances from critical structures greater than 10 mm returned a risk of 0, whilst distances < 3mm returned a risk of 1(Sparks et al., 2017a). The overall risk for trajectory was calculated along the whole of the intracerebral length of the trajectory.

5.3.5 Ablation zone modelling:

Following generation of the CAP and manual trajectories for each patient 'expected ablation zones' were produced using a 15 mm diameter dilation of the initial trajectory. ROIs within the expected ablation zone were extracted and the paired structure volumes calculated. For the purpose of the anatomical volume, laser ablation zone modelling and trajectory optimisation, only the part of the hippocampus anterior to the tectal plate was considered(Spencer et al., 1984b). From the post-ablation MRI scans, taken intra-operatively immediately after the final ablation, the achieved ablation cavities were manually segmented. ROIs within the achieved ablation cavity was then extracted and compared with the calculated (expected) modelled ablation cavities of the manual trajectory to determine the validity of using a 15 mm diameter ablation zone estimation.

5.3.6 Statistical Analysis:

Statistical analysis was performed using SPSS 24. Mann-Whitney-U and Kruskal-Wallis tests were performed for non-parametric comparisons. Correlation between ROI ablation volumes was calculated using a Pearson correlation. A p-value <0.05 was taken to be significant.

5.3.7 Institutional review board approval:

#15D.106 – "Volumetric Analysis of MRIs in Patients with Mesial Temporal Lobe Epilepsy Treated with Stereotactic Laser Amygdalohippocampectomy" (Thomas Jefferson University Hospital)

5.4 **Results**

Patient demographics Twenty five patients (12 male) with MTS who had previously undergone LITT were studied (see Table 16). Post-LITT outcome data were available for all patients with a mean follow up duration of 24.4 +/- 14.1 months (mean +/- S.D.). At last follow up 44% (11/25) of patients were seizure-free. One patient with class 3 outcome underwent a

further LITT ablation 12 months following the first with no improvement in outcome. Three of the other patients with class 3 outcome and both of the patients with class 4 outcome subsequently underwent ATL lobe resection. ATLR resulted in seizure freedom in 2 of the 3 class 3 outcome patients.

Table 16: Study patients demographics and clinical features

Patient	Age	Gender	Duration of epilepsy (years)	Hemispheric language Dominance	Side of ablation	Follow up duration (months)	Modified Engel outcome at last follow up	Complications following LITT	Comments
1	25	Male	23	Left	Left	30	1	None	
2	35	Male	5	Left	Left	11	3	None	
3	29	Male	16	Left	Left	10.5	3	Transient blurry vision, single episode of psychosis requiring hospitalization	
4	29	Female	2	Left	Left	15	2	None	
5	11	Male	4	Left	Right	8	3	None	Underwent ATL 8 months post-LITT
6	56	Female	40	Left	Left	61.5	1	None	
7	57	Female	44	Left	Left	14	3	None	
8	19	Male	3	Left	Right	35	1	None	
9	65	Male	10	Left	Left	8	4	None	Underwent ATL 8 months post-LITT
10	48	Female	40	Left	Right	26.5	2	None	Also has parafalcine meningioma
11	41	Female	15	Left	Left	41	1	None	

12	20	Female	19	Left	Right	18	3	Transient anxiety with panic attacks	Underwent ATL 18 months post-LITT
13	66	Male	31	Left	Left	17	1	None	
14	23	Female	22	Left	Left	29.5	3	Contralateral superior quadrantanopsia	Underwent reablation 12 months post-LITT
15	66	Female	unknown	Left	Left	27	3	None	"Epilepsy since childhood"
16	29	Male	24	Left	Left	31.5	1	Transient increased anxiety	
17	54	Female	58	Left	Right	45	1	None	
18	52	Female	14	Left	Left	6	4	None	Underwent ATL 6 months post-LITT
19	58	Male	8	Left	Left	4.5	2	Committed suicide	Pre-existing mood disorder
20	52	Female	13	Right	Right	29	1	Transient CN IV palsy	
21	59	Male	37	Left	Left	37	1	None	
22	14	Male	unknown	Left	Left	24	2	None	"Epilepsy since childhood"
23	34	Female	33	Left	Left	27	1	None	
24	49	Male	24	Left	Left	15	3	None	Underwent ATL 15 months post-LITT
25	43	Female	15	Left	Left	40	1	None	
Mean	41.4	M:F = 12:13	21.7	L:R = 24:1	L:R = 19:6	26.5 (Median)			
S.D.	17.2		14.9						

5.4.1 Trajectory characteristics:

The mean trajectory length was 8mm less with CAP than manual planning ($p = 0.007$). The overall risk score was lower with CAP trajectories ($p < 0.001$) were significantly (Table 17).

Table 17: Summary of qualitative safety metrics for manual and CAP generated trajectories

	Manual trajectory (mean +/- SD)	CAP trajectory (mean +/- SD)	p-value
Length (mm)	90 +/- 12	82 +/- 6	0.007*
Drilling angle (deg)	31.1 +/- 7.8	32.3 +/- 8.5	0.47
Proportion of trajectory within centre of AHC	0.50 +/- 0.40	0.55 +/- 0.20	0.66
Overall risk score	2.02 +/- 0.64	0.96 +/- 0.20	<0.001*

*denotes statistical significance with $p<0.05$

With the variability in the individual anatomy of the lateral ventricles, depth of the collateral sulcus and extent of sclerosis of the hippocampus a feasible entry point through the lateral aspect of the inferior occipital gyrus was achieved by CAP in 72% (18/25) of cases. In all instances, the amygdala, in which the centre-point was transformed by 3 mm medial, 3 mm anterior and 3 mm inferior, could be used as the target point. The remaining entry points traversed the lateral aspect of the middle occipital gyrus in 20% cases (5/25) and the posterior-most aspect of the middle temporal gyrus in 8% cases (2/25).

5.4.2 ROI model ablation volumes:

Following the implementation of a 15 mm laser ablation diameter to both the CAP and manually planned trajectories, CAP trajectories significantly increased the modelled ablation volume of the AHC from 2748 +/- 771 mm^3 (mean+/-S.D.) to 3282+/- 605 mm^3 (mean+/-S.D.) equating to an extra 11.34% of the total anatomical volume ($p = 0.0075$). Amygdala ablation volumes increased by an extra 15.7% of the total anatomical volume ($p = 0.0004$). The residual (unablated) depth of the mesial hippocampal head reduced by 73% ($p < 0.001$). CAP planned

trajectories, resulted in an 11.3% decrease of the anatomical volume of PHG being ablated (p = 0.02) and reduction in distance of the centre of the trajectory from the brainstem by 1.85 mm (p = 0.0052). (See Table 18).

5.4.3 Actual and expected cavity volumes

Ablation cavities from the post-ablation images of the manually planned trajectories were manually segmented for all patients and volumes calculated. A total implemented mean ablation cavity volume of 6675 +/- 2470 mm^3 was achieved, whilst the total volume of grey matter within the ablation cavity was 3259 +/- 1352 (mean+/-S.D.). The mean proportion of the implemented ablation cavity containing grey matter was 49%; the remaining half of the ablation cavity was in white matter.

The volumes of the achieved AHC ablations were compared with the expected AHC ablations when a 15 mm diameter ablation zone was applied to the manually planned and CAP trajectories. The estimated correlation coefficient was 0.64 with 95% confidence interval (0.38 to 0.89), suggesting a significant linear association ($R^2 = 0.535$, $p < 0.001$). Differences between actual and modelled ablation volumes, when implementing a cylindrical 15 mm ablation zone, are shown in Table 19.

Table 18: Expected ablation volumes and parameters of anatomical regions of interest

Structure	Anatomical volume (mm^3) (mean +/- SD)	Manual trajectory ROI volume ablated (mm^3) (mean +/- SD)	Manual trajectory % ROI ablated (mean +/- SD)	CAP trajectory ROI volume ablated (mm^3) (mean +/- SD)	CAP trajectory % ROI ablated (mean +/- SD)	p-value
Amygdala	1648.19 +/- 359.53	739.84+/- 372.29	45.80+/-20.45	994.03+/- 318.77	61.16+/- 15.82	0.0004*
Hippocampus	2987.22 +/- 477.36	2003.28+/- 565.33	67.68 +/- 17.55	2079.32+/- 488.46	70.18 +/- 14.44	0.6152
AHC	4792.43 +/- 735.75	2748.30+/- 771.30	57.82 +/- 15.05	3282.49+/- 604.62	69.16 +/- 11.54	0.0075*
ENCx	2318.75 +/- 562.01	246.85+/- 271.41	11.35 +/- 13.85	212.89+/- 270.77	8.87 +/- 10.77	0.7005
PHG	3023.94 +/- 506.75	621.94+/- 495.06	20.77 +/- 16.15	358.60+/- 258.02	12.56 +/- 9.78	0.0243*
Total	10135.12 +/- 1395.68	3686.26+/- 959.25	36.73 +/- 9.76	3932.00+/- 793.52	39.31 +/- 8.73	0.3116
Residual (unablated)	N/A	4.45+/- 1.58	N/A	1.19+/- 1.37	N/A	<0.0001*

depth of MHH (mm)						
Distance from brainstem (mm)	N/A	11.75+/- 2.81	N/A	9.90+/- 2.18	N/A	0.0052*

*Abbreviations: AHC – Amygdalohippocampal complex; ENCx – Entorhinal cortex; PHG – Parahippocampal gyrus; MHH – Mesial hippocampal head. *denotes statistical significance with p<0.05.*

Table 19: Error between expected and achieved ablation volumes

Structure	Achieved manual trajectory ROI ablation	Expected manual trajectory ROI ablation	Estimation error as a proportion of anatomical volume (%)
Amygdala	741.92 +/- 423.93	739.84 +/- 372.29	-2.08%
Hippocampus	1630.32 +/- 580.90	2003.28 +/- 565.33	+12.49%
AHC	2510.54 +/- 887.46	2748.30 +/ - 771.30	+4.96%
ENCx	269.23 +/- 368.17	246.85 +/- 271.41	-0.97%
PHG	478.87 +/- 447.05	621.94 +/- 495.06	+4.73%
Total ROIs	3258.59 +/- 1351.81	3686.26 +/- 959.25	+4.22%

Abbreviations: AHC – Amygdalohippocampal complex; ENCx – Entorhinal cortex; PHG – Parahippocampal gyrus; ROI – Region of Interest.

5.4.4 Correlation with seizure freedom outcome:

There was no significant difference between seizure-free outcome and absolute total volume of ROI ablation ($p = 0.73$) or residual depth of the mesial hippocampal head ($p = 0.43$). A trend was found between seizure-free outcome and the baseline anatomical volume of the amygdala, but this failed to reach significance ($p = 0.08$).

5.5 **Discussion**

5.5.1 Application of computer-assisted planning in neurosurgery

CAP was first introduced to neurosurgery during the 1980s as a means of calculating frame-based coordinates during stereotactic brain biopsies (Davis et al., 1988). Advances have included the addition of multimodal imaging(Cardinale et al., 2015; Nowell et al., 2016a), 3D model generation(Rodionov et al., 2013), pathology segmentation, atlas and whole-brain parcellation integration(Sparks et al., 2017a). The most recent advances in CAP have been in automated trajectory planning for deep brain stimulation and SEEG procedures. Through the implementation of constraints such as maximising distance from blood vessels, avoidance of crossing sulcal boundaries, ensuring an orthogonal drilling angle to the skull, minimising intracerebral trajectory length and optimising grey matter sampling, algorithms can provide trajectories with improved safety metrics at a fraction of the planning time (Nowell et al., 2016b; Sparks et al., 2017a). Blinded external validation studies of CAP generated electrodes have shown that they achieve feasibility ratings similar to manually planned trajectories and may even provide feasible trajectories when manually planned trajectories are deemed infeasible(Vakharia et al., 2018e). Using the EpiNav^{TM} software we have applied parameters to automate LITT trajectories for the management of mesial temporal sclerosis to improve trajectory safety metrics and maximise ROI ablation volumes beyond that of manually planned trajectories in a fully automated fashion (see Figure 22 for the processing pipeline).

5.5.2 Correlation of ROI ablation with seizure and neuropsychological outcomes

In contemporary series, seizure-free outcomes following LITT for mesial temporal sclerosis have varied between 54%(Willie et al., 2014) and 80% (Wu et al., 2015). In the study by Wu et al., seizure freedom was achieved in 80%. All patients had mesial temporal sclerosis, whilst in the study that achieved 54%, only 7 of 13 had unilateral mesial temporal sclerosis. This highlights the need for careful patient selection. A later study by Kang et al. (Kang et al., 2016) reported longer-term follow up on the same patient cohort as Wu et al. Seizure freedom fell to 60% at two years. In another series, 23 patients had at least one year follow up and 65% of patients had an Engel class 1 outcome(Jermakowicz et al., 2017b). Jermakowicz et al. also report the lack of ablation of the mesial hippocampal head as being associated with poorer outcome(Jermakowicz et al., 2017b). Lateral trajectories through the hippocampus and lack of mesial temporal sclerosis also showed a trend towards a more unsatisfactory outcome. There

was no relation between the absolute ROI ablation volume and seizure freedom rates or neuropsychological outcomes. These findings correlate with the results of the current study, whereby there was also no relationship between postoperative seizure freedom rates and absolute total ROI ablation volumes. We report seizure freedom rates of 44% at a median follow up of 26.5 months. This is slightly lower than other studies in the published literature, but this likely reflects the normal variation and impact of individual outcomes on group level statistics in small case series. Nevertheless, this remains a minimally invasive alternative to open temporal lobe resection and repeat LITT or open surgery can still be performed if LITT is unsuccessful.

5.5.3 Potential effect on neuropsychological outcomes

Drane et al. compared patients undergoing SLAH with standard or tailored ATLR and showed in the dominant hemisphere, SLAH resulted in significantly less post-operative decline in famous face recognition and common noun naming(Drane et al., 2015). In the non-dominant hemisphere, ATLR resulted in a significant comparative decline in famous face recognition only. Given that both methods involve lesioning of the amygdala and hippocampus, it can be inferred that collateral damage to the surrounding cortical and subcortical structures compromises neuropsychological function. The CAP generated trajectories resulted in a significant reduction in the expected PHG ablation compared to manually planned trajectories. Furthermore, entry through the inferior occipital gyrus spares the lateral temporal neocortex, temporal pole and temporal stem. Prospective studies are required to determine whether this will lead to less post-operative neuropsychological morbidity.

5.5.4 Optimisation of laser trajectories

Few studies have critically assessed implemented trajectories to improve AHC ablation volume. Our aim was to validate CAP trajectories, with regards to AHC ablation volume and safety metrics, when compared to manually planned trajectories. Wu et al. compared trajectories and ablation volumes after the implementation of a systematic method of manual trajectory planning(Wu et al., 2015). The method described is very similar to the approach automated by the CAP trajectories. This resulted in an increase in the amygdala ablation from 42% to 66% and hippocampal ablation from 52% to 61%. In the current study, CAP generated trajectories were anatomically constrained and cumulative distance from the sulci was maximised and used as a basis of risk stratification. Given these constraints, there was a small

window between the collateral sulcus and the inferior surface of the occipital horn of the lateral ventricle through which trajectories could pass, which Wu et al. (Wu et al., 2015) originally described as the 'posteroinferior corridor'. Due to the anatomical variation in the depth of the collateral sulcus and the size of the occipital horn of the lateral ventricle, a trajectory through the inferior occipital gyrus was only feasible in 72% (18/25) of cases. In the remaining cases, a more lateral and superior entry point was required through the posterior middle temporal and the lateral middle occipital gyri respectively. Even with the application of the systematic method to increase ablation volume of manually planned trajectories, as described by Wu et al(Wu et al., 2015), the CAP trajectories provided an increased ablation of the AHC volume by 11.34% and reduced the depth of the mesial hippocampal head remnant to ~1 mm. The incidence of significant intracranial haemorrhage following LITT cannot be accurately distinguished from the literature due to the low number of published reports. Nevertheless, given that there were no haemorrhages in this case series, this does not mean that the risk of haemorrhage is zero. As a result, we implemented a risk stratification method based on the cumulative distance from critical structures such as vasculature or sulci (in cases where vascular segmentation could not be performed). Based on data from SEEG studies we model risk from 0 to 1 along the entire length of the trajectory(Sparks et al., 2016). Any point along the planned trajectory where a critical structure is within 3 mm is attributed a risk score of 1, whilst those greater than 10 mm are given a risk of 0. In this study, CAP trajectories halved the overall trajectory risk score.

5.5.5 Significance and limitations

Here we provide the first automated CAP pipeline for optimising laser trajectory planning utilising a single T1 weighted MRI image. This system is fully customisable to allow the user to anatomically constrain both entry and target points, stratify for ROI contact (central core of hippocampus) as well as defining critical structures to be avoided. To date, the only independent prognostic factor for seizure outcome following LITT is the residual (unablated) hippocampal head(Jermakowicz et al., 2017b), which CAP trajectories would reduce. Furthermore, the safety profile of the trajectory, as determined by the cumulative distance from the sulcal segmentation, is improved. The implication is that CAP trajectories may result in improved seizure freedom rates and improved safety profiles, although this remains to be proven through a prospective clinical trial. If future prospective studies are to be undertaken to determine if ROI ablation volume correlates with improved seizure freedom rates we estimate

~250 patients would need to be enrolled to detect an increased seizure freedom rate of 20% with a power of 90% at a significant level of p = 0.05. The current study is underpowered to detect such a difference statistically.

LITT is likely to become more prevalent for the treatment of mesial temporal lobe epilepsy as short term outcomes have been shown to be comparable to open surgical intervention. As such, as the number of institutions performing LITT increases each will undergo a learning curve. The increase in adoption will inevitably lead to variability in patient outcomes and complication rates making initial comparisons to other modalities difficult. CAP may provide a solution whereby a uniform and objective means of generating laser trajectories overcomes the initial learning curve potentially providing sustained and reliable outcomes. As newer evidence emerges and experience grows the algorithm can be continuously modified to ensure optimal trajectories are implemented uniformly.

The accuracy of ROI segmentation is based on the parcellation algorithm implemented within the model development stage. In this study, we implemented GIF(Cardoso et al., 2015b), a whole-brain parcellation, instead of a dedicated hippocampal segmentation. This has the added benefit of including nearby anatomical ROIs, such as the PHG, ENCx as well as allowing ventricular, sulcal and cortical entry ROI model generation simultaneously, at the relative expense of hippocampal segmentation accuracy. GIF was derived from healthy controls. As such when applied to populations with mesial temporal sclerosis it has a tendency to over-estimate the size of the hippocampus. All GIF segmentations were checked manually at the time of model generation and the over-segmentation of the hippocampus was minor. Given that the same segmentations were used for both manual and CAP trajectory assessment any error in the parcellation would effectively cancel out.

Due to the retrospective nature of this comparison study, it was not possible to prospectively control for baseline image quality. In addition, the patients did not undergo dedicated vascular imaging, such as MRV, so vascular segmentation was not possible. Sulcal models were used as proxy critical structures to avoid deep vasculature, whilst trajectories that conflicted with surface veins, based on gadolinium enhance T1 images, were considered not feasible and the next risk-stratified trajectory, was selected. Future prospective studies should include standardised structural and vascular imaging protocols. The patient cohort was derived from a single centre and limited to two surgeons. Further studies should aim to be multi-centre in their design to validate the algorithm against variability in practice.

Finally, the application of a 15 mm diameter ablation zone around the CAP and manual trajectories to provide an 'expected' ablation cavity was not an exact estimation of the actual 'achieved' ablation volumes. One reason for this is that the laser ablation zone in vivo is not cylindrical as the lateral ventricles and basal cisterns act as heat sinks dissipating the thermal energy. These anatomical features result in a non-linear ablation cavity that could not be easily modelled based on current clinical experience, due to patient variability. The intimate proximity of the hippocampus to the lateral ventricle and basal cisterns may explain why the expected cavity, based on a uniform ablation zone, disproportionately over-estimated hippocampal ablation compared to the other ROIs. The estimated ablation cavity for both manual and CAP generated electrodes were calculated in the same fashion, to ensure uniformity during the comparison and account for any potential inaccuracy.

5.6 **Conclusion**

We present a novel, fully automated CAP system for the generation of LITT trajectories to maximise mesial temporal ROI ablations, improve trajectory safety metrics and maximise the ablation of the mesial hippocampal head when compared to manually planned and implemented trajectories. CAP also significantly reduces collateral damage to nearby structures, such as the parahippocampal gyrus, which may reduce the cognitive effects of the procedure. We have also validated a 15 mm diameter ablation zone model as a predictor of ROI ablation volume. Prospective studies of CAP are needed to determine if this method is associated with improved seizure outcomes and reduced neuropsychological deficits.

6 Optimising Trajectories in Computer-Assisted Planning for Cranial Laser Interstitial Thermal Therapy: A Machine Learning Approach. Based on (Li et al., 2019a)

6.1 **Abstract**

6.1.1 Objective

Laser interstitial thermal therapy (LITT) is an alternative to open surgery for drug-resistant focal mesial temporal lobe epilepsy (MTLE). Studies suggest maximal ablation of the mesial hippocampal head and amygdalohippocampal complex (AHC) improve seizure freedom rates whilst better neuropsychological outcomes are associated with sparing of the parahippocampal gyrus (PHG). Optimal trajectories avoid sulci and CSF cavities and maximize distance from vasculature. Computer-assisted planning (CAP) improves these metrics, but the combination of entry and target zones has yet to be determined to maximize ablation of the AHC whilst sparing the PHG. We apply a machine learning approach to predict entry and target parameters and utilize these for CAP.

6.1.2 Methods

Ten patients with hippocampal sclerosis were identified from a prospectively managed database. CAP LITT trajectories were generated using entry regions that include the inferior occipital, middle occipital, inferior temporal and middle temporal gyri. Target points were varied by sequential AHC erosions and transformations of the centroid of the amygdala. In total 7600 trajectories were generated and ablation volumes of the AHC and PHG were calculated. Two machine learning approaches (Random Forest and Linear Regression) were investigated to predict composite ablation scores and determine entry and target point combinations that maximise ablation of the AHC whilst sparing the PHG.

6.1.3 Results

Random Forests and Linear Regression predictions had a high correlation with the calculated values in the test set ($\rho = 0.7$) for both methods. Maximal composite ablation scores were associated with entry points around the junction of the inferior occipital, middle occipital and middle temporal gyri. The optimal target point was anteromedial amygdala. These

parameters were then used with CAP to generate clinically feasible trajectories that optimize safety metrics.

6.1.4 Conclusion

Machine learning techniques accurately predict composite ablation score. Prospective studies are required to determine if this improves seizure-free outcome whilst reducing neuropsychological morbidity following LITT for MTLE.

6.2 Introduction

As described in Chapter 5, LITT has emerged as a novel therapy for mesial temporal lobe epilepsy due to the ability to modulate the extent of the ablation cavity in real-time through MR-thermography and providing seizure freedom rates comparable to open surgery (Gross et al., 2018; Willie et al., 2014) with potentially improved neuropsychological outcomes (Drane et al., 2015). The extent of ablation of the mesial hippocampal head has been shown to be an independent predictor of seizure freedom (Jermakowicz et al., 2017b), whilst sparing the parahippocampal gyrus (PHG) correlates with improved neuropsychological outcome (Drane, 2017; Drane et al., 2015).

To aid LITT trajectory planning and improve ablation volumes a systematic manual method utilising the 'posterior-inferior corridor' has been proposed (Wu et al., 2015). Comparisons of manually planned with computer-assisted planning of trajectories showed that the latter improved AHC ablation, reduced the unablated mesial hippocampal head remnant, spared the PHG and enhanced safety metrics (Vakharia et al., 2018d). CAP also provides a uniform objective method of trajectory planning that could help to overcome the initial learning curve associated with implementing a novel technology.

Here we aim to implement machine learning techniques with CAP to determine the optimal parameters for LITT that will maximise AHC ablation, sparing of PHG and distance from critical structures such as the brainstem, sulci and vasculature.

6.3 Methodology

6.3.1 Subjects

Ten consecutive pre-operative patients with mesial temporal sclerosis (*5* left) that were eligible for LITT were identified from a prospectively maintained database at The National Hospital for Neurology and Neurosurgery, London. From a single *T1* MPRAGE acquisition with a voxel size of 1 mm isotropic (*TE/TR/TI = 3.1/7.4/400 ms*; flip angle *11°*; parallel imaging acceleration factor *2*) whole brain parcellations and synthetic CT (pseudoCT) images were generated using geodesic information flow (Cardoso et al., 2015a) and a multi-atlas information propagation scheme(Burgos et al., 2013), respectively. Patient-specific 3D models of the cortex, ventricular system, brainstem, AHC, PHG, EnC and sulci were extracted from the whole brain

parcellation (see). EpiNav™ (UCL, CMIC) was then used to generate CAP trajectories based on a previously described algorithm(Vakharia et al., 2018d).

6.3.2 Computer-assisted planning

In brief, the algorithm aims to minimise the intracerebral catheter length, drilling angle from orthogonal to the skull and PHG ablation, whilst maximising distance from sulci, ventricles and intracranial vasculature, ablation of the mesial hippocampal head and AHC and distance from the brainstem (see Figure 23). Both sulci and intracranial vasculature are regarded as critical structures where the minimum distance was set to *3 mm*. The overall risk score was calculated based on a cumulative distance from critical structures along the entire length of the trajectory and normalised between *0-2*(Sparks et al., 2017b). See Equation 2:

To determine the optimal trajectory parameters, CAP trajectories were calculated for all possible combinations of the following parameters for each patient:

1. Entry zones (Inferior occipital gyrus (IOG), middle occipital gyrus (MOG), inferior temporal gyrus (ITG) and middle temporal gyrus (MTG).

2. Morphological erosions (circumferential diminution) of the AHC (0, 1 and 2 mm)

3. Target zones (translations of the centroid of the amygdala by 0-3 mm in the X, Y and Z planes)

Based on these parameter combinations a total of *760* trajectories per patient were generated using CAP and a composite score was calculated by the following equation:

Equation 3: Composite Score

$$Composite\ Score\ (ml) = \frac{AHC_{ablation}}{AHC_{anatomical\ volume}} - \frac{PHC_{ablation}}{PHC_{anatomical\ volume}}$$

where, AHC and PHC indicate the volumes (*ml*) of the correspondent structures.

Figure 23: Pipeline for machine learning and application parameters for individual patient planning

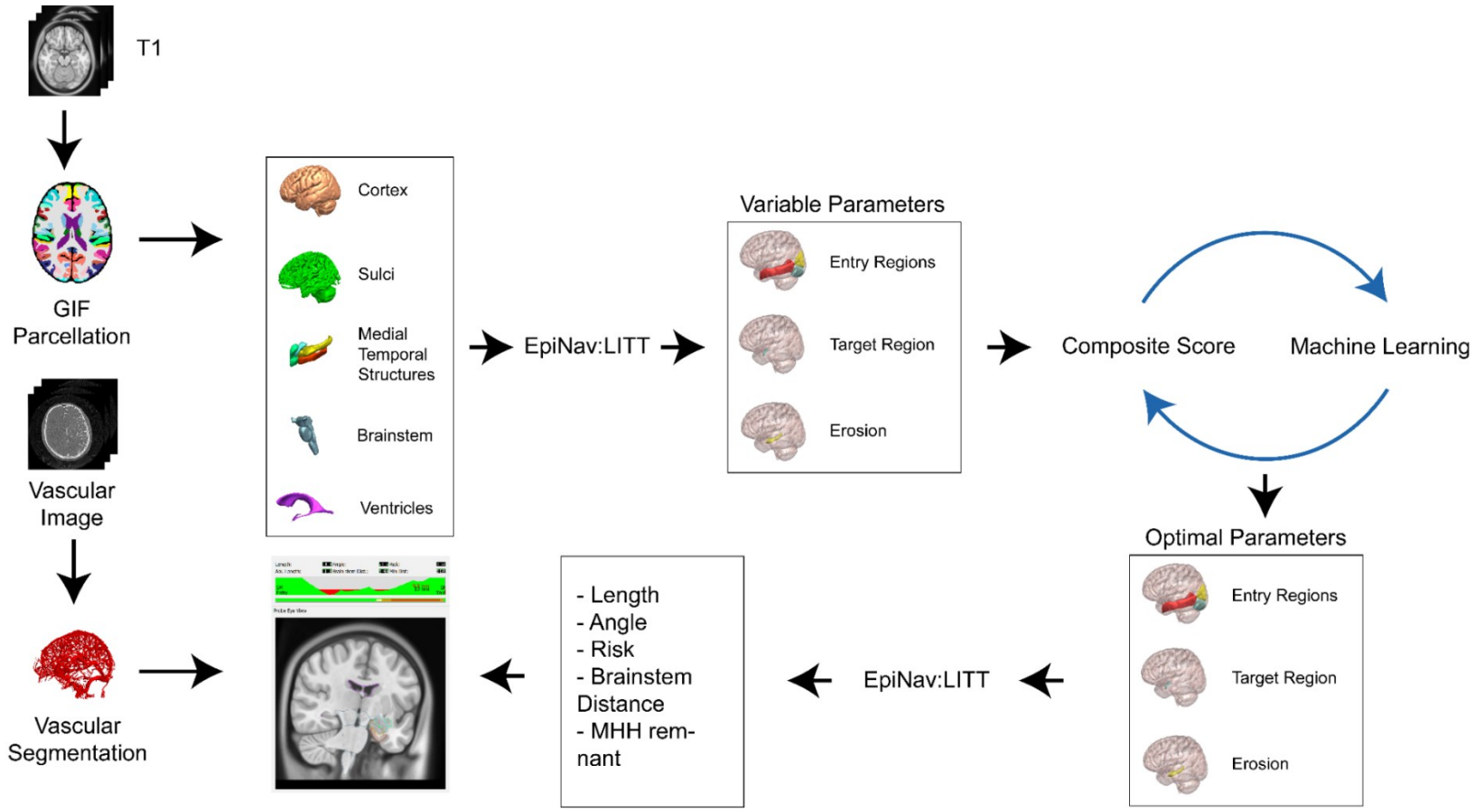

Figure 23 Legend: Trajectory planning requires a single T1 image from which a whole brain parcellation and pCT (not shown) are generated using geodesic information flows (GIF). Important structures required for planning were automatically segmented from the GIF parcellation and 3D models were generated of the cerebral cortex, sulci, mesial temporal lobe structures (hippocampus, amygdala, entorhinal cortex, parahippocampal gyrus), brainstem and ventricles. The automated trajectories were then calculated using EpiNav based on all possible combinations of entry region, target region and AHC erosion. Composite scores for each of the trajectories were calculated. Machine learning was performed on 50% (training set) and composite score predictions were compared with the actual values in the remaining 50% (test set). Optimal parameters for entry region, target region and erosion were defined. In combination with patient-specific vascular segmentations the optimal parameters could be then used as the basis for computer-assisted planning (CAP) to optimise safety metrics such as laser catheter intracerebral length, drilling angle, estimated risk, distance from brainstem and mesial hippocampal head (MHH) remnant following simulated ablation (based on 15 mm ablation diameter).

6.3.3 Machine learning

Two different supervised regression-based machine learning models (Random Forest and Linear Regression) were configured using R (R Core Team, 2018) and auxiliary packages: ggplot2 (Wickham, 2009), randomForest (Liaw et al., 2002), stringr (Wickham, 2018), cowplot (Wilke, 2017), RColorBrewer (Neuwirth, 2014), and reshape2 (Wickham, 2007).

All composite scores were normalised using the maximum score in each patient, in order to guarantee the comparability of these indices. The data was then split into training and testing sets. The training set of *5* patients (*3800* trajectories) was selected at random. The data from the remaining *5* patients (*3800* trajectories) were then used as the test dataset to validate the predictive accuracy of the model.

Both Linear Regression and Random Forest (Breiman, 2001) models were trained on the first portion of the data, according to the parameters entry area (MTG, MOG, IOG, ITG), translations of the centroid of the amygdala (axial, sagittal, and coronal planes), and the

magnitude of erosion of the AHC. For the Random Forest method, 100 trees were used. Linear Regression was performed according to the following equation:

Equation 4: Regression Score

$$Score = \sum_i C_i V_i$$

Where, *C* is the coefficient and *V* is the variable. The index *i* identifies the different variables/coefficient shown in Figure 25.

We then applied the trained predictors to the (unseen) test data and evaluated the obtained results. Pearson correlations between the predicted and actual values were obtained, as well as, the root mean square of the errors. The most critical parameters to maximise the composite score were then evaluated. The study was approved the National Research Ethics Committee London, reference 12/LO/0377. Individual patient consent was sought for use of anonymized perioperative imaging.

6.4 **Results**

Both Linear Regression and Random Forest approaches showed similar results. The predicted scores reproduce the structure with good accuracy as shown by a Pearson correlation of $\rho = 0.7$ for both methods suggesting a strong correlation. Linear Regression and Random Forest models featured a root mean squared error of *RMSE = 0.13* and *RMSE = 0.12*, respectively. Figure 24 shows the predicted values and actual scores.

Figure 24: Validation accuracies of machine learning models

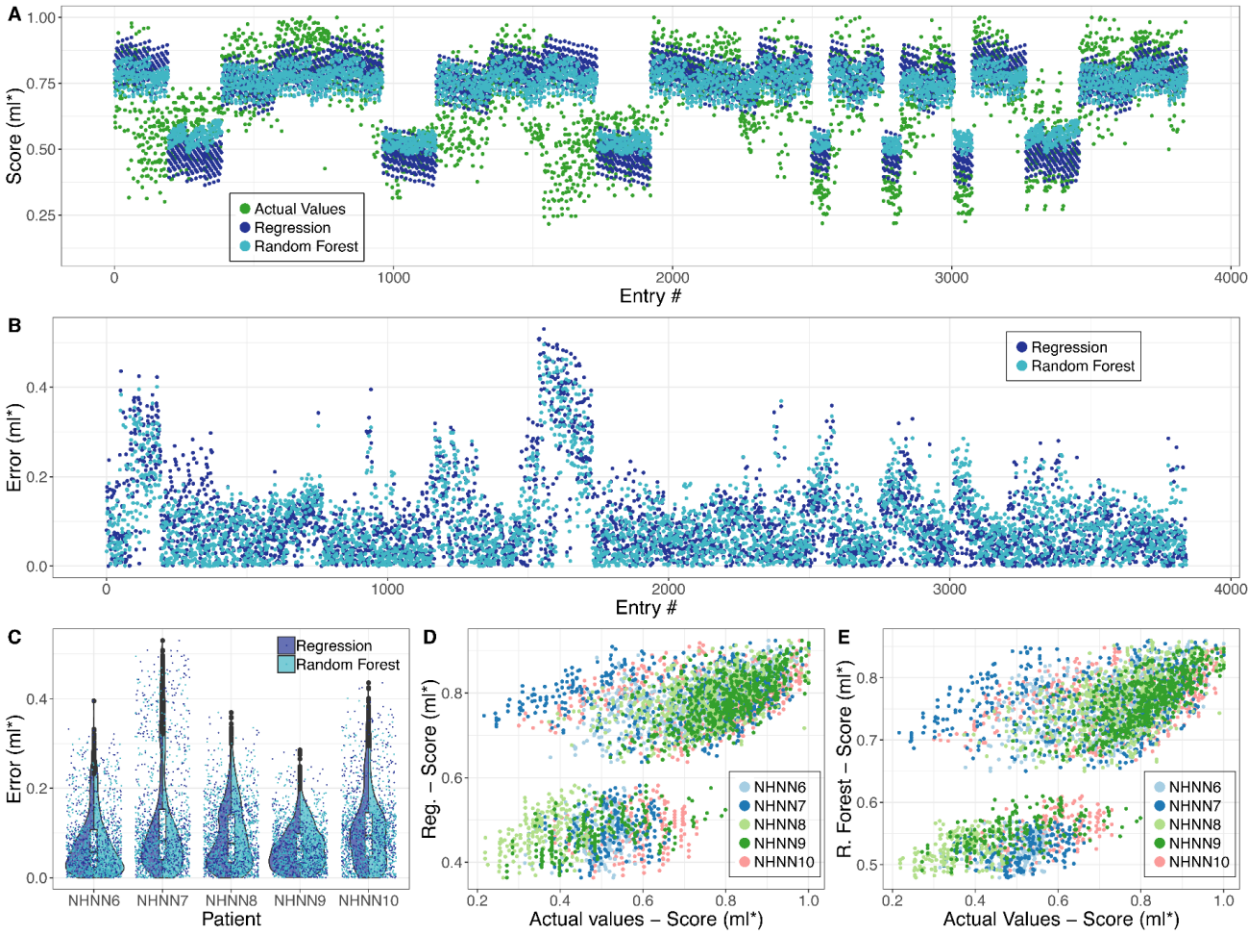

Figure 24: Evaluation of the accuracy of trained models (Linear Regression and Random Forest). ***A)*** *Comparison between values predicted by both models and composite scores for all entries in every patient of the test set.* ***B)*** *Error for both models, i.e., the difference between predicted and calculated composite scores, for all entries in every patient of the test set.* ***C)*** *Violin plots of distributions of errors shown in B.* ***D)*** *Scatter plot of composite scores versus predicted score (Linear Regression) for all entries in every patient of the testing set, each patient is represented by a different colour.* ***E)*** *Scatter plot of composite versus predicted scores (Random Forest) for all entries in every patient of the test set, each patient is represented by a different colour. Both models were capable of reproducing the overall trend of data with good accuracy, with a Pearson correlation of $\rho = 0.7$ for the Linear Regression model and $\rho = 0.7$ for the Random Forest model. Some of the patients exhibit a worse fitting and higher errors, e.g., NHNN7 and NHNN10. ml*: millilitres (normalised).*

When identifying the most important component features, both Linear Regression and Random Forest methods provide similar results. Figure 25 shows the coefficients for each variable of the Linear Regression. According to the values, in order to maximise the ablation score, one should prioritise an entry which is centred at the junction of the IOG, MTG and MOG (see Figure 26 B and D) and apply an anterior and mesial translation to the centroid of the amygdala. Figure 26 C and D show an example CAP trajectory generated using the optimal parameters derived from the Linear Regression.

Figure 25: Regression Model Coefficients for Entry and Target Points

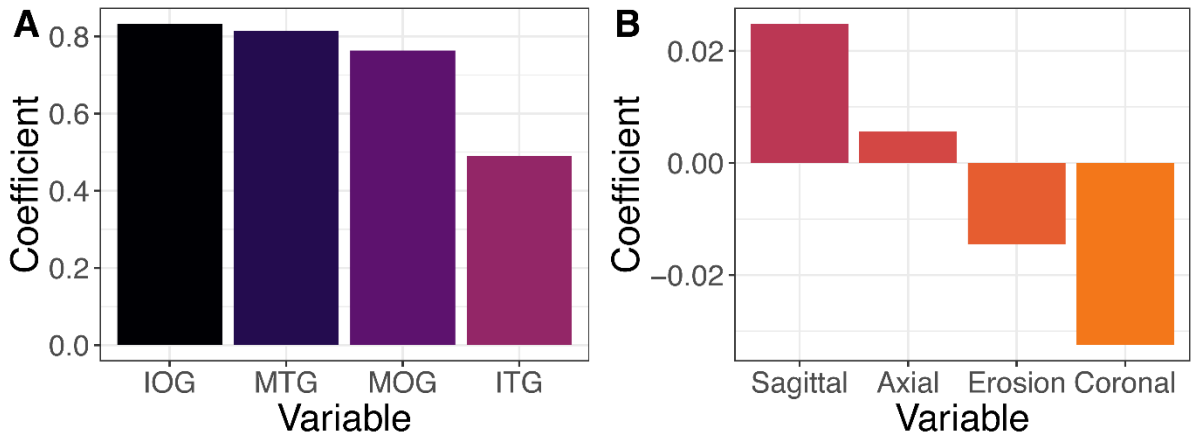

Figure 25 Legend: Coefficient C_i for each variable V_i of the estimated linear model. A) Coefficients for entry areas B) Coefficients for target areas (translations of the centroid of the amygdala) and erosion of the AHC. Coronal shifts and erosion of the AHC impact negatively on the predicted scores. Note coefficients for entry points at an order of magnitude greater than for target points.

Figure 26: Machine Learning Derived Entry and Target Points for LITT:MTLE

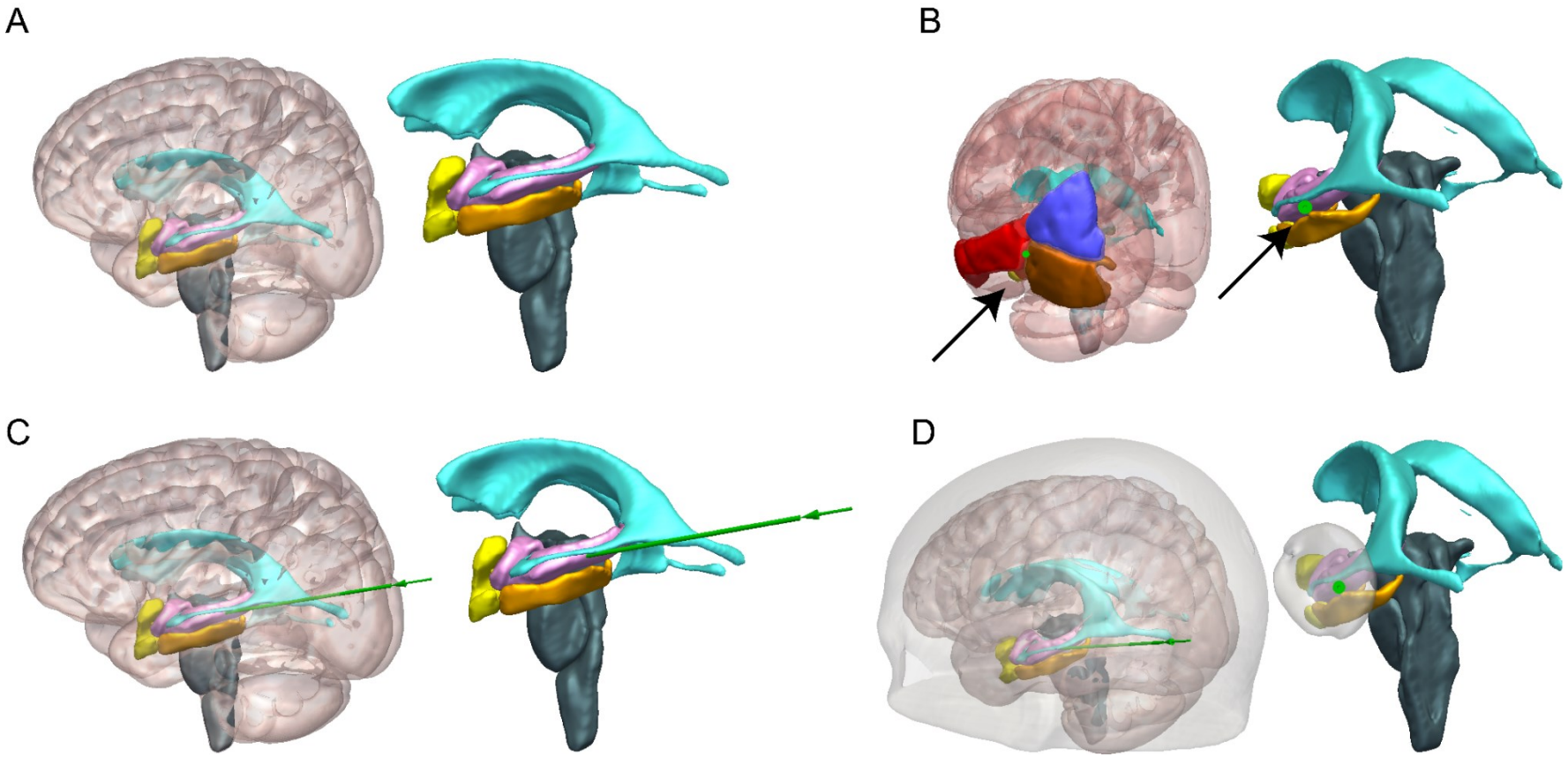

Figure 26: Anatomical structures and example LITT trajectory for amygdalohippocampectomy, shown with and without the transparent cortical overlay. ***A)*** *Automated segmentation of patient-specific anatomical structures including the lateral ventricles (cyan), amygdalohippocampal complex (pink), entorhinal cortex (yellow), parahippocampal gyrus (orange) and brainstem (teal).* ***B)*** *Probes-eye view along trajectory (green), shown by implementing optimal entry point (black arrow) through junction of middle occipital gyrus (yellow), inferior occipital gyrus (pink) and middle temporal gyrus (orange),* ***C)*** *Lateral view of trajectory shown in B, revealing entry into the hippocampus at the level of the tectum without crossing the occipital horn of the lateral ventricle and* ***D)*** *Automated LITT trajectory with overlaying transparent scalp and cortex. The right pane shows the optimal entry zone at the level of the cortex based on the results of the linear Regression.*

6.5 **Discussion**

Here we utilise machine learning algorithms to define the junction between the IOG, MOG and MTG as the optimal entry and anterior and medial translation of the amygdala as the target point parameters for LITT trajectories. Application of these parameters results in maximal ablation of the amygdalohippocampal complex and sparing of the parahippocampal gyrus. The implication is that this may result in improved seizure-free outcome and reduced neuropsychological morbidity.

6.5.1 Laser interstitial thermal therapy

As discussed in Chapter 5, LITT for MTLE is a novel minimally invasive approach for selective amygdalohippocampectomy (Hoppe et al., 2017). As with all novel therapies, there is an initial learning curve and early outcome results can be variable. To date, most case series of LITT for MTLE are limited in number *(< 30*), provide short follow up durations of *6-24* months and lack comprehensive reporting of secondary outcomes, such as neuropsychological morbidity.

An 'open-label' comparative study comparing open microsurgery to LITT for mesial temporal sclerosis revealed a significant decline in naming or recognition tasks in *> 80%* (32/39) following open surgery that was not observed in any patients following LITT (Drane et al., 2015). This suggests naming and recognition is sub-served by the parahippocampal gyrus and

surrounding white matter fibre tracts running within the temporal stem (uncinate fasciculus and inferior fronto-occipital fasciculus) or basal temporal regions (inferior longitudinal fasciculus) that are relatively spared following LITT.

A further study correlated LITT trajectories with seizure outcome at a mean follow up duration of *22.4* months in *23* patients (Jermakowicz et al., 2017b). Trajectories passing more mesially within the hippocampal head were more likely to be associated with seizure-free outcome.

6.5.2 Computer-assisted planning

In Chapter 5, CAP was previously applied to LITT amygdalohippocampal ablation and compared to independently generated trajectories in 25 patients (Vakharia et al., 2018d). Using parameters derived from expert opinion the entry point was restricted to the inferior occipital gyrus. The target point of the centroid of the amygdala was translated by 3 mm anteriorly, mesially and inferiorly to improve ablation of the mesial hippocampal head, maximise amygdala and entorhinal cortex ablation and prevent heat dissipation to the pallidum respectively.

As is conventional in LITT trajectory planning an extra-ventricular approach was implemented, entering the hippocampus at the level of the tectum and maximising distance from the brainstem to prevent inadvertent thermal injury (Wu et al., 2015). Due to individual patient anatomical variability, an entry point through the inferior occipital gyrus was only possible in *72%* (*18/25*) of cases with the remainder passing through the middle occipital and middle temporal gyri. Ablation volumes with CAP were significantly improved by *11%* for the AHC whilst the unablated mesial hippocampal head and PHG volume were reduced by *73%* and *11%* respectively (Vakharia et al., 2018d). In the current study, we have implemented machine learning to determine the optimal trajectory parameters that enhance mesial hippocampal ablation and spare the PHG. Through the calculation of *760* trajectories per patient across *10* patients, we computed all possible trajectory combinations and utilised machine learning to predict a normalised composite score of ablation volumes.

Compared to our previous study in Chapter 5, these results suggest that the application of the machine learning parameters would increase the composite ablation scores by a further *10%*, based on the refined entry point and if the coronal translation and AHC erosion are not applied. We anticipate that if these trajectories were implemented for prospective LITT

ablations there may be an improvement in the seizure-free outcome rate and reduced neuropsychological morbidity.

6.5.3 Machine learning results

In order to identify the optimal parameters for LITT amygdalohippocampal ablation that maximise the ablation composite score, we trained both linear regression and random forest machine learning models. To prevent overfitting, the models were trained on half of the dataset and then validated on the remaining unseen data. Both linear regression and random forest methods show similar outputs when compared to the actual scores, indicating high reliability for the machine learning models.

The results showed good correlation with the composite scores and low root mean square error suggesting a good predictive accuracy. From all the parameters, the entry area had the most relevant impact on the composite score with IOG, MTG and MOG having the greatest contribution. These findings are consistent with the postero-inferior corridor described by Wu et al.(Wu et al., 2015), which is the only study in the literature that has been able to systematise manual LITT trajectory planning to improve ablation volume.

With regards to the target regions, translation of the centroid of the amygdala anteriorly (sagittal plane) and mesially (axial plane) resulted in the greatest increase in composite score whilst erosion of the AHC and inferior translation (coronal plane) had a negative impact. This would be expected as inferior trajectories ablate more of the PHG and spare the superior amygdala.

6.5.4 Limitations

Only *10* patients, from a single centre, were included in this study. The large number of possible unique trajectory combinations resulted in *7600* CAP generated trajectories for evaluation. Future studies using larger datasets from a range of institutions and a number of neurosurgeons performing manual planning will be required to assess the external validity and robustness of CAP. Furthermore, the application of the Linear Regression results from this study will allow a more focused investigation of trajectory parameter combinations, therefore, reducing the number of CAP generated trajectories per patient.

All imaging was derived from a single centre and the acquisition quality of the T1 image has significant implications for the whole brain parcellation. It is unclear whether T1 acquisitions with movement artefact or sequences with poorer grey-white matter differentiation would result in less accurate structure segmentation and alter the CAP trajectory output.

The GIF whole brain parcellation was derived from a control dataset. The resulting segmentation of the hippocampus over-estimated hippocampal volume in our cohort of mesial temporal sclerosis patients by ~*12%* (Vakharia et al., 2018d). A whole brain parcellation derived from patients with mesial temporal sclerosis may, therefore, provide more accurate hippocampal segmentation. Given that the Linear Regression results revealed a negligible effect of AHC erosion on the composite score, however, this is unlikely to have a significant effect on the result.

6.6 **Conclusion**

To our knowledge, this is the first direct clinical application of machine learning in pre-operative planning for stereotactic neurosurgical procedures. LITT is a novel therapy and given the potential neuropsychological benefits with comparable seizure freedom rates it is likely to be a viable alternative to hippocampal resection in the near future, as it spares temporal neocortex, requires a shorter hospital stay, reduced risk of complications and quicker recovery. As more neurosurgical units adopt this technology it is vital that prior experience from high volume centres is integrated within the decision making and pre-operative planning process to minimise the learning effect on patients.

The use of machine learning in this context has allowed quantification of hitherto unidentified trajectory parameter combinations to be determined. When used with CAP this allows contemporary research findings to be applied systematically and objectively across all centres. A prospective clinical trial implementing these machine learning parameters is required to determine if this translates into improved seizure-free outcomes and reduced neuropsychological morbidity.

7 Multicentre validation of automated trajectories for selective laser amygdalohippocampectomy. Based on (Vakharia et al., 2019a)

7.1 **Abstract**

7.1.1 Objective

Laser interstitial thermal therapy (LITT) is a novel minimally invasive alternative to open mesial temporal resection in drug-resistant mesial temporal lobe epilepsy (MTLE). The safety and efficacy of the procedure are dependent on the pre-planned trajectory and the extent of the planned ablation achieved. Ablation of the mesial hippocampal head has been suggested to be an independent predictor of seizure freedom, whilst sparing of collateral structures is thought to result in improved neuropsychological outcomes. We aim to validate an automated trajectory planning platform against manually planned trajectories to objectively standardize the process.

7.1.2 Methods

Using the EpiNav™ platform we compare automated trajectory planning parameters derived from expert opinion and machine learning to undertake a multicentre validation against manually planned and implemented trajectories in 95 patients with MTLE. We estimate ablation volumes of regions of interest and quantify the size of the avascular corridor through the use of a risk score as a marker of safety. We also undertake blinded external expert feasibility and preference ratings.

7.1.3 Results

Automated trajectory planning employs complex algorithms to maximize ablation of the mesial hippocampal head and amygdala, whilst sparing the parahippocampal gyrus. Automated trajectories resulted in significantly lower calculated risk scores and greater amygdala ablation percentage, whilst overall hippocampal ablation percentage did not differ significantly. Estimated damage to collateral structures was also reduced. Blinded external expert raters were significantly more likely to prefer automated to manually planned trajectories.

7.1.4 Conclusion

Retrospective studies of automated trajectory planning show much promise in improving safety parameters and ablation volumes during LITT for MTLE. Multi-centre validation provides evidence that the algorithm is robust and blinded external expert ratings indicate that the trajectories are clinically feasible. Prospective validation studies are now required to determine if automated trajectories translate into improved seizure freedom rates and reduced neuropsychological deficits.

7.2 **Introduction**

Building from the work presented in Chapters 5 and 6 we have demonstrated improved trajectory metrics including risk score, trajectory length and greater estimated ablation volumes of the AHC over manually planned trajectories using EpiNav™ CAP. We next applied a machine learning approach to optimise the LITT trajectory parameters that resulted in a further increase in the estimated ablation of the AHC by ~10% whilst sparing ablation of the parahippocampal gyrus (PHG)(Li et al., 2019a). This revealed that optimal entry points cluster around the temporo-occipital junction and optimal target points are at the anterior medial aspect of the amygdala. It is unclear, however, if these machine learnt trajectories are generalizable to external surgeons with varied planning practices.

In this study, we perform a multicentre validation of automated trajectories derived from both expert-derived (see Chapter 5) and machine learnt parameters (see Chapter 6) and compare these to expert manually planned trajectories for MTLE LITT. Comparators include trajectory metrics, estimated ablation volumes, and external blinded feasibility ratings.

7.3 **Methods:**

The manuscript was prepared in accordance with the STROBE statement(Elm et al., 2007).

7.3.1 Patient inclusion

Ninety-five patients from three high volume epilepsy surgery services (Thomas Jefferson University Hospital n = 25, Harbor View Medical Center n = 48 and Columbia University Medical Center n = 22) were included in this multi-centre validation study following a prospective power calculation (see 2.f.iii). Each centre has an extensive series and established expertise in using LITT to MTLE. Consecutive patients were included if they had received LITT for MTLE and either had concordant semiology, scalp EEG and imaging features or had onset confirmed within the hippocampus following SEEG investigation. Ethical approval for the study was provided by institutional review board approval at each of the collaborating institutions for the retrospective use of anonymized imaging: (Thomas Jefferson University Hospital: #15D.106, Harbor View Medical Center: #STUDY0006292, Columbia University Medical Center: #AAAS3264.)

7.3.2 Manual trajectory generation

Implemented laser catheter trajectories were determined from the post-operative MRI scans from three different LITT centres. Post-operative T1 MR images, taken intra-operatively immediately after the final ablation, were registered to the pre-operative MRI scans within EpiNav™ using a rigid transformation(Modat et al., 2014) and manually checked to ensure accurate registration. In cases where rigid registration failed, due to an insufficient field of view, a landmark registration using the anterior and posterior commissures was applied. Implemented (manually planned) trajectories were then reconstructed by manual selection of the entry and target points on the post-operative T1 MRI scans. Manual Trajectories were denoted as Trajectory 1.

7.3.3 Automated trajectory generation

Computer-assisted planning for automated generation of LITT trajectories using EpiNav™ was performed prior to the assessment of the manually implemented trajectory and has been previously described. For a more in-depth description of the CAP algorithm see (Li et al., 2019a; Vakharia et al., 2018d). In brief, a pre-operative T1 image is used to generate a patient-specific whole-brain parcellation(Cardoso et al., 2015a) and pseudoCT(Burgos et al., 2014) using Geodesic information flows (GIF). The corresponding whole-brain parcellation is then used to derive models of the cerebral cortex, inferior occipital gyrus, lateral ventricles, sulci, brainstem, amygdala, hippocampus, entorhinal cortex, and parahippocampal gyrus (Figure 27).

The lateral ventricle was defined as a no-entry zone, whilst vasculature, brain stem segmentation, and sulcal models were included as critical structures. Minimum distance from critical structures was set at 3 mm. Trajectories were limited to a maximum length of 120 mm, to prevent excess parenchymal transgression, and a drilling angle orthogonal to the skull of <30 degrees to prevent skiving at the bone during drilling(Vakharia et al., 2018d). Minimum distance to the brainstem and LGN was set to 7.5 mm for all automated trajectories to prevent excess heat transmission.

In this study, we compare clinical feasibility and estimated ablation volumes for three automated trajectories based on our previous work. The first was constrained to entry through the inferior occipital gyrus targeting the centroid of the amygdala (denoted as Trajectory 2). This represents the benchmark parameter for automated planning and most closely replicates

manual planning(Wu et al., 2015). The second incorporates the trajectory parameters derived from expert consensus(Vakharia et al., 2018d) and incorporates an entry point through the inferior occipital gyrus targeting a 3 mm anterior, medial and inferior translation of the centroid of the amygdala (denoted as Trajectory 3). Finally, the third trajectory employs trajectory parameters derived from machine learning(Li et al., 2019a). These include an entry point at the temporo-occipital junction, targeting a 3 mm anterior and medial translation of the centroid of the amygdala without an inferior translation (denoted as Trajectory 4).

Figure 27: Automated Model Generation For Multi-center LITT Validation

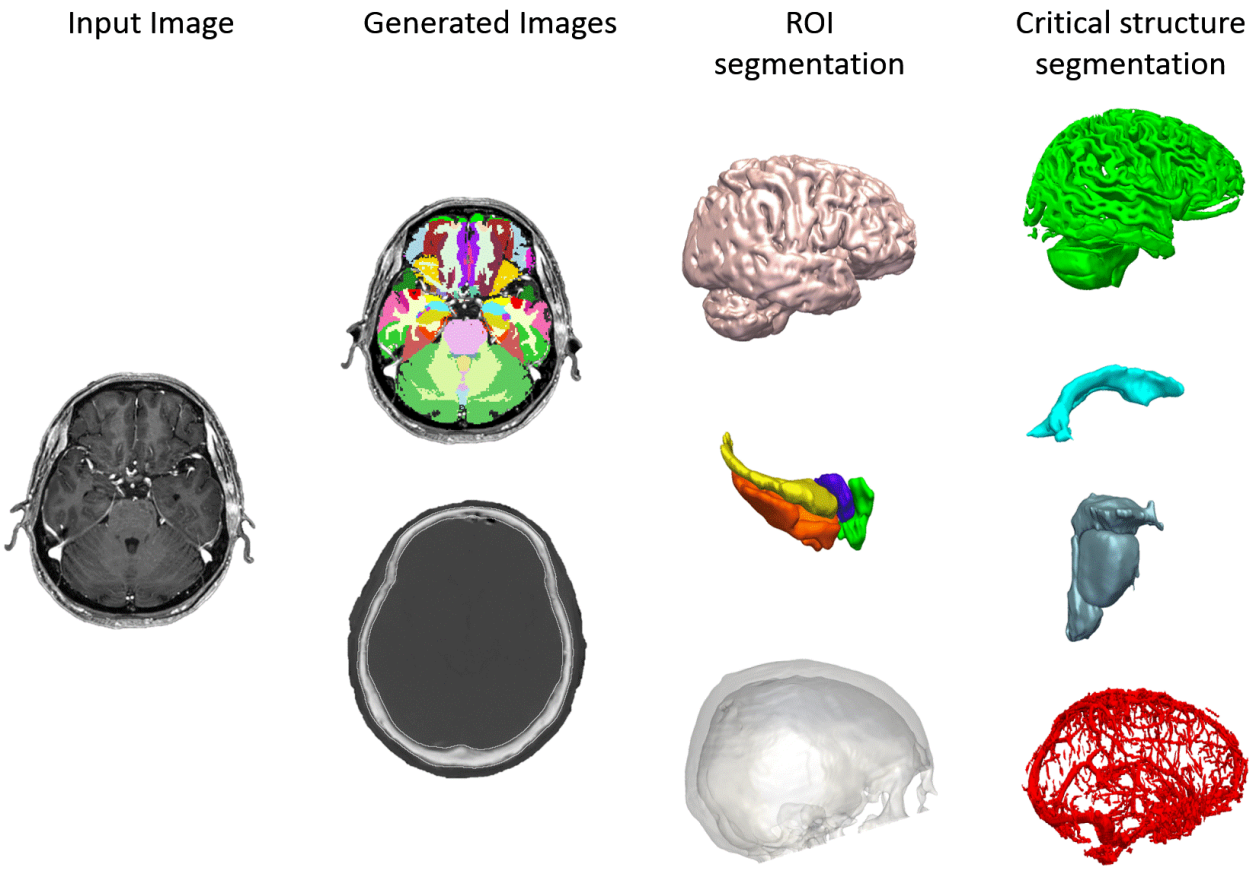

Figure 27 Legend: Summary of model generation. Input image consists of a single volumetric Gadolinium enhanced T1 image from which a whole brain parcellation and pseudo-CT image are generated. Regions of interest segmented from the GIF parcellation include the cortical surface, hippocampus (yellow), amygdala (purple), parahippocampal gyrus (orange) and entorhinal cortex (green). Skull model segmented from the pseudo-CT. Critical structures segmented from GIF parcellation include sulci, lateral ventricles, and brainstem. Vascular segmentation from Gadolinium enhanced T1 image following application of a Sato filter(Zuluaga et al., 2015).

7.3.4 Trajectory parameter analysis

For each of the 4 corresponding trajectories (one manual and three automated) per patient, the calculated trajectory parameters were calculated and returned in an automated fashion. Calculation of the risk score has been described previously(Sparks et al., 2017a) and provides a numerical representation for the size of the avascular corridor. In brief, the risk score is calculated by assigning 128 nodes along the trajectory and measuring the distance from vasculature at each of the indices. The same number of nodes are assigned regardless of the trajectory length to preven longer trajectories from accruing greater risk scores. The risk score is then normalized to provide a score of >1 if the trajectory to vessel distance was less than the user-defined safety margin (3 mm in this case). A uniform 5-15 mm diameter ablation zone(Vakharia et al., 2018d) (see Figure 28) was then applied to each trajectory and the volume of overlap with the amygdala, hippocampus, entorhinal cortex, and parahippocampal gyrus, as determined from the brain parcellation, was automatically calculated in each case. The estimated ablation volumes were normalized by the pre-operative volume to provide the percentage of ablation for each structure.

7.3.5 Expert ratings

Three expert neurosurgeons were selected as blinded raters. Each was provided with four trajectories from 23 randomly selected patients (92 trajectory ratings in total). To assess interrater variability the first 16 randomly selected patients were sent to all raters and the remainder were uniquely assigned. Raters were blinded to the trajectory generation method and were asked to rate the feasibility of the entry, trajectory and target points of the four laser trajectories. Feasibility criteria were based on whether the expert raters would be willing to

implant the trajectory as part of their current surgical practice. Raters were also asked to rank the blinded trajectories in order of preference from 1-4, with 1 being the most and 4 the least preferred.

7.3.6 Statistical Analysis

Trajectory parameters for the four trajectories per patient were analyzed using an ANOVA with post-hoc pair-wise comparisons and Bonferroni correction for multiple comparisons.

Expert ratings between three independent neurosurgeons were assessed using a mixed effects logistic regression model estimating the binomial probability distribution of trajectory feasibility (=1) compared to infeasibility (=0). Cohen's Kappa statistic for pairwise assessments between the expert raters was also performed. Analysis of expert preference was performed using Pearson's χ^2 and an ordinal logistic regression model. Statistical analysis was performed using SPSS 25 (IBM Corp., Armonk, N.Y., USA) and Stata Statistical Software: Release 15 (College Station, TX: StataCorp LLC).

A prospective sample size calculation was performed to determine the number of patients to sample to be able to detect a reduction in risk score of at least 0.2 units using a two-sample t-test with a significance level of 1% and a power of 90%. In performing this calculation, it was assumed that the standard deviation of risk score is 0.25 (estimates derived from pilot data and previous work). In total, 92 patients would need to be recruited to achieve this. This sample size would also allow detection of at least 10% difference in ablation volumes at a power of 0.9 given a 0.14 standard deviation.

Figure 28: Method For Reconstructing And Modelling Ablation Volumes Of Manually Planned And Implemented Laser Trajectories

A *B* *C*

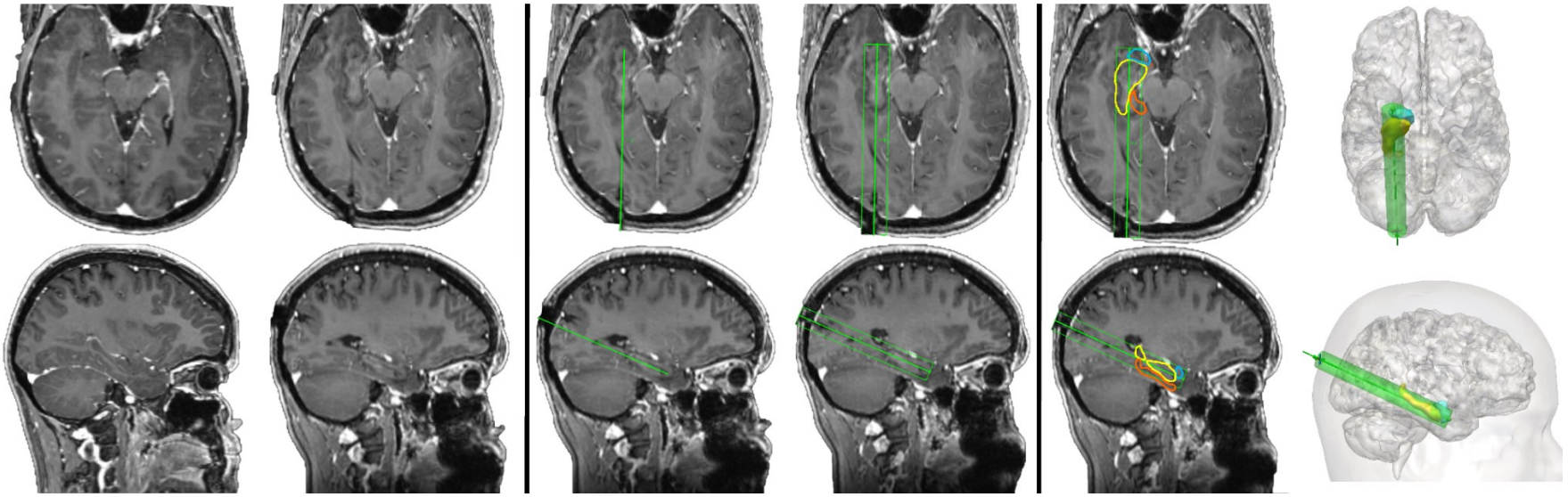

Figure 28 Legend: a) Axial and sagittal images of pre- (left) and post-LITT ablation (right) in the same patient. b) Manual trajectory recreated from post-LITT ablation (left) and with estimated 15 mm diameter uniform ablation cavity applied (right). c) Overlap of estimated ablation cavity with regions of interest (amygdala: blue, hippocampus: yellow and parahippocampal gyrus: orange) used to calculate ablation volume and also shown on the 3D model (right). Note: Parahippocampal gyrus not shown on the 3D models for clarity.

7.4 **Results**

7.4.1 Trajectory metrics

Mean trajectory parameters for the 4 calculated trajectories (one manual and three automated) are shown inTable 20. A one-way analysis of variance (ANOVA) model suggested a significant difference in the mean planned trajectory length, drilling angle to bone and risk score ($p<0.0001$). Post-hoc analysis with Bonferroni correction (see Figure 31) revealed manually planned trajectories had significantly longer trajectory lengths and greater risk scores compared to the automated trajectories (1 vs 2-4). Drilling angle to the skull was significantly less (i.e. more orthogonal to the bone) with trajectories 1-3 compared to trajectory 4.

Table 20: Comparison of Trajectory Metrics Between Generation Methods

	1 (Manual)	2 (Automated-Centroid of amygdala)	3 (Automated-Antero-inferior mesial amygdala)	4 (Automated-Antero-mesial amygdala)	Statistical significance (ANOVA model)
Length (mm)	103.6±10.0	93.5±8.4	95.8±8.2	89.0±7.4	p<0.000*
Angle (deg)	29.3±6.5	28.8±6.8	28.9±6.2	31.8±6.0	p=0.003*
Risk score	1.3±0.1	1.1±0.2	1.1±0.2	1.1±0.2	p<0.000*
Brainstem distance (mm)	7.3±2.4	6.7±2.3	6.5±2.1	7.0±2.1	P=0.053

* denoted statistical significance following correction for multiple comparisons

7.4.2 Ablation volumes

A one-way ANOVA revealed a significant difference in the mean ablation length, total ablation volume, amygdala ablation (%), hippocampal ablation (%), entorhinal cortex ablation (%), and parahippocampal gyrus ablation (%) (Table 21) between trajectories. Post-hoc analysis with Bonferroni correction (Table 22) revealed manual trajectories had a significantly shorter ablation length (mm) compared to the automated trajectories (1 vs 3; 1 vs 4). Manual trajectories also had a significantly greater total ablation volume (1 vs 2; 1 vs 4) but achieved a significantly smaller percent ablation of the amygdala (1 vs 3; 1vs 4) and hippocampus (1 vs 4). Finally, manual trajectories resulted in a significantly greater percent ablation of the entorhinal cortex (1 vs 2; 1 vs 3; 1 vs 4) and parahippocampal gyrus (1 vs 2; 1 vs 4).

Table 21: Comparison of estimated ablation volumes between the different trajectory generation methods:

	1 (Manual)	2 (Automated-Centroid of amygdala)	3 (Automated-Antero-inferior mesial amygdala)	4 (Automated-Antero-mesial amygdala)	Statistical significance (ANOVA model)
Ablation Length (mm)	24.9±11.0	27.1±6.9	30.4±6.8	28.6±7.7	p<0.000*
Ablation volume (mm^3)	3535.7±1021.4	3021.1±906.3	3630.4±830.9	3203.9±998.6	p<0.000*
Amygdala ablation (%)	45.3±22.2	44.5±16.2	58.7±14.0	64.2±20	p<0.000*
Hippocampal ablation %)	67.3±16.3	65.2±14.5	67.9±12.8	61.6±13.8	p<0.012*
Entorhinal cortex ablation (%)	17.8±18.0	2.1±4.4	7.2±8.1	8.7±7.7	p<0.000*
Parahippocampal ablation (%)	25.1±17.9	17.1±14.00	28.3±17.8	11.0±11.6	p=0.000*

* denoted statistical significance following correction for multiple comparisons

Table 22: Post-hoc analysis of trajectory metrics with Bonferroni correction applied

		1	2	3	4
Length (mm)	1	-	p<0.000	p<0.000	p<0.000
	2	p<0.000	-	p=0.367	p=0.003
	3	p<0.000	p=0.367	-	p<0.000
	4	p<0.000	p=0.003	p<0.000	-
Angle (deg)	1	-	p=1	p=1	p=0.047
	2	p=1	-	p=1	p=0.009
	3	p=1	p=1	-	p=0.010
	4	p=0.047	p=0.009	p=0.010	-
Risk score	1	-	p<0.000	p<0.000	p<0.000
	2	p<0.000	-	p=1	p=0.670
	3	p<0.000	p=1	-	p=0.280
	4	p<0.000	p=0.670	p=0.280	-
Ablation length (mm)	1	-	p=0.410	p<0.000	p<0.013
	2	p=0.410	-	p=0.039	p=1
	3	p<0.000	p=0.039	-	0.874
	4	p<0.013	p=1	p=0.874	-
	1	-	p=0.001	p=1	p=0.094

Ablation Volume (mm^3)	2	p=0.001	-	p=0.000	p=1
	3	p=1	p<0.000	-	p=0.012
	4	p=0.094	p=1	p=0.012	-

7.4.3 Feasibility ratings

Mixed-effects logistic regression models (see Table 23) were applied to subjects, with a random effect to account for clustering of trajectories within patients, in whom ratings were provided by all three raters and revealed a significant difference between trajectory generation methods, despite correction for the significant difference between raters (test statistic = 59.61, 2 d.f., $p<0.01$). Overall, automated trajectories 2-4 were significantly more likely to be rated as feasible by external raters (test statistic = 24.21, 3 d.f., $p<0.01$), despite the manual trajectories having been stereotactically implanted in all patients.

Table 23: Mixed Effects Logistic Regression Model of Trajectory Feasibility Ratings (1-4) from Raters (A-C):

Variable	Odds Ratio Estimate	95% Confidence Interval
Trajectory 1 (reference group)	1	N/A
Trajectory 2	2.46	(1.47, 4.13)
Trajectory 3	3.08	(1.83, 5.17)
Trajectory 4	2.89	(1.72, 4.85)
Rater A (reference group)	1	N/A
Rater B	3.53	(2.25, 5.53)
Rater C	5.21	(3.30, 8.23)

**Note, odds refers to the odds of a trajectory being rated feasible.*

Comparison of ordinal rater preferences between trajectory generation methods revealed 'fair' agreement(Landis et al., 1977) between all raters with a Cohen's Kappa statistic of 0.333 (rater 1 vs rater 2), 0.235 (rater 1 vs rater 3) and 0.333 (rater 2 vs rater 3). Pearson's χ^2 analysis revealed a significant difference ($p<0.001$) between the observed and expected distribution of expert preference ratings between trajectory generation methods. Ordinal logistic regression was then performed to examine if there was any difference between trajectory preference ratings after accounting for raters. This revealed the manual trajectories (method 1) had the greatest probability of being assigned the lowest rater preference i.e. preference 4. (Table 24 and Figure 29)

Figure 29: Rater Preference Ranking By Method

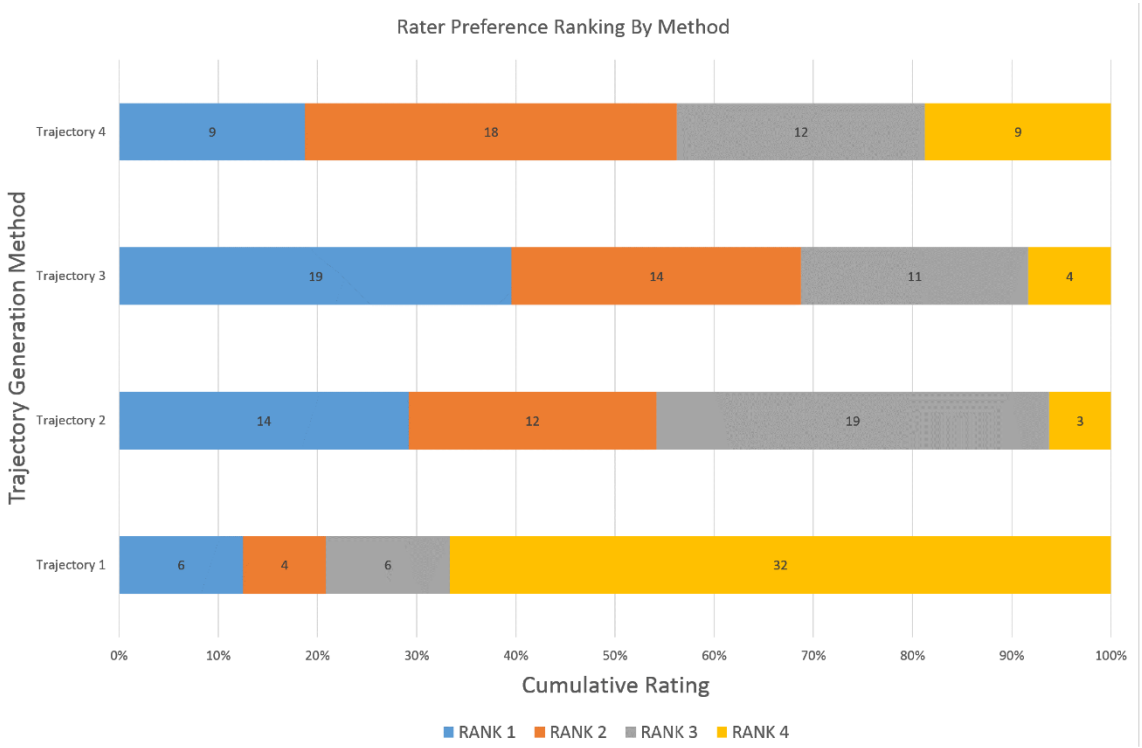

Figure 29 Legend: Summary of blinded expert rater preferences (Rank 1-4) by trajectory generation method (1-4). Trajectory 1 (manually planned) was significantly more like to be ranked 4th (least favourable) compared to trajectories 2-4 (automated).

Table 24: Estimated frequency of rater preferences and estimated probabilities by trajectory generation method, from the fitted ordinal logistic regression model:

Trajectory	Rater preference Count (Estimated probability*)				Total
	1	2	3	4	
1	6 (0.04)	4 (0.09)	6 (0.25)	32 (0.62)	48
2	14 (0.30)	12 (0.29)	19 (0.26)	3 (0.14)	48
3	19 (0.40)	14 (0.29)	11 (0.21)	4 (0.21)	48
4	9 (0.24)	18 (0.28)	12 (0.30)	9 (0.30)	48
Total	48	48	48	48	

*Estimated probabilities of rank for each method as predicted by the ordinal logistic regression model.

7.5 **Discussion**

7.5.1 Key results

LITT trajectory planning requires optimization of a number of complex parameters including trajectory metrics for safety and ROI ablation for seizure freedom and neuropsychological outcome(Donos et al., 2018; Drane et al., 2015; Gross et al., 2018; Kang et al., 2016). We present a multicentre validation of different automatically generated stereotactic trajectories using the EpiNav™ platform and compare these to manually planned (implemented) trajectories from three different institutions. We also provide trajectory feasibility ratings from 3 external blinded experts. We find that automated trajectories are significantly shorter and have improved risk scores. We also show that automated trajectories have increased ablation length and amygdala ablation (%) with decreased parahippocampal gyrus ablation (%). External

blinded experts were significantly more likely to prefer and rate automated trajectories (2-4) as feasible.

7.5.2 Summary of LITT studies to date

Single-centre case series report LITT for MTLE is a safe and effective first-line alternative to open temporal lobe surgery in cases of mesial temporal sclerosis or where mesial temporal seizure onset has been proven by SEEG(Donos et al., 2018; Gross et al., 2018; Jermakowicz et al., 2017b; Kang et al., 2016; Petito et al., 2018; Tao et al., 2017; Youngerman et al., 2018). A recent meta-analysis of LITT for MTLE has suggested an overall seizure freedom rate of 50% at 12-36 months rising to 62% when considering 'lesional' cases only(Grewal et al., 2019). Despite a slightly lower seizure freedom rate compared to open surgery, the minimally invasive nature of the procedure and superior patient satisfaction makes LITT an attractive first-line alternative. To date, there have not been any randomized comparisons of LITT to open surgery, but a prospective parallel group study has shown superior post-operative object recognition and naming following LITT(Drane et al., 2015). The focal nature of the ablation and lack of damage to the surrounding critical structures and temporal neocortex have been suggested as possible reasons for this. The FLARE (ClinicalTrials.gov Identifier: NCT02820740) and SLATE trials (ClinicalTrials.gov Identifier: NCT02844465) are two open-labelled prospective studies from Monteris Medical and Medtronic Inc., respectively, that are currently on-going. As with any novel technology, there is an associated learning curve and it is possible, therefore, that early case series may both underestimate the therapeutic potential of LITT and overestimate the risks.

Despite the promise of LITT as an alternative first-line therapy, a single case series has reported an overall complication rate of 22.4%(Pruitt et al., 2017), including catheter misplacement, intracranial haemorrhage, device malfunction, hemiparesis, cranial neuropathy, and visual field deficits(Gross et al., 2018; Jermakowicz et al., 2017a; Pruitt et al., 2017; Vakharia et al., 2018d; Waseem et al., 2017). Intracranial haemorrhage may be due to catheter misplacement resulting in an unplanned conflict with a vessel, inability to visualize small vessels on radiographic images, or due to planning trajectories through corridors that are not avascular. To this end, we calculate 'risk score' as a mathematical representation of the size of the avascular corridor for the entire planned trajectory. Due to the complexity of the calculation, it is not possible for the surgeon to calculate this during manual planning and as such they must depend on their experience to estimate this. Intraventricular haemorrhage was described in one

of three cases of LITT for MTLE in the series by Pruitt et al(Pruitt et al., 2017). Trajectories passing through the ventricles are therefore avoided where possible due to the risk of intraventricular haemorrhage, CSF leak, and potential heat sink effect.

Visual field deficits (VFD) are the most common complication associated with LITT for MTLE and include contralateral superior quadrantanopia and hemianopia(Gross et al., 2018). Superior quadrantanopias result from ablation cavities extending posterior to the hippocampus into the optic radiation postero-laterally within the sagittal striatum(Gross et al., 2018), whilst homonymous hemianopia may result from heat transfer to the lateral geniculate nucleus (LGN) during posterior hippocampal ablation(Jermakowicz et al., 2017a). EpiNav™ generated trajectories run inferior to the lateral ventricle and therefore prevent excessive heat transfer to the sagittal striatum (lateral to the body of the hippocampus) so are less likely to result in superior quadrantanopia secondary to optic radiation injury. The ambient cistern and choroidal fissure separate the body of the hippocampus from the ventral diencephalon (superiorly) and brainstem (medially), respectively. Patients at most risk of heat transfer to the LGN and therefore homonymous hemianopia have been identified as those with low choroidal fissure CSF volume. EpiNav™ maximizes distance from the brainstem, based on a user-specified parameter, in order to prevent thermal injury. The LGN is included within the brainstem segmentation and represents the most lateral aspect. Through maximizing the distance from the brainstem EpiNav automatically maximizes distance from the LGN (see Figure 30).

Transient cranial neuropathies (Oculomotor and Trochlear nerves) have been reported and are thought to result from heat transfer medially at the tentorium during ablation of the mesial hippocampal head and entorhinal cortex(Gross et al., 2018; Vakharia et al., 2018d). We have previously shown that EpiNav™ generated trajectories maximize ablation of the mesial hippocampal head(Vakharia et al., 2018d), as this has also been suggested to be an independent predictor of postoperative seizure freedom(Jermakowicz et al., 2017b). Extra care will, therefore, be required when implementing EpiNav™ generated trajectories as these patients may be at a theoretically higher risk of this complication.

Figure 30: Example Computer-assisted planning Trajectory and Proximity to Collateral Structures

a)

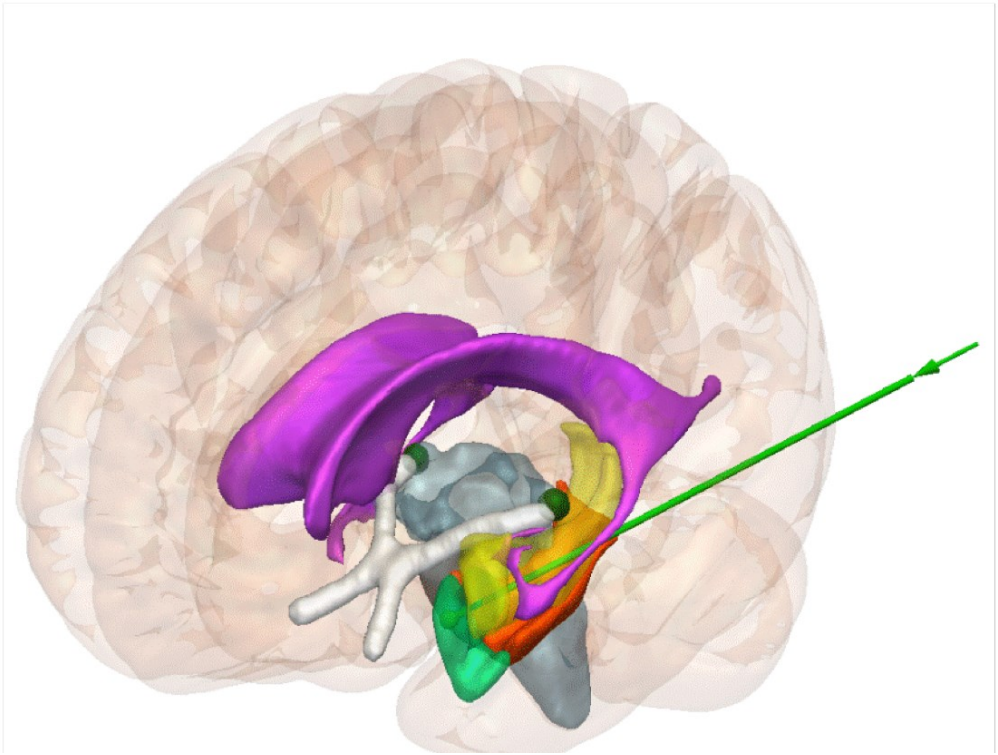

b)

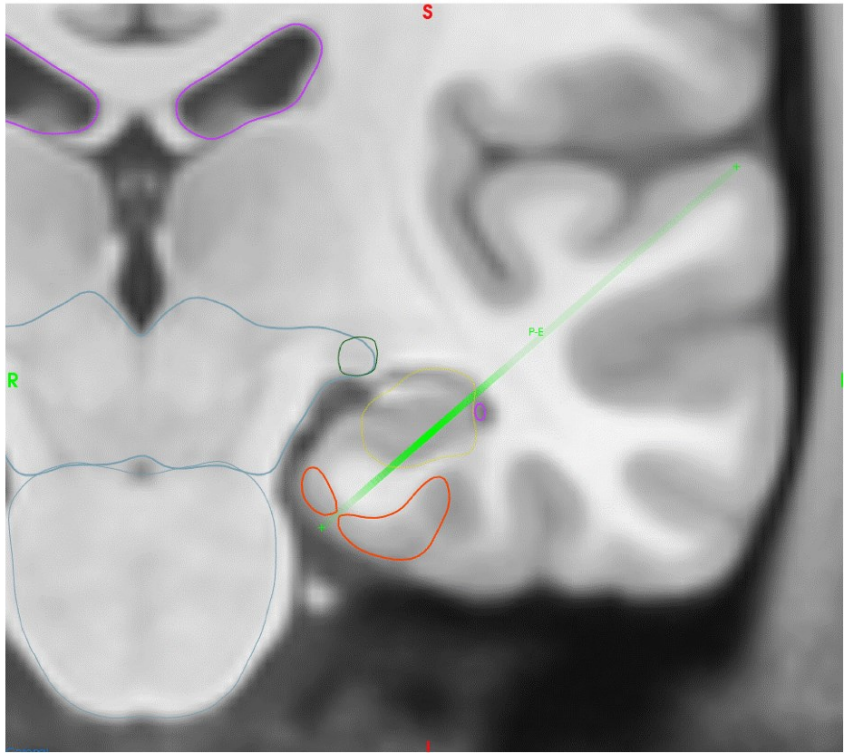

Figure 30 Legend: Template-based a) 3D model and b) coronal MRI of an automated left sided LITT trajectory (light green) at the level of the LGN (dark green) showing its incorporation within the brainstem segmentation (blue). Entire LITT trajectory overlaid on to 2D coronal slice with intra-hippocampal (opaque green) and extra-hippocampal (transparent green) portions. Position of trajectory at the level of LGN. Amygdalohippocampal complex (yellow), lateral ventricles (pink), parahippocampal gyrus (orange), entorhinal cortex (teal) and optic tract (white) also shown.

7.5.3 Ablation parameters

The extent of mesial hippocampal head ablation has been shown to correlate with seizure-free outcome in a single centre case series(Jermakowicz et al., 2017b), but this finding has not been replicated in larger series. This suggests a complex correlation that may be affected by other, as yet undefined, ablation parameters as well as patient selection. Furthermore, the total ablation volume of the hippocampal ablation does not correlate with seizure freedom rate, despite correction for pre-operative anatomical volume(Donos et al., 2018; Gross et al., 2018; Vakharia et al., 2018d). The extent of hippocampal resection in the open surgical literature has also failed to show a significant correlation with seizure freedom rates in MTLE(Schramm et al., 2011a). We hypothesize therefore that there is a critical volume of amygdala and hippocampal ablation or resection that encompasses the seizure onset zone resulting in seizure freedom. Given that this is likely to be patient specific and no study has been able to estimate this, the EpiNav™ algorithm maximizes ablation of the hippocampal head and body, whilst sparing the tail, which is vital for the preservation of episodic memory(Bonelli et al., 2013) (Figure 31). EpiNav™ (trajectories 3 and 4) resulted in a significantly greater ablation of the amygdala compared to manually planned trajectories, with significantly improved risk scores (trajectories 2, 3 and 4) and only a small reduction in hippocampal ablation (trajectory 4). The parahippocampal gyrus ablation was also significantly reduced (trajectory 2 and 4), which has been suggested to be essential for preserving neuropsychological function(Aminoff et al., 2013; Drane, 2017; Zola-Morgan et al., 1989, 1994).

Figure 31: Comparison of Manual and Computer-assisted Planning Trajectories in a Single Patient

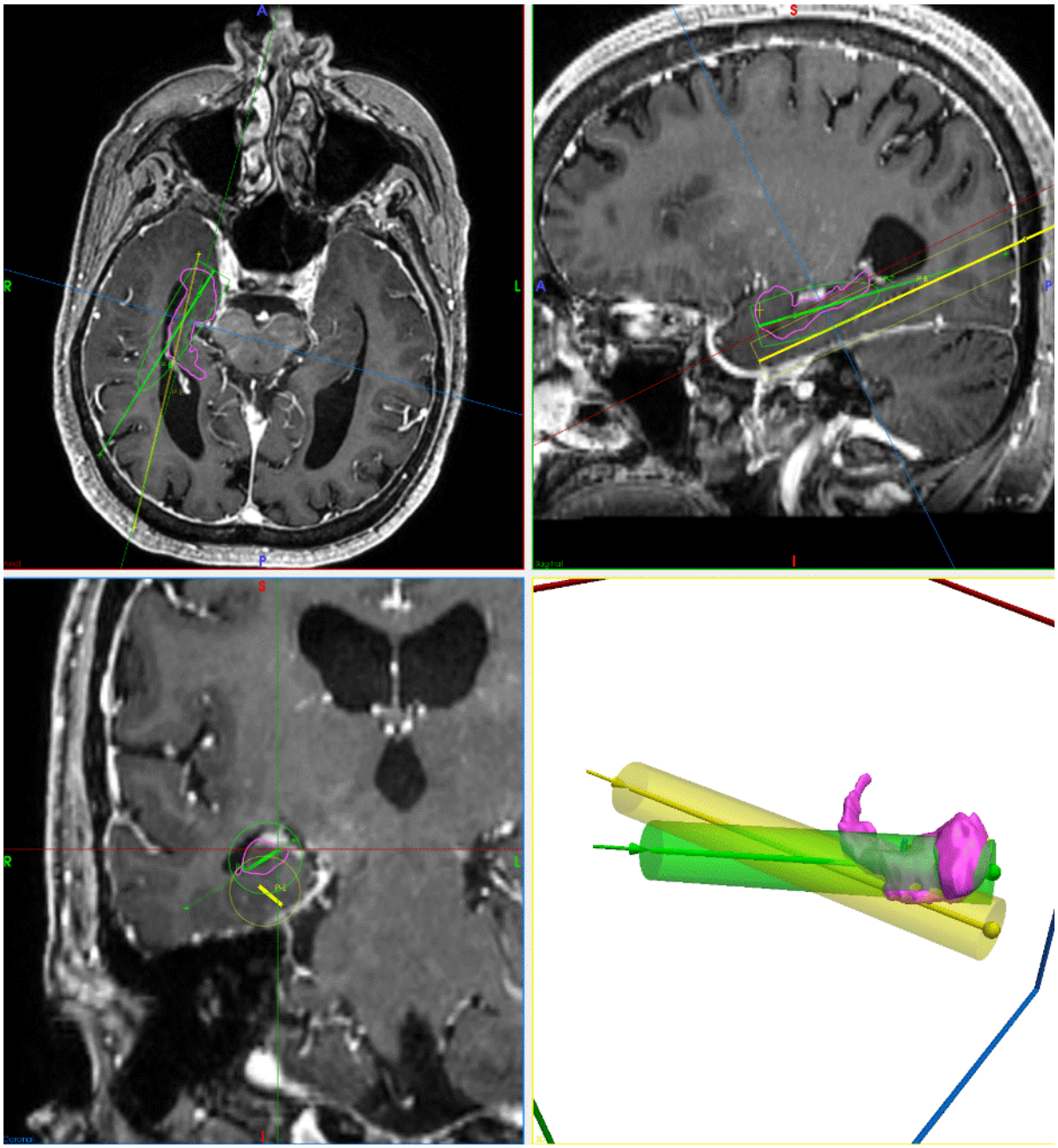

Figure 31 Legend: Orthogonal planes and a 3D model showing an example of trajectory 1 (manual: yellow) and trajectory 4 (automated: green) superimposed on the pre-operative T1 image, with estimated ablation zones (15 mm diameter cylinders) and amygdalohippocampal complex (pink). The more lateral entry point of the automated trajectory allows more medial target points without significantly reducing the brainstem distance. The more medial target

points also allow greater ablation of the amygdala and mesial hippocampal head with reduced posterior hippocampal ablation. The more superior target points result in significantly less parahippocampal gyrus ablation.

7.5.4 External Expert Feasibility Ratings

We undertook a multicentre retrospective validation of the algorithm to 1) ensure that the algorithm is generalizable across centres, 2) maintains performance with imaging from different institutions and 3) compare the algorithm to a variety of planning practices from different neurosurgeons. External expert raters were blinded to the trajectory generation methods and asked to rate the entry, trajectory, and target feasibility individually. After reviewing the 4 trajectories per patient, the raters then ordered them based on preference according to their current clinical practice. The trajectory parameters, including ablation volumes and risk scores, were not provided to the external experts so as not to bias the ratings. There was significant variation between the ratings provided by the external blinded raters for trajectory feasibility, whilst ordinal ratings between trajectory preference rankings showed fair correlation. Correcting for the difference between surgeons we found automated trajectories were significantly more likely to be rated as preferred compared to manual trajectories. Given that the EpiNav™ platform optimizes trajectory heuristics that are normally considered by neurosurgeons during planning, we hypothesize that this is why automated trajectories were more broadly acceptable. In addition, trajectory 3 was used in our initial comparative study(Vakharia et al., 2018d) and was derived from expert consensus. By comparison, trajectory 4 entry was defined solely through machine learning parameters(Li et al., 2019a). Taking into account the trajectory safety metrics, ablation volume estimations and external expert feasibility ratings, we would advocate providing the surgeon with a choice of trajectories 3 and 4 for use in future prospective validation studies.

7.5.5 Generalisability

As more centres perform LITT for MTLE each will face a learning curve which may result in increased complication rates and poorer seizure-free outcomes until this is overcome. Automated trajectory algorithms optimize planning parameters in an objective and systematic fashion based on user-defined parameters(Vakharia et al., 2018d). The EpiNav™ platform is

based on the current literature to date and therefore benefits from the combined learning curves of multiple centres as well as the incorporation of machine learning parameters(Li et al., 2019a). As further data is acquired the algorithm is adaptable to incorporate and optimized these features continually. Consistent planning strategies across institutions are key to ensuring standardized outcomes and reducing patient morbidity.

7.5.6 Limitations

The main limitation of this work is that it is a retrospective comparison of simulated EpiNav™ automated trajectories to manually planned and implemented trajectories in the same patients. As such we do not have the actual parameters that would be achieved if the automated trajectories were implemented or the seizure freedom and neuropsychological outcomes associated with the automated trajectories. A retrospective analysis based purely on calculated trajectory parameters does, however, allow different trajectories to be modelled and compared in the same patient allowing for direct comparisons between trajectory metrics. In addition, we have previously shown that the estimated ablation volumes accurately reflect that which were achieved following ablation(Vakharia et al., 2018d), which relies on the assumption of a uniform 5-15 mm diameter ablation cavity. A recent study of laser ablation dynamics has also corroborated this to be the case in both the axial and sagittal dimensions of the ablation cavity (see Figure 3 in (Jermakowicz et al., 2018)). We acknowledge that thermal ablation patterns are non-linear and vary significantly between patients, but we are currently unable to model this complexity at an individual patient basis. To prevent systematic bias, comparisons between the manual and automated trajectories were based on the same calculated ablation volumes.

A further limitation is that the automated trajectory generation pipeline within EpiNav™ is based on the use of a whole brain parcellation algorithm. In this study, we used GIF(Cardoso et al., 2015a), but the pipeline can be used with other parcellation methods including Freesurfer (Dale et al., 1999). Given that the whole brain parcellations are developed and typically validated on brain MRI scans from healthy controls, it is likely that they may over-segment regions of atrophy such as the hippocampus in severe mesial temporal sclerosis. To mitigate this the whole brain parcellations were manually checked for accuracy in all cases and the same ROI segmentations were used for all ablation volume comparisons.

Comparison of trajectory feasibility ratings and preference order between the external expert raters showed significant differences and only fair correlation, respectively. Given the

variety in surgical practices associated with LITT trajectory planning, we implemented a mixed effects logistic regression model and have shown that the differences in trajectory feasibility ratings between methods were still significant despite accounting for the differences between the expert raters.

7.6 **Conclusions**

Building on our previous work we provide a large multicentre validation study of 95 patients across 3 neurosurgical centres. This is the largest validation of an automated trajectory planning system to date. We show that the algorithm is robust to different MRI acquisition parameters and all automated trajectories were consistently given higher preference ratings compared to the manual trajectory. These results justify a prospective validation study to determine if the automated trajectory metrics and estimated ablation parameters result in improved safety, seizure freedom rates and reduced neuropsychological morbidity compared to current manual planning. Future work should also aim to integrate diffusion-weighted imaging to consider critical white matter fibre tracts that are important for visual and neuropsychological function. Although not available currently, non-linear estimations of the expected ablation cavity would also enhance this work.

We propose that there is now sufficient evidence to warrant a prospective study of optimized LITT trajectories, that maximises ablation of the amygdalo-hippocampal complex, whilst sparing the adjacent neocortex and white matter projections of the optic radiation and inferior fronto-occipital fasciculus.

8 Automated trajectory planning for anterior two-thirds laser Corpus Callosotomy: A feasibility study with probabilistic tractography validation. Based on (Vakharia et al., 2020)

8.1 **Abstract**

8.1.1 Objective

Anterior two-thirds corpus callosotomy is an effective palliative neurosurgical procedure for drug-refractory epilepsy that is most commonly used to treat drop-attacks. Laser interstitial thermal therapy is a novel stereotactic ablative technique that has been utilised as a minimally invasive alternative to resective and disconnective open neurosurgery. Case series have reported success in performing laser anterior two-thirds corpus callosotomy. Computer-assisted planning algorithms may help to automate and optimise multi-trajectory planning for this procedure. We aim to undertake a simulation-based feasibility study of computer-assisted corpus callosotomy planning in comparison with expert manual plans in the same patients.

8.1.2 Methods

Ten patients were selected from a prospectively maintained database. Patients had previously undergone diffusion-weighted imaging and digital subtraction angiography as part of routine SEEG care. Computer-assisted planning was performed using the EpiNav™ platform and compared to manually planned trajectories from two independent blinded experts. Estimated ablation cavities were used in conjunction with probabilistic tractography to simulate the expected extent of interhemispheric disconnection.

8.1.3 Results

Computer-assisted planning resulted in significantly improved trajectory safety metrics (risk score and minimum distance to vasculature) compared to blinded external expert manual plans. Probabilistic tractography revealed residual interhemispheric connectivity in 1/10 cases following computer-assisted planning compared to 4/10 and 2/10 cases with manual planning.

8.1.4 Conclusion

Computer-assisted planning successfully generates multi-trajectory plans capable of LITT anterior two-thirds corpus callosotomy. Computer-assisted planning may provide a means of standardising trajectory planning and serves as a potential new tool for optimising trajectories.

A prospective validation study is now required to determine if this translates into improved patient outcomes.

8.2 **Introduction**

Open corpus callosotomy was first described by van Wagenen and Herren in 1940 to prevent "*the disordered wave of nerve impulses… spreading widely to other parts of the neopallial portion of the brain*"(VAN WAGENEN et al., 1940). In modern epilepsy surgery, corpus callosotomy is performed as a palliative procedure for drug-refractory focal epilepsy associated with tonic, atonic or tonic-clonic seizures where the seizure onset zone appears multifocal or generalized and resection or ablation is not possible(Vakharia et al., 2018a). Atonic 'drop attacks' are commonly associated with Lennox-Gestaut syndrome and similar epilepsy-related encephalopathies(Asadi-Pooya et al., 2008). A less invasive and reversible alternative to corpus callosotomy is vagal nerve stimulation (VNS). A meta-analysis comparing corpus callosotomy with VNS found corpus callosotomy to be significantly more effective that VNS in reducing atonic seizure frequency in patients with Lennox-Gestaut syndrome(Lancman et al., 2013), but due to the less invasive nature VNS is more commonly undertaken first(Englot et al., 2017). Less common indications for corpus callosotomy include treatment for refractory recurrent status epilepticus, refractory complex partial seizures with rapid secondary generalisation of presumed frontal lobe onset and no obvious focus, refractory generalized tonic-clonic and refractory absence seizures(Asadi-Pooya et al., 2008).

Minimally invasive approaches to anterior two-thirds corpus callosotomy have been described utilising stereotactic radiosurgery(Pendl et al., 1999) and laser interstitial thermal therapy (LITT)(Ho et al., 2016; Lehner et al., 2018; Palma et al., 2018; Pruitt et al., 2017). We aimed to develop a computer-assisted planning algorithm to optimise the interhemispheric disconnection and associated safety metrics for LITT anterior two-thirds corpus callosotomy. As part of a feasibility study, we compare computer-assisted planning derived trajectories with blinded expert manual plans in the same patients and quantify the extent of disconnection using fibre tractography. This is carried out to establish the feasibility of the approach in epilepsy patients without gross structural abnormalities and not necessarily those who are candidates for corpus callosotomy.

8.3 **Methods**

8.3.1 Patient Inclusion

LITT corpus callosotomy trajectory planning was performed on 10 patients (6 male) selected from a prospectively maintained database. Computer-assisted planning was

undertaken prior to manual planning by two external blinded experts (YB and JTW).Selection criteria included having undergone bilateral digital subtraction angiography (DSA), as part of their routine SEEG care, and pre-operative diffusion-weighted imaging. All patients had previously undergone SEEG implantation at the National Hospital for Neurology and Neurosurgery between 2017 and 2019.

8.3.2 Ethical Approval

This study was approved by the Research Ethics Committee London, reference: 12/LO/0377. Written consent was obtained from all patients prior to inclusion in the study.

8.3.3 Image requirements

The automated pipeline included a 1mm isotropic 3D-T1 magnetization-prepared rapid acquisition with gradient echo (MPRAGE) (TE/TR/TI 3.1/7.4/400 ms, field of view (FOV) 224 × 256 × 256 mm, matrix 224 × 256 × 256), gadolinium-enhanced T1 SPGR (T1+Gad) and digital subtraction angiography (DSA) images. A whole brain parcellation and pseudoCT image were generated from the T1 MPRAGE sequence using GIF (Burgos et al., 2014; Cardoso et al., 2015b). Models of the cortex, lateral ventricles, non-dominant superior frontal gyrus, dominant superior frontal gyrus, dominant middle frontal gyrus non-dominant superior parietal lobule and non-dominant angular gyrus were automatically segmented from the GIF parcellation (see Figure 32).

Figure 32: Derivation of models from source imaging

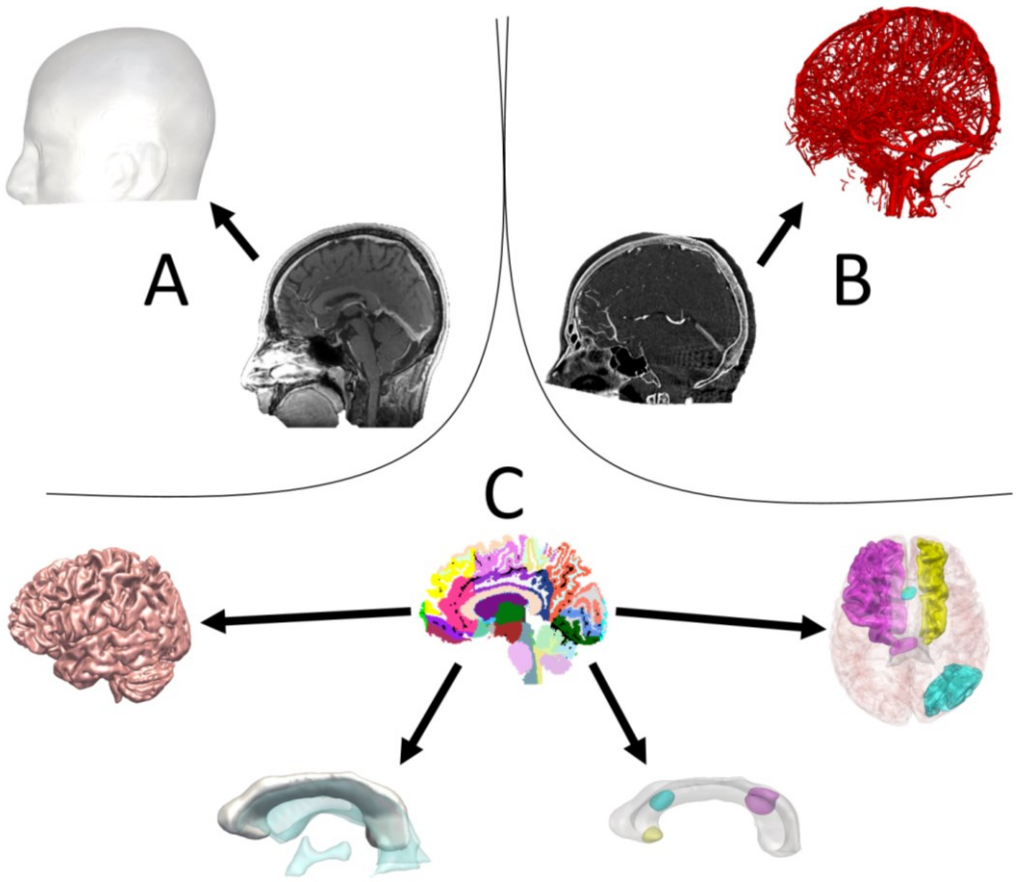

Figure 32 Legend: A) Scalp model generated from the T1 image through thresholding. B) Vascular segmentation and skull model (not shown) generated from raw digital subtraction angiography acquisition. C) Cortex, corpus callosum, ventricular system, anterior, middle and posterior target points and corresponding entry regions generated from GIF parcellation.

8.3.4 Computer-assisted planning trajectories

Computer-assisted planning was performed using the EpiNav™ platform as described in Chapters 2-7 (Sparks et al., 2016, 2017a; Vakharia et al., 2018e; Zombori et al., 2014) with trajectory entry and target points as well as default parameters determined from pilot data and expert consensus (see Table 25). The trajectory planning algorithm was set to undertake the ablation using 3 unique LITT trajectories. The trajectories consisted of (1) a non-dominant frontal trajectory targeting the rostrum of the corpus callosum, (2) a non-dominant parietal trajectory targeting the genu of the corpus callosum and (3) a dominant frontal lobe trajectory targeting the posterior body of the corpus callosum. As is conventional for anterior two-third corpus callosotomy the splenium was spared. Target points were generated in an automated fashion from the GIF parcellation through a series of morphometric dilations and Boolean operations. In brief, the corpus callosum and subcallosal, anterior, middle and posterior cingulate cortices were segmented from the GIF parcellation. The subcallosal gyrus, anterior, middle and posterior cingulate cortices were then dilated by 7 mm and regions of overlap were then selected to create 3 regions of interest. The resulting regions were then constrained to their overlap with the corpus callosum to generate the anterior, middle and posterior target regions (see Figure 33).

Due to patient-specific anatomical and vascular variability, restricting trajectories to a single gyral entry region could lead to the algorithm finding a local optima and not the global optima within the feasible search regions. To overcome this phenomenon 5 trajectories were initially planned and returned to the user as part of the automated algorithm in all patients. The user (in this case author VNV) then reviewed and selected the most feasible dominant frontal trajectory (between superior and middle frontal gyrus entry points) and non-dominant parietal trajectory (between superior parietal lobule and angular gyrus entry points) to be used in conjunction with the non-dominant frontal trajectory.

EpiNav™ optimises a number of different parameters that are considered by the neurosurgeon during trajectory planning. These include the intracerebral trajectory length, drilling angle to the skull, the proportion of the catheter within the corpus callosum, minimum distance from vasculature and size of the avascular corridor, expressed as a risk score. The risk score is a normalised score of the cumulative distance from vasculature for the trajectory at 128 nodes equally placed along the trajectory. A score of <1 signifies that the trajectory is >3 mm from vasculature along its entire course.

Table 25: LITT Callosotomy default parameters:

Trajectory No.	Entry ROI	Target ROI	Max Length*	Max Angle
1	Right Superior Frontal Gyrus	Anterior Target	60	15
2	Right Superior Parietal Lobule	Middle Target	110	35
3	Right Angular Gyrus	Middle Target	110	35
4	Right Superior Frontal Gyrus	Posterior Target	90	35
5	Right Middle frontal Gyrus	Posterior Target	90	35

*Where length is measured from skull surface overlying entry ROI to target ROI.

Figure 33: Derivation of target points from GIF parcellation

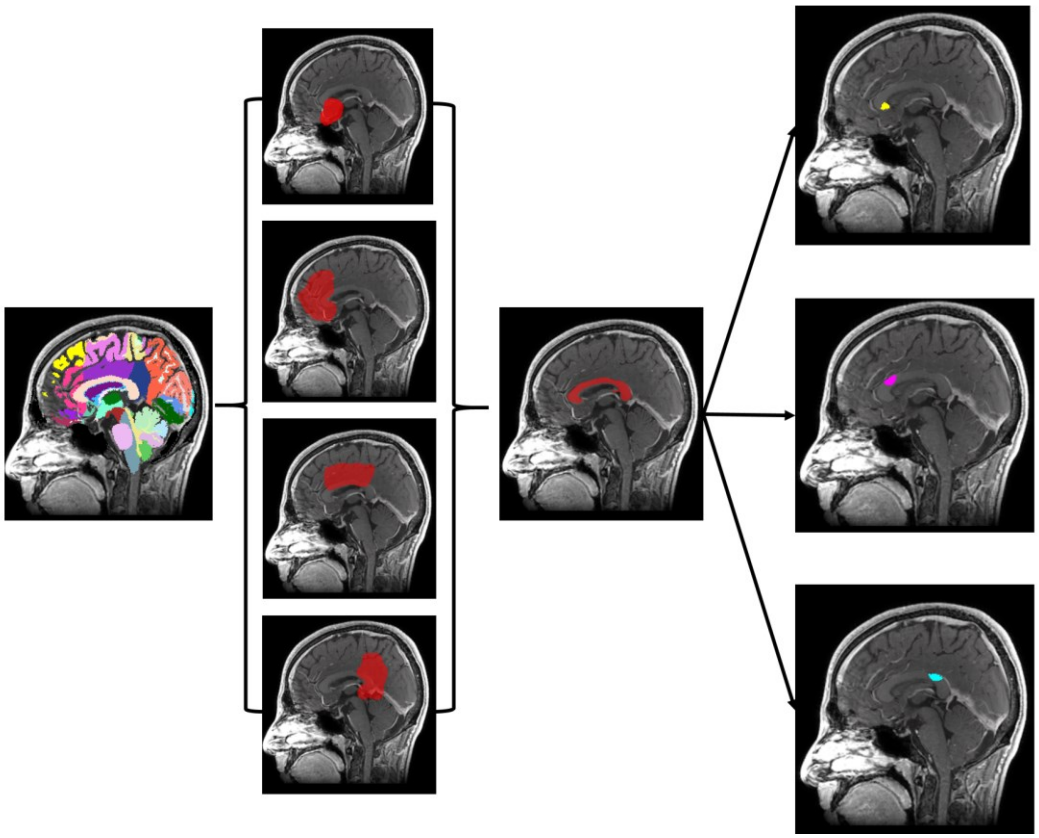

Figure 33 Legend: The patient-specific GIF parcellation was used to segment and dilate the subcallosal, anterior, middle and posterior cingulate gyri by 7 mm. The regions of overlap between the dilated models e.g. subcallosal gyrus and anterior cingulum overlap, were then overlapped with the corpus callosum resulting in 3 unique target points at the rostrum, genu and posterior body of the corpus callosum.

8.3.5 Vascular segmentation

Digital subtraction angiography was acquired as part of the routine care prior to performing SEEG at the study institution. This was performed through a femoral puncture in an interventional radiology suit equipped with biplane fluoroscopy. Bilateral internal carotid artery injections were performed in all patients and exported as bone-stripped and bone-retained images. The bone-retained images were used for rigid registration to the T1+Gad reference image whilst vessel segmentation was performed on the bone-stripped image utilising a vessel extraction algorithm and thresholding. The parameters of transformation obtained from the

registration of the bone-retained images were then applied to the 3D vascular models. Registrations were checked manually for accuracy.

8.3.6 Manual planning

Manual planning was performed by two blinded external neurosurgeon (YB and JTW) with expertise in LITT for corpus callosotomy on all ten of the T1+Gad images. Entry and target points were manually selected by the neurosurgeon based on their current clinical practice using EpiNav. The neurosurgeons were blinded to the pre-calculated computer-assisted plans. Feasibility of the trajectories was based on the individual neurosurgeon performing the manual planning, or reviewing the computer-assisted plans, and was defined as feasible if the neurosurgeon was willing to implement the trajectory based on their current clinical practice.

8.3.7 Ablation volume generation

Simulated laser ablation cavities for both the computer-assisted and manually generated trajectories were generated based on the number of expected pull-backs of the catheter assuming a conservative ablation diameter estimation of 5-15 mm. The number of pull-backs was calculated by dividing the length of the laser catheter within the corpus callosum segmentation by 7 mm. The simulated ablation cavities relating to all three laser catheters were then saved as regions of interest and used as part of the tractography validation.

8.3.8 Probabilistic Tractography

Diffusion-weighted MRI data were acquired using a single-shot EPI readout with 2 mm isotropic resolution (TE/TR = 74.1/7600 ms) and a total of 115 volumes were scanned using a multi-shell approach (11, 8, 32, and 64 gradient directions at b-values: 0, 300, 700, and 2500 s/mm^2, respectively). A single b=0-image with reverse phase-encoding was also acquired for distortion correction. Diffusion data were corrected for scanner drift(Vos et al., 2017) and eddy current-induced distortions, subject movement and susceptibility-induced distortions using FSL v5.10 eddy and topup tools (Andersson et al., 2003, 2016). Fibre orientation distributions were estimated in each voxel using multi-tissue constrained spherical deconvolution in MRtrix3 (Jeurissen et al., 2014; Smith et al., 2012).

Tractography of right and left hemispheric connectivity was performed using MRtrix3 employing constrained spherical deconvolution estimated fibre orientation distributions and

streamline propagation with the iFOD2 algorithm. Anatomically constrained tractography was applied to prevent biologically implausible streamline generation(Smith et al., 2012) using the tissue segmentation from the GIF parcellation. A seed region of interest was manually drawn on a paramedian sagittal plane at the depth of the cingulate sulcus on the registered T1 image. A corresponding symmetrical inclusion region of interest was drawn at the same location on the contralateral hemisphere. A total of 5000 streamlines were generated for each patient (See Figure 34). Calculated ablation cavities from both the computer-assisted and manually generated trajectories were added as exclusion zones to the tractography in each patient to simulate the change in right and left hemisphere connectivity following LITT corpus callosotomy. Residual hemispheric connectivity were defined as regions of the corpus callosum through which propagated streamlines remained after application of the exclusion masks derived from the simulated ablation cavities. These regions were binarised and converted to 3D meshes for volume measurement.

Figure 34: Derivation of interhemispheric connectivity using fibre tractography

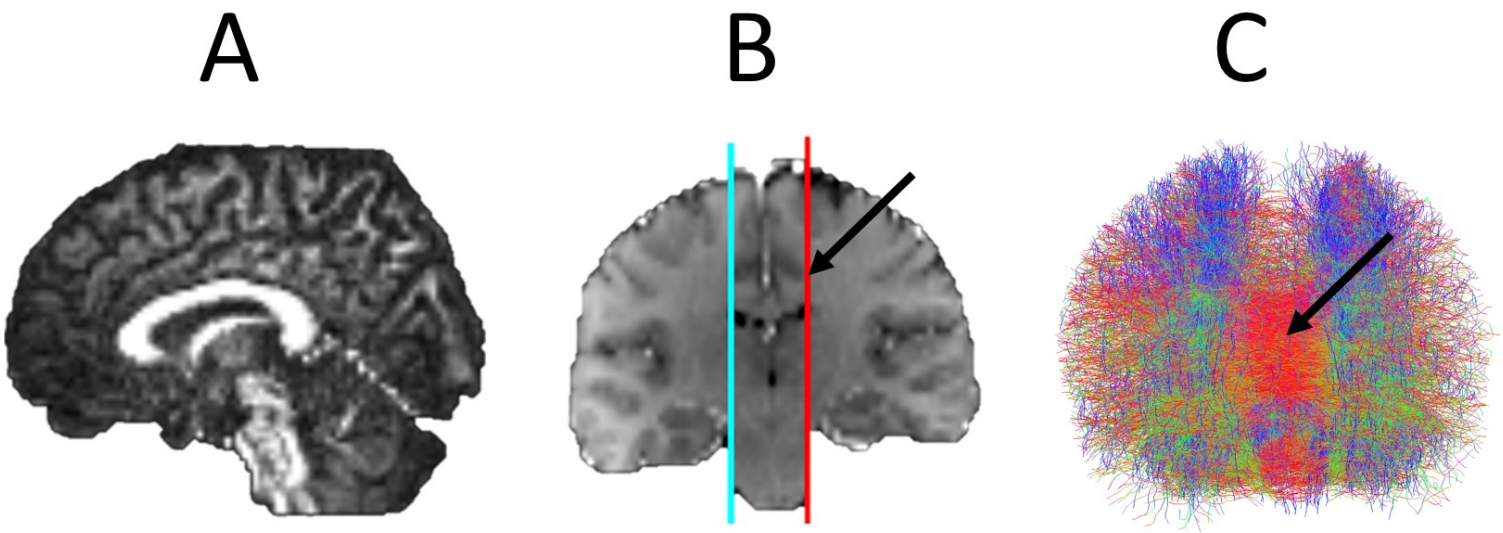

Figure 34 Legend: A) FA image in sagittal place revealing corpus callosum. B) Coronal T1 image registered to FA image with the seed (cyan) and inclusion (red) regions drawn manually on a paramedian sagittal plane at the level of the depth of the cingulate sulcus (arrow). C) Anterior view of resulting tractography consisting of 5000 streamlines with corpus callosum fibres visible in red (arrow).

Figure 35 Trajectory planning, ablation volume generation and tractographic validation.

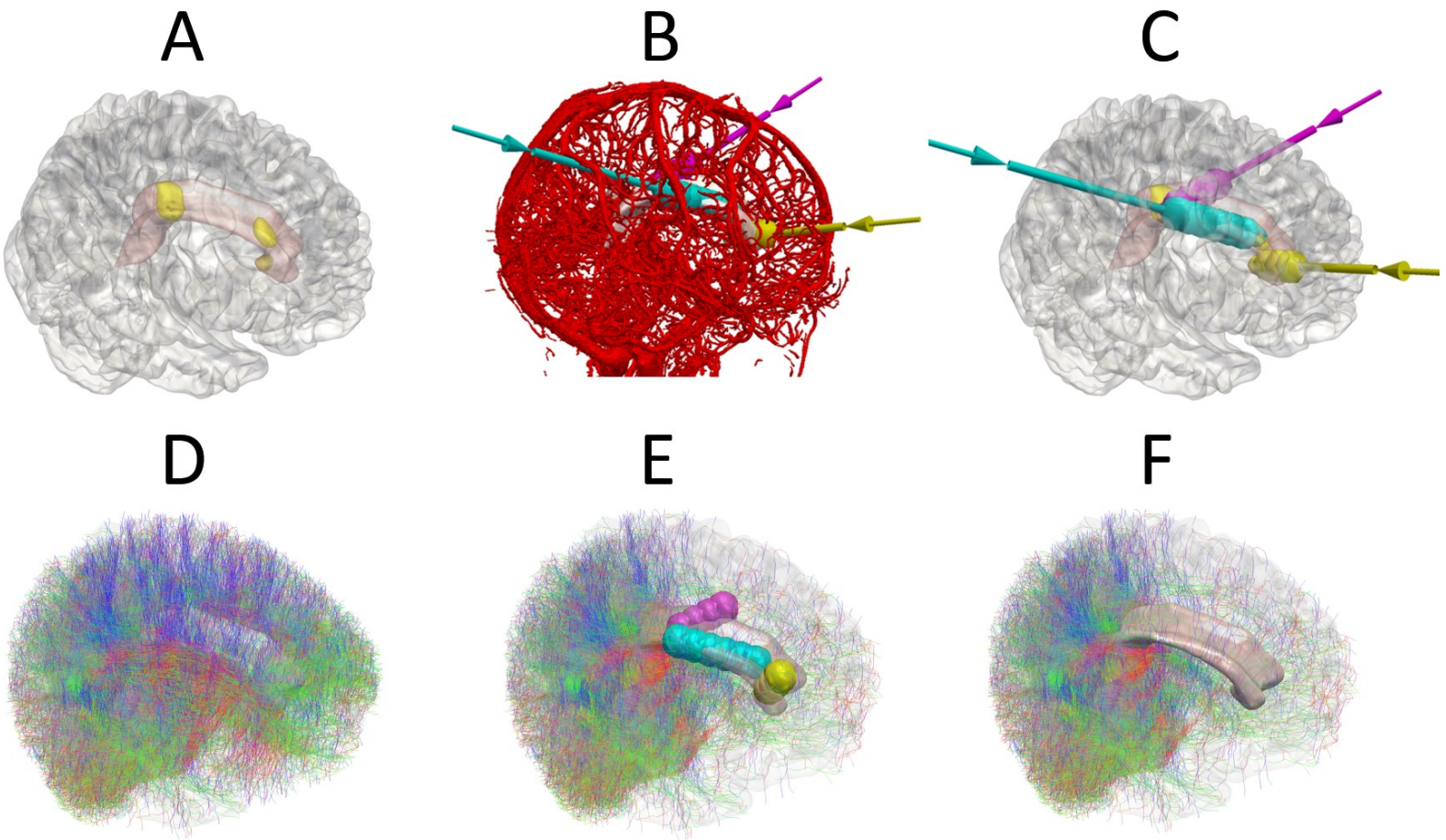

Figure 35 *Legend: Superior and lateral view of A) the right hemisphere (transparent white) with underlying corpus callosum (pink) and computer-assisted planning target points (yellow). B) Result of computer-assisted planning with three trajectories and vascular segmentation. C) Computer-assisted planning trajectories without vascular segmentation revealing the calculated number of ablations and pull-backs required for each trajectory. D) Tractography of right and left hemisphere connectivity. E) Simulated ablations for the trajectories and the corresponding effect on the hemispheric connectivity. F) The corresponding change in hemispheric connectivity shown without the simulated ablations revealing complete disconnection of streamlines passing through the corpus callosum.*

8.3.9 Statistical Analysis

Comparison of trajectory metrics between computer-assisted and manually generated plans from two independent blinded expert neurosurgeons was performed by implementing an ANOVA model and appropriate post-hoc tests with Bonferroni correction. All statistical analyses were performed using SPSS25 (Armonk, NY: IBM Corp.).

8.4 **Results**

8.4.1 Safety metrics

Computer-assisted planning was able to calculate feasible trajectories in all 10 patients. Compared to both of the manually derived trajectory sets the computer-assisted plans returned a statistically significant reduction in the risk score ($p<0.001$) and minimum distance to vasculature (mm) ($p<0.001$) (see Table 26). There was no significant difference between the computer-assisted planning and the manually planned trajectories, or between the two sets of manually planned trajectories, for intracerebral length ($p = 0.213$) and drilling angle to the skull ($p = 0.098$).

Table 26: Comparison of manual and computer-assisted planning trajectory metrics

	Manual Plan 1 Mean±SD	Manual Plan 2 Mean±SD	Computer-assisted plan Mean±SD	p-value
Intracerebral length (mm)	93.6 ±22.7	100 ±26.6	89.7 ±21.9	0.213
Drilling angle to skull (deg)	20.8 ±10.0	23.9 ±14.1	17.5 ±9.3	0.098
Risk score	1.3 ±0.1	1.3 ±0.1	1.1 ±0.1	0.000*
Minimum distance to vasculature (mm)	0.9 ±1.0	0.8 ±0.8	1.9 ±1.2	0.000*

8.4.2 Tractography validation

Based on the simulated ablation cavities, 4 out of 10 patients following manual trajectory planning had residual hemispheric connectivity through the anterior two-thirds of the corpus callosum compared to 1 out of 10 following computer-assisted planning. In all cases, the residual interhemispheric connectivity was at the anterior-most aspect of the genu of the corpus callosum and related to cortical vasculature restricting the non-dominant frontal lobe trajectory from targeting the rostrum. The mean volume of the unablated anterior two-thirds corpus callosum was 0.69 cm^3 compared to an intentionally unablated splenium volume of 3.5 cm^3 and total corpus callosum volume of 15.4 cm^3.

Figure 36: Fibre tractography validation example of computer-assisted and manual planning ablation cavities:

Baseline tractography of interhemispheric structural connectivity

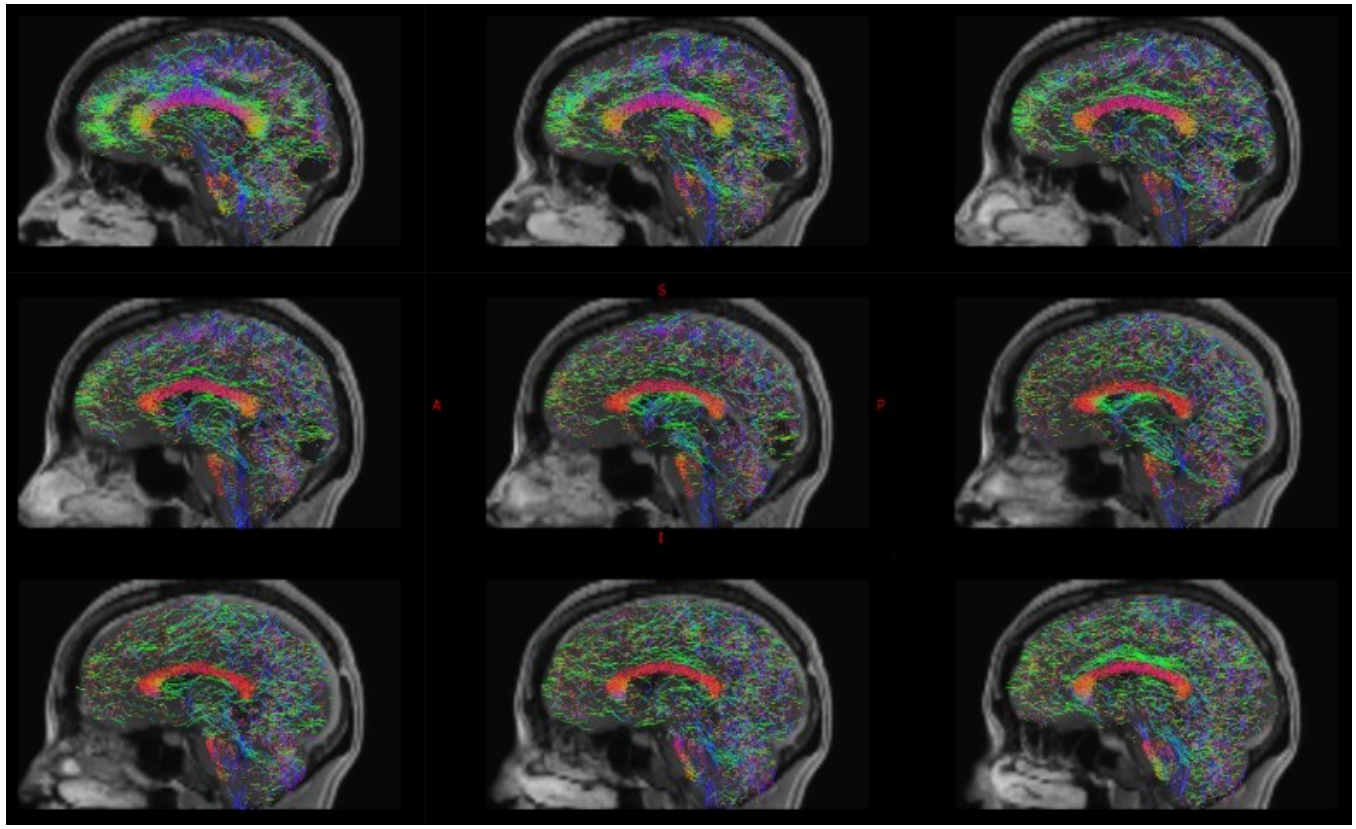

Computer-assisted plan estimated ablation volumes

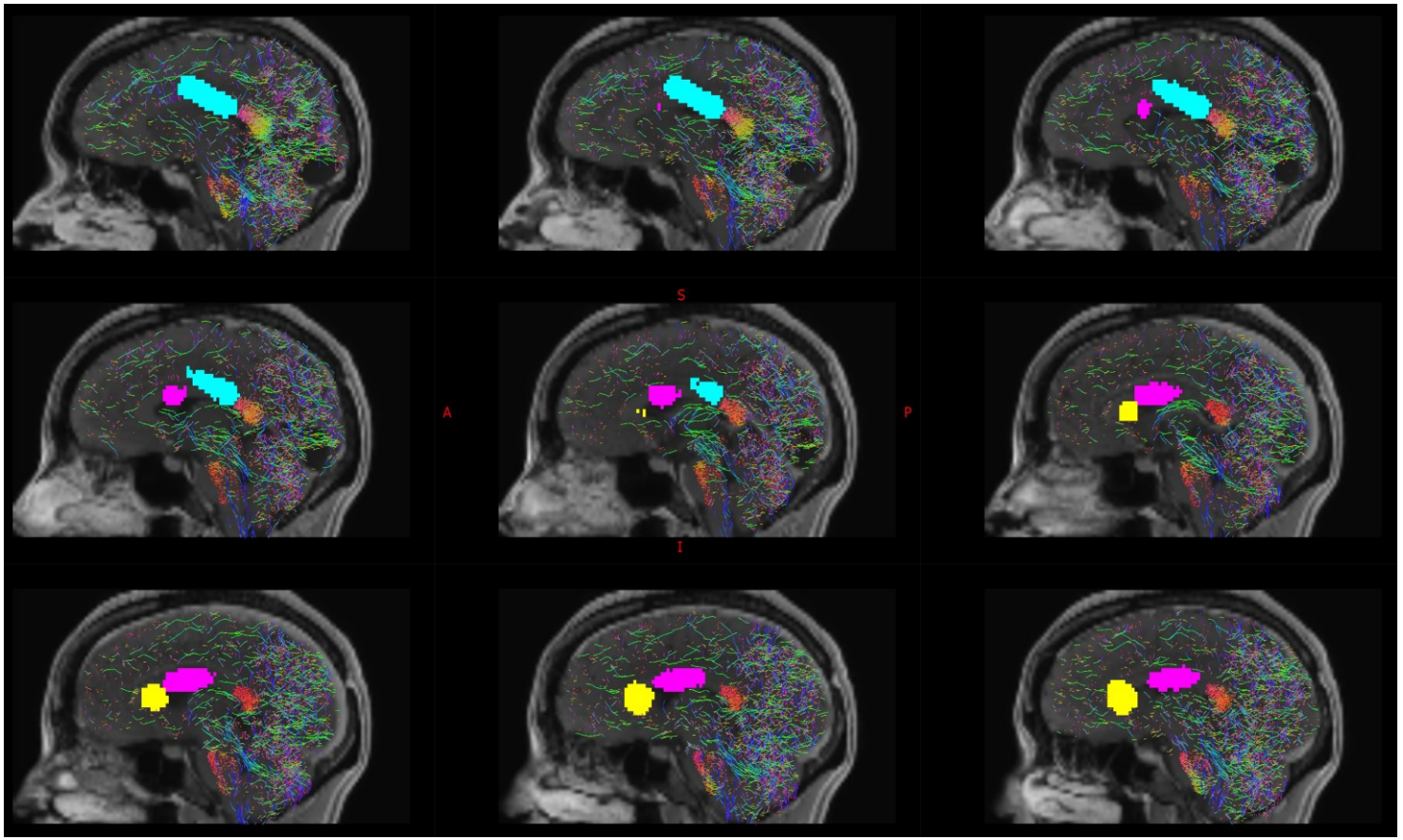

Computer-assisted plan simulated change in structural connectivity

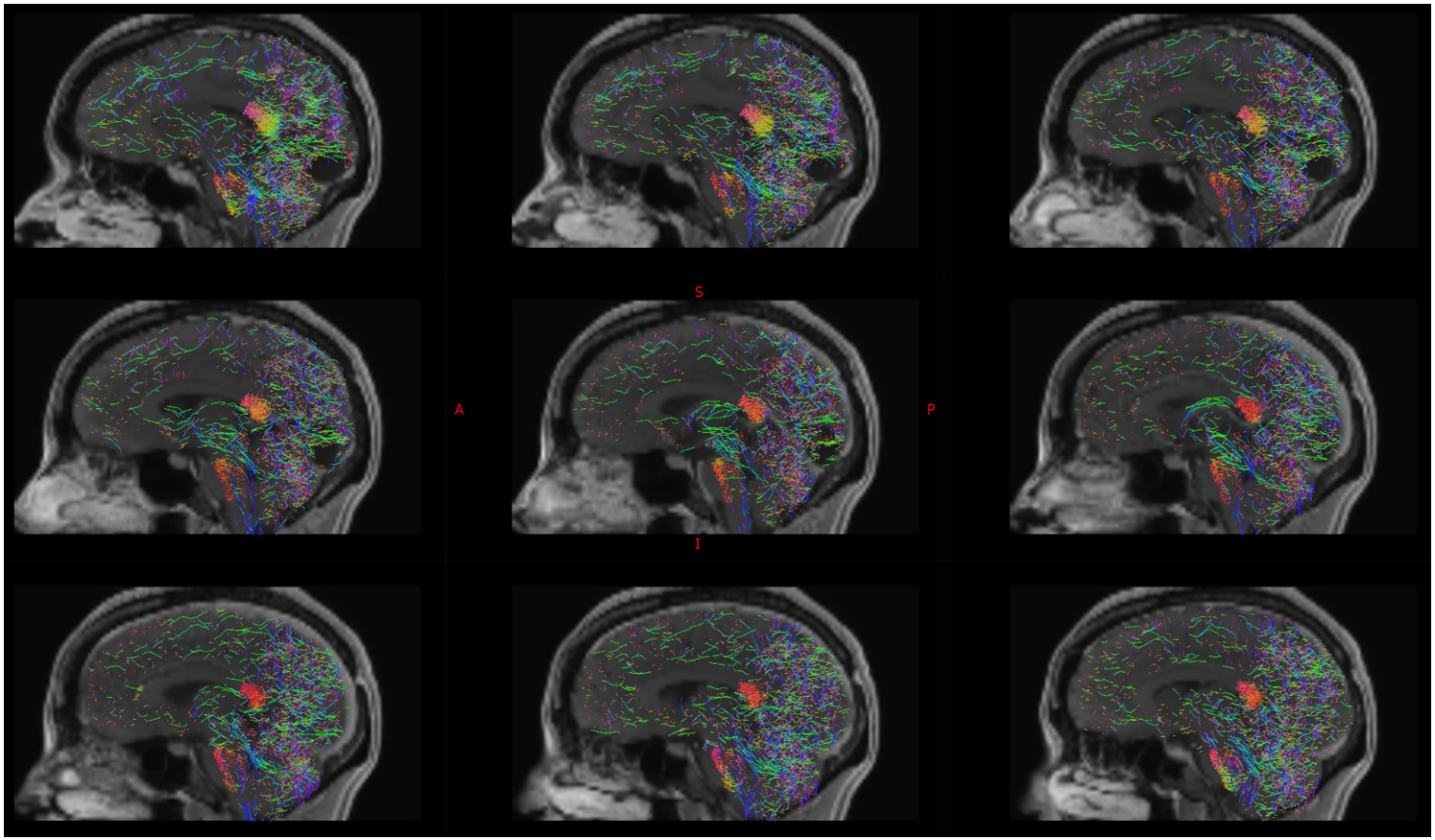

Manual planning estimated ablation volumes

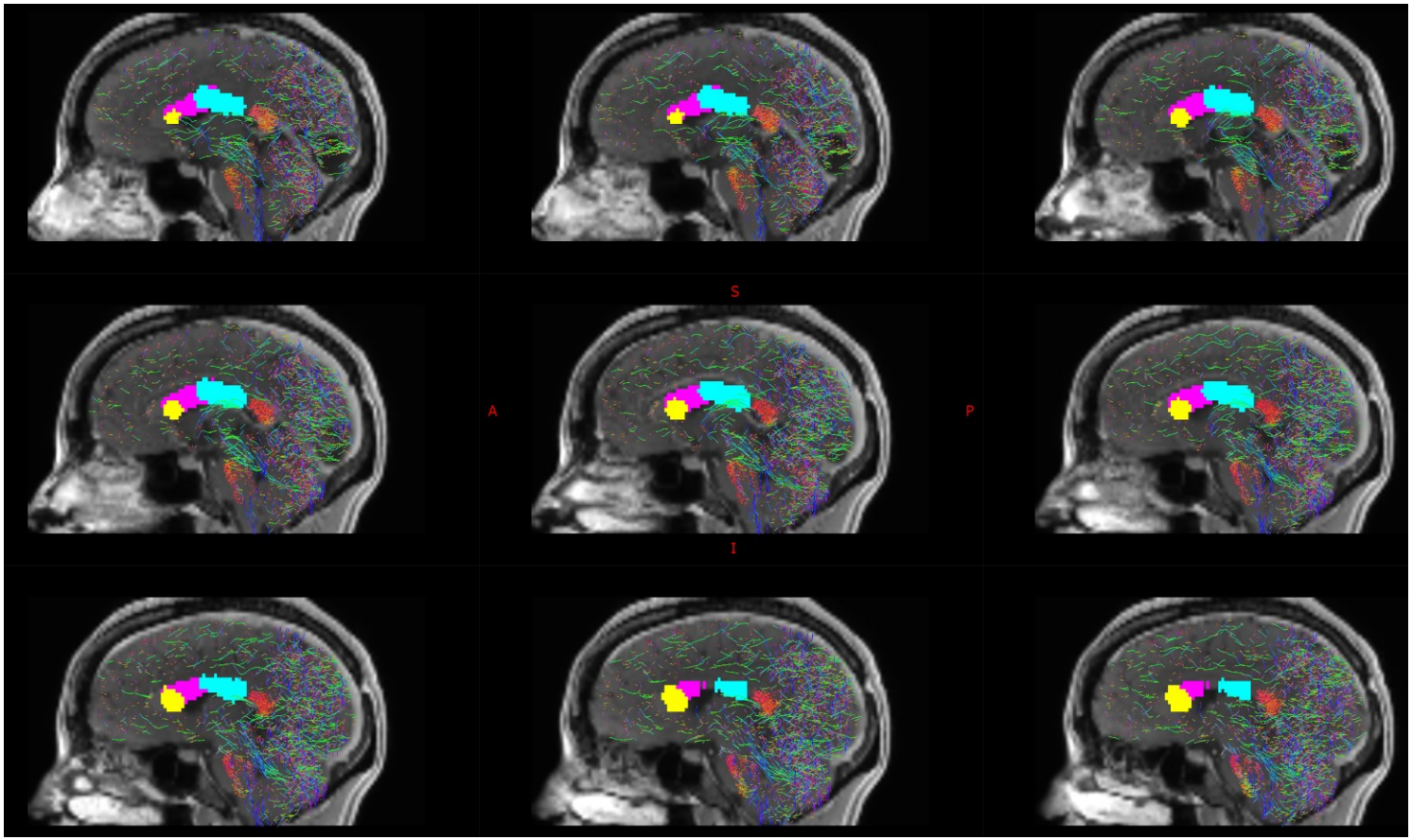

Manual plan simulated change in structural connectivity

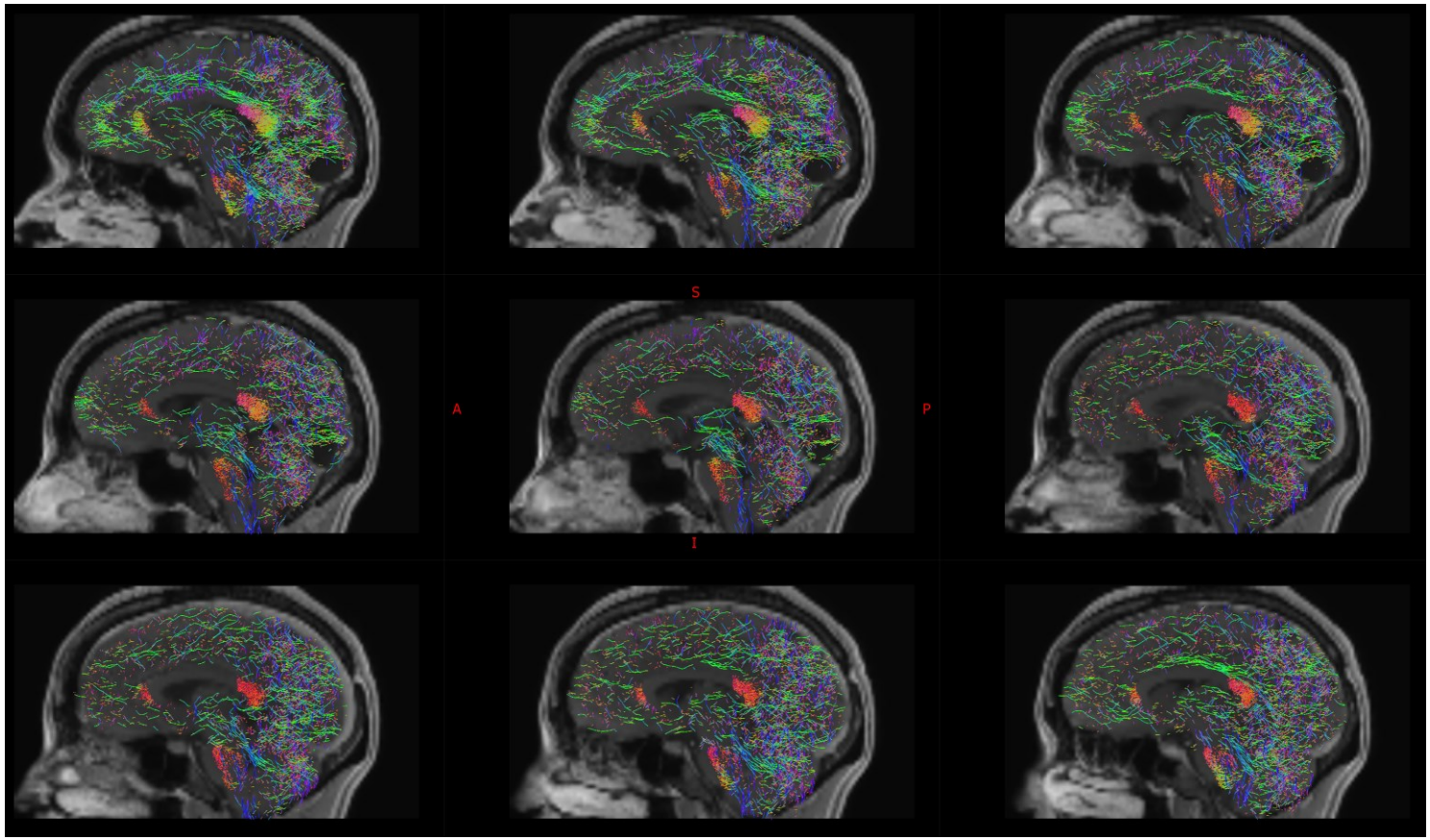

Figure 36 *Legend: Example of residual interhemispheric connectivity identified from probabilistic tractography shown on median and paramedian sagittal planes. Streamline directionality encoded as red: right-left, blue: superior-inferior and green: anterior-posterior. Baseline interhemispheric probabilistic tractography in a single subject (top panel). Corresponding computer-assisted (middle left panel) and manual (middle right panel) plan derived estimated ablation volumes with the non-dominant frontal trajectory to the rostrum of corpus callosum shown in yellow, the non-dominant parietal trajectory to the genu of corpus callosum shown in magenta and the dominant frontal trajectory to the posterior body of the corpus callosum shown in cyan. Simulated effect of computer-assisted (bottom left panel) and manual (bottom right panel) plan estimated ablation cavities on structural interhemispheric connectivity, revealing residual connectivity at the genu of the corpus callosum associated with the manual plan compared to the computer-assisted plan (shown as red streamlines at the genu of the corpus callosum in the bottom right panel).*

8.5 **Discussion**

8.5.1 Key Results:

We show that computer-assisted planning was able to successfully plan feasible trajectories for LITT corpus callosotomy with a significantly improved risk score and minimum distance from vasculature. Employing probabilistic tractography of interhemispheric connectivity and simulated ablation cavities we demonstrate residual interhemispheric connectivity in 4/10 cases following expert 1 and 2/10 cases following expert 2 manual planning compared to 1/10 cases following computer-assisted planning.

8.5.2 Open corpus callosotomy

The corpus callosum is the principal site of interhemispheric connectivity consisting of both myelinated and unmyelinated fibres. Disconnection of interhemispheric connectivity through the anterior two-thirds of the corpus callosum is an effective palliative procedure that is most commonly undertaken for drop attacks and tonic, atonic or tonic-clonic seizure as part of Lennox-Gestaut syndrome(Asadi-Pooya et al., 2008). Pre-operative independent prognostic factors include younger age, drop attacks with associated epilepsy syndrome, MRI negative and IQ > 50. Anatomically the corpus callosum lies within the interhemispheric fissure and is intimately related to the lateral ventricles. It is subdivided into the rostrum, genu, body and splenium. The different anatomical regions of the corpus callosum have been shown to demonstrate a consistent topographic organisation(Fabri et al., 2014). The rostrum of the corpus callosum principally connects the orbitofrontal regions and the genu, also known as the forceps minor, connects the medial and lateral surfaces of the prefrontal cortex. The mid-body of the corpus callosum connects the pre-motor cortices whilst the posterior body connects the motor and sensory cortices. Posterior parietal, temporal and occipital connectivity pass through the anterior, middle and posterior aspects of the splenium respectively. Open anterior two-thirds corpus callosotomy is performed through a bicoronal incision and midline craniotomy to expose the superior sagittal sinus. Interhemispheric dissection is performed with the callosomarginal and pericallosal arteries being identified and preserved. Corpus callosotomy is then performed through microsuction and sharp dissection until the ependyma of the lateral ventricle is encountered(Smyth et al., 2017a). Some centres propose complete corpus callosotomy as an initial one-stage procedure(Smyth et al., 2017b) whilst others have advocated posterior corpus callosotomy alone(Paglioli et al., 2016). In most surgical practices, anterior two-thirds corpus

callosotomy is performed initially with a second stage complete corpus callosotomy being performed if this fails due to the risk of developing a disconnection syndrome(Graham et al., 2016). For this reason, we have chosen to simulate anterior two-thirds callosotomy and not complete callosotomy. Other post-operative complications associated with corpus callosotomy are usually transient but may include language impairments, neuropsychological impairments, hemiparesis and urinary incontinence. The adverse effects associated with corpus callosotomy are usually less severe and better tolerated in children.

Compared to VNS, open corpus callosotomy has been found to lead to significantly improved outcomes for atonic seizures associated with Lennox-Gestaut syndrome(Lancman et al., 2013), yet due to its invasive nature, it is reserved as second-line therapy. Descriptions of laser corpus callosotomy are limited to small case series, but initial results demonstrate that it is a feasible minimally invasive alternative to primary open anterior two-thirds corpus callosotomy or as a second stage completion callosotomy (see Table 27).

Table 27: Summary of case reports in the literature

Authors	Number of patients	Number of Trajectories	Objective	Outcome	Complications
(Ho et al., 2016)	1	1	Second stage completion callosotomy following failed open anterior two-thirds corpus callosotomy	>50% seizure frequency reduction 4 months after ablation	Nil
(Pruitt et al., 2017)	3	3	Not reported	Not reported	One patient suffered from catheter malposition
(Lehner et al., 2018)	5	3	Anterior 2/3 corpus callosotomy	>80% seizure frequency reduction in 4 patients	One patient suffered a misplaced device requiring a second surgery. Another patient suffered a cortical haematoma at the entry site.
(Tao et al., 2018)	2	2	Anterior 2/3 corpus callosotomy	Freedom from disabling seizures at 18 months in one patient and >90% seizure frequency reduction at 7 months	Nil
(Palma et al., 2018)	3	Not reported	Second stage completion callosotomy following failed open anterior	Not reported	Nil

			two-thirds corpus callosotomy		
(Ball et al., 2018)	1	2	Anterior 2/3 corpus callosotomy	Engel 2 outcome	Nil
(Karsy et al., 2018)	1	3	Anterior 2/3 corpus callosotomy	Not reported	Not reported

8.5.3 Computer-assisted planning and LITT corpus callosotomy

Computer-assisted planning has previously been described for stereotactic trajectory planning associated with DBS(Essert et al., 2012), SEE(De Momi et al., 2014b; Sparks et al., 2017a; Vakharia et al., 2018e), brain tumour biopsy(Marcus et al., 2019) and laser ablation of the mesial temporal lobe(Vakharia et al., 2018d) as a means of optimising and objectively standardizing clinical practice. This is the first description of an automated algorithm for optimising laser trajectories associated with anterior two-thirds corpus callosotomy. LITT is a novel minimally invasive method of creating thermal ablations within the brain that can be modulated in near real-time through MR thermography and application of the Arrhenius damage model(Lagman et al., 2017). A laser fibre and cooling catheter are stereotactically implanted into regions of the brain and ablations 5-20 mm in diameter are performed(Hoppe et al., 2017). The catheter can then be withdrawn and consecutive ablations performed to form a confluent ablation cavity. Based on a conservative estimate of a 15 mm ablation diameter we model 7 mm pull-backs for this purpose. The corpus callosum has a curved morphology whilst the laser catheters are currently restricted to linear trajectories. As a result, multiple trajectories are required to ensure that the corpus callosum is ablated to prevent residual connectivity and persistent seizure propagation(Karsy et al., 2018; Lehner et al., 2018). To attain this we aimed to automatically derive patient-specific target and entry points that would ensure interhemispheric disconnection through the corpus callosum whilst optimising the safety metrics considered by surgeons when planning stereotactic trajectories. There is currently no consensus within the literature regarding the use of 2 or 3 laser catheter trajectories. Two catheters may reduce the potential risk of implantation but could also result in incomplete disconnection. Based on expert experience we have therefore developed a 3 catheter algorithm

to mirror their current clinical practice. This was achieved through the use of patient-specific whole brain parcellations in which morphometric dilations and Boolean operations were performed (see Figure 33).

An important consideration during trajectory planning is haemorrhage risk. In clinical practice, surgeons choose avascular corridors between the entry and target points to prevent conflict with intracerebral vessels. We quantify the size of the avascular corridor using a risk score and also measure the minimum distance to vasculature(Sparks et al., 2017a). We make the pragmatic assumption that the greater the size of the avascular corridor the smaller the chance of haemorrhage. We accept that this has not been validated, as doing so would require a prohibitively large observational series, but we have incorporated this metric into the computer-assisted planning algorithm as it closely replicates clinical practice. Another important benefit for maximising distance from vasculature is the heat-sink effect associated with blood flow in close proximity to the intended ablation cavity(Jermakowicz et al., 2018). Other factors that are optimised include the intracerebral length of the trajectory in order to prevent unnecessary parenchymal transgression, orthogonal drilling angle to the skull to prevent skiving during drilling and consequent inaccurate bolt/catheter placement and proportion of the trajectory within the corpus callosum.

Thermal injury to the adjacent fornix and cingulate gyri must also be avoided to prevent memory impairment and neuropsychological dysfunction, respectively. Given that the extent of the ablation cavity is modulated in near real time MR thermography we are unable to model this. Computer-assisted planning trajectories tended to have a more lateral and dorsal position within the corpus callosum compared to manually planned trajectories. The lateral positioning is due to the location of the pericallosal arteries lying on the dorsum of the corpus callosum in the midline. Injury to these could result in stroke or catastrophic haemorrhage. Additionally, the fornices lie closest to the posterior body of the corpus callosum in the midline. A potential consequence of a more lateral and dorsal trajectory, however, is increased cingulate cortex ablation. A prospective clinical trial would be required to compare the neuropsychological sequelae and safety of the trajectories.

Post-operatively adequate disconnection following LITT corpus callosotomy has been described through a multimodal approach including contrast-enhanced MRI, diffusion-weighted imaging, functional MRI, cortico-cortical evoked potentials and resting EEG(Lehner et al., 2018).

In addition, diffusion-weighted imaging and tractography alone have been shown to be highly accurate methods of quantifying post-callosotomy disconnection following open surgery(Choudhri, A.F., Whitehead, M.T., McGregor, 2013). As we are comparing simulated ablation cavities between computer-assisted and manual trajectory plans in the same patients we implemented probabilistic tractography to validate the extent of interhemispheric disconnection through the corpus callosum between the two methods. The different anatomical regions of the corpus callosum have been shown to demonstrate a consistent topographic organisation. The rostrum of the corpus callosum principally connects the orbitofrontal regions and the genu, also known as the forceps minor, connects the medial and lateral surfaces of the prefrontal cortex. The mid-body of the corpus callosum connects the pre-motor cortices whilst the posterior body connects the motor and sensory cortices. Posterior parietal, temporal and occipital connectivity pass through the anterior, middle and posterior aspects of the splenium respectively. We show that the extent of callosal disconnection through the rostrum, genu and body was no worse with computer-assisted planning compared to manually planned trajectories. In cases where residual connectivity was present after the application of simulated ablation cavities, this was on average 0.69 cm3. Unfortunately, we are unable to comment on the clinical significance of this.

8.5.4 Limitations:

The principal limitation of this feasibility study is that the LITT ablations are simulated and have not been prospectively implemented in patients. The corresponding cavities are modelled based on a 5-15 mm cylindrical ablation diameter(Jermakowicz et al., 2018; Vakharia et al., 2018d). Subsequently, we are unable to compare the corresponding outcomes with regards to alterations in seizure frequency that would be obtained were the trajectories implemented as part of LITT disconnection procedures. We feel this feasibility study is a necessary first step to ensure the computer-assisted planning algorithm is able to satisfy the requirements of anterior two-thirds of the corpus callosum under simulated conditions prior to undertaking a prospective clinical validation study. The simulated ablation volumes and number of catheter pull-backs required to achieve the desired ablation volume are based on a cylindrical ablation diameter. The product literature suggests that ablation diameters of between 5-20 mm may be achieved, but due to asymmetrical heat sinks, we conservatively model the maximum ablation diameter as 15 mm with 7 mm pullbacks to generate confluent ablation cavities. Heat dissipation to the adjacent white matter and cingulate cortices may also cause the surgeon to

limit the ablation to prevent unintended damage to these structures. To date, no validated non-linear method exists to estimate the effect of heatsinks on thermal ablation cavities on a patient-specific basis, but this would improve the accuracy of the simulation.

Secondly, for the calculation of the risk score, we utilised vascular segmentations derived from DSA. We acknowledge that DSA is not routinely acquired for LITT procedures. The patients were selected from a prospectively maintained database of SEEG procedures and subsequently, DSA was already acquired as part of their routine care. The algorithm would also work with MRV/A or CTA derived vascular segmentations. Given that the same segmentations were used for the calculation of the risk scores for both manual and computer-assisted plans this would not affect the comparison.

Finally, the automated entry and target point generation are dependent on the whole brain GIF parcellation. We have not tested the algorithm on other common whole brain parcellations, such as FreeSurfer (Martinos Centre for Biomedical Imaging, Charlestown, MA). Inaccuracies in the whole brain parcellation due to poor initial image quality must be checked prior to performing automated trajectory planning as this may adversely affect the trajectory planning.

8.6 **Conclusion**

Computer-assisted LITT anterior two-thirds corpus callosotomy trajectory planning is feasible employing a three trajectory technique. Compared to expert manually planned trajectories in the same patients, the computer-assisted planning algorithm was able to significantly optimise a number of heuristic parameters that surgeons employ during manual stereotactic trajectory planning. In addition, simulated ablation cavities and subsequent tractography revealed residual interhemispheric connectivity in 1 of 10 cases following computer-assisted planning compared to 2 and 4 of 10 cases following expert manual planning. Computer-assisted planning, therefore, provides a systematic and objective method of trajectory planning that may lead to standardised care. This has especially important implications for novel techniques, where initial learning curves are present at introduction. Prospective validation studies are now needed so that therapeutic efficacy can be determined. Future work is now focused on determining whether fewer catheter trajectories can be employed on an individual basis from the anatomical and morphological characteristics of the

corpus callosum. More accurate modelling of heat dissipation in this region would also allow greater inferences regarding potential damage to nearby critical structures, such as the cingulate gyri and the fornix, as the algorithm is able to identify these as critical structures and minimise heat dissipation to them.

9 Accuracy of intracranial electrode placement for stereoelectroencephalography: A systematic review and meta-analysis.Based on (Vakharia et al., 2017b)

9.1 **Abstract**

9.1.1 Objective

Stereoelectroencephalography (SEEG) is a procedure in which electrodes are inserted into the brain to help define the Epileptogenic Zone. This is performed prior to definitive epilepsy surgery in patients with drug-resistant focal epilepsy when non-invasive data are inconclusive. The main risk of the procedure is haemorrhage occurring in 1-2% of patients. This may result from inaccurate electrode placement or a planned electrode damaging a blood vessel that was not detected on the pre-operative vascular imaging. Proposed techniques include the use of a stereotactic frame, frameless image guidance systems, robotic guidance systems and customized patient-specific fixtures.

9.1.2 Methods

Using the Preferred Reporting Items for Systematic Reviews and Meta-Analysis (PRISMA) guidelines a structured search of the PubMed, Embase and Cochrane databases identified studies that involve: 1) SEEG placement as part of the pre-surgical work up in patients with 2) drug-resistant focal epilepsy in which 3) accuracy data has been provided.

9.1.3 Results

326 publications were retrieved of which 293 were screened following removal of duplicate and non-English language studies. Following application of the inclusion and exclusion criteria, 15 studies were included in the qualitative and quantitative synthesis of the meta-analysis. Accuracies for SEEG electrode implantations have been combined using random-effects meta-analysis and stratified by technique.

9.1.4 Conclusion

The published literature regarding the accuracy of SEEG implantation techniques is limited. No prospective case-controlled clinical trials compare different SEEG implantation techniques. Significant systematic heterogeneity exists between the identified studies preventing any meaningful comparison between techniques. The recent introduction of robotic trajectory guidance systems has been suggested to provide a more accurate method of implantation, but supporting evidence is limited to Class 3 only. New techniques must be compared to the previous 'gold-standard' through well designed and methodologically sound studies before they are introduced into widespread clinical practice.

9.2 **Introduction**

Stereoelectroencephalography (SEEG) is a procedure that was developed by Talairach and Bancaud(Talairach et al., 1962) and is undertaken as part of the pre-surgical evaluation of patients in whom non-invasive investigations are unable to accurately define the Epileptogenic zone (EZ). The EZ can be defined as the "minimal area of the cortex that must be resected to produce seizure-freedom"(Lüders et al., 2006). As part of the investigations before epilepsy surgery patients undergo detailed non-invasive clinical, neurophysiological, neuropsychological, neuropsychiatric and multi-modal imaging investigations(National Institute for Health and Clinical Excellence et al., 2012). If these non-invasive investigations are concordant and the EZ can be accurately determined, such as in most cases of hippocampal sclerosis, then the patient can safely undergo surgery with good clinical outcomes(De Tisi et al., 2011). In cases where non-invasive investigations are non-concordant, invasive intracranial recordings are required, which may take the form of a subdural grid, SEEG electrode insertion or both(Enatsu et al., 2016). A recent meta-analysis has highlighted that the main complications associated with SEEG include intracranial haemorrhage, infection, implant malfunction and malposition(Mullin et al., 2016a). Before SEEG electrode insertion trajectories are carefully planned with prior knowledge of the critical neurovascular structures(Cardinale et al., 2015; Zuluaga et al., 2015). Computer-aided planning has been employed in this regard to determine the safest trajectories that maximize grey matter sampling whilst ensuring a safe distance from vasculature(Nowell et al., 2016a, 2016b). Understanding the accuracy of the implantation method is necessary to incorporate a safe threshold away from blood vessels during trajectory planning. Cardinale et al, following a prospective analysis of 500 patients in which 6496 electrodes were implanted, calculated a safe distance of 2.88 mm based on the mean entry point error (0.86 mm) with the addition of 3 standard deviations (3 x 0.54 mm) and the probe radius (0.4 mm)(Cardinale et al., 2013). This, therefore, provides a 99% estimate of confidence that a safe trajectory can be implanted should any vessels be greater than this distance away. Accuracy of SEEG implantations is therefore paramount for electrode implantation as the corridors for implantation between cerebral vasculature are narrow, especially when multiple electrodes are implanted. Another potential consequence of inaccurate electrode placement is the inability to achieve electrophysiological recordings from the intended anatomical brain region. Target points for SEEG electrodes are chosen based on the hypothesis generated from the summation of information provided by the non-invasive investigations. The SEEG recordings help to define the epileptogenic zone and hence, the region for resection that will result in seizure freedom. Electrode malposition,

therefore, exposes patients to the risks of SEEG unnecessarily, and of failure to achieve identification of the epileptogenic zone. The published literature describes several different techniques including the use of a stereotactic frame, frameless image guidance, robotic trajectory guidance and custom patient-specific fixture systems. A recent review of the history of SEEG techniques and those used in high-volumes centres has recently been published(Cardinale et al., 2016b). We aimed to undertake a meta-analysis of all the published literature in which patients with refractory focal epilepsy that have undergone SEEG implantation to determine which provides the most accurate when compared to the preoperatively planned trajectories. This will guide surgeons as to which technique is safest and aid in determining a safe threshold when planning SEEG trajectories.

9.3 **Methods**

The meta-analysis was registered with the PROSPERO database and was assigned the registration number CRD42016047839 through which the review protocol can be reviewed.

Using the Preferred Reporting Items for Systematic Reviews and Meta-Analysis (PRISMA) guidelines(Liberati et al., 2009) a structured search of the PubMed, Embase and Cochrane databases was undertaken. The last date of the search was undertaken on the 16/09/16. Eligibility for inclusion in the meta-analysis included peer-reviewed publications in which full-length English language manuscripts were available through electronic indexing comprising:

i. Pre-clinical or clinical studies of patients with refractory focal Epilepsy
ii. Undergoing SEEG implantation as part of pre-surgical evaluation
iii. The technique for insertion has been described
iv. Post-implantation imaging has been performed (CT or MRI)
v. The method for measurement of deviation from the planned trajectory has been described
vi. The accuracy of the implantation has been measured from the post-operative imaging

Two independent researchers applied the search criteria using the search terms:

- ((drug resist*) OR refractory) AND epilepsy

- (((Stereoelectroencephalography) OR stereo EEG) OR SEEG) OR depth electrode)

In total 328 studies were identified. Following removal of duplicate and non-English language studies 296 manuscripts' titles and abstracts were screened. After applying the eligibility criteria, there were 35 articles that were analysed. A comparison of the articles for inclusion between the two independent researchers was undertaken and revealed high concordance between the identified studies. Any discrepancy was resolved through mutual review and involvement of the senior author. The remaining 17 studies were included in the qualitative and 15 in the quantitative synthesis. (See Figure 37)

Figure 37: PRISMA 2009 Flow diagram

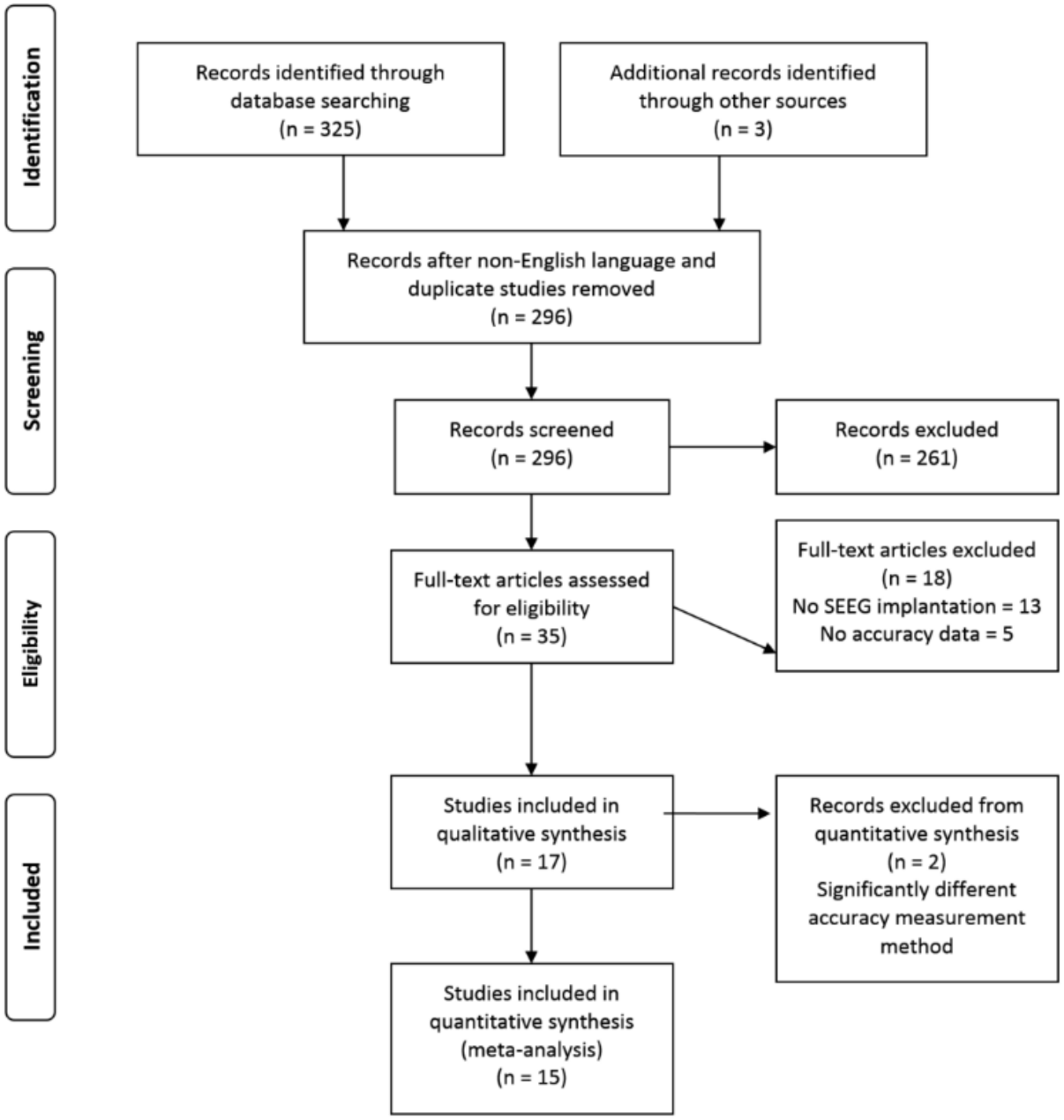

Figure 37 *Legend: Summary of search strategy (based on The PRISMA Statement, www.prisma-statement.org)*

Data extraction was performed using a table with a predefined set of criteria. The risk of bias and methodological quality of the included studies was calculated using the methodological index for non-randomized studies (MINORS) in which rating scores out of 16 and 24 for non-comparative and comparative studies respectively are generated(Slim et al., 2003). Low scores suggest methodologically flawed studies. There was good internal consistency between the ratings from the two independent assessors as defined by a Cronbach's alpha of 0.86. Mean accuracy of implantation results for entry point or target point error were combined using an inverse variance method and stratified by technique. Studies were weighted from the random-effects analysis. Statistical analysis was performed using SPSS 24 and Stata (Version 14).

9.4 **Results**

9.4.1 Study quality

From the 17 studies included in the qualitative synthesis, one study was preclinical, one study contained a combination of pre-clinical and clinical results and the remaining studies were all clinical. In the majority of studies (11/17), no comparison between different techniques of implantation was undertaken. From the remaining 6 studies, 5 compared outcome results to retrospective data sets (historical cohorts) and the single preclinical study compared two robotic trajectory guidance systems prospectively. One of the studies by Gonzalez-Martinez et al. (Gonzalez-Martinez et al., 2013) used previously published data as a historical comparison for a prospective study and therefore appeared twice (once for the stand-alone results and again for the comparison). Two studies were removed from the quantitative analysis because the method used to assess accuracy was deemed sufficiently different to prevent any meaningful results comparison. (see table 28)

Table 28: Summary of Data Synthesis

Publication	MINORS	Study type	Frame / Frameless	Technique	Number of patients	Total number of electrodes	Error Measure / Grading scale	EP error (mm) from plan	TP error (mm) from plan	Angle error (deg) from plan	Complications	Comments
Dorfer et al. (2016)(24) (Level 3)	15	Preclinical phantom	Frameless	iSYS1 vs Vertek arm (Medtronic) Prospective	1 phantom	5 iSYS1 vs 5 Vertek arm	Lateral deviation	iSYS1 = 0.6 +/- 0.4 Vertek arm = 1.4 +/ -0.5 (mean +/- SD)	iSYS1= 0.8 +/- 0.7 mm Vertek arm = 1.4+/-0.7 mm (mean +/- SD)	Not specified	N/A	Reduction in time for alignment to trajectory with iSYS1
		Clinical	Frameless	iSYS1 Prospective	16	93	Lateral deviation	iSYS1 = 1.54 +/- 0.8 iSYS1 + K-wire = 1.18 +/- 05	iSYS1 = 1.82 +/- 1.1 iSYS1 + K-wire = 1.66 +/- 1.12	Not specified	0	1. Further improvement in iSYS1 accuracy following modification of technique with K-wire (p = 0.021) 2. Comparison to retrospective Vertek arm cohort using skin

								(mean +/- SD)	(mean +/- SD)			fiducials where iSYS1 insertions used bone fiducials 3. Reduction in EP (60%) and TP (40%) error with iSYS1 compared to Vertek probe technique in historical controls
				Vertek arm (Medtronic) Retrospective	Not specified	Not specified	Lateral deviation	Vertek arm = 3.5 +/- 1.5 (mean +/- SD)	Vertek arm = 3.0 +/- 1.9 (mean +/- SD)	Not specified	Not specified	
Roessler et al. 2016 (25) (Level 3)	10	Clinical	Frameless combined with intraoperative MRI	Brainlab navigation of reduction tube and immobilization with two fixation arms (Lyla retractors) Prospective	6	58	Euclidean distance	1.4 +/- 1.2 (mean +/- SD)	3.2 +/- 2.2 (mean +/- SD)	Not specified	Nil	1. Mean time for electrode implantation 12 mins (50% quicker than frame-based SEEG) 2. Intraoperative MRI registration accuracy 1-2 mm. 3. Frameless system 28% cheaper compared to frame-based system 4. Relatively short electrode lengths (mean = 37.3 mm)
Narváez-Martínez et al. 2016 (17)	9	Clinical	Frameless combined with O-arm	Vertek arm (Medtronic) Prospective	10	69	Not specified	Not specified	1.39 (mean)	Not specified	Nil	1. Mean time for electrode implantation 34.7 mins

(Level 4)												
González-Martínez et al. 2016(22) (Level 3)	12	Clinical	Frameless (Leksell frame used as fixation device)	ROSA Robotic assistant device Prospective	100	1245	Euclidean distance	1.2 (interquartile range 0.78-1.83)	1.7 (interquartile range 1.20-2.30)	Not specified	Total complication rate of 4% per patient (3% asymptomatic and 1% symptomatic haemorrhage) Risk of major haemorrhagic complication 0.08% per electrode	1. Mean time for electrode implantation 30 mins using the ROSA 2. Registration accuracy <0.75 mm 3. EP and TP target errors measured in 500 consecutive electrode insertions using the ROSA 4. ROSA implantations were a means of 222 minutes shorter than frame-based implantations (p<0.001) 5. No significant difference between mean entry point error and complication rate between ROSA and historical frame-based control
	9		Frame-based	Leksell frame Retrospective	100	1310	Euclidean distance	1.1	Not specified	Not specified	Total complication rate of 3% per patient (2% asymptomatic and 1% transient symptomatic haemorrhage) Risk of haemorrhagic	

											complication 0.2% per electrode	
Verburg et al. 2015(26) (Level 4)	8	Clinical	Frameless	VarioGuide (BrainLab) Retrospective	7	89	Euclidean distance	Not specified	3.5 Median (95% CI 2.9-3.9)	Not specified	One patient required decompressive hemicraniectomy following symptomatic haemorrhage (14%) Risk of haemorrhagic complication 1.1% per electrode	1. Laser surface registration accuracy not specified 2. Poor fixation of single electrode resulted in 13.7 mm maximum error of electrode
Hou et al. 2014(23) (Level 3)	16	Clinical	Frameless	Navigus tool Prospective	36	173	Lateral deviation	Not specified	2.03+/- 0.98 (mean +/- SD)	Not specified	Nil	1. Mean time for electrode implantation of 19.4 mins in frameless compared to 34.5 mins in frame-based group ($p<0.05$) 2. Surface tracing registration accuracy not specified 3. Electrode implantation accuracy worse in the temporal compared to frontal
			Frame-based	Leksell frame Retrospective	28	62	Lateral deviation	Not specified	1.79+/- 0.82 (mean +/- SD)	Not specified	Haematoma rate 3% in frame-based group (all asymptomatic)	

												lobe (p<0.05)
Meng et al. 2014(29) (Level N/A)	18	Pre-clinical	Frameless	Robot arm with Polaris Prospective	1 phantom	12	Euclidean distance	Not specified	1.16+/- 0.38 (mean +/- SD)	Not specified	N/A	1. Scalp fiducial marker based registration accuracy not specified 2. Accuracy errors are for trajectory alignment not following electrode or bolt placement. Drilling and placement errors are not measured. 3. Trajectory location time < 6mins for 12 electrodes 4. Robotic device not clinically available
			Frameless	Robot arm with Optotrak Prospective	1 phantom	12	Euclidean distance	Not specified	0.62 +/- 0.23 (mean +/- SD)	Not specified	N/A	
Nowell et al. 2014 (10) (Level 4)	12	Clinical	Frameless	Vertek arm (Medtronic) Prospective	22	187	Lateral deviation	Not specified	3.66 +/- 2.21 (mean +/- SD)	Not specified	Haematoma rate of 4.5% (asymptomatic)	1. Scalp fiducial marker based registration accuracy not specified 2. Intraparenchymal electrode deviation reported 3. Median time for implantation 137 mins (range 80-167 mins) 4. Eight electrodes failed to

												reach their neurophysiological target
Balanescu et al. 2014 (16) (Level 4)	10	Clinical	Frameless	Custom patient specific frame Prospective	4	53	Lateral deviation for Entry point and Euclidean distance for target point	0.68 mean (interquartile range 0.30-0.98)	1.64 mean (interquartile range 0.84-2.50)	Not specified	Nil	1. Low number of patients 2. Only orthogonal and up to 2 oblique trajectories possible 3. No adjustable components 4. Requires 2 stage procedure (one week apart)
Cardinale et al. 2013(11) (Level 3)	16	Clinical	Frame-based	Talairach frame Retrospective	37	517	Euclidean distance	1.43 median (interquartile range 0.91-2.21) Error >2mm in 29.5% >3mm in 11.4%	2.69 median (interquartile range 1.89-3.67)	Not specified	Overall major complication rate 2.4% per patient and 0.03% per electrode. 4 major haemorrhagic complications with frame-based system and none with frameless	1. Significant improvement in both EP and TP accuracy with Neuromate implantations over the traditional Talaraich frame ($p<2.2x10^{16}$) 2. Likely that post-operative haemorrhage rate was underestimated as post-op MRI or fan-beam CT were not undertaken 3. Higher risk of ble eding from EP error 4. Angiographic data used for trajectory planning
			Frameless	Neuromate robotic stereotactic	81	1050	Euclidean distance	0.78 median (interquartile range	1.77 median (interquartile range	Not specified		

				device (Renishaw) Prospective				0.49-1.08) EP error >2mm in 3.7% >3mm in 0.5%	1.25-2.51)			
Munyon et al. 2013 (Level 4)	8	Clinical	Frame-based	With subdural grid placement Retrospective	6	31	Euclidean distance	Not specified	1.0 +/- 0.15 mm (mean +/- SD)	Not specified	Not specified	1. Centre of planned craniotomy equidistant from fixation posts. 2. No significant difference between accuracy of electrode placement when craniotomy for subdural grid was performed 3. Intraoperative brain shift not accounted for
Ortler et al. 2011(20) (Level 3)	11	Clinical	Frameless	Vogele-Bale-Hohner (maxillary fixation) system Retrospective	3	6	Lateral deviation	2.17 +/- 2.19 mm (mean +/- SD)	2.43 +/- 0.98 mm (mean +/- SD)	Not specified	Small subcortical haemorrhage	1. Only intrahippocampal depth electrodes placed in the longitudinal axis of the hippocampus included 2. Entry point error values taken at 4cm behind the tip of

			Frame-based	Fischer – Leibinger Stereotactic frame Retrospective	6	11	Lateral deviation	1.37 +/- 0.55 mm (mean +/- SD)	1.80 +/- 0.39 mm (mean +/- SD)	Not specified	Nil	electrode for uniformity not at skull surface 3. Aiming device calculated accuracy accepted when alignment to plan <0.5 mm and <1 deg
Mascott et al. 2006 (Level 4)	8	Clinical	Frameless	SureTrak (Medtronic) with variety of systems incl. Leyla retractor arm (Aesculap) and Vertek arm (Medtronic)	7	42	Euclidean distance	Not specified	3 +/- 1.5 mm (mean +/- SD) 2.4 +/- 1 (mean +/- SD) following depth correction	Not specified	Not specified	1. No rigid (bolt) fixation of electrode to the skull resulting in depth inaccuracies 2. Bone fiducials used to provide consistent registration accuracy
Mehta et al. 2005 (28) (Level 4)	12	Clinical	Frameless	Guide Frame-DT (Medtronic)	20	41	Lateral deviation and Anatomical Target Localisation grading system	Not specified	3.1 +/- 0.5 mm (mean +/- SD) from planned trajectory	Not specified	Nil	1. Guidance based on MRI alone (not MRI and CT fusion) 2. Skin fiducials used 3. Electrode placement through craniotomy at the same time as grid placement (no rigid

									0.4 +/- 0.9 mm from the edge of the anatomical structure			skull fixation) 4. Occipitotemporal approach statistically more inaccurate ($p < 0.05$)
Van Roost et al. 1998(19) (Level 4)	9	Clinical	Frame-based	Fischer – Leibinger Stereotactic frame	164	212	Anatomical Target Localisation	Not specified	Target accuracy: Hippocampal head 97% (63% direct and 34% marginal) Hippocampal body 96% (58% direct and 38% marginal) Amygdala 75% (2%	Electrode inclination to hippocampus in AP orientation 93% correct, 6% too steep and 1% too flat	Subcortical haemorrhage 2.12% Infection 2.12% Risk of permanent neurological deficit of 0.7%	1. Only intrahippocampal depth electrodes placed in the longitudinal axis of the hippocampus included 2. Anatomical target localization accuracy provided not a deviation from the plan

									direct and 73% marginal)			
Davies et al. 1996(18) (Level 4)	7	Clinical	Frameless	Freehand neuronavigation guided following craniotomy for grid placement	12	15	Distance from hippocampus	Not specified	0.8 mm (range 0-5 mm)	Not specified	Nil	1. Only intrahippocampal depth electrodes placed orthogonally into the temporal lobe included 2. Distance to the edge of the anatomical structure measured on post-operative MRI not compared to the pre-operative plan 3. SEEG electrode placement following craniotomy for grid placement 4. No correction for brain shift

Calculated MINORS scores were a median 9/16 for non-comparative and 15.5/24 for the comparative studies suggesting that studies had significant methodological flaws. Included studies provided Level 3 evidence for individual case-control studies and Level 4 evidence for case-series. No randomized control trials in this area were identified. No studies included blinding or provided a prospective power calculation. Follow up periods were adequate for the purposes of accuracy determination in all cases as for inclusion eligibility, all accuracy data were derived from the post-operative imaging. From the comparative studies, control groups were rarely adequately balanced with regards to baseline characteristics.

9.4.2 Accuracy measurement

No consistent means of measuring accuracy within the published studies were identified. The error between the planned and implanted trajectories were measured using Euclidian distance in 8/17 studies and lateral deviation in 5/17. A single study (Balanescu et al., 2014) combined both measures using lateral deviation for the entry point and Euclidian distance for the target point and one study did not specify how the errors were measured (Narvaez-Martinez et al., 2016).

9.4.3 Accuracy data

From all the studies, accuracy data has been provided for 13 different implantation systems (5 frameless, 3 frame-based, 3 robotic trajectory guidance and one patient-specific custom frame system). Two studies were excluded from the quantitative analysis, as the method of accuracy was determined as the distance from the edge of an anatomical structure opposed to distance from the planned trajectory(Davies et al., 1996; Van Roost et al., 1998).

The combined accuracy of the:

a) Frameless systems were Entry Point (EP) Error mean 2.45 mm (0.39, 4.51 95% CI) and Target Point (TP) error mean 2.89 mm (2.34, 3.44 95% CI).
b) Frame-based systems were EP error mean 1.43 mm (1.35, 1.51 95% CI) and TP error mean 1.93 mm (1.05, 2.81 95% CI).
c) Robotic trajectory guidance systems were EP error 1.17 mm (0.80, 1.53 95% CI) and TP error 1.71 mm (1.66, 1.75 95% CI).

Figure 38: Forest Plot for a) Entry Point

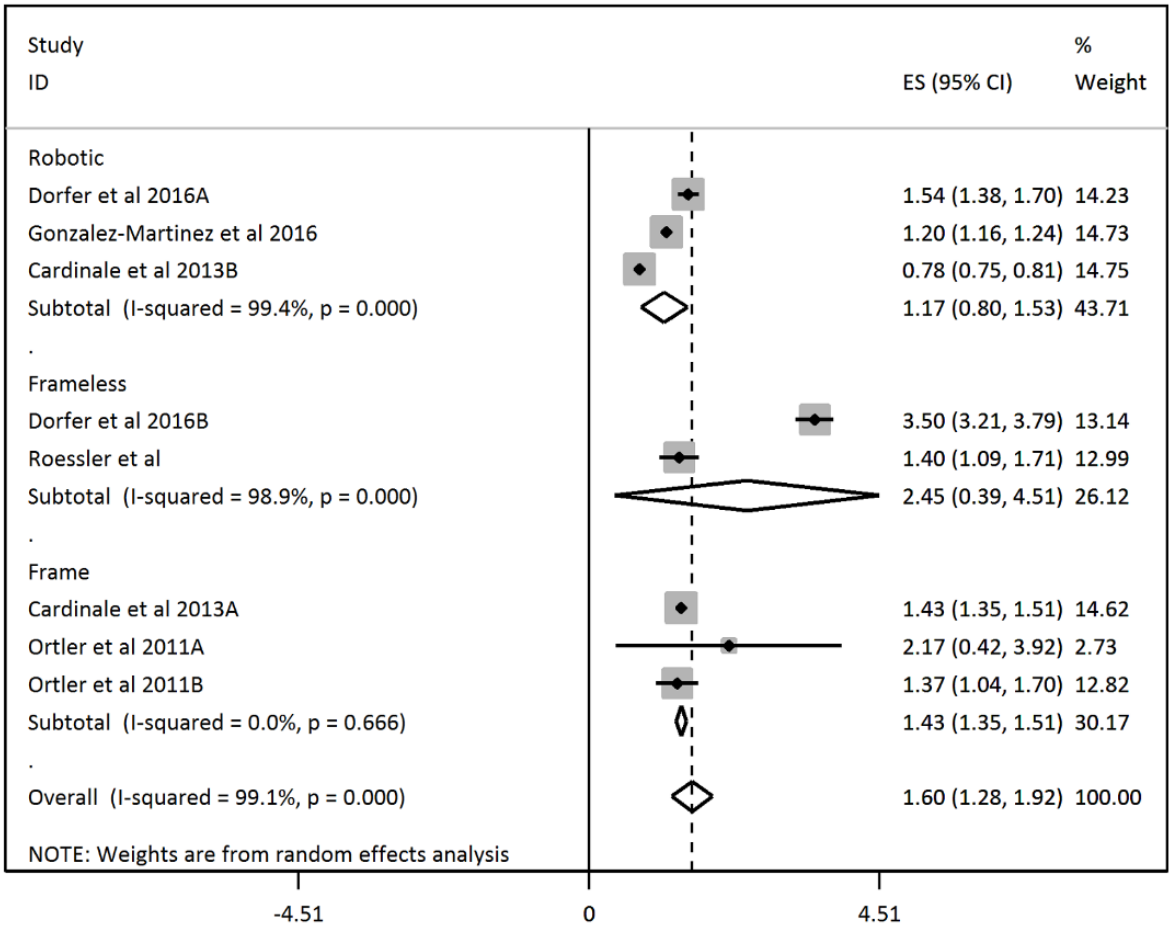

b) Target Point

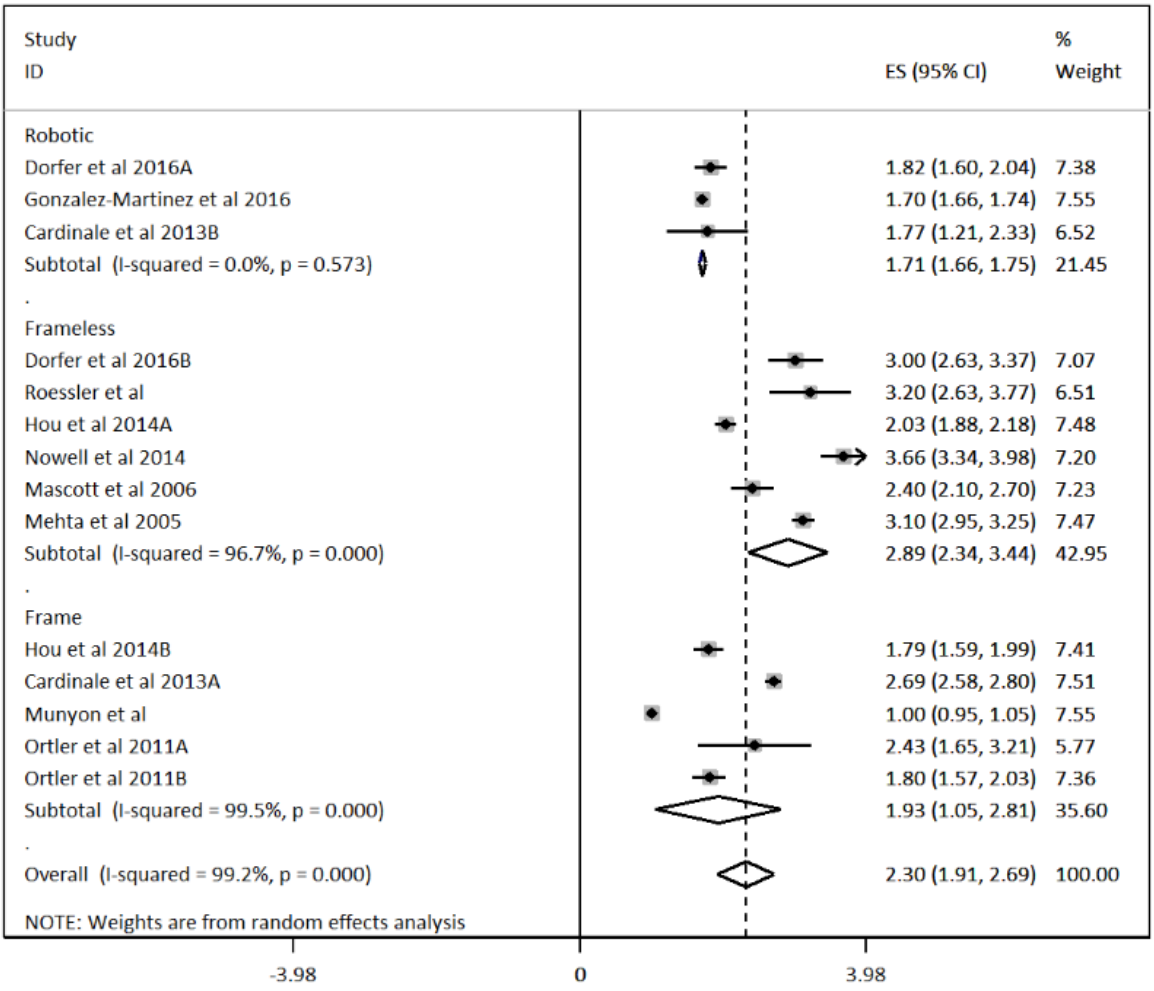

Figure 38 Legend: Forest plot a) Entry point b) Target point accuracy based on operative implantation technique. Mean (solid diamond) and 95% confidence interval (solid line) provided with percentage weighting based on inverse variance method. Group (subtotal) and overall mean with 95% confidence interval for the mean (hollow diamond) provided with statistic (I-squared) and p-value for heterogeneity showing significant heterogeneity between robotic and frameless studies preventing meaningful comparison.

9.5 **Discussion**

9.5.1 Accuracy measures

Entry point error is the difference in the actual from the planned position at which the electrode passes through the skull. This can be affected by misregistration of the neuronavigation system, inaccurate alignment and deflection during drilling. Target point error is the difference in the actual from the planned position of the electrode at the target site. Target point accuracy is affected by the angle at which the electrode passes through the skull (even when the entry point is accurate), deflection of the electrode at the dura or within the brain, rigidity of the electrode and depth to which the introducer is inserted. The choice of insertion technique has a greater effect on the entry point error, but the stability of the system will also affect the angle of entry, which in turn has a direct impact on the target point accuracy. The entry and target point accuracies are based on the segmentation of the electrode positions on the postoperative CT scan and have been measured in a variety of ways, although Euclidean distance and lateral deviation were most commonly used. Comparison of accuracies between the two methods can lead to inaccuracy as the Euclidean distance takes into account depth inaccuracies, whilst lateral deviation does not. Given that Euclidean distance was used in 8/17 and lateral deviation in 5/17 studies, this introduces significant heterogeneity and prevents meaningful comparisons between studies using different accuracy measures. Given that none of the compared techniques for the implantation of SEEG electrodes directly affect depth error, as this is surgeon controlled, some authors advocate the use of lateral shift over Euclidean distance. We were unable to consider studies that used lateral deviation and Euclidean distance separately due to the small number in the literature and have therefore opted to amalgamate them whilst recognizing the imprecision that this introduces. A uniform rating scale is required to facilitate accurate comparisons between different studies. There is a large variation in the number of patients and electrodes in the published studies ranging from 6 electrodes in 3 patients(Ortler et al., 2011) to 1050 electrodes in 81 patients(Cardinale et al., 2013). To account for this, the studies in the meta-analysis were weighted using an inverse variance method. The overall incidence of haemorrhage from SEEG electrode implantation is estimated to be 0.18% per electrode(Mullin et al., 2016a). Given the relatively small numbers of studies and variable complication reporting in some studies, we are unable to correlate accuracy with haemorrhage rate.

9.5.2 Frame-based systems

Five studies provided accuracy data for the Leksell, Fischer-Leibinger and Talairach frame-based systems. All studies were retrospective and data were provided as historical control groups for the comparison to frameless(Hou et al., 2014; Ortler et al., 2011) and robotic trajectory guidance systems, ROSA(Gonzalez-Martinez et al., 2013, 2016) and Neuromate(Cardinale et al., 2013), providing Level 3 evidence. Hou et al. (Hou et al., 2014) used a frameless system involving the Navigus tool in a prospective cohort of 36 patients in which 173 electrodes were implanted compared to the historical use of the Leksell frame in 28 patients for the insertion of 62 electrodes. Surface tracing registration was used for the frameless system and did not reveal any significant difference in the overall electrode accuracy between the frameless and Leksell frame accuracies. The use of surface tracing is thought to be less accurate to bone fiducials and is likely to have reduced the accuracy of the frameless implantation technique. There was a significant reduction in the time taken for electrode implantation from 34.5 to 19.4 minutes using the frameless system, compared to frame-based. This represents the only published study in which the baseline characteristics of the case and control groups have been matched. Ortler et al. (Ortler et al., 2011) compared the Fischer-Leibinger frame in 6 patients with the frameless Vogele-Bale-Hohner maxillary fixation system in 3 patients for the purpose of bilateral longitudinal hippocampal electrode insertion. There was no difference in accuracy found between the two systems with the Fischer-Leibinger and Vogele-Bale-Hohner systems providing EP errors of 2.17 mm+/-2.19 (Mean +/- SD) and 1.37 mm+/-0.55 (Mean +/- SD) respectively and TP errors of 2.43 mm+/-0.98 (Mean +/- SD) and 1.80 mm+/-0.39 (Mean +/- SD) respectively. The overall number of patients in the study was very small and there was a lack of a prospective power calculation. As such it likely the study was inadequately powered to detect a clinically significant difference.

Cardinale et al. (Cardinale et al., 2013) compared a historical cohort of 37 patients that had undergone 517 electrode insertions using the Talaraich stereotactic frame with 81 patients undergoing 1050 electrodes using the Neuromate robotic trajectory guidance system. There was a significant improvement in both the entry and target point accuracy with the Neuromate robotic system over the historical cohort of patients implanted with the Talairach frame ($p<2.2x10^{16}$). Entry point error reduced from a median of 1.43 mm (IQR 0.91-2.21) to 0.78 mm (IQR 0.49-1.08). In a similar study by Gonzalez-Martinez et al. (Gonzalez-Martinez et al., 2016) the implantation of 1245 electrodes in 100 patients using the ROSA robotic trajectory guidance

system was compared with a historical cohort of 100 patients implanted with 1310 electrodes using the Leksell frame. EP error was not significantly different between the two methods. No target point error was provided for the Leksell frame historical cohort. Historical comparison data in this study was provided as a means of reference and not for formal statistical comparison. The calculated heterogeneity statistic for EP accuracy between frame-based systems was 0%. Excluding the small study by Ortler et al. (Ortler et al., 2011), the remaining studies had very tight confidence intervals suggesting valid comparisons can be made between frame-based techniques.

9.5.3 Frameless systems

The frameless systems included in the analysis include the Vertek arm (Medtronic)(Dorfer et al., 2017; Narvaez-Martinez et al., 2016; Nowell et al., 2014), Varioguide (BrainLab)(Roessler et al., 2016; Verburg et al., 2016), Navigus tool (Medtronic)(Hou et al., 2014) and the Guide Frame-DT (Medtronic)(Mehta et al., 2005). A single study compared the use of the iSYS1 robotic trajectory guidance system for the insertion of 93 electrodes in 16 patients with a historical cohort using the Vertek arm frameless technique(Dorfer et al., 2017). The number of patients and baseline characteristics of the historical cohort was not specified. There was a 60% reduction in the EP error from 3.5 mm+/-1.5 (Mean +/- SD) with the Vertek arm to 1. 4 mm+/-0.8 (Mean +/- SD) with the iSYS1 robotic trajectory guidance system. TP error was reduced by 30% from 1.82 mm+/-1.1 (Mean +/- SD) to 1.18 mm+/-0.6 (Mean +/- SD). Historical comparison data in this study were provided as a means of reference and not for formal statistical comparison. All other studies using frameless systems were case-series in which accuracy data were measured and therefore provides Level 4 evidence. The calculated heterogeneity statistic for frameless techniques included in the meta-analysis was 98.9% suggesting that significant heterogeneity exists between individual studies that prevents any meaningful comparisons between the different frameless techniques. Combined accuracy data is provided for different frameless techniques, but the significant heterogeneity between the studies prevents any meaningful conclusions from being drawn.

9.5.4 Robotic guidance systems

The robotic trajectory guidance systems include the ROSA(Gonzalez-Martinez et al., 2016), Neuromate(Cardinale et al., 2013) and iSYS1(Dorfer et al., 2017). As stated comparisons between the robotic trajectory guidance systems previously have been with retrospective

frame-based and frameless systems. A single preclinical prospective comparison between a robotic arm using different guidance systems (Polaris and Optotrak) has been published(Meng et al., 2014). Twelve electrodes were inserted into a single phantom using each technique. This device, however, is not clinically available and therefore are no clinical publications of its use to date. There have been no prospective clinical comparisons of robotic trajectory guidance systems with other techniques or between robotic trajectory guidance systems. The calculated heterogeneity statistic for robotic techniques included in the meta-analysis was 99.4% suggesting that significant heterogeneity exists between individual studies that again prevents any meaningful comparisons between the different robotic techniques. Combined accuracy data is provided for different robotic techniques, but the significant heterogeneity between the studies prevents any meaningful conclusions from being drawn.

9.6 **Conclusion**

The accuracy of SEEG electrode implantation using a variety of techniques has been published. Studies to date are mostly single-centre case series providing Level 4 evidence. Some studies have provided comparisons between different implantation techniques, but all clinical comparisons have been of retrospective cohorts (Level 3), with variable study quality. Calculated heterogeneity statistics suggest meaningful comparisons between studies can only occur between different frame-based techniques and not between frameless or robotic techniques. The lack of a uniform measure of accuracy likely contributes to this heterogeneity and reduces the validity of the pooled data such that no meaningful conclusions can be drawn. There is some limited evidence suggesting that robotic trajectory guidance systems may provide greater levels of accuracy compared to both frameless and frame-based systems, but the studies are of low quality and provide low levels of evidence. There is, therefore, a need for high-quality prospective control trials between different SEEG implantation techniques to define which methods provide the highest levels of accuracy.

10 Improving Patient Safety During Introduction Of A Novel Robotic Trajectory Guidance System (iSYS-1) Through Cumulative Summation Analysis. Based on (Vakharia et al., 2018b)

10.1 **Abstract**

10.1.1 Objective

To implement cumulative summation analysis (CUSUM) as an early warning detection and quality assurance system for the pre-clinical testing of the iSYS1 novel robotic trajectory guidance system.

10.1.2 Methods

Anatomically accurate 3D printed skull phantoms were created for three patients that had previously undergone implantation of 21 stereoelectroencephalography (SEEG) electrodes using the current standard of care (frameless technique). Implantation schema were recreated using the iSYS1 system and paired accuracy measures were compared with the previous frameless implantations. Entry point, target point and implantation angle accuracy were measured from post-implantation CT scans. CUSUM analysis was undertaken prospectively.

10.1.3 Results

The iSYS1 trajectory guidance system significantly improved electrode entry point accuracies from 1.90+/-0.96 mm (Mean+/-SD) to 0.76+/-0.57 mm (Mean+/-SD) without increasing implantation risk. CUSUM analysis was successful as a continuous measure of surgical performance and acted as an early warning detection system. The surgical learning curve, although minimal, showed improvement after insertion of the 8th electrode.

10.1.4 Conclusions

The iSYS1 trajectory guidance system did not show any increased risk during phantom preclinical testing when performed by neurosurgeons who had no previous experience of its use. CUSUM analysis is a simple technique that can be applied to all stages of the IDEAL framework as an extra patient safety mechanism. Further clinical trials are required to prove the efficacy of the device.

10.2 **Introduction**

Novel surgical procedures and devices have the potential to improve patient outcomes and safety through the translation of technological advancements to healthcare. The introduction of robotic devices to a number of surgical specialities over the last decade has seen them become applied to numerous procedures(Díaz et al., 2017). Novel medical devices or procedures are associated with a learning curve and patients are exposed to potential risks until efficacy can be proven and long-term outcome data are acquired(Collins et al., 2014),(Novara et al., 2015). Surgical device trials have the added complication of user-dependent outcomes and the learning curve/surgeon contribution to outcome is difficult to predict, especially when trying to assess the external validity of a particular device or procedure. The regulation with regards to approval of devices is varied in different countries and a recent cross-sectional study showed less than half of the devices in which clinical studies are undertaken go on to achieve regulatory U.S. Food and Drug Administration (FDA) approval(Marcus et al., 2016). Of the devices that are cleared for regulatory approval, 43% were found to have been cleared without the publication of a single clinical study under the 510(k) clearance, where only substantial equivalence to another approved device is necessary. Alarmingly, a study of medical devices for orthopaedic surgery revealed that those approved using the 510(k) clearance were 11.5 times more likely to be recalled than devices that underwent clinical studies prior to pre-market approval(Day et al., 2016). The IDEAL framework is a collaborative approach between surgeons and trial methodologists to provide structured guidance, similar to that employed for drug trials, for the transition of medical devices from ideas (stage 1) to long term outcome studies (stage 4)(McCulloch et al., 2013). The IDEAL framework, however, does not provide a continuous method for surgical vigilance towards the early detection of harm or the potentially negative effect of learning curves. Cumulative summation analysis (CUSUM) is a simple, early warning system that compares outcomes of a new intervention or procedure against an established risk or failure rate that can be used longitudinally to monitor the outcome and surgical performance(Kim et al., 2015; Sivaraman et al., 2017; Sood et al., 2014). CUSUM analysis has been used in prospective robot-assisted randomised control trials(Kim et al., 2015) and case-control studies in which historical outcome data is used to provide a baseline for comparison. The latter use has been successfully applied to assess learning curves of particular surgical(Guend et al., 2016; Wang et al., 2016; Watson et al., 2015) and non-surgical interventions(Balsyte et al., 2010; Young et al., 2005). CUSUM analysis acts as an early warning

mechanism to inform investigators if an intervention is exposing patients to a higher than expected risk of adverse events, but does not replace conventional statistical methods.

Stereoelectroencephalography (SEEG) is a neurosurgical procedure in which multiple electrodes (usually 8-14) are placed within the brain to identify the seizure onset zone in patients with drug-refractory focal epilepsy, to determine if a resection would be feasible. To date four techniques have been described to implant multiple intracerebral electrodes, including stereotactic frame-based(Serletis et al., 2014), frameless(Nowell et al., 2014), robotic(Cardinale et al., 2013; Minchev et al., 2017; Mullin et al., 2016b) and custom 3D printed fixture methods(Balanescu et al., 2014). Electrode trajectories are pre-planned to ensure that electrodes are a safe distance from intracranial arteries and veins(Rodionov et al., 2013; Sparks et al., 2016; Zuluaga et al., 2015), as damage to these vessels could result in a life-threating haemorrhage that caused mortality or significant morbidity(Mullin et al., 2016a). The accuracy with which the electrode conforms to the pre-planned trajectory is therefore dependent on the implantation method. We have previously carried out a meta-analysis of accuracy related to the surgical implantation methodology and found a paucity of evidence within the literature comparing implantation techniques(Vakharia et al., 2017b). Studies to date have been of poor quality amounting to Level 3 evidence. There have been no prospective comparisons of different implantation techniques. Here we provide an example in which CUSUM analysis has been used as an early warning tool to compare a novel robotic device for the insertion of intracerebral Stereoelectroencephalography (SEEG) electrodes with the currently used frameless technique(Nowell et al., 2014).

10.3 **Methods**

10.3.1 Stereoelectroencephalography technique

The frameless implantation technique used as the standard of care at the study institution has been described previously(Nowell et al., 2014). In brief, the technique involves the use of a mechanical arm in combination with a precision aiming device and Stealth S7 neuronavigation system (Medtronic Inc). After registration of the patient to the neuronavigation system, using bone fiducials as registration points, pre-planned trajectories on the Stealth station are used to align the mechanical arm and precision aiming device. Using a series of reduction tubes, the trajectory is then drilled through the skull and the electrode bolt is screwed into the skull. A stylet is then passed through the bolt and following this, the electrode is inserted to the target

point. In a similar fashion, the novel iSYS1 trajectory guidance system (Medizintechnik Gmbh) is a small device that interfaces with the S7 Stealth neuronavigation system and through a series of iterative steps aligns to the pre-planned trajectory. Similar to the precision aiming device, the iSYS1 has a working channel through which reduction tubes are placed to allow drilling and insertion of the skull bolt followed by the electrode. Both procedures are performed with the same two neurosurgeons working together.

10.3.2 Phantom generation

Three patients who previously had a total of 21 electrode implantations using the conventional frameless method were selected on the basis of a power calculation, representative range of anatomical targets and drilling angles to the skull. The skull models for each of the patients were 3D printed (3D Systems Inc., High Wycombe, UK) with bone fiducials in-situ using a commercially available realistic bone-like substitute (Duraform PA) and covered with a synthetic skin substitute. The two neurosurgeons who had previously undertaken the implantation on the patients then repeated the implantation procedure on these phantoms, using the iSYS1 robotic trajectory guidance system. All equipment, including the drill, and electrode bolts were kept consistent for both implantation techniques. The two neurosurgeons had previously seen a demonstration of the iSYS1 system and were aware of the instructions for use but had not received any previous practical training.

Following implantation, the 3D printed skulls underwent a CT scan and the planned and actual (implanted) bolt trajectories were compared using a lateral deviation method (see Figure 40) for both the entry point, projected target point and angle error(Nowell et al., 2014). The results were compared to the actual post-operative patient implantation for the same planned trajectories using EpiNav^{TM} (Nowell et al., 2016b).

Figure 39: Phantom implantation

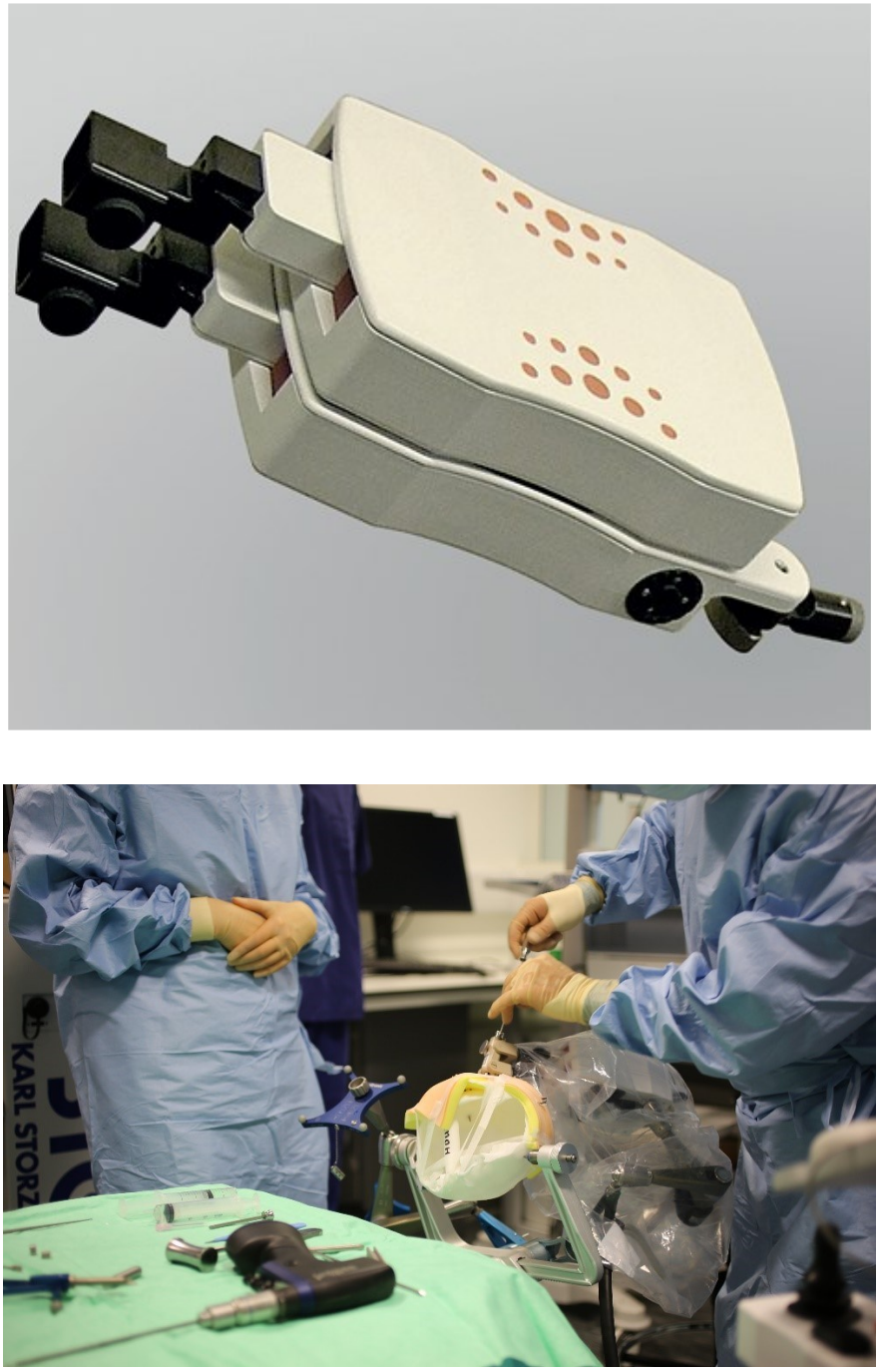

Figure 39 *Legend: Top panel: Robotic positioning unitImplantation. Bottom panel: Using the iSYS1 robotic trajectory guidance system on a phantom head recreated to replicate the SEEG implantation in a patient.*

Figure 40: Calculation of lateral deviation error

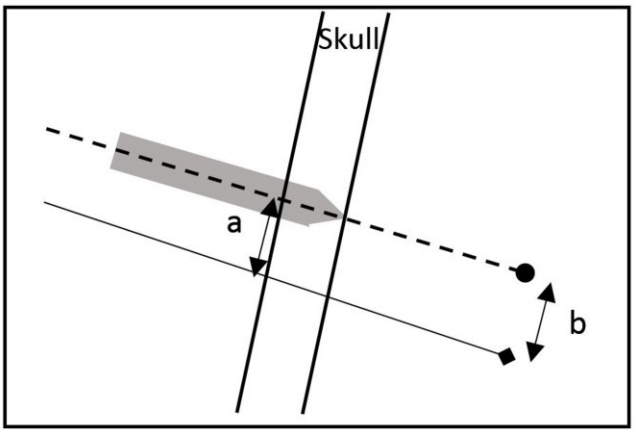

Figure 40: Schematic of implantation accuracy metrics include entry point, projected target point and angle error to the skull. The solid line (diamond) indicates planned electrode and dashed line (circle) indicates the bolt axis trajectory. Entry point (a) and projected target point (b) error measured as the lateral deviation from the plan.

10.3.3 Cumulative summation analysis

Cumulative summation analysis is calculated using the following equation:

Equation 5: Cumulative Summation Analysis

$$\sigma_n = (\sigma_{n-1} + Xi_n) - Xo_n$$

where σ_n is the cumulative summation after n attempts, Xi_n is the result of the intervention following the nth attempt and Xo is the established risk or failure rate of the control to which the on-going attempts are compared. Xo can be calculated either on a case by case basis (Xo_n) as with paired control trials in this case, or as an overall frequency if this is known. When σ_n is plotted for subsequent attempts, the gradient of the graph provides information regarding whether the intervention is performing better (negative gradient) or worse (positive gradient) than the control intervention. A change in the gradient from negative to positive following the introduction of a new intervention, therefore, serves as an early warning that outcomes are worse than in the control group, even though this may not yet have reached statistical significance. Each of the electrode bolt insertion accuracies using the iSYS1 on the phantom (Xi_n)

were compared with the patient insertions using the frameless technique (Xo_n). The analysis was also undertaken using a 3 mm accuracy safety margin based on the accuracy data provided by Cardinale et al. (Cardinale et al., 2013).

10.3.4 Statistical analysis

The power calculation assumed a significance level of $\alpha = 0.05$, power of $1-\beta = 0.95$ to detect a 0.8 mm improvement in entry point accuracy with an estimated standard deviation of 0.7 mm based on previously published data(Dorfer et al., 2017). Based on this, paired results from 20 electrodes would, therefore, be required. Following implantation paired electrode bolt insertion accuracies for the entry point, projected target point and angle error were tested using both the Kolmogorov-Smirnov and Shapiro-Wilk tests to confirm a Gaussian distribution. A student's paired t-test (2-tailed) was then performed using SPSS 24.

10.4 **Results:**

10.4.1 Phantom testing accuracy

Figure 41: Pre-clinical Comparative Implantation Accuracy data

a) Comparison of frameless manual versus iSYS1 implantation error

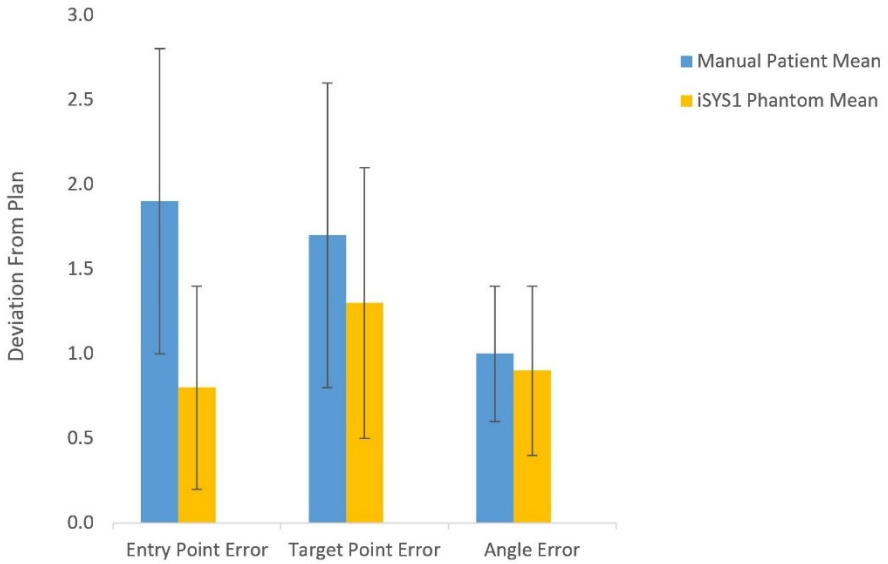

b) Comparison of the grade of electrode insertion

Grade	Deviation from plan (Greater of EP or TP)
1	<1 mm
2	<2 mm
3	<3 mm
4	>or = 3 mm

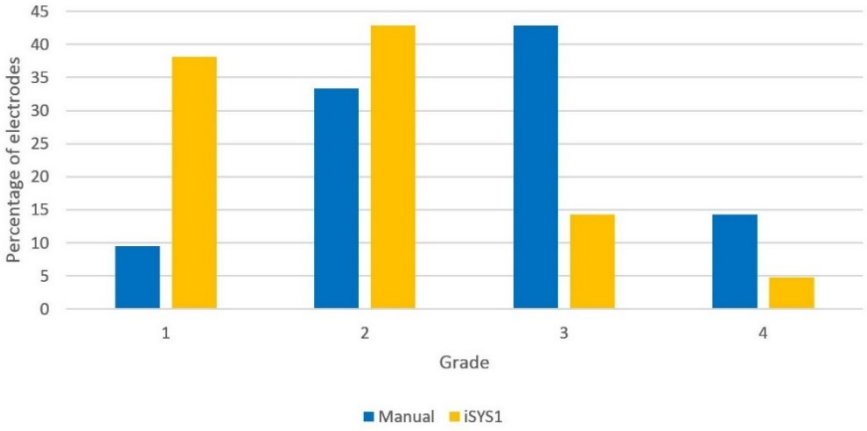

Figure 41 legend: a) Comparison of the entry point, target point and entry angle deviation from the plan with manual patient and iSYS phantom implantations. b) A suggested grading system for the clinical relevance of implantation error and proportion of manual patient and iSYS phantom electrodes within error tolerances.

10.4.2 Cumulative summation analysis results

Figure 42: CUSUM plots

a) Entry Point CUSUM

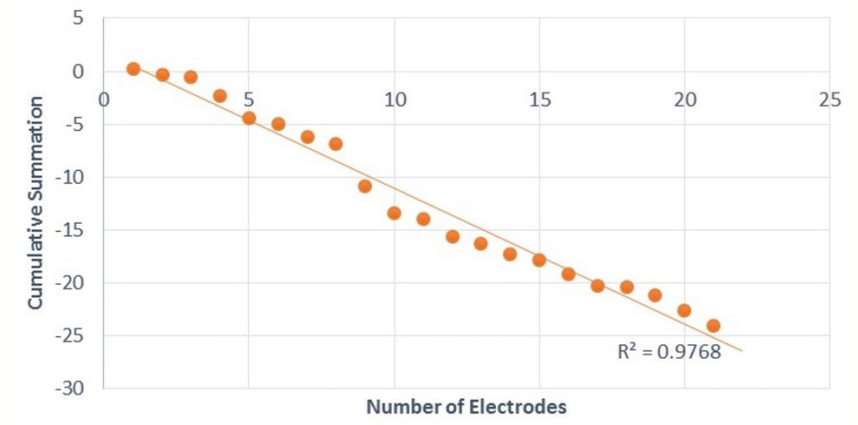

b) Angle Error CUSUM

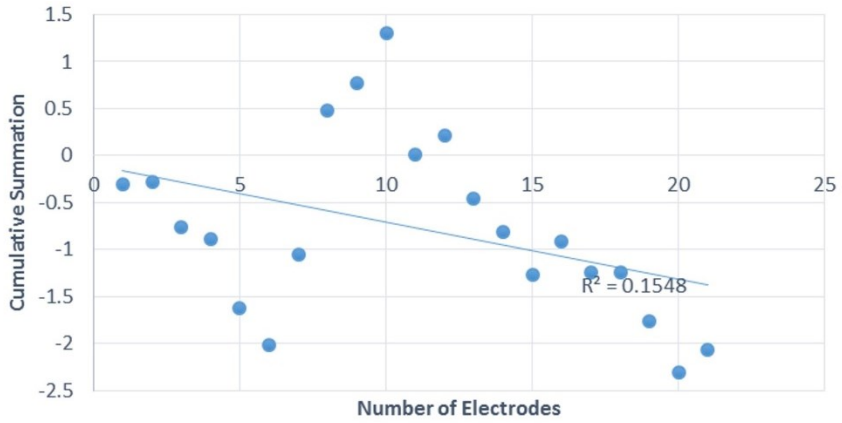

c) Target Point CUSUM

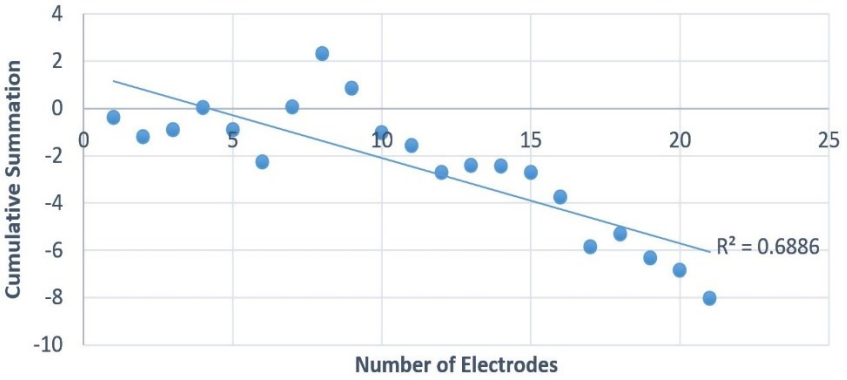

Figure 42: a) CUSUM for entry point error b) target point error and c) angle error. A negative gradient implies that the intervention (iSYS1) is more beneficial than the control (frameless) implantation. Any change to a positive gradient should alert the investigators to an increase in the potential risk of the implantation (as can be seen between electrodes 6-8 in c). b). The end of the learning curve is taken as the point where the positive gradient becomes negative or where the gradient is most negative. In figure 42a, the learning curve for entry point error becomes most negative after electrode 8. In figure 42b, the target point error becomes negative after electrode 8. In figure 42c, the angle error learning curve becomes negative after electrode 10, but there is a poor correlation between intervention and angle error.

Comparison of the frameless insertion of the SEEG electrodes in the patients with the iSYS1 system on the 3D phantoms resulted in a statistically significant ($p<0.01$) improvement in the entry point accuracy from 1.90+/-0.96 mm (Mean+/-SD) to 0.76+/-0.57 mm (Mean+/-SD) respectively. Projected target point accuracy improved from 1.72+/-0.98 mm (Mean+/-SD) to 1.34+/-0.86 mm (Mean+/-SD) but was not statistically significant ($p=0.17$). Angle error from the plan non-significantly improved from 0.95+/-0.39 degrees (Mean+/-SD) to 0.88+/-0.55 degrees (Mean+/-SD) ($p=0.59$).

The CUSUM analyses for the Entry point, Target point and Angle error are shown in Figure 42. The Entry point and Target point plots reveal a negative trend line with high correlation ($R^2 = 0.98$ and 0.69 respectively) indicating that the iSYS1 implantation technique is beneficial and does not increase risk. The angle error CUSUM, however, shows a wide variation with poor correlation ($R^2 = 0.15$) suggesting that the implantation method had LITTle or no effect on this.

10.4.3 Learning curve assessment

The end of the learning process is where the positive gradient of the curve becomes negative or the region in which the gradient becomes most negative. The CUSUM analysis curves (Figure 42), suggest that the overall learning effect was minimal and the maximal improvement with iSYS1 as compared to the frameless technique occurred after the 8th electrode.

10.5 **Discussion**

The transition of medical devices to the clinical setting through use by early adopters of technology has the potential to cause patient harm before the long term risks and benefits can be determined through methodologically sound clinical trials. In contrast to drug trials, where Phase 1 and 2 trials are performed on small numbers of patients to prevent harm, only 60% of devices were found to have published clinical trials prior to attaining regulatory approval. The IDEAL collaboration is an attempt to provide a framework for device trials analogous to that of a drug trial, in which small scale studies are performed using few patients to determine the device safety and efficacy prior to larger comparative studies in which long-term data can be gathered. During this period, robust early warning mechanisms are required that will detect any potentially deleterious effects of the device and thereby prevent patient harm. Here we have utilised a CUSUM Analysis to compare paired electrode insertions in an anatomically accurate

phantom using the iSYS1 robotic trajectory guidance system with previous frameless implantation in patients.

10.5.1 Comparison with other studies

CUSUM analysis has been used in a number of surgical and non-surgical fields to assess the learning curve of operators and as a continuous quality assurance indicator. Through the collection of prospective outcomes, real-time comparisons can be undertaken between prospective control groups, retrospective cohorts or previously established risk/failure rates. The main use of CUSUM analysis currently is to assess surgeon learning curves and training for new techniques, but it also has the potential to be applied as a quality assurance indicator, to surgeon revalidation and as an early warning detector in clinical trials.

To date, there have been no prospective control trials comparing SEEG insertion techniques. This is likely due to the requirement for a single unit to have a surgeon or group of surgeons who are capable of performing more than one implantation technique. There is some evidence from studies in which one technique has replaced another. Cardinale et al. (Cardinale et al., 2013), compared historical SEEG electrode implantation accuracy using the Talaraich frame with the Neuromate (Renishaw) robot. No prospective controlled trial data are available to suggest the superiority of one over the other. Given that the Neuromate (Renishaw) robot is now the standard of care in that unit, it would be ethically challenging to perform a prospective trial comparing it to the previous technique. The scenario of a single neurosurgical unit not having the surgical expertise to use more than one technique could be overcome through multi-centre trials, but individual surgeon specific performance is difficult to account for methodologically. Furthermore, comparison of techniques between different units may introduce a systematic bias. Another important consideration is how the learning effect will be overcome when comparing a new technique with less surgeon familiarity with a previously established one. CUSUM analysis may overcome this. Using paired electrode data, we showed that the performance of a novel device could be continuously monitored and any change in safety performance over time detected. By recreating an anatomically accurate phantom replica of a patient's skull using 3D printing technology, the same electrode trajectories could be implemented by the same surgeons to control for any systemic bias. During clinical trials, data monitoring committees are established to preside over serious adverse events and have the power to close trials prematurely when one arm of the trial shows significant benefit over

another. For an adverse event to reach statistical significance, a significant number of patients are exposed to risk. Our prospective power calculation revealed that 20 electrodes would be needed to statistically detect a 0.8 mm improvement in entry point accuracy. CUSUM analysis cannot replace statistical tests but does allow trends in beneficial or adverse events to be monitoring closely and could potentially alert investigators to deleterious outcomes before they become statistically significant. We found that using the iSYS1 trajectory guidance system implantation entry point accuracies were significantly improved ($p<0.01$) from 1.90+/-0.96 mm (Mean+/-SD) to 0.76+/-0.57 mm (Mean+/-SD). These results are consistent with a study by Dorfer et al. (Dorfer et al., 2017), in which preclinical testing of the iSYS1 device improved entry point accuracy to 0.6+/-0.4 mm (Mean+/-SD) from 1.4+/-0.5 mm (Mean+/-SD) with the frameless technique. The same group also reported entry point accuracy of 1.18 +/-0.5 mm (Mean+/-SD) in 93 electrodes in 16 patients, after slight modification of the technique. Cardinale et al. (Cardinale et al., 2013) have found a mean entry point accuracy of 0.78 mm using the Neuromate (Renishaw) for SEEG, and Mullin et al. (Mullin et al., 2016b) found a mean entry point accuracy of 1.2 mm using the ROSA system.

Based on these accuracy data Cardinale et al. recommended the institution of a safety margin of 3mm based on the following (see Equation 1: Planning Safety Margin Chapter 2.1.3) Overall, 1% of electrodes would deviate outside a 3 S.D. safety margin, which was deemed acceptable. When the CUSUM analysis is repeated on the basis of a 3 mm entry point safety margin and an accepted 1% violation rate, the iSYS1 device performed within this threshold for all implanted electrodes.

10.5.2 Study Limitations

Limitations of our study include the small study size (21 electrodes) and differences in the use of a 3D printed phantom compared to a patient. We tried to use a material that had similar properties to real bone, but the bone substitute was slightly harder.

The control group was derived from *in vivo* frameless implantations and we accept it may have been methodologically better if the frameless implantation method was also used on the phantoms. We compared the same surgeons to prevent inter-surgeon variability, but they have more experience with the frameless technique than with the iSYS1 robotic device. We found there was a very minimal learning curve associated with first-time use of the iSYS1 device and at all times, entry point accuracy was found to be more accurate than the frameless

technique. We do not feel that previous experience through implantation of electrodes in the patient using the frameless method would have resulted in an increase in the accuracy of the iSYS1 phantom implantation because the robotic implantations were performed on retrospectively implanted patients many months after the patient implantations. Furthermore, given that the iSYS1 trajectory guidance system performs the alignment automatically, we cannot envisage how prior experience with the skulls can improve the accuracy of the implantation.

We focussed on entry point accuracy over target point accuracy. The reason for this is that entry point accuracy and angle are the main factors that can be controlled by the surgeon. Given that the electrodes are flexible and inserted in a blind fashion, there is a potential for them to deviate within the brain. Our phantoms did not have a brain material within them and as such, we could not accurately compare actual target points. To account for this, we calculated projected target points based on the bolt tip and extrapolated this to a uniform distance for both manual and iSYS1 implantations. The majority of intracranial haemorrhages following SEEG implantation are extra-axial, most likely as a result of damage to cortical veins. Although there does remain a risk of haemorrhage along the entire intracranial length of the electrode small inaccuracies at the target are unlikely to prevent measurement of the inter-ictal and ictal electrophysiology from the target structure of interest.

10.6 **Conclusion**

The introduction of novel medical devices to clinical practice is associated with an inherent risk. A large proportion of devices are approved without rigorous clinical trial data, or long term follow up. Here we have shown that CUSUM analysis is an effective tool in the assessment of a novel robotic device for SEEG electrode insertion. As part of the preclinical testing, we recreated implantation schemes and implemented these using an anatomically accurate skull phantom. Entry point accuracy was statistically improved using the iSYS1 robotic trajectory guidance system. CUSUM analysis can be used as an early warning tool in conjunction with all stages of the IDEAL framework to enhance patient safety. A thorough independent appraisal of both the clinical and economic factors is required before medical devices can be widely adopted. Even with the use of methodologically sound clinical trials, patients are exposed to potential risks and it is an ethical obligation incumbent on all trial investigators to mitigate this risk as far as possible through early complication detection.

11 Comparison of robotic and manual implantation of intracerebral electrodes: a single-centre, single-blinded, randomised controlled trial.

11.1 **Abstract**

11.1.1 Introduction

We report a single-centre, single-blinded randomised control parallel-group trial of stereoelectroencephalography (SEEG) electrode placement in patients with refractory focal epilepsy.

11.1.2 Methods

Thirty-two patients consented for the study comparing conventional frameless SEEG electrode insertion utilising the precision-aiming device (PAD) versus the iSYS1 robotic trajectory guidance system. Electrodes were inserted to define the epileptic focus in the brain. The primary outcome measure was operative time (minutes) for insertion of the cranial bolts. Secondary outcomes were accuracy of implantation (entry point, angle and target point), total operative time, postoperative haemorrhage rate, infection rate and postoperative neurological deficit rate.

11.1.3 Results

Thirty-two patients were recruited, completed the trial and analysed. The iSYS1 robotic guidance system gave a significantly shorter mean operative time for intracranial bolt insertion, 6.36 min (95%CI 5.72-7.07) versus 9.06 min (95%CI 8.16- 10.06), ratio of median estimate (iSYS1/PAD) 0.70 (95%CI 0.61-0.81), p=0.0001. The PAD group had a better median target point accuracy 1.58 mm (95%CI 1.38- 1.82) versus 1.16 mm (95%CI 1.01- 1.33)), p=0.004. The mean electrode implantation angle error was 2.13^{o} for the iSYS1 group and 1.71^{o} for the PAD groups (p=0.023).. There was no statistically significant difference for any other outcome. Three patients (2 PAD) had small asymptomatic haemorrhages noted on post-operative imaging that did not require intervention.

11.1.4 Conclusion

Operative time for individual SEEG bolt insertion was significantly shorter with the iSYS1 robotic trajectory guidance system than the PAD. Target point accuracy was significantly greater with the PAD, this margin was not of clinical relevance for cerebral cortical SEEG.

11.1.5 Trial registration

ISRCTN17209025 (https://doi.org/10.1186/ISRCTN17209025)

11.1.6 Funding

Wellcome Trust (WT106882) and Medtronic Inc. provided equipment support through an external research program application (ERP ref: 221)

11.2 **Introduction**

11.2.1 Scientific background and rationale

Robotic surgical systems have seen exponential growth, both in the number of installations and breadth of procedures performed, over the last decade. The main applications have been in laparoscopic and thoracoscopic procedures (Childers et al., 2018). Randomised control trials for some indications have not shown a benefit for robotic-assistance over conventional laparoscopic surgery(Jayne et al., 2017). The economic cost of robotic surgery includes the purchase or lease of devices, associated instruments, consumables and service contracts, and increased utilisation of hospital resources, including increased operating room time and staff training. Within the United Kingdom, the period 2011-2012 marked an inflexion point when the number of robotic prostatectomies exceeded both laparoscopic and open procedures for the first time(Marcus et al., 2017).

Comparatively, uptake of robotic systems for cranial neurosurgical procedures has been slow, despite early technological innovation and adoption(Wang et al., 2017). The first robot-assisted stereotactic brain biopsy utilising a modified PUMA industrial robot was performed in 1985 with improved procedure time and intra-operative accuracy(Kwoh et al., 1988). Global installations of stereotactic trajectory guidance systems increased in the last decade, with common cranial indications including brain biopsy(Marcus et al., 2018), deep brain stimulation(Neudorfer et al., 2018), stereoelectroencephalography (SEEG)(Cardinale et al., 2013; Vakharia et al., 2017b) and therapeutic drug delivery(Barua et al., 2013).

SEEG is a procedure in which 7-16 electrodes are stereotactically implanted within predefined regions of the brain, to localize the source of drug-resistant focal epilepsy, in order to guide definitive resections to cure epilepsy (Vakharia et al., 2018a). Recent years have seen a shift away from subdural grid placement towards SEEG due to the more favourable side effect profile(Abou-Al-Shaar et al., 2018). Initially, SEEG electrodes were implanted using a stereotactic frame(Reif et al., 2016; Talairach et al., 1962). The restrictive, repetitive and time-consuming nature of frame-based approaches led to the development of frameless systems, which may give worse implantation accuracies(Vakharia et al., 2017b). Due to the number of electrodes implanted within individual patients and the requirement for precise implantation, SEEG has been suggested as being suitable for stereotactic robotic assistance. Despite the growth in the number and applications of robotic trajectory guidance systems, meta-analysis reveals that high-

quality evidence supporting their use is limited(Vakharia et al., 2017b). To date, there are no reported prospective studies comparing robotic devices with manual frame-based or frameless systems.

This suggests novel robotic devices were introduced, without parallel-group comparisons to the conventional methods. This may expose patients to increased harm until the associated learning curve is overcome, and outcome accuracy related to the device can be compared. We, therefore, undertook a randomised control trial of a novel robotic trajectory guidance device, the iSYS1 (Medizintechnik GmbH), to assess the real-world consequences of implementing this technology based on Stage 3 of the IDEAL framework for surgical innovation(Ergina et al., 2013; McCulloch et al., 2013).

11.2.2 Specific objectives and hypotheses

The primary aim of this trial was to determine whether the iSYS1 robotic trajectory guidance system required less operative time for SEEG bolt insertion than the conventional frameless method utilising the precision-aiming device (PAD). Secondary aims were to identify effects on implantation accuracy, infection and intracranial haemorrhage rates.

11.3 **Methods**

The study was approved by the Health Research Authority on 20/02/2017, REC reference: 17/EE/0016 and the Medicines & Healthcare products Regulatory Agency, MHRA Reference: CI/2017/0026. The trial protocol was prospectively registered available online and presented to key opinion leaders prior to recruitment(Vakharia et al., 2016a, 2017a). No changes to the methods or design were made after the trial started. The manuscript was prepared following CONSORT guidelines(Lancet, 2010).

11.3.1 Trial design

A single centre, single-blinded randomised controlled trial of SEEG electrode implantation methods in patients with drug-refractory focal epilepsy.

11.3.2 Participants

We included patients with drug-refractory focal epilepsy, due to undergo SEEG implantation as part of their pre-surgical evaluation, aged between 18-80 years and able to provide informed consent.

Exclusion criteria included pregnancy, uncorrectable coagulopathy, lack of capacity to consent and patients deemed unfit for general anaesthesia. Following a multi-disciplinary team discussion, all patients were given a patient information sheet before providing written informed consent. Written informed consent was taken by a delegated member of the research team and combined with a pre-operative hospital visit for digital subtraction angiography, 2-6 weeks prior to implantation. Patients were considered enrolled in the trial once randomised using Sealed Envelope™.

11.3.3 Interventions

Electrode trajectory planning was undertaken using the EpiNav™ platform (Sparks et al., 2017a; Vakharia et al., 2018e) prior to randomization to implantation method to prevent allocation bias. In brief, EpiNav™ is a complex clinical decision support software for SEEG trajectory planning, employing a semi-automated method based on user-defined parameters. Target and entry regions of interest are determined by a multi-disciplinary team of neurologists, neurophysiologists, neurosurgeons, neuropsychologists and neuropsychiatrists based on the non-invasive pre-surgical structural and functional MRI, PET, scalp video EEG, neuropsychological and psychiatric evaluations. EpiNav™ returns trajectories that minimise intracerebral length, drilling angle to the skull and maximises both absolute and cumulative distance from blood vessels (risk score) and grey-matter sampling. The algorithm ensures trajectories are >10 mm from each other to prevent an intracranial collision. All plans were checked by a neurophysiologist and amended as appropriate by a neurosurgeon before implementation.

Patients were randomised to SEEG insertion using either the PAD or the iSYS1 trajectory guidance system. All patients underwent insertion of bone fiducials under local anaesthesia for registration to the Medtronic S7 neuronavigation system. To minimise any confounding factors, the only difference in methodology between the two intervention arms was the device used for alignment of the drill guide to the pre-operatively planned trajectories.

Table 29 and Figure 43 show the individual steps involved in each of these procedures:

Table 29: Operative steps associated with each implantation method

Precision-aiming device:	iSYS1 trajectory guidance system:
1. Insertion of 6 bone fiducials under local anaesthesia	
2. CT scan	
3. General anaesthesia	
4. Placement of Mayfield Clamp	
5. Routine prep and drape	
6. Registration to S7 neuronavigation system with registration accuracy <0.6 mm	
7. Freehand marking of entry points	
8. (A) Alignment of the precision-aiming device to first electrode trajectory	(A) Rough alignment of iSYS1 trajectory guidance system to a satisfactory position
(B) Achievement of trajectory with a target point accuracy of <0.7mm (current clinically accepted threshold)	(B) Precise alignment of iSYS1 trajectory guidance system to the final position with an accuracy <0.1 mm (device threshold).
9. Skin incision at the defined entry point	
10. Steinmann pin used to define entry point prior to the drilling of trajectory	
11. Accuracy of trajectory checked with Vertek probe	
12. Insertion of the intracranial bolt	
13. Accuracy of trajectory checked with Vertek probe and new entry point set	
14. Removal of mechanical arm	
15. Measurement of electrode trajectory length (from top of the intracranial bolt to target point)	

16. Repeat steps 2-10 for each electrode to be inserted
17. Insertion of the stylet to the predefined length derived from step 10
18. Insertion of the electrode to the predefined length derived from step 10
19. Repeat steps 12-13 for each electrode to be inserted
20. Removal of bone fiducials
21. Placement of sutures to close the incision

Figure 43: iSYS1 robotic trajectory guidance implantation method

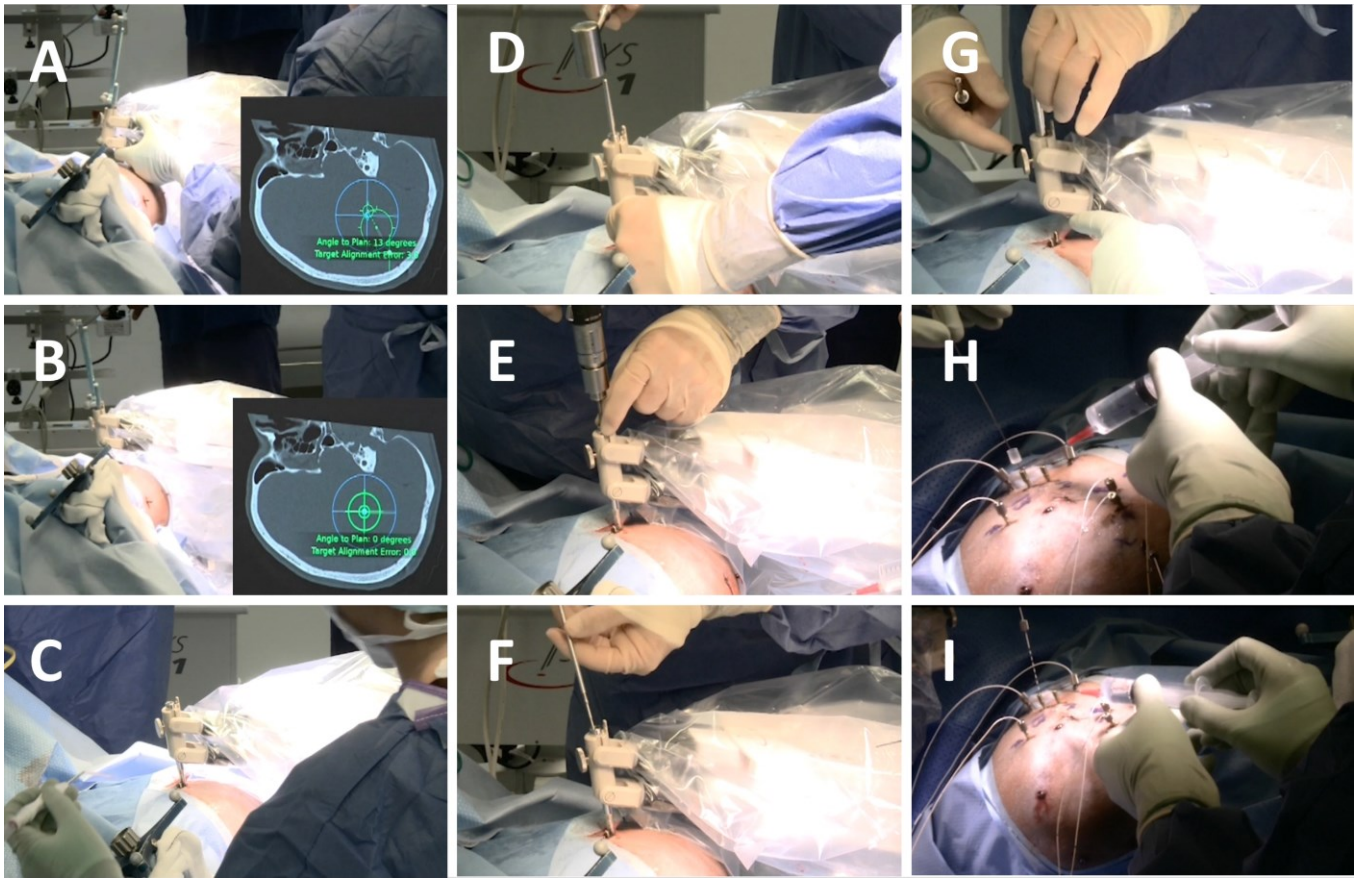

Figure 43 *Legend: Steps for iSYS1 insertion of SEEG electrode. A) The Vertek probe is inserted into the working channel of the iSYS1 device and the surgeon locks the device in rough alignment with the predefined trajectory. B) The iSYS1 automatically aligns the working channel to the trajectory achieving an alignment accuracy of ≤0.1 mm to the target and 0 degrees to the plan. C) The Vertek is removed from the working channel and replaced by a reduction tube. An incision is made in the skin to allow the reduction tube to contact the underlying skull. D) A Steinmann pin is then inserted through the reduction tube and with gentle tapping, a divot in the skull surface is made to define the entry point. E) Drilling of the skull is performed through the reduction tube. F) The skull anchor bolt is then fixed to the screwdriver and screwed into the skull through the reduction tube. G) The reduction tube is removed from the working channel of the iSYS1 device to reveal the implanted bolt. H) The iSYS1 device is then moved for insertion of the remainder of the bolts. After placement of all of the bolts, a stylet is placed through the bolt to the target point and then removed. G) The electrodes are then placed through the bolts to the predefined depth.*

11.3.4 Outcomes

The primary outcome was the operative time (minutes) for individual SEEG bolt insertion defined as the time taken from the start of alignment to removal of the Vertek arm after bolt insertion. These steps were common to both techniques (see steps 8-14 in Table 29) providing systematic and objective time points. Secondary outcomes included accuracy of SEEG electrode placement, the incidence of clinically and non-clinically significant haemorrhages, infection rate and new postoperative neurological deficit rate.

SEEG electrode placement accuracy measures were undertaken for the entry and target points using lateral deviation between the implemented and planned trajectory in an automated fashion. The algorithm automatically segmented and reconstructed the individual electrodes based on the contacts identified from the post-operative CT as described in (Granados et al., 2018a). All segmentations were manually checked to ensure the correct contacts were assigned to the relevant electrodes. Entry point accuracies were back-projected and measured at the scalp surface. Due to the potential for the bolt to be displaced or bent following insertion, particularly in the temporal region, where the bone may be thin, or in patients with violent hypermotor seizures, we opted not to use the bolt axis to define the implemented trajectory. Instead, the most superficial contacts within the first 20 mm of the electrode were identified and a line of best fit was back-projected to the scalp surface to mark the implemented entry

point of the electrode. The error in the angle of insertion was also determined based on the line of best fit.

Clinically and non-clinically significant haemorrhages were detected on postoperative neurological examination and post-operative imaging, respectively. All patients underwent a CT scan of the head immediately post-implantation and an MRI scan of the brain within 48 hours. Radiological images were reported by a neuroradiologist blinded to the treatment arm allocation. Clinically significant haemorrhages were defined as those in which the patient had a postoperative complaint or neurological deficit and with a corresponding haemorrhage on the postoperative imaging. Non-clinically significant haemorrhages were defined as haemorrhages without any neurological consequence or clinical sequelae.

Clinical examination for neurological deficits was performed immediately postoperatively and at subsequent clinical interactions at 24 and 48 hours. The electrode insertion sites were checked by the clinical teams, who were blinded to the implantation method, and any infection reported. All patients received prophylactic antibiotics for the duration of the SEEG implantation as part of institutional microbiology policy.

11.3.5 Randomisation

We randomly assigned patients to the PAD or ISYS1 trajectory guidance implantation systems (using a 1:1 ratio), employing a computer-generated random sequence and random permuted blocks. An independent statistician created and tested the randomisation list which was then uploaded onto a computerised system provided by SealedEnvelope. A designated member of the surgical team randomised patients by logging into the online system after a patient had given informed consent 2 to 7 days prior to the scheduled surgery date. No members of the trial team were aware of block sizes to ensure that allocation was concealed.

11.3.6 Blinding

The patients, trial statistician and reporting radiologists were blinded to the intervention arm. For practical and logistical reasons, it was not possible to blind the surgical and research team members.

11.3.7 Sample size

The sample size was based on a difference of 20% in the median time for SEEG bolt insertion between the robotic and conventional frameless insertion groups, which indicated that each group should contain 90 electrodes for a two-sample t-test with a 5% significance level and 90% power. This assumed that electrode insertion times have a log-normal distribution and

accounted for the clustering of electrodes within patients, with an estimated intraclass correlation coefficient of 0.2 and an average cluster size of 10 electrodes per patient. This would imply that nine patients per group needed to be recruited; we increased this to a sample size of 16 patients per group to account for the possibility of patient drop-out and variable cluster size(O'Keeffe et al., 2017).

11.3.8 Statistical methods:

All analyses used intention-to-treat principles (with patient data analysed by the group to which the patient was randomised). We analysed the electrode insertion time (minutes) using random-effects linear modelling, to account for electrode clustering within patients with log-transformed times owing to right skewness in the insertion time distribution. We analysed electrode-level continuous secondary outcomes (skull entry point accuracy, target point accuracy and error of angle of implantation) using similar random effects linear models (with a log-transformation). Categorical secondary outcomes (numbers of haemorrhages, infections and neurological deficits) were summarised in tables by the randomised group. We performed all analyses using R (version 3.5.1).

11.3.9 Role of the funding source

The sponsor of the study had no role in the study design, data collection or analysis and writing of the manuscript. External audit of trial data and procedures were performed at four stages during the trial, including a closeout visit. In addition to the trial management group, trial steering and independent data monitoring committees were established for trial oversight. The corresponding author had full access to the data and has final responsibility for the decision to submit for publication.

11.4 **Results**

11.4.1 Recruitment

We recruited thirty-two patients from 21/10/2017 to 19/03/2019. All patients completed follow-up and were included in the quantitative analysis, with no switching between treatment groups. We randomly assigned 16 patients to the iSYS1 intervention (with 160 electrodes implanted) and 16 patients to the PAD group (with 168 electrodes implanted).

11.4.2 Baseline data

Baseline characteristics were evenly balanced between the two groups, although more males were assigned to the iSYS1 group (Table 30).

Table 30: Demographic variables, stratified by randomised group.

Variable		Randomised group	
		iSYS1	PAD
Sex	Male	12	6
	Female	4	10
Side of implantation	Left	8	8
	Right	8	8

Variable	Randomised group	No. of patients	Mean (SD)	Median	Minimum	Maximum
Age (years)	iSYS1	16	35.9 (8.2)	37.3	21.2	47.5
	PAD	16	32.5 (6.1)	33.4	22.0	42.0
Number of electrodes implanted	iSYS1	16	10.0 (1.6)	10.0	7	13
	PAD	16	10.5 (1.9)	10.5	7	14

11.4.3 Numbers analysed

Figure 44: Consort diagram showing recruitment and follow-up of patients

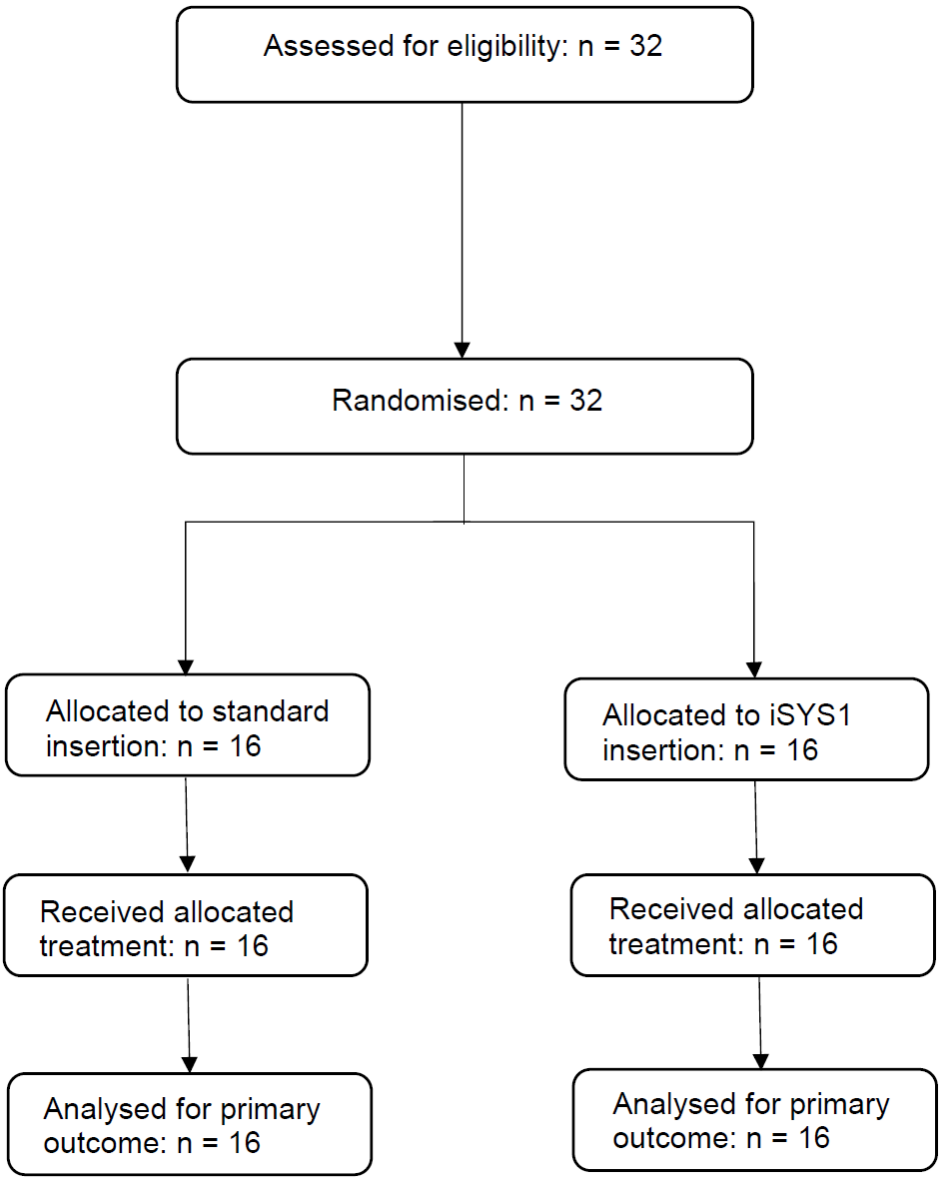

11.4.4 Outcomes and estimation

The primary outcome of individual bolt insertion implantation time for each electrode was significantly less for the iSYS group (median of 6.36 minutes (95% CI 5.72 to 7.07) than for the PAD group (median of 9.06 minutes (95% CI 8.16 to 10.06) P=0.0001). We estimated the ratio of median insertion times (per electrode) for iSYS1 group/PAD group as 0.70 with 95% CI

(0.61 to 0.81). This suggests an estimated reduction of insertion time per electrode of 30%, on average, for the iSYS1 group compared to the PAD group.

Regarding secondary outcomes, electrode target point accuracy differed significantly between groups (median TPA estimates (95% CI) were 1.58mm (1.38 to 1.82) and 1.16mm (1.01 to 1.33) for the iSYS1 and PAD groups, respectively, P = 0.004). Electrode angle of implantation error differed significantly between groups (median angle error estimates (95% CI) were 2.13 degrees (1.87 to 2.41) and 1.71 degrees (1.51 to 1.94) for the iSYS1 and PAD groups, respectively, P = 0.023). Other secondary clinical outcomes did not differ significantly between groups (Table 31). Mean total operative time was 211.1±71.4 minutes (mean±SD) with the PAD and 181.9±45.8 minutes (mean±SD) with the iSYS1 (p = 0.29, t-test 30 D.O.F.). The entry point implantation accuracy of the PAD was 1.4±0.7 mm (mean±SD) compared with 1.2±0.6 mm (mean±SD) with the iSYS1 (p = 0.33, t-test on 30 D.O.F.).

Table 31: Summary of post-operative outcomes by treatment group.

	iSYS1 group	PAD group	Ratio of median estimate (iSYS1/PAD groups) (95% CI)	P-value
Electrode insertion time (mins) Median (95% CI)	6.36 (5.72 to 7.07)	9.06 (8.16 to 10.06)	0.70 (0.61 to 0.81)	0.0001
Total operative time (min)* (Mean±SD)	181.9±45.8	211.1±71.4	0.92 (0.78, 1.08)	0.293
Entry point accuracy (mm)* Median (95% CI)	1.09 (0.99 to 1.20)	1.17 (1.06 to 1.29)	0.93 (0.81 to 1.07)	0.334
Target point accuracy (mm)* Median (95% CI)	1.58 (1.38 to 1.82)	1.16 (1.01 to 1.33)	1.37 (1.12 to 1.67)	0.004
Error of angle of implantation (degrees)* Median (95% CI)	2.13 (1.87 to 2.41)	1.71 (1.51 to 1.94)	1.24 (1.04 to 1.48)	0.023
Post-operative haemorrhage	1/16 (6.25%)	2/16 (12.5%)		
Post-operative infection	0/16 (0%)	0/16 (0%)		
Post-operative neurological deficit	0/16 (0%)	0/16 (0%)		

*Difference estimate adjusted by the number of electrodes inserted. For electrode-level data, n = 160 for the iSYS1 group and n = 168 for the PAD group (with the exception of entry point accuracy, target point accuracy and angle error in the iSYS1 group where n = 159).

As an early warning system to detect potential harm following the introduction of the novel medical device, we prospectively implemented a cumulative summation analysis. Subgroup analysis of the outcomes within chronological recruitment quartiles did not reveal any significant differences, suggesting that there was no detectable learning curve for the novel device(Vakharia et al., 2018b).

11.4.5 Harms

Adverse events related to SEEG insertion were noted in three patients, two of whom were in the PAD group. These were asymptomatic small volume haemorrhages detected on the immediate postoperative CT without clinical sequelae. The haemorrhages were located in subarachnoid space of the sylvian fissure following insular implantation, the subdural space and within the parenchyma at the cortical insertion site of an electrode. The haemorrhages were not related to electrode misplacement or inaccuracy and review of the pre-operative angiography did not reveal a vessel conflict when registered and fused to the post-implantation CT. As a result, these were not considered adverse device effects. There were no serious adverse events in either intervention arm of the trial.

11.5 **Discussion**

The use of the iSYS1 robotic stereotactic trajectory alignment device significantly reduced SEEG bolt insertion time by 30%. Based on an average number of implanted electrodes of 10, this equated to a mean reduction in total operative time of around 30 minutes, but this difference was not statistically significant, in the comparison of the overall operative times. The target point and angle of insertion accuracy of the iSYS1, however, was significantly worse by an average 0.5 mm and 0.4 degrees, respectively. For cerebral SEEG implantations, these differences were not clinically relevant as this falls within the 3mm safety margin applied during trajectory planning. There was no difference in entry point accuracy between the two groups.

11.5.1 Strengths and limitations

Strengths of this study include a comparison of a novel robotic device (iSYS1) that closely aligns with the current operative workflow and assigning the same surgeons to both intervention arms to mitigate bias. We employed a pragmatic study design in which we compared the conventional method of SEEG insertion which is established at the study institution with a novel robotic device that the surgeons had less experience of, reflecting the real-world adoption of intraoperative robotic technologies. The main limitation of our study is that it is in a single centre. Due to the highly specialised nature of SEEG implantations, these procedures are concentrated at high volume epilepsy centres. We have previously ascertained that when a novel technique is introduced, this often supersedes the previous method without prospective parallel-group comparisons(Vakharia et al., 2017b). A multi-centre study would improve the generalisability and robustness of the results but could also potentially introduce bias as a result of different practices between surgeons and institutions.

Another potential limitation is the choice of robotic device. There are a number of different robotic devices available. We opted to compare the iSYS1 for a number of reasons. Firstly, the surgical workflow with the iSYS1 closely follows that of the frameless manual method that is currently used at our institution (see

Table 29). Only the alignment portion (step 8) of the 21 steps outlined, differs. This allows a direct comparison of the contribution of the iSYS1 to the manual alignment arm, therefore, minimising confounding factors. Further, the iSYS1 system is compact and portable, with a small footprint, and established familiar interface through the Stealth station, relative cost and likely applicability of the findings to the stereotactic neurosurgical fraternity. Other robotic devices such as the NeuroMate and ROSA have not previously been shown to be more accurate or quicker than conventional stereotactic methods in a head to head prospective comparison. Typically, each surgical epilepsy centre has expertise with only a single robotic device, so we chose not to undertake a head to head comparison between robotic devices in the first instance.

11.5.2 Generalisability

We compared the robotic device to the PAD frameless implantation system and not to a frame-based system as this reflects the standard of care at the study institution and has been performed since July 2012. To optimize accurate trajectory alignment and safety of the PAD procedure, a number of modifications and improvements have been applied, which have recently been reported(Rodionov et al., 2019). These include the application of bone fiducials for registration to the neuronavigation system and use of 'trajectory guidance' during alignment (StealthStation S7 Cranial version 2.2.6 or later, Medtronic Inc.). To ensure implantation quality assurance, thresholds were set for image registration and electrode-trajectory alignment. Image registration utilising bone fiducials was applied to both arms of the study and only optical registration accuracies of <0.6 mm were accepted. Image registration was repeated after draping of the patient and bone fiducials were left exposed during the procedure to allow registration to be checked and redone as necessary. 'Trajectory guidance' allows the alignment device, in this case, the Vertek probe, to align to both the entry and target points of the trajectory. This is in contrast to 'target guidance', which reports the alignment accuracy at the target point regardless of the cortical entry. The iSYS1 and the PAD were aligned according to the pre-operatively planned trajectories provided by the S7 neuronavigation system via the Vertek probe. Any systematic inaccuracy as a result of the optical registration or guidance would, therefore, be equally applied to both intervention arms. The accuracy of alignment to the pre-planned trajectory on the neuronavigation system for each electrode, regardless of the implantation method, had to achieve <0.7 mm prior to commencement of drilling and bolt insertion. Due to the predefined accuracy threshold, implantation time was taken as the primary outcome measure between the two methods. An important distinction between the two intervention arms is platform stability. Both the PAD and the iSYS1 are fixed to the vertek mechanical arm. During drilling, any inadvertent lateral forces applied by the surgeon may result in a slight displacement of the mechanical arm and inaccurate angle of insertion with a consequent target point error. The PAD technique allows the trajectory alignment accuracy to be monitored continuously through the use of the SureTrak system. Deterioration in accuracy during the PAD technique would prompt the surgeon to realign before continuing with drilling. The iSYS1 did not have the same ability to detect this as continuous trajectory alignment accuracy measures were not possible during drilling and may be exacerbated by the moment introduced by the weight of the device (1.2kg). This may be one potential reason for the greater target point and insertion angle errors despite similar entry point accuracies.

11.5.3 Interpretation

Before commencing the randomised control trial, we undertook a PRISMA systematic review and mixed-effects meta-analysis of published SEEG methods and their corresponding accuracies(Vakharia et al., 2017b). The meta-analysis was registered on the PROSPERO database (registration number CRD42016047839), through which the review protocol can be accessed(Vakharia et al., 2016b).

Using the Preferred Reporting Items for Systematic Reviews and Meta-Analysis (PRISMA) guidelines(Liberati et al., 2009), we undertook a structured search of the PubMed, Embase and Cochrane databases. The last date of the search was undertaken on the 16/09/16. After applying eligibility criteria, 35 articles were subject to full manuscript review. A comparison of the articles for inclusion between the two independent researchers was undertaken and revealed high concordance between the identified studies. In total, 17 studies were included in the qualitative and 15 in the quantitative synthesis (see Figure 45).

Following the completion of the trial, we repeated the search with the same systematic review methodology and updated the qualitative and quantitative analysis with subsequent manuscripts published after 16/09/16. The last date for the updated search was 30/04/2019. A total of 524 publications were returned, indicating an additional 196 additional publications during the trial period. After removal of non-English language and duplicate manuscripts, an additional 163 study title and abstracts were screened. Twenty-six manuscripts underwent full-text assessment, and a further 3 studies were included in the quantitative synthesis. The remaining studies could not be included as they failed to reach the eligibility criteria or effects size and standard deviations were not provided (see Figure 46).

Figure 45: Updated PRISMA 2009 Flow Diagram

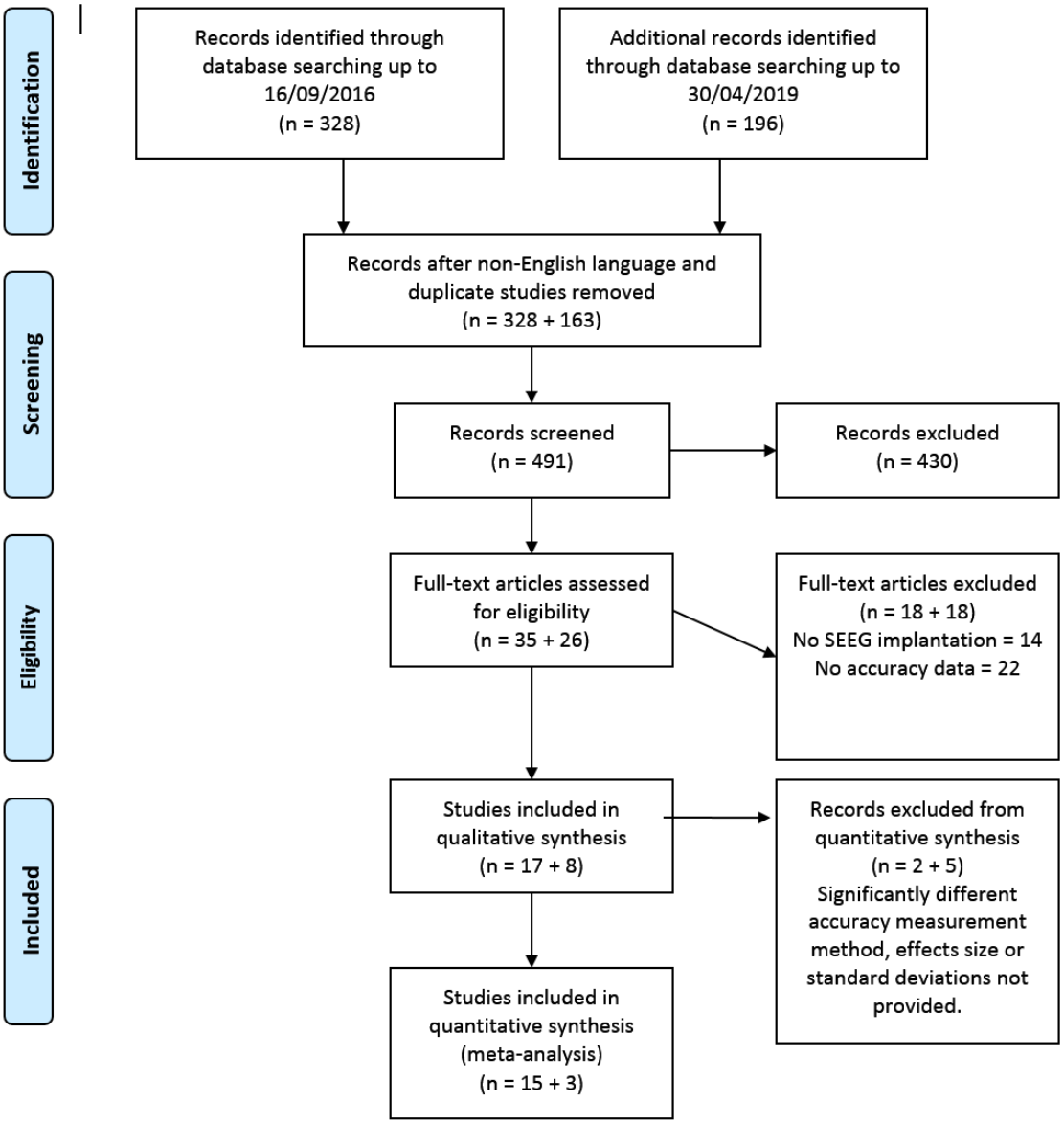

From: Moher D, Liberati A, Tetzlaff J, Altman DG, The PRISMA Group (2009). *P*referred *R*eporting *I*tems for *S*ystematic Reviews and *M*eta-*A*nalyses: The PRISMA Statement. PLoS Med 6(7): e1000097. doi:10.1371/journal.pmed1000097

For more information, visit www.prisma-statement.org.

Figure 46: Updated Forest plot:

A) Entry Point Accuracies (mm)

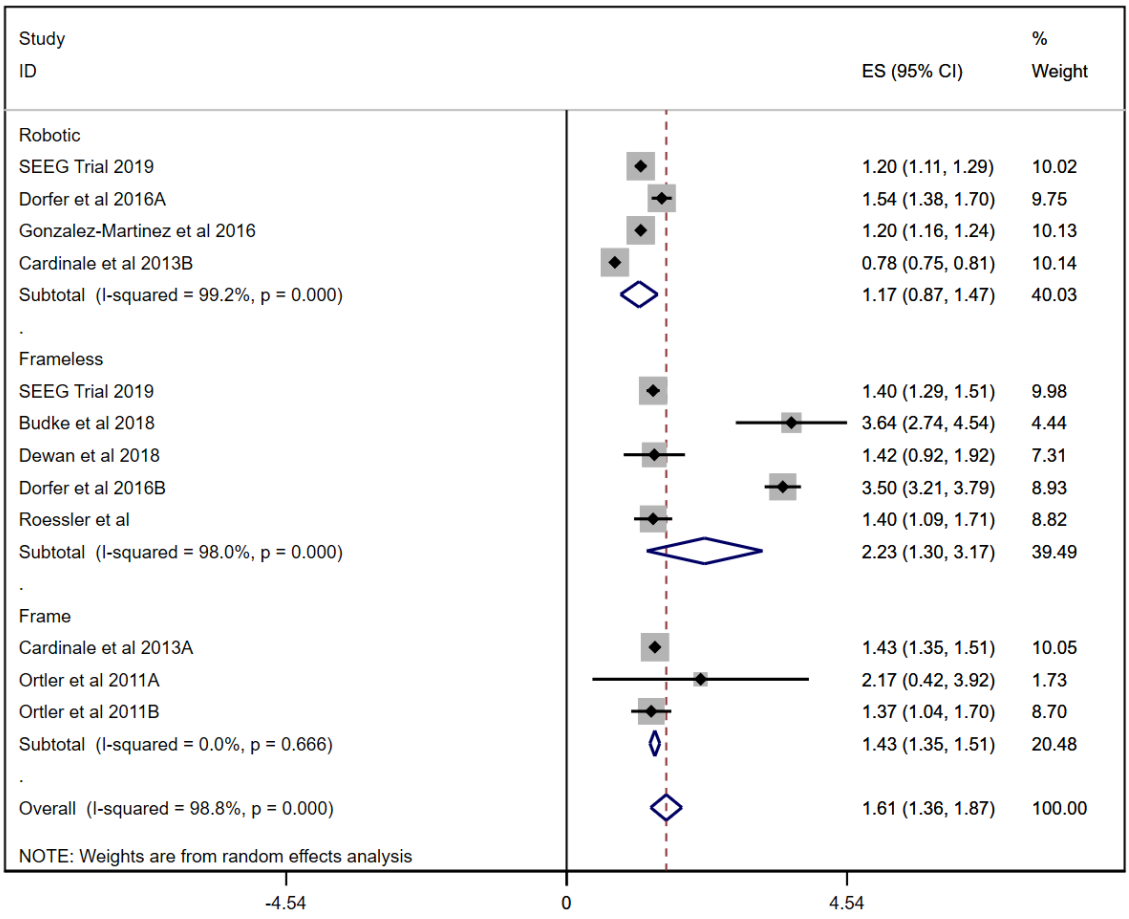

B) Target Point Accuracies (mm)

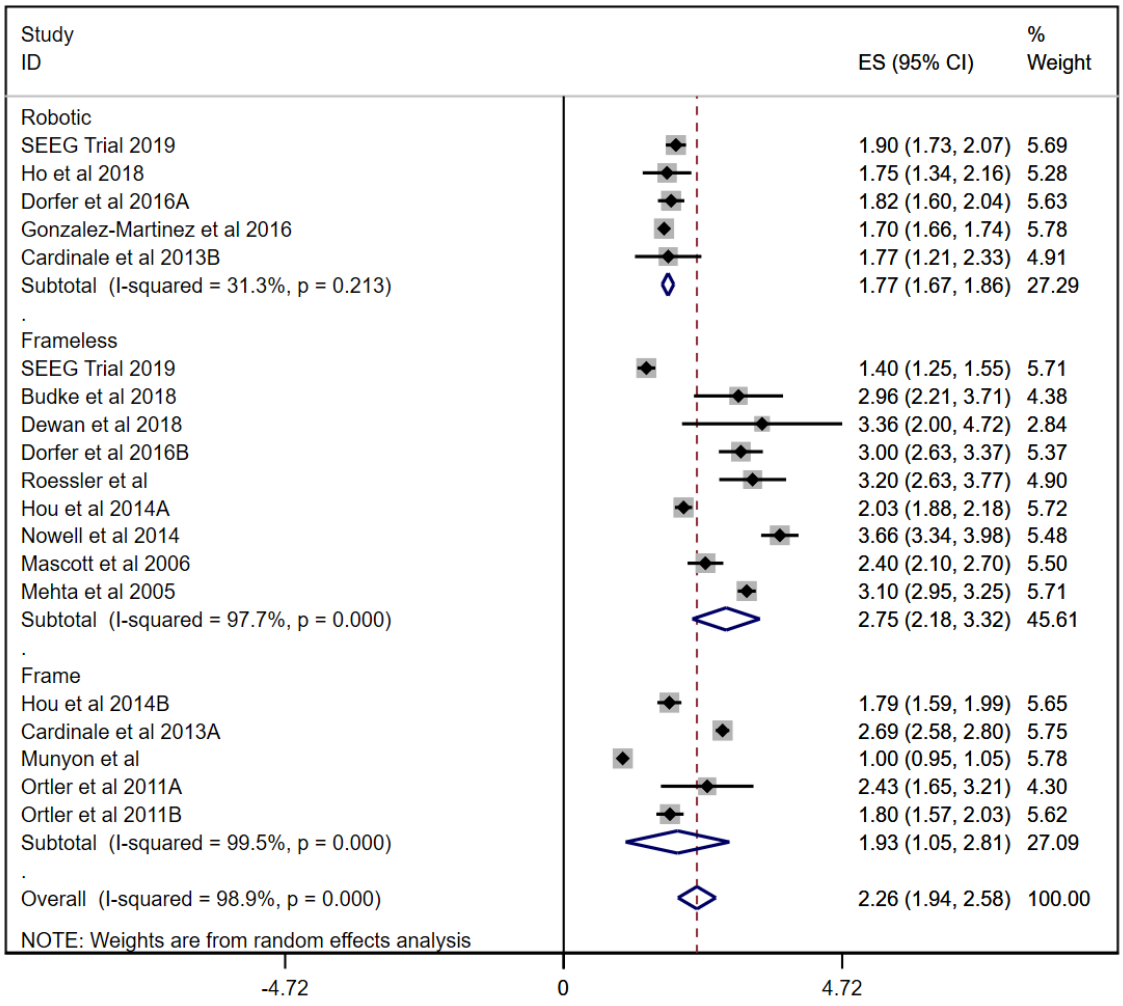

Legend Figure 46: Representation of the PAD and iSYS1 entry (A) and target (B) errors as part of a random-effects meta-analysis of the published literature to date (last search 30/04/19). This suggests that both the PAD and iSYS1 arms used in this study provided accuracies similar to that of other robotic devices in the published literature. There was no overlap in the 95% confidence intervals of the PAD arm with any other studies in the frameless subgroup, suggesting that in the current study the PAD target point accuracy achieved was greater than other studies in the reported literature. We hypothesise that this is due to the stringent alignment accuracy criteria set during the alignment step and the continuous accuracy tracking during the drilling stage.

11.6 **Conclusion**

This study shows that the iSYS1 robotic trajectory device reduces SEEG implantation time compared to the frameless PAD device. The overall operation time, however, including positioning, draping, neuronavigation setup and placing electrodes was not significantly less with the iSYS1. For SEEG, the iSYS1 robotic guidance system offers a consistent and effective solution.

The entry and target point accuracies of both devices were similar to the reported results of other robotic devices such as the Neuromate (Renishaw, Gloucestershire, UK) and ROSA (Medtech, Montpellier, France) and were satisfactory for the placement of cerebral SEEG. They would also be suitable for placement of shunts and cerebral biopsies. Further research should focus on cost-benefit analyses of introducing robotic devices into clinical services and prospective head-to-head comparisons between different robotic devices in these and other indications such as DBS, where the accuracy differences may be more clinically relevant.

12 Future work and concluding remarks

12.1 **Machine learning of planning preferences and global networking**

A significant limitation of computer-assisted planning algorithms is that they are dependent on the quality of the imaging provided, user-defined planning parameters and reflect the planning practices at the institution from which they were developed. This subsequently limits the generalizability of the software and its applicability to other SEEG programs. One potential method to overcome this is the use of machine learning to modify the planning parameters and practices to that of the individual user. One such method is the use of spatial priors. The current computer-assisted planning systems are all, to some extent, restricted by the whole brain parcellation and the sub-segmentation of individual structures. If the hippocampus, for example, is not subdivided into head, body and tail and the user, therefore, cannot choose from these options when specifying the trajectory targets. It is common practice to place SEEG electrodes within both the hippocampal head and body during an investigation of a patient with presumed temporal lobe onset seizures. Furthermore, it is prefered to place the targets within the medial aspect of the structures to ensure as many contacts are within the target structure when approaching from a lateral neocortical entry zone. The experience gained from previous manual implantations can, therefore, be used to inform the preferred entry and target regions of common trajectories and be used prospectively to guide future implantations. It has been proposed, therefore that the whole brain parcellation initially acts as the default and machine learning algorithms are then able to modify the regions based on the surgeons planning preferences. The other major advantage of a priors based system is that once it is developed specifically for that institution, there is no longer a dependency on the whole-brain parcellation which itself is limited by the parcellation algorithm and the image acquisition quality. This would also allow imaging with artefacts, such as those due to patient movement that ordinarily would fail the parcellation algorithm to be used. The generation time of the whole-brain parcellation can take between 2 and 24 hours depending on the algorithm and computing power available. A movement towards a priors based planning system could also result in real-time computer-assisted planning without the need for significant preprocessing time.

The generation of multicenter priors is also an attractive proposition which would allow external sites to emulate the practices of other more established institutions. Given a large enough database of trajectories, it may also be possible to develop a palette of common trajectories that provide the ‘standard’ set of entry and target point combinations for particular

seizure types. In ‘temporal plus’ epilepsy, for example, an anterior temporal resection is estimated to convey only 15% seizure freedom rates compared to 75% in unilateral temporal lobe epilepsy because a proportion of the epileptogenic zone extends beyond the lateral neocortex and mesial temporal components(Barba et al., 2016). In such cases, an SEEG is commonly performed with targets placed in the amygdala, anterior hippocampus, posterior hippocampus, temporo-occipital junction, orbitofrontal cortices, cingulate cortices, parietal cortex and the insula. Libraries of common implantation schema may, therefore, allow the clinical team to choose the combination of electrode trajectories that best fits the hypothesis derived from the presurgical evaluation and add or remove additional electrodes as required.

Recent preliminary data has also suggested that it may be possible to cluster implantation schema into a discrete number of strategy subtypes(Scorza et al., 2018). Following a retrospective review of implantation strategies at a national epilepsy referral centre in Milan, the group applied a K-NN clustering algorithm to identify that all of their implantations could be divided into one of eight types based on the trajectory entry and target structures. For these authors, a library of eight implantation schema combined with entry and target point priors would provide an attractive solution for computer-assisted planning. Another possible extension of machine learning for this purpose would be in the form of a ‘recommender’ system. These are also a form of clustering algorithm that calculate the association strengths between individual and combinations of items within data structures. Commonly used in shopping websites theses systems analyse combinations of chosen items and return other items that may be linked i.e. “other shoppers also bought …”. Within CAP algorithms, it may be possible to develop libraries of common implantation schema that may be returned to the surgeon with suggestions for further trajectories based on the combination of prior selected electrodes and the implantation practices of other institutions.

The implication is that the computer-assisted algorithms may also be able to aid in the refinement of implantation strategies. Both of these factors are likely to improve the feasibility and external validity of the planning algorithms in the future and will facilitate the comparison of data between sites.

The ‘internet of things’ (IoT) is a concept that has been coined to describe devices that are interconnected via the internet to integrate and share information. In commercial settings, this has been used to develop smart fridges, for example, that can monitor their contents and

order replenishments when stocks are low. Extensions of this technology can also use the list of fridge contents to cross-reference recipes on the internet and return meal suggestions as well as providing dietary advice. The 'use-by dates' can also be stratified to ensure the food is consumed in a timely fashion thereby reducing waste and prevent ingestion of potentially contaminated expired food substances. Other examples include the use of 'smart' devices such as telephones and watches to control domestic appliances including lights, heaters, cookers, CCTV and baths remotely. Although this may seem abstract to epilepsy surgery the IoT, in combination with machine learning, has the potential to revolutionise and systematise surgical practices on a global scale. A surgeon in one country, for example, may plan an SEEG procedure using a CAP or neuronavigation system. If these devices were connected to the IoT with a global central repository of SEEG procedures connected to real-time complication reporting the machine learning aspect may be able to detect and highlight potentially dangerous trajectories before the implantation based on the trajectory metrics. With sufficient data, that could only be achieved through a global collaboration, the concept of an electrode risk score as a surrogate for implantation safety would be redundant and replaced with an actual probability of haemorrhage. Furthermore, with knowledge of the implantation strategy and the clinical semiology, it may be possible to provide anatomical electrode targets based on the experience from previous SEEG implantations.

12.2 **Connectivity driven SEEG**

Epilepsy is now widely accepted as a network disorder and the fundamental principles of SEEG are to identify the seizure onset zone and spread through the ictal network. Rapid spread to adjacent anatomical structures occurs through a combination of both long and short association fibres whilst in vitro animal models have shown that cortical propagation occurs over a longer time-course in a heterogenous manner based on the variability in GABAergic inhibition(Wenzel et al., 2017). SEEG is limited by the number of electrodes that can be implanted and is, therefore, susceptible to a sampling bias. In pseudo-temporal lobe epilepsy, where the ictal onset is outside of the temporal lobe there is a rapid propagation to the temporal lobe which consequently mimics temporal lobe epilepsy clinically and electrophysiologically. Previous studies have also shown that resection of the seizure onset zone and any regions that demonstrate ictal activity within 10 seconds of the seizure onset confer a greater seizure-free post-operative outcome. It stands to reason that if an anatomical structure is considered to be part of the ictal network and SEEG sampling of the structure is

required, then the regions with the greatest structural connectivity to the regions of interest should be sampled. Whole-brain connectomes derived from diffusion fibre tractography provide a unique opportunity to study the underlying structural connectivity in vivo. On an individual basis, this could be used to guide SEEG trajectory planning by identifying subregions of anatomical structures that are most likely to be connected and therefore part of the ictal network.

Figure 47: Structural connectivity of the insula cortex in suspected pseudo-temporal or temporal plus epilepsy

Left MTLE: Right MTE:

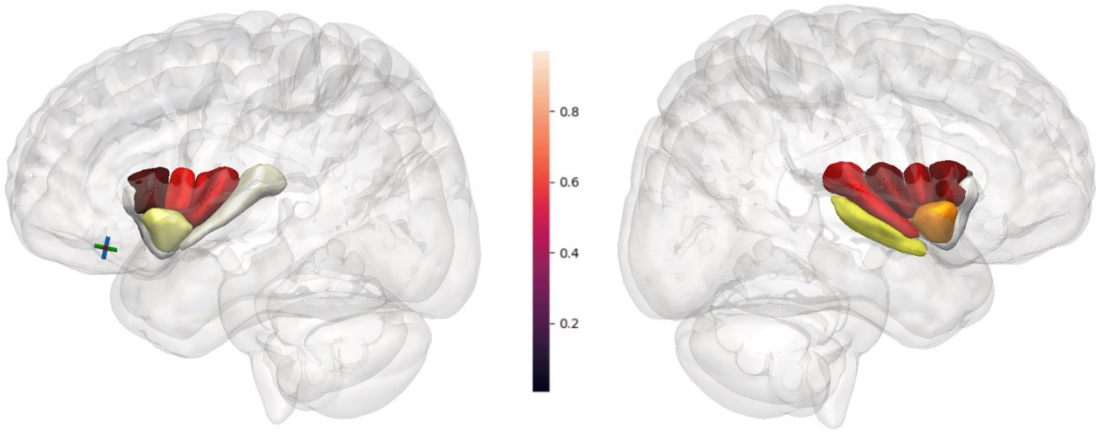

Figure 47 Legend: Preliminary work undertaken as part of the thesis in patients with suspected pseudo-temporal or temporal plus epilepsy that underwent invasive evaluation with SEEG revealed differential structural connectivity of the ipsilateral amygdalohippocampal complex. Left MTLE patients showed preferential structural connectivity to the transverse insula gyrus, the posterior long insula gyrus and the apex of the insula. Conversely, in right MTLE, the transverse temporal gyrus showed relatively greater connectivity. Mean connectivity values for 10 patients (5 right) are shown.

Preliminary work on patients with suspected pseudo-temporal and temporal plus epilepsy has identified differential connectivity within anatomical structures that are likely to be part of the ictal network, such as the insula, cingulate, orbitofrontal, parieto-occipital and temporo-occipital cortices (see Figure 47 for connectivity to the insula). In combination with

CAP, weightings can be attributed based on the structural connectivity within the anatomical regions of choice and the combination of the region with the greatest connectivity and the lowest risk score may provide the optimal region for sampling. Prospective validation of this method is required and if successful would represent a paradigm shift in modern SEEG planning.

Figure 48: Lowest risk scores for CAP trajectories calculated for each of the subregions of the insula

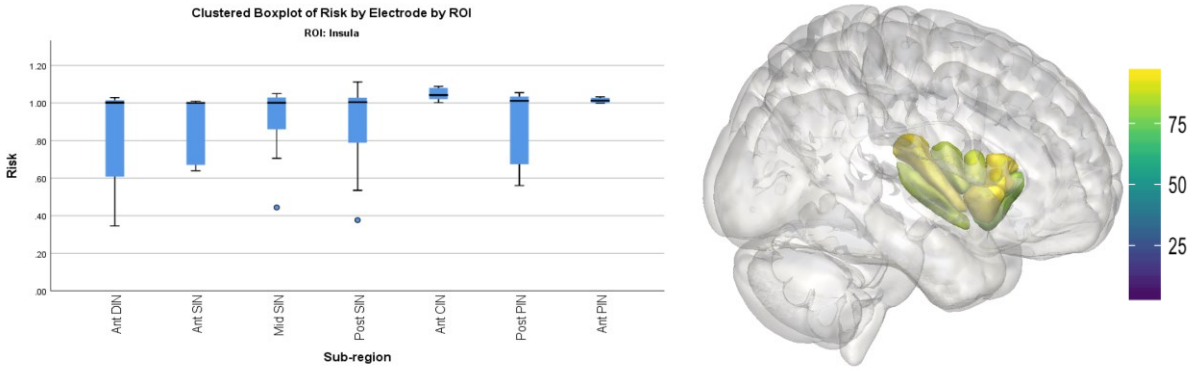

Figure 48 Legend: Boxplot of median risk scores with 95% CI for CAP generated trajectories targeting each of the insula subregions (left) and surface representation of the risk shown as a heat map with the corresponding key for colour coding (right). Ant DIN = Transverse insula gyrus, Ant SIN = Anterior short insula gyrus, Mid SIN = Middle short insula gyrus, Post SIN = Posterior short insula gyrus, Ant CIN = Apex of the insula, Ant PIN = Anterior long insula gyrus and Post PIN = Posterior short insula gyrus.

12.3 Incorporation of seizure semiology, scalp and intracranial electrophysiology into computer-assisted planning algorithms

Clinical history, seizure semiology and electrophysiological information from scalp EEG recordings are critical constituents of the presurgical evaluation of epilepsy and if discordant, would necessitate invasive EEG evaluation before definitive surgical intervention. Currently, this information is perceived by the clinician and the formulation of the symptomatogenic and irritative zones is based on their prior experience and biases. Seminal work on ictal semiology has revealed that seizure activity in particular regions of the brain is attributable to anatomical structures in a highly stereotyped manner, but this may vary between patients and between

seizures in the same patients. Some semiological features may be lateralising but not localising and their absence in some seizures does not necessarily indicate the lack of ictal activity in that structure.

Figure 49: Cortical representations of different seizure semiologies:

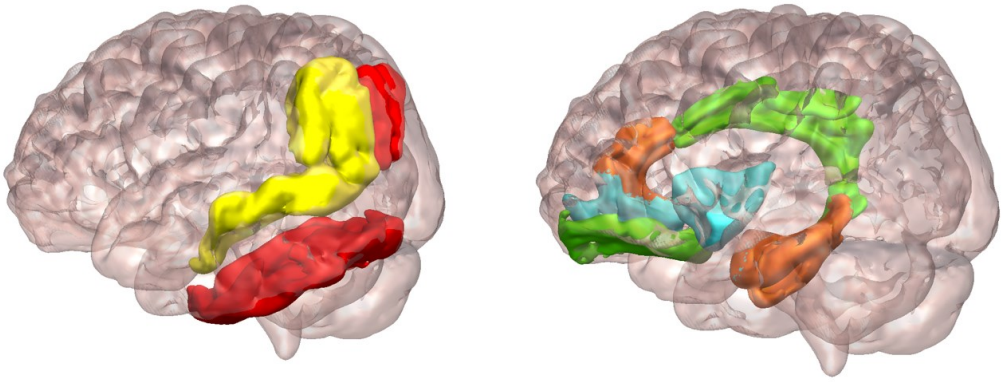

Figure 49 Legend: Left panel demonstrating the cortical representations of complex visual auras (red) and complex auditory auras (yellow). Right panel demonstrating the cortical representations of automotor seizures (orange), dialeptic (loss of consciousness) phase (green) and autonomic features (cyan).

Figure 50: Cortical representation of scalp EEG activity and PET hypometabolism:

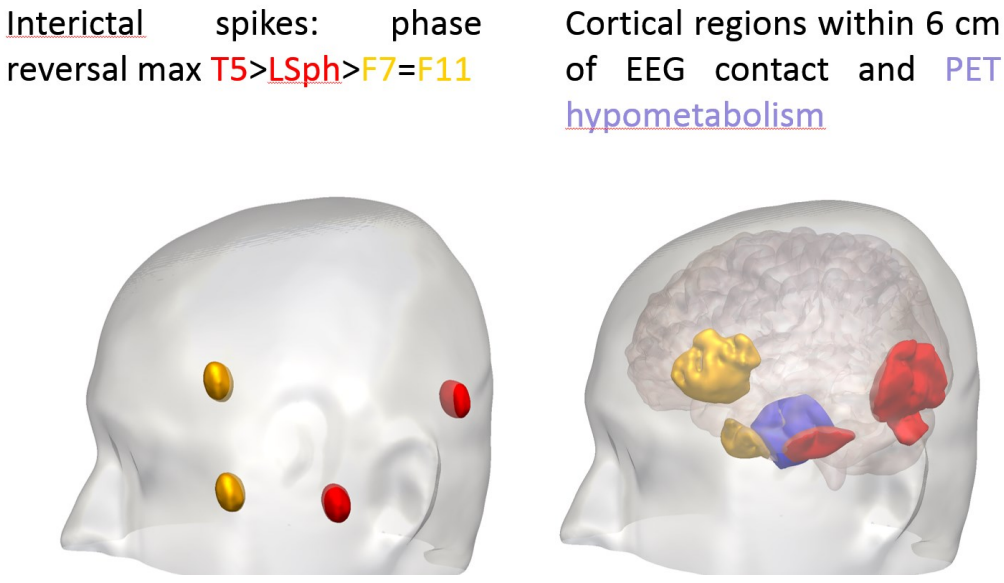

Figure 50 Legend: Left panel demonstrates the location of scalp EEG contacts based on the EEG 10-20 system in which epileptic spikes are recorded between seizures and their relative amplitudes measured from a referential montage depicted by colour (red indicates the larger amplitude of spikes compared to orange). Right panel demonstrates the region of the brain within a 6 cm diameter sphere of the active contact and the region of PET hypometabolism (blue).

The cortical regions attributable to the seizure semiology and the scalp inter-ictal EEG with the region of PET hypometabolism can be incorporated into SEEG planning and linked to the corresponding SEEG data.

Figure 51: Illustrative example of where cortical representations of seizure semiology, scalp EEG and PET hypometabolism were used to place SEEG trajectories.

A)

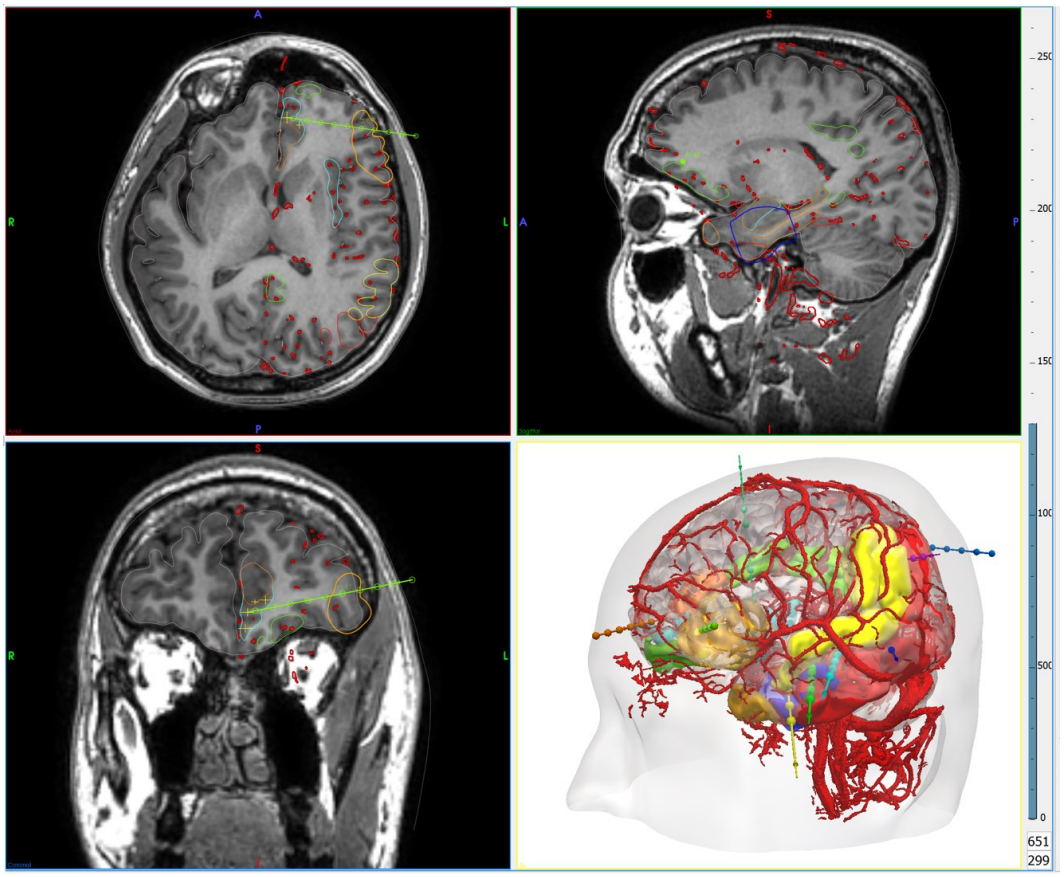

B)

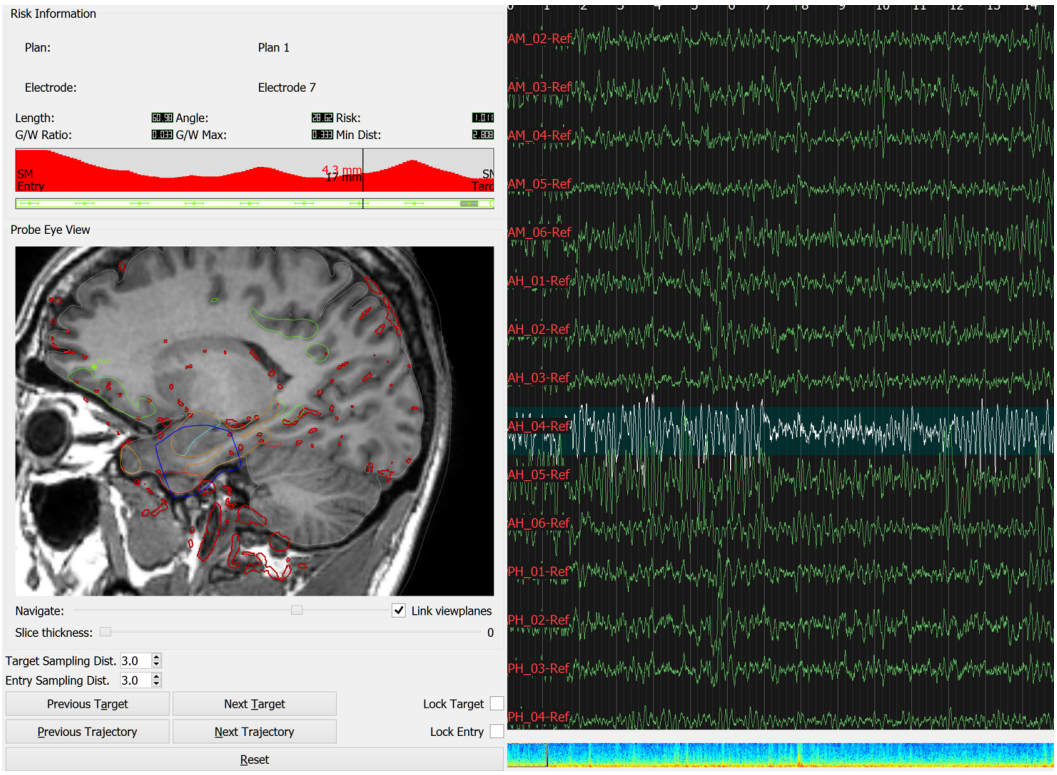

Figure 51 Legend: A) SEEG trajectories planned using CAP to include the cortical regions from the semiology, scalp EEG and PET hypometabolism allowing one electrode to transgress a number of the different anatomical regions of interest to maximise exploration efficiency. B) SEEG electrophysiological recording in the same patient revealing ictal onset (white trace) in contact 4 of the anterior hippocampal electrode with location shown on the probe's eye view image. Note this seizure onset corresponded with the centre of the PET hypometabolism shown by the blue outline.

Data from patients that have undergone SEEG evaluation following by surgical resection in which the seizure-free outcome in known would also lend itself to machine learning techniques that would ultimately improve resection planning and prediction of the postoperative outcomes. The region of ictal activity during the SEEG recording that coincides with the seizure semiology identified during the video-telemetry would allow an atlas of semiology and cortical regions to be developed. A major limitation of this methodology would be due to the limited spatial resolution of SEEG implantations, which would ultimately result in sampling bias. This could mislead investigators into assigning a semiological feature to ictal

activity in a particular cortical region simply because an electrode contact is in that region, whereas it may be attributable to a cortical region that is not being sampled that has synchronous activity. One method of mitigating a sampling bias would be to utilise the additional information gained from surgical resections and seizure-free outcome. A potential study would be to assign pre-operative seizure semiologies to post-operative ablation cavities and normalise these to an atlas space. In doing so, one can generate a map of resection cavities and then assign weights based on whether the patients achieved seizure freedom post-operatively. Semiologies present in patients that achieved seizure-freedom would accrue a positive weighting and those that did not achieve a seizure-free outcome would be assigned a negative weighting. Combinations and presence of particular semiologies and scalp EEG activity could then ultimately be used to plan idealised surgical resections and better inform predictions of seizure-free outcomes for pre-operative patient counselling.

12.4 **Electrode bending and curved intracranial trajectories**

Given sufficient data, it has also been shown that machine learning techniques can be applied to electrode implantations and accurately predict the degree of electrode bending within the brain. Given that current automated planning systems are based on linear trajectories, knowledge of the potential bending may allow for compensatory corrections to be incorporated at the planning stage. Robotic devices are in development to allow real-time steering within the brain and hence implantation of curved trajectories, which may be useful to sample from sites are difficult to access with straight-line trajectories, such as the temporal pole and fusiform gyrus, and for planning curved LITT trajectories, for example, to ablate the corpus callosum with only one entry point. Challenges for the future would be to reduce the current size of these devices so that they can pass through the brain without creating significant injury.

12.5 **Conclusion**

Computer-assisted SEEG trajectory planning has significantly advanced in the last decade due to increased computing power and collaboration between clinicians and engineers. The rise in the number of commercially available robotic trajectory guidance systems will aid in the translation and implementation of computer-assisted planning. Together with robotic devices, computer-assisted planning can be integrated into clinical workflows as part of a pipeline to standardize SEEG trajectories, overcome early learning curves associated with this technique and aid both resective and ablative therapies. The imaging and computer-assisted planning

principles outlined within this thesis can equally be applied to neuro-oncology for planning stereotactic brain biopsies and maximal safe resection of intrinsic brain tumours, potentially utilising port-based systems to minimise white matter injury. Furthermore, the techniques for accurately accessing regions of the brain safely are not limited to lesioning and the placement of electrodes but is also well-posed to deliver focal therapies in the brain including focal drug delivery and implantation of viral vectors that enable genetic modification in specific areas of the brain. I look forward to applying and developing these applications further in the future.

References

Abosch, A., Bernasconi, N., Boling, W., Jones-Gotman, M., Poulin, N., Dubeau, F., Andermann, F., & Olivier, A. (2002). Factors predictive of suboptimal seizure control following selective amygdalohippocampectomy. *Journal of Neurosurgery*, *97*(5), 1142–1151. https://doi.org/10.3171/jns.2002.97.5.1142

Abou-Al-Shaar, H., Brock, A. A., Kundu, B., Englot, D. J., & Rolston, J. D. (2018). Increased nationwide use of stereoencephalography for intracranial epilepsy electroencephalography recordings. *Journal of Clinical Neuroscience : Official Journal of the Neurosurgical Society of Australasia*, *53*, 132–134. https://doi.org/10.1016/j.jocn.2018.04.064

Ahmed, B., Brodley, C. E., Blackmon, K. E., Kuzniecky, R., Barash, G., Carlson, C., Quinn, B. T., Doyle, W., French, J., Devinsky, O., & Thesen, T. (2015). Cortical feature analysis and machine learning improves detection of "MRI-negative" focal cortical dysplasia. *Epilepsy & Behavior : E&B*, *48*, 21–28. https://doi.org/10.1016/j.yebeh.2015.04.055

Alomar, S., Mullin, J. P., Smithason, S., & Gonzalez-Martinez, J. (2017). Indications, technique, and safety profile of insular stereoelectroencephalography electrode implantation in medically intractable epilepsy. *Journal of Neurosurgery*, 1–11. https://doi.org/10.3171/2017.1.JNS161070

Aminoff, E., Kveraga, K., & Moshe, B. (2013). The role of the parahippocampal cortex in cognition. *Trends Cogn Sci*, *17*(8), 379–390. https://doi.org/10.1016/j.tics.2013.06.009.The

Andersson, J. L. R., Skare, S., & Ashburner, J. (2003). How to correct susceptibility distortions in spin-echo echo-planar images: application to diffusion tensor imaging. *NeuroImage*, *20*(2), 870–888. https://doi.org/10.1016/S1053-8119(03)00336-7

Andersson, J. L. R., & Sotiropoulos, S. N. (2016). An integrated approach to correction for off-resonance effects and subject movement in diffusion MR imaging. *NeuroImage*, *125*, 1063–1078. https://doi.org/10.1016/j.neuroimage.2015.10.019

Asadi-Pooya, A. A., Sharan, A. D., Nei, M., & Sperling, M. R. (2008). Corpus callosotomy. *Epilepsy & Behavior*, *13*(1), 271–278. https://doi.org/10.1007/s00701-015-2619-x

Asadollahi, M., Sperling, M. R., Rabiei, A. H., & Asadi-pooya, A. A. (2017). *parietal lobe epilepsy : clinical manifestations and surgery outcome*. *19*(1), 35–39.

Bahuleyan, B., Robinson, S., Nair, A. R., Sivanandapanicker, J. L., & Cohen, A. R. (2013). Anatomic hemispherectomy: historical perspective. *World Neurosurgery*, *80*(3–4), 396–398.

https://doi.org/10.1016/j.wneu.2012.03.020

Balanescu, B., Franklin, R., Ciurea, J., Mindruta, I., Rasina, A., Bobulescu, R. C., Donos, C., & Barborica, A. (2014). A personalized stereotactic fixture for implantation of depth electrodes in stereoelectroencephalography. *Stereotactic and Functional Neurosurgery*, *92*(2), 117–125. https://doi.org/10.1159/000360226

Balestrini, S., Francione, S., Mai, R., Castana, L., Casaceli, G., Marino, D., Provinciali, L., Cardinale, F., & Tassi, L. (2015). Multimodal responses induced by cortical stimulation of the parietal lobe: A stereo-electroencephalography study. *Brain*, *138*(9), 2596–2607. https://doi.org/10.1093/brain/awv187

Ball, T., Sharma, M., White, A. C., & Neimat, J. S. (2018). Anterior Corpus Callosotomy Using Laser Interstitial Thermal Therapy for Refractory Epilepsy. In *Stereotactic and functional neurosurgery* (Vol. 96, Issue 6, pp. 406–411). https://doi.org/10.1159/000495414

Balsyte, D., Schäffer, L., Burkhardt, T., Wisser, J., Zimmermann, R., & Kurmanavicius, J. (2010). Continuous independent quality control for fetal ultrasound biometry provided by the cumulative summation technique. *Ultrasound in Obstetrics and Gynecology*, *35*(4), 449–455. https://doi.org/10.1002/uog.7545

Barba, C., Rheims, S., Minotti, L., Guénot, M., Hoffmann, D., Chabardès, S., Isnard, J., Kahane, P., & Ryvlin, P. (2016). Temporal plus epilepsy is a major determinant of temporal lobe surgery failures. *Brain*, *139*(2), 444–451. https://doi.org/10.1093/brain/awv372

Barbaro, N., Quigg, M., Ward, M., Chang, E., Broshek, D., Langfitt, J., Guofen, Y., Laxer, K., Cole, A., Sneed, P., Hess, C., Wei, Y., Manjari, T., Heck, C., Miller, J., Garcia, P., Andrew, M., Fountain, N., Vincenta, S., … Evelyn, T. (2018). Radiosurgery versus open surgery for mesial temporal lobe epilepsy: The randomized, controlled ROSE trial. *Epilepsia*, *59*(6), 1198–1207. https://doi.org/10.1111/epi.14045

Barros, G., Lang, M. J., Mouchtouris, N., Sharan, A. D., & Wu, C. (2017). Impact of trajectory planning with susceptibility-weighted imaging for intracranial electrode implantation. *Operative Neurosurgery*, *15*(1), 60–65. https://doi.org/10.1093/ons/opx215

Barua, N. U., Lowis, S. P., Woolley, M., O'Sullivan, S., Harrison, R., & Gill, S. S. (2013). Robot-guided convection-enhanced delivery of carboplatin for advanced brainstem glioma. *Acta Neurochirurgica*, *155*(8), 1459–1465. https://doi.org/10.1007/s00701-013-1700-6

Bauer, P. R., Reitsma, J. B., Houweling, B. M., Ferrier, C. H., & Ramsey, N. F. (2014). Can fMRI safely replace the Wada test for preoperative assessment of language lateralisation? A

meta-analysis and systematic review. *Journal of Neurology, Neurosurgery & Psychiatry*, *85*(5), 581–588.

Baxendale, S., Wilson, S. J., Baker, G. A., Barr, W., Helmstaedter, C., Hermann, B. P., Langfitt, J., Reuner, G., Rzezak, P., Samson, S., & Smith, M. Lou. (2019). Indications and expectations for neuropsychological assessment in epilepsy surgery in children and adults: Executive summary of the report of the ILAE Neuropsychology Task Force Diagnostic Methods Commission: 2017-2021. *Epilepsia*, *60*(9), 1794–1796. https://doi.org/10.1111/epi.16309

Beisse, F., Lagrèze, W. A., Schmitz, J., & Schulze-Bonhage, A. (2014). Gesichtsfelddefekte nach epilepsiechirurgischen Eingriffen: Bedeutung f??r die Fahrerlaubnis. *Ophthalmologe*, *111*(10), 942–947. https://doi.org/10.1007/s00347-013-3013-9

Bell, G. S., de Tisi, J., Gonzalez-Fraile, J. C., Peacock, J. L., McEvoy, Andrew W Harkness, William FJ Foong, J., Pope, R. A., Diehl, B., Sander, J. W., & Duncan, J. S. (2017). Factors affecting seizure outcome after epilepsy surgery; an observational series. *Journal of Neurology, Neurosurgery & Psychiatry*, *88*(11), 933–940.

Benet, A., Hervey-Jumper, S. L., Sanchez, J. J. G., Lawton, M. T., & Berger, M. S. (2016). Surgical assessment of the insula. Part 1: surgical anatomy and morphometric analysis of the transsylvian and transcortical approaches to the insula. *Journal of Neurosurgery*, *124*(2), 469–481. https://doi.org/10.3171/2014.12.JNS142182

Bennett, O. F., Kanber, B., Hoskote, C., Cardoso, M. J., Ourselin, S., Duncan, J. S., & Winston, G. P. (2019). Learning to see the invisible: A data-driven approach to finding the underlying patterns of abnormality in visually normal brain magnetic resonance images in patients with temporal lobe epilepsy. *Epilepsia*, *60*(12), 2499–2507. https://doi.org/10.1111/epi.16380

Berg, A. T., Langfitt, J., Shinnar, S., Vickrey, B. G., Sperling, M. R., Walczak, T., Bazil, C., Pacia, S. V, & Spencer, S. S. (2003). How long does it take for partial epilepsy to become intractable? *Neurology*, *60*(2), 186–190.

Beriault, S., Al Subaie, F., Mok, K., Sadikot, A. F., & Pike, G. B. (2011). Automatic trajectory planning of DBS neurosurgery from multi-modal MRI datasets. *Medical Image Computing and Computer-Assisted Intervention : MICCAI ... International Conference on Medical Image Computing and Computer-Assisted Intervention*, *14*(Pt 1), 259–266.

Bériault, S., Subaie, F. Al, Collins, D. L., Sadikot, A. F., & Pike, G. B. (2012). A multi-modal approach to computer-assisted deep brain stimulation trajectory planning. *International*

Journal of Computer Assisted Radiology and Surgery, *7*(5), 687–704. https://doi.org/10.1007/s11548-012-0768-4

Bernhardt, B. C., Fadaie, F., Liu, M., Caldairou, B., Gu, S., Jefferies, E., Smallwood, J., Bassett, D. S., Bernasconi, A., & Bernasconi, N. (2019). Temporal lobe epilepsy. *Neurology*, *92*(19), e2209 LP-e2220. https://doi.org/10.1212/WNL.0000000000007447

Besson, P., Bernasconi, N., Colliot, O., Evans, A., & Bernasconi, A. (2008). Surface-based texture and morphological analysis detects subtle cortical dysplasia. *Medical Image Computing and Computer-Assisted Intervention : MICCAI ... International Conference on Medical Image Computing and Computer-Assisted Intervention*, *11*(Pt 1), 645–652.

Besson, P., Dinkelacker, V., Valabregue, R., Thivard, L., Leclerc, X., Baulac, M., Sammler, D., Colliot, O., Lehéricy, S., Samson, S., & Dupont, S. (2014). Structural connectivity differences in left and right temporal lobe epilepsy. *NeuroImage*, *100*, 135–144. https://doi.org/10.1016/j.neuroimage.2014.04.071

Blümcke, I. (2009). Neuropathology of focal epilepsies: A critical review. *Epilepsy and Behavior*, *15*(1), 34–39. https://doi.org/10.1016/j.yebeh.2009.02.033

Blumcke, I., Spreafico, R., Haaker, G., Coras, R., Kobow, K., Bien, C. G., Pfäfflin, M., Elger, C. E., Widman, G., Schramm, J., Becker, A. J., Braun, K. P., Leijten, F. S., Baayen, J. C., Aronica, E., Chassoux, F., Hamer, H. M., Stefan, H., Rössler, K., … Avanzini, G. (2017). Histopathological Findings in Brain Tissue Obtained during Epilepsy Surgery. *New England Journal of Medicine*, *377*(17), 1648–1656. https://doi.org/10.1056/NEJMoa1703784

Bonelli, S. B., Thompson, P. J., Yogarajah, M., Powell, R. H. W., Samson, R. S., McEvoy, A. W., Symms, M. R., Koepp, M. J., & Duncan, J. S. (2013). Memory reorganization following anterior temporal lobe resection: a longitudinal functional MRI study. *Brain : A Journal of Neurology*, *136*(Pt 6), 1889–1900. https://doi.org/10.1093/brain/awt105

Bonilha, L., Lee, C. Y., Jensen, J. H., Tabesh, A., Spampinato, M. V., Edwards, J. C., Breedlove, J., & Helpern, J. A. (2015). Altered microstructure in temporal lobe epilepsy: A diffusional kurtosis imaging study. *American Journal of Neuroradiology*, *36*(4), 719–724. https://doi.org/10.3174/ajnr.A4185

Bonini, F., McGonigal, A., Scavarda, D., Carron, R., Regis, J., Dufour, H., Peragut, J.-C., Laguitton, V., Villeneuve, N., Chauvel, P., Giusiano, B., Trebuchon, A., Bartolomei, F., Régis, J., Dufour, H., Péragut, J. C., Laguitton, V., Villeneuve, N., Chauvel, P., … Bartolomei, F. (2017). Predictive Factors of Surgical Outcome in Frontal Lobe Epilepsy Explored with

Stereoelectroencephalography. *Neurosurgery*, *0*(0), 1–9. https://doi.org/10.1093/neuros/nyx342

Borchers, S., Himmelbach, M., Logothetis, N., & Karnath, H.-O. (2011). Direct electrical stimulation of human cortex - the gold standard for mapping brain functions? In *Nature reviews. Neuroscience* (Vol. 13, Issue 1, pp. 63–70). https://doi.org/10.1038/nrn3140

Bourdillon, P., Ryvlin, P., Isnard, J., Montavont, A., Catenoix, H., Mauguière, F., Rheims, S., Ostrowsky-Coste, K., & Guénot, M. (2017). Stereotactic Electroencephalography Is a Safe Procedure, Including for Insular Implantations. *World Neurosurgery*, *99*, 353–361. https://doi.org/10.1016/j.wneu.2016.12.025

Bower, R. S., Wirrell, E., Nwojo, M., Wetjen, N. M., Marsh, W. R., & Meyer, F. B. (2013). Seizure outcomes after corpus callosotomy for drop attacks. *Neurosurgery*, *73*(6), 993–1000. https://doi.org/10.1227/NEU.0000000000000161

Breiman, L. (2001). Random Forests. *Machine Learning*, *45*(1), 5–32. https://doi.org/10.1023/A:1010933404324

Brunenberg, E. J. L., Vilanova, A., Visser-Vandewalle, V., Temel, Y., Ackermans, L., Platel, B., & ter Haar Romeny, B. M. (2007). Automatic trajectory planning for deep brain stimulation: a feasibility study. *Medical Image Computing and Computer-Assisted Intervention : MICCAI ... International Conference on Medical Image Computing and Computer-Assisted Intervention*, *10*(Pt 1), 584–592.

Bujarski, K. A., Hirashima, F., Roberts, D. W., Jobst, B. C., Gilbert, K. L., Roth, R. M., Flashman, L. A., McDonald, B. C., Saykin, A. J., Scott, R. C., Dinnerstein, E., Preston, J., Williamson, P. D., Thadani, V. M., Joshi, A. a, Chaudhari, A. J., Li, C., Dutta, J., Cherry, S. R., … Leahy, R. M. (2011). Long-term seizure, cognitive, and psychiatric outcome following trans–middle temporal gyrus amygdalohippocampectomy and standard temporal lobectomy. *October*, *55*(20), 6197–6214. https://doi.org/10.1088/0031-9155/55/20/011.DigiWarp

Burgos, N., Cardoso, M. J., Modat, M., Pedemonte, S., Dickson, J., Barnes, A., Duncan, J. S., Atkinson, D., Arridge, S. R., Hutton, B. F., & Ourselin, S. (2013). Attenuation correction synthesis for hybrid PET-MR scanners. *Medical Image Computing and Computer-Assisted Intervention : MICCAI ... International Conference on Medical Image Computing and Computer-Assisted Intervention*, *16*(Pt 1), 147–154.

Burgos, N., Cardoso, M. J., Thielemans, K., Modat, M., Pedemonte, S., Dickson, J., Barnes, A., Ahmed, R., Mahoney, C. J., Schott, J. M., Duncan, J. S., Atkinson, D., Arridge, S. R., Hutton,

B. F., & Ourselin, S. (2014). Attenuation correction synthesis for hybrid PET-MR scanners: application to brain studies. *IEEE Transactions on Medical Imaging*, *33*(12), 2332–2341. https://doi.org/10.1109/TMI.2014.2340135

Burrows, A. M., Marsh, W. R., Worrell, G., Woodrum, D. A., Pollock, B. E., Gorny, K. R., Felmlee, J. P., Watson, R. E., Kaufmann, T. J., Goerss, S., & Van Gompel, J. J. (2016). Magnetic resonance imaging–guided laser interstitial thermal therapy for previously treated hypothalamic hamartomas. *Neurosurgical Focus*, *41*(4), E8. https://doi.org/10.3171/2016.7.FOCUS16218

Cardinale, F., Casaceli, G., Raneri, F., Miller, J., & Lo Russo, G. (2016a). Implantation of Stereoelectroencephalography Electrodes: A Systematic Review. *Journal of Clinical Neurophysiology*, *33*(6), 490–502. https://doi.org/10.1097/WNP.0000000000000249

Cardinale, F., Casaceli, G., Raneri, F., Miller, J., & Lo Russo, G. (2016b). Implantation of Stereoelectroencephalography Electrodes. *Journal of Clinical Neurophysiology*, *33*(6), 490–502.

Cardinale, F., Cossu, M., Castana, L., Casaceli, G., Schiariti, M. P., Miserocchi, A., Fuschillo, D., Moscato, A., Caborni, C., Arnulfo, G., & Lo Russo, G. (2013). Stereoelectroencephalography: Surgical methodology, safety, and stereotactic application accuracy in 500 procedures. *Neurosurgery*, *72*(3), 353–366. https://doi.org/10.1227/NEU.0b013e31827d1161

Cardinale, F., Pero, G., Quilici, L., Piano, M., Colombo, P., Moscato, A., Castana, L., Casaceli, G., Fuschillo, D., Gennari, L., Cenzato, M., Lo Russo, G., & Cossu, M. (2015). Cerebral Angiography for Multimodal Surgical Planning in Epilepsy Surgery: Description of a New Three-Dimensional Technique and Literature Review. *World Neurosurgery*, *84*(2), 358–367. https://doi.org/10.1016/j.wneu.2015.03.028

Cardoso, M. J., Modat, M., Wolz, R., Melbourne, A., Cash, D., Rueckert, D., & Ourselin, S. (2015a). Geodesic Information Flows: Spatially-Variant Graphs and Their Application to Segmentation and Fusion. *IEEE Transactions on Medical Imaging*, *34*(9), 1976–1988. https://doi.org/10.1109/TMI.2015.2418298

Cardoso, M. J., Modat, M., Wolz, R., Melbourne, A., Cash, D., Rueckert, D., & Ourselin, S. (2015b). Geodesic Information Flows: Spatially-Variant Graphs and Their Application to Segmentation and Fusion. *IEEE Transactions on Medical Imaging*, *34*(9), 1976–1988. https://doi.org/10.1109/TMI.2015.2418298

Celis, M. A., Moreno-Jimenez, S., Larraga-Gutierrez, J. M., Alonso-Vanegas, M. A., Garcia-Garduno, O. A., Martinez-Juarez, I. E., & Fernandez-Gonzalez, M. C. (2007). Corpus callosotomy using conformal stereotactic radiosurgery. *Child's Nervous System : ChNS : Official Journal of the International Society for Pediatric Neurosurgery*, *23*(8), 917–920. https://doi.org/10.1007/s00381-007-0356-z

Chang, E. F., Quigg, M., Oh, M. C., Dillon, W. P., Ward, M. M., Laxer, K. D., Broshek, D. K., & Barbaro, N. M. (2010). Predictors of efficacy after stereotactic radiosurgery for medial temporal lobe epilepsy. *Neurology*, *74*(2), 165–172. https://doi.org/10.1212/WNL.0b013e3181c9185d

Chaudhary, U. J., Carmichael, D. W., Rodionov, R., Thornton, R. C., Bartlett, P., Vulliemoz, S., Micallef, C., McEvoy, A. W., Diehl, B., Walker, M. C., Duncan, J. S., & Lemieux, L. (2012). Mapping preictal and ictal haemodynamic networks using video-electroencephalography and functional imaging. *Brain : A Journal of Neurology*, *135*(Pt 12), 3645–3663. https://doi.org/10.1093/brain/aws302

Childers, C. P., & Maggard-Gibbons, M. (2018). Estimation of the Acquisition and Operating Costs for Robotic SurgeryEstimation of the Acquisition and Operating Costs for Robotic SurgeryLetters. *JAMA*, *320*(8), 835–836. https://doi.org/10.1001/jama.2018.9219

Choi, H., Hayat, M. J., Zhang, R., Hirsch, L. J., Bazil, C. W., Mendiratta, A., Kato, K., Javed, A., Legge, A. W., Buchsbaum, R., Resor, S., & Heiman, G. A. (2016). Drug-resistant epilepsy in adults: Outcome trajectories after failure of two medications. *Epilepsia*, *57*(7), 1152–1160. https://doi.org/10.1111/epi.13406

Choudhri, A.F., Whitehead, M.T., McGregor, A. L. et al. (2013). Diffusion tensor imaging to evaluate commissural disconnection after corpus callosotomy. *Neuroradiology*, *55*(1397). https://doi.org/https://doi.org/10.1007/s00234-013-1286-y

Chung, H. W., Chou, M. C., & Chen, C. Y. (2011). Principles and limitations of computational algorithms in clinical diffusion tensor MR tractography. *American Journal of Neuroradiology*, *32*(1), 3–13. https://doi.org/10.3174/ajnr.A2041

Ciccarelli, O., Parker, G. J. M., Toosy, A. T., Wheeler-Kingshott, C. A. M., Barker, G. J., Boulby, P. A., Miller, D. H., & Thompson, A. J. (2003). From diffusion tractography to quantitative white matter tract measures: a reproducibility study. *NeuroImage*, *18*(2), 348–359. https://doi.org/10.1016/s1053-8119(02)00042-3

Clavien, P. A., Barkun, J., De Oliveira, M. L., Vauthey, J. N., Dindo, D., Schulick, R. D., De

Santibañes, E., Pekolj, J., Slankamenac, K., Bassi, C., Graf, R., Vonlanthen, R., Padbury, R., Cameron, J. L., & Makuuchi, M. (2009). The clavien-dindo classification of surgical complications: Five-year experience. *Annals of Surgery*, *250*(2), 187–196. https://doi.org/10.1097/SLA.0b013e3181b13ca2

Clusmann, H., Schramm, J., Kral, T., Helmstaedter, C., Ostertun, B., Fimmers, R., Haun, D., & Elger, C. E. (2002). Prognostic factors and outcome after different types of resection for temporal lobe epilepsy. *Journal of Neurosurgery*, *97*(5), 1131–1141. https://doi.org/10.3171/jns.2002.97.5.1131

Coan, A. C., Kubota, B., Bergo, F. P. G., Campos, B. M., & Cendes, F. (2014). 3T MRI quantification of hippocampal volume and signal in mesial temporal lobe epilepsy improves detection of hippocampal sclerosis. *American Journal of Neuroradiology*, *35*(1), 77–83. https://doi.org/10.3174/ajnr.A3640

Collins, J. W., Tyritzis, S., Nyberg, T., Schumacher, M. C., Laurin, O., Adding, C., Jonsson, M., Khazaeli, D., Steineck, G., Wiklund, P., & Hosseini, A. (2014). Robot-assisted radical cystectomy (RARC) with intracorporeal neobladder - what is the effect of the learning curve on outcomes? *BJU International*, *113*(1), 100–107. https://doi.org/10.1111/bju.12347

Cordes, D., Haughton, V. M., Arfanakis, K., Wendt, G. J., Turski, P. A., Moritz, C. H., Quigley, M. A., & Meyerand, M. E. (2000). Mapping functionally related regions of brain with functional connectivity MR imaging. *American Journal of Neuroradiology*, *21*(9), 1636–1644. https://doi.org/10.1016/j.amepre.2011.10.016

Cossu, M., Fuschillo, D., Casaceli, G., Pelliccia, V., Castana, L., Mai, R., Francione, S., Sartori, I., Gozzo, F., Nobili, L., Tassi, L., Cardinale, F., & Lo Russo, G. (2015). Stereoelectroencephalography-guided radiofrequency thermocoagulation in the epileptogenic zone: a retrospective study on 89 cases. *Journal of Neurosurgery*, *123*(6), 1358–1367. https://doi.org/10.3171/2014.12.JNS141968

Curry, D. J., Gowda, A., McNichols, R. J., & Wilfong, A. A. (2012). MR-guided stereotactic laser ablation of epileptogenic foci in children. *Epilepsy and Behavior*, *24*(4), 408–414. https://doi.org/10.1016/j.yebeh.2012.04.135

Dale, A. M., Fischl, B., & Sereno, M. I. (1999). Cortical surface-based analysis. I. Segmentation and surface reconstruction. *NeuroImage*, *9*(2), 179–194. https://doi.org/10.1006/nimg.1998.0395

David, O., Bastin, J., Chabardes, S., Minotti, L., & Kahane, P. (2010). Studying network mechanisms using intracranial stimulation in epileptic patients. *Frontiers in Systems Neuroscience*, *4*, 148. https://doi.org/10.3389/fnsys.2010.00148

Davies, K. G., Phillips, B. L., & Hermann, B. P. (1996). MRI confirmation of accuracy of freehand placement of mesial temporal lobe depth electrodes in the investigation of intractable epilepsy. *British Journal of Neurosurgery*, *10*(2), 175–178.

Davis, D. H., Kelly, P. J., Marsh, W. R., Kall, B. A., & Goerss, S. J. (1988). Computer-assisted stereotactic biopsy of intracranial lesions in pediatric patients. *Pediatric Neuroscience*, *14*(1), 31–36.

Day, C. S., Park, D. J., Rozenshteyn, F. S., Owusu-Sarpong, N., & Gonzalez, A. (2016). Analysis of FDA-Approved Orthopaedic Devices and Their Recalls. *The Journal of Bone and Joint Surgery. American Volume*, *98*(6), 517–524. https://doi.org/10.2106/JBJS.15.00286

de Boer, H. M., Mula, M., & Sander, J. W. (2008). The global burden and stigma of epilepsy. *Epilepsy & Behavior : E&B*, *12*(4), 540–546. https://doi.org/10.1016/j.yebeh.2007.12.019

De Momi, E., Caborni, C., Cardinale, F., Casaceli, G., Castana, L., Cossu, M., Mai, R., Gozzo, F., Francione, S., Tassi, L., Lo Russo, G., Antiga, L., & Ferrigno, G. (2014a). Multi-trajectories automatic planner for StereoElectroEncephaloGraphy (SEEG). *International Journal of Computer Assisted Radiology and Surgery*, *9*(6), 1087–1097. https://doi.org/10.1007/s11548-014-1004-1

De Momi, E., Caborni, C., Cardinale, F., Casaceli, G., Castana, L., Cossu, M., Mai, R., Gozzo, F., Francione, S., Tassi, L., Lo Russo, G., Antiga, L., & Ferrigno, G. (2014b). Multi-trajectories automatic planner for StereoElectroEncephaloGraphy (SEEG). *International Journal of Computer Assisted Radiology and Surgery*, *9*(6), 1087–1097. https://doi.org/10.1007/s11548-014-1004-1

De Momi, E., Caborni, C., Cardinale, F., Castana, L., Casaceli, G., Cossu, M., Antiga, L., & Ferrigno, G. (2013a). Automatic trajectory planner for StereoElectroEncephaloGraphy procedures: A retrospective study. *IEEE Trans Biomed Eng*, *60*(4), 986–993. https://doi.org/10.1109/TBME.2012.2231681

De Momi, E., Caborni, C., Cardinale, F., Castana, L., Casaceli, G., Cossu, M., Antiga, L., & Ferrigno, G. (2013b). Automatic trajectory planner for StereoElectroEncephaloGraphy procedures: a retrospective study. *IEEE Transactions on Bio-Medical Engineering*, *60*(4), 986–993. https://doi.org/10.1109/TBME.2012.2231681

De Tisi, J., Bell, G. S., Peacock, J. L., McEvoy, A. W., Harkness, W. F., Sander, J. W., & Duncan, J. S. (2011). The long-term outcome of adult epilepsy surgery, patterns of seizure remission, and relapse: A cohort study. *The Lancet*, *378*(9800), 1388–1395. https://doi.org/10.1016/S0140-6736(11)60890-8

Delev, D., Wabbels, B., Schramm, J., Nelles, M., Elger, C. E., von Lehe, M., Clusmann, H., & Grote, A. (2016). Vision after trans-sylvian or temporobasal selective amygdalohippocampectomy: a prospective randomised trial. *Acta Neurochirurgica*, *158*(9), 1757–1765. https://doi.org/10.1007/s00701-016-2860-y

Desai, A., Bekelis, K., Thadani, V. M., Roberts, D. W., Jobst, B. C., Duhaime, A. C., Gilbert, K., Darcey, T. M., Studholme, C., & Siegel, A. (2013). Interictal PET and ictal subtraction SPECT: Sensitivity in the detection of seizure foci in patients with medically intractable epilepsy. *Epilepsia*, *54*(2), 341–350. https://doi.org/10.1111/j.1528-1167.2012.03686.x

Di Rocco, C., & Iannelli, A. (2000). Hemimegalencephaly and intractable epilepsy: complications of hemispherectomy and their correlations with the surgical technique. A report on 15 cases. *Pediatric Neurosurgery*, *33*(4), 198–207. https://doi.org/55953

Díaz, C. E., Fernández, R., Armada, M., & García, F. (2017). A research review on clinical needs, technical requirements, and normativity in the design of surgical robots. *International Journal of Medical Robotics and Computer Assisted Surgery*, *13*(4), 1–10. https://doi.org/10.1002/rcs.1801

Diehl, B., & Luders, H. O. (2000). Temporal lobe epilepsy: when are invasive recordings needed? *Epilepsia*, *41 Suppl 3*, S61-74.

Donos, C., Breier, J., Friedman, E., Rollo, P., Johnson, J., Moss, L., Thompson, S., Thomas, M., Hope, O., Slater, J., & Tandon, N. (2018). Laser ablation for mesial temporal lobe epilepsy: Surgical and cognitive outcomes with and without mesial temporal sclerosis. *Epilepsia*, *59*(7), 1421–1432. https://doi.org/10.1111/epi.14443

Dorfer, C., Minchev, G., Czech, T., Stefanits, H., Feucht, M., Pataraia, E., Baumgartner, C., Kronreif, G., & Wolfsberger, S. (2017). A novel miniature robotic device for frameless implantation of depth electrodes in refractory epilepsy. *Journal of Neurosurgery*, *126*(5), 1622–1628. https://doi.org/10.3171/2016.5.JNS16388

Doucet, G. E., Pustina, D., Skidmore, C., Sharan, A., Sperling, M. R., & Tracy, J. I. (2015). Resting-state functional connectivity predicts the strength of hemispheric lateralization for language processing in temporal lobe epilepsy and normals. *Human Brain Mapping*, *36*(1),

288–303. https://doi.org/10.1002/hbm.22628

Drane, D. L. (2017). MRI-Guided stereotactic laser ablation for epilepsy surgery: Promising preliminary results for cognitive outcome. *Epilepsy Research*. https://doi.org/10.1016/j.eplepsyres.2017.09.016

Drane, D. L., Loring, D. W., Voets, N. L., Price, M., Ojemann, Jeffrey G. Willie, J. T., Saindane, Amit M. Phatak, V., Ivanisevic, M., Millis, S., Ojemann, J. G., Willie, J. T., Saindane, A. M., Phatak, V., Ivanisevic, M., Millis, S., Helmers, S. L., Miller, J. W., Meador, K. J., & Gross, R. E. (2015). Better object recognition and naming outcome with MRI-guided stereotactic laser amygdalohippocampotomy for temporal lobe epilepsy. *Epilepsia*, *56*(1), 101–113. https://doi.org/10.1111/epi.12860

Duffau, H. (2014a). Diffusion Tensor Imaging Is a Research and Educational Tool, but Not Yet a Clinical Tool. *World Neurosurgery*, *82*(1–2), e43–e45. https://doi.org/10.1016/j.wneu.2013.08.054

Duffau, H. (2014b). The dangers of magnetic resonance imaging diffusion tensor tractography in brain surgery. *World Neurosurgery*, *81*(1), 56–58. https://doi.org/10.1016/j.wneu.2013.01.116

Duffau, H., Moritz-Gasser, S., & Mandonnet, E. (2014). A re-examination of neural basis of language processing: Proposal of a dynamic hodotopical model from data provided by brain stimulation mapping during picture naming. *Brain and Language*, *131*, 1–10. https://doi.org/10.1016/j.bandl.2013.05.011

Duffau, H., Thiebaut De Schotten, M., & Mandonnet, E. (2008). White matter functional connectivity as an additional landmark for dominant temporal lobectomy. *Journal of Neurology, Neurosurgery and Psychiatry*, *79*(5), 492–495. https://doi.org/10.1136/jnnp.2007.121004

Duncan, J. S., & Hamani, C. (2015). Stimulating the brain for epilepsy. In *Neurology* (Vol. 84, Issue 8, pp. 768–769). https://doi.org/10.1212/WNL.0000000000001297

Duncan, J. S., Winston, G. P., Koepp, M. J., & Ourselin, S. (2016). Brain imaging in the assessment for epilepsy surgery. *The Lancet Neurology*, *15*(4), 420–433. https://doi.org/10.1016/S1474-4422(15)00383-X

Ebeling, U., & Reulen, H. J. (1988). Neurosurgical topography of the optic radiation in the temporal lobe. *Acta Neurochirurgica*, *92*(1–4), 29–36. https://doi.org/10.1007/BF01401969

Elias, W. J., Sansur, C. A., & Frysinger, R. C. (2009). Sulcal and ventricular trajectories in stereotactic surgery. *Journal of Neurosurgery*, *110*(2), 201–207. https://doi.org/10.3171/2008.7.17625

Ellis, J. A., Mejia Munne, J. C., Wang, S. H., McBrian, D. K., Akman, C. I., Feldstein, N. A., & McKhann, G. M. (2016). Staged laser interstitial thermal therapy and topectomy for complete obliteration of complex focal cortical dysplasias. *Journal of Clinical Neuroscience*, *31*, 224–228. https://doi.org/10.1016/j.jocn.2016.02.016

Elm, E. Von, Altman, D. G., Egger, M., Pocock, S. J., Gøtzsche, P. C., & Vandenbroucke, J. P. (2007). *The Strengthening the Reporting of Observational Studies in Epidemiology (STROBE) statement : guidelines for reporting observational studies*. 1453–1457.

Enatsu, R., & Mikuni, N. (2016). Invasive Evaluations for Epilepsy Surgery: A Review of the Literature. *Neurologia Medico-Chirurgica*, *56*(5), 221–227. https://doi.org/10.2176/nmc.ra.2015-0319

Engel, J. J., McDermott, M. P., Wiebe, S., Langfitt, J. T., Stern, J. M., Dewar, S., Sperling, M. R., Gardiner, I., Erba, G., Fried, I., Jacobs, M., Vinters, H. V., Mintzer, S., & Kieburtz, K. (2012). Early surgical therapy for drug-resistant temporal lobe epilepsy. *JAMA - Journal of the American Medical Association*, *307*(9), 922–930.

Englot, D. J., Birk, H., & Chang, E. F. (2017). Seizure outcomes in nonresective epilepsy surgery: an update. *Neurosurgical Review*, *40*(2), 181–194. https://doi.org/10.1007/s10143-016-0725-8

Englot, D. J., & Chang, E. F. (2014). Rates and predictors of seizure freedom in resective epilepsy surgery: An update. *Neurosurgical Review*, *37*(3), 389–404. https://doi.org/10.1007/s10143-014-0527-9

Englot, D. J., Nagarajan, S. S., Imber, B. S., Raygor, K. P., Honma, S. M., Mizuiri, D., Mantle, M., Knowlton, R. C., Kirsch, H. E., & Chang, E. F. (2015). Epileptogenic zone localization using magnetoencephalography predicts seizure freedom in epilepsy surgery. *Epilepsia*, *56*(6), 949–958. https://doi.org/10.1111/epi.13002

Englot, D. J., Wang, D. D., Rolston, J. D., Shih, T. T., & Chang, E. F. (2012). Rates and predictors of long-term seizure freedom after frontal lobe epilepsy surgery: a systematic review and meta-analysis. *Journal of Neurosurgery*, *116*(5), 1042–1048. https://doi.org/10.3171/2012.1.JNS111620

Ergina, P. L., Barkun, J. S., McCulloch, P., Cook, J. A., & Altman, D. G. (2013). IDEAL framework

for surgical innovation 2: observational studies in the exploration and assessment stages. *BMJ*, *346*. https://doi.org/10.1136/bmj.f3011

Esquenazi, Y., Kalamangalam, G. P., Slater, J. D., Knowlton, R. C., Friedman, E., Morris, S. A., Shetty, A., Gowda, A., & Tandon, N. (2014). Stereotactic laser ablation of epileptogenic periventricular nodular heterotopia. *Epilepsy Research*, *108*(3), 547–554. https://doi.org/10.1016/j.eplepsyres.2014.01.009

Essert, C., Haegelen, C., Lalys, F., Abadie, A., & Jannin, P. (2012). Automatic computation of electrode trajectories for Deep Brain Stimulation: A hybrid symbolic and numerical approach. *International Journal of Computer Assisted Radiology and Surgery*, *7*(4), 517–532. https://doi.org/10.1007/s11548-011-0651-8

Fabri, M., Pierpaoli, C., Barbaresi, P., & Polonara, G. (2014). Functional topography of the corpus callosum investigated by DTI and fMRI. *World Journal of Radiology*, *6*(12), 895–906. https://doi.org/10.4329/wjr.v6.i12.895

Federico, P., Abbott, D. F., Briellmann, R. S., Harvey, A. S., & Jackson, G. D. (2005). Functional MRI of the pre-ictal state. *Brain : A Journal of Neurology*, *128*(Pt 8), 1811–1817. https://doi.org/10.1093/brain/awh533

Feindel, K. W. (2013). Can we develop pathology-specific MRI contrast for “MR-negative” epilepsy? *Epilepsia*, *54*(2009), 71–74. https://doi.org/10.1111/epi.12189

Feng, E.-S., Sui, C.-B., Wang, T.-X., & Sun, G.-L. (2016). Stereotactic radiosurgery for the treatment of mesial temporal lobe epilepsy. *Acta Neurologica Scandinavica*, *134*(6), 442–451. https://doi.org/10.1111/ane.12562

Ferran Prados, M. Jorge Cardoso, Ninon Burgos, Claudia AM Wheeler-Kingshott, S. O. (2016). NiftyWeb: web based platform for image processing on the cloud. *International Society for Magnetic Resonance in Medicine (ISMRM) 24th Scientific Meeting and Exhibition - Singapore*.

Fischl, B. (2012). FreeSurfer. *NeuroImage*, *62*(2), 774–781. https://doi.org/10.1016/J.NEUROIMAGE.2012.01.021

Fisher, R. S., Acevedo, C., Arzimanoglou, A., Bogacz, A., Cross, J. H., Elger, C. E., Engel, J., Forsgren, L., French, J. A., Glynn, M., Hesdorffer, D. C., Lee, B. I., Mathern, G. W., Moshé, S. L., Perucca, E., Scheffer, I. E., Tomson, T., Watanabe, M., & Wiebe, S. (2014). ILAE Official Report: A practical clinical definition of epilepsy. *Epilepsia*, *55*(4), 475–482. https://doi.org/10.1111/epi.12550

Fisher, R. S., Cross, J. H., D'Souza, C., French, J. A., Haut, S. R., Higurashi, N., Hirsch, E., Jansen, F. E., Lagae, L., Moshé, S. L., Peltola, J., Roulet Perez, E., Scheffer, I. E., Schulze-Bonhage, A., Somerville, E., Sperling, M., Yacubian, E. M., & Zuberi, S. M. (2018). Instruction manual for the ILAE 2017 operational classification of seizure types. In *Zeitschrift fur Epileptologie* (Vol. 31, Issue 4). https://doi.org/10.1007/s10309-018-0217-7

Fisher, R., Salanova, V., Witt, T., Worth, R., Henry, T., Gross, R., Oommen, K., Osorio, I., Nazzaro, J., Labar, D., Kaplitt, M., Sperling, M., Sandok, E., Neal, J., Handforth, A., Stern, J., DeSalles, A., Chung, S., Shetter, A., … Graves, N. (2010). Electrical stimulation of the anterior nucleus of thalamus for treatment of refractory epilepsy. *Epilepsia*, *51*(5), 899–908. https://doi.org/10.1111/j.1528-1167.2010.02536.x

Focke, N. K., Bonelli, S. B., Yogarajah, M., Scott, C., Symms, M. R., & Duncan, J. S. (2009). Automated normalized FLAIR imaging in MRI-negative patients with refractory focal epilepsy. *Epilepsia*, *50*(6), 1484–1490. https://doi.org/10.1111/j.1528-1167.2009.02022.x

Foldvary-Schaefer, N., & Unnwongse, K. (2011). Localizing and lateralizing features of auras and seizures. *Epilepsy and Behavior*, *20*(2), 160–166. https://doi.org/10.1016/j.yebeh.2010.08.034

Fonov, V., Evans, A. C., Botteron, K., Almli, C. R., Mckinstry, R. C., & Collins, D. L. (2011). NeuroImage Unbiased average age-appropriate atlases for pediatric studies. *NeuroImage*, *54*(1), 313–327. https://doi.org/10.1016/j.neuroimage.2010.07.033

French, J. A. (2007). First-choice drug for newly diagnosed epilepsy. *The Lancet*, *369*(9566), 970–971. https://doi.org/10.1016/S0140-6736(07)60470-X

French, J. A., & Gazzola, D. M. (2013). Antiepileptic drug treatment: New drugs and new strategies. *CONTINUUM Lifelong Learning in Neurology*, *19*(3), 643–655. https://doi.org/10.1212/01.CON.0000431380.21685.75

Friedman, E. (2014). Epilepsy imaging in adults: getting it right. *AJR. American Journal of Roentgenology*, *203*(5), 1093–1103. https://doi.org/10.2214/AJR.13.12035

Gaillard, W. D., Bookheimer, S. Y., Hertz-Pannier, L., & Blaxton, T. A. (1997). The noninvasive identification of language function. Neuroimaging and rapid transcranial magnetic stimulation. *Neurosurgery Clinics of North America*, *8*(3), 321–335.

Gibson, E., Li, W., Sudre, C., Fidon, L., Shakir, D. I., Wang, G., Eaton-Rosen, Z., Gray, R., Doel, T., Hu, Y., Whyntie, T., Nachev, P., Modat, M., Barratt, D. C., Ourselin, S., Cardoso, M. J., & Vercauteren, T. (2018). NiftyNet: a deep-learning platform for medical imaging. *Computer*

Methods and Programs in Biomedicine, *158*, 113–122. https://doi.org/10.1016/J.CMPB.2018.01.025

Giorgi, C., Broggi, G., Casolino, D., Franzini, A., & Pluchino, F. (1989a). Computer assisted analysis of neuroradiological data in planning neurosurgical procedures. *Journal of Neurosurgical Sciences*, *33*(1), 19–22.

Giorgi, C., Casolino, S. D., Franzini, A., Servello, D., Passerini, A., Broggi, G., & Pluchino, F. (1989b). Computer-assisted planning of stereotactic neurosurgical procedures. *Child's Nervous System : ChNS : Official Journal of the International Society for Pediatric Neurosurgery*, *5*(5), 299–302.

Gleichgerrcht, E., Fridriksson, J., Rorden, C., & Bonilha, L. (2017). NeuroImage : Clinical Connectome-based lesion-symptom mapping (CLSM): A novel approach to map neurological function ☆. *NeuroImage: Clinical*, *16*(August), 461–467. https://doi.org/10.1016/j.nicl.2017.08.018

Gonzalez-Martinez, J., Bulacio, J., Alexopoulos, A., Jehi, L., Bingaman, W., & Najm, I. (2013). Stereoelectroencephalography in the "difficult to localize" refractory focal epilepsy: Early experience from a North American epilepsy center. *Epilepsia*, *54*(2), 323–330. https://doi.org/10.1111/j.1528-1167.2012.03672.x

Gonzalez-Martinez, J., Bulacio, J., Thompson, S., Gale, J., Smithason, S., Najm, I., & Bingaman, W. (2016). Technique, Results, and Complications Related to Robot-Assisted Stereoelectroencephalography. *Neurosurgery*, *78*(2), 169–180. https://doi.org/10.1227/NEU.0000000000001034

Gooneratne, I. K., Mannan, S., de Tisi, J., Gonzalez, J. C., McEvoy, A. W., Miserocchi, A., Diehl, B., Wehner, T., Bell, G. S., Sander, J. W., & Duncan, J. S. (2017). Somatic complications of epilepsy surgery over 25 years at a single center. *Epilepsy Research*, *132*, 70–77. https://doi.org/10.1016/j.eplepsyres.2017.02.016

Gottlieb, S. (2017). *Statement from FDA Commissioner Scott Gottlieb, M.D., on advancing new digital health policies to encourage innovation, bring efficiency and modernization to regulation*. https://www.fda.gov/newsevents/newsroom/pressannouncements/ucm587890.htm

Graham, D., Tisdall, M. M., & Gill, D. (2016). Corpus callosotomy outcomes in pediatric patients: A systematic review. *Epilepsia*, *57*(7), 1053–1068. https://doi.org/10.1111/epi.13408

Granados, A., Mancini, M., Vos, S. B., Lucena, O., Vakharia, V., Rodionov, R., Miserocchi, A.,

McEvoy, A. W., Duncan, J. S., Sparks, R., & Ourselin, S. (2018a). A Machine Learning Approach to Predict Instrument Bending in Stereotactic Neurosurgery. In *International Conference on Medical Image Computing and Computer-Assisted Intervention* (pp. 238–246).

Granados, A., Vakharia, V., Rodionov, R., Schweiger, M., Vos, S. B., O'Keeffe, A. G., Li, K., Wu, C., Miserocchi, A., McEvoy, A. W., Clarkson, M. J., Duncan, J. S., Sparks, R., & Ourselin, S. (2018b). Automatic segmentation of stereoelectroencephalography (SEEG) electrodes post-implantation considering bending. *International Journal of Computer Assisted Radiology and Surgery*. https://doi.org/10.1007/s11548-018-1740-8

Grewal, S. S., Alvi, M. A., Lu, V. M., Wahood, W., Worrell, G. A., Tatum, W., Jr, R. E. W., & Gompel, J. J. Van. (2019). Magnetic Resonance-Guided Laser Interstitial Thermal Therapy Versus Stereotactic Radiosurgery for Medically Intractable Temporal Lobe Epilepsy: A Systematic Review and Meta-Analysis of Seizure Outcomes and Complications. *World Neurosurgery*, *122*, e32–e47. https://doi.org/10.1016/j.wneu.2018.08.227

Grivas, A., Schramm, J., Kral, T., von Lehe, M., Helmstaedter, C., Elger, C. E., & Clusmann, H. (2006). Surgical treatment for refractory temporal lobe epilepsy in the elderly: seizure outcome and neuropsychological sequels compared with a younger cohort. *Epilepsia*, *47*(8), 1364–1372. https://doi.org/10.1111/j.1528-1167.2006.00608.x

Gross, R. E., Stern, M. A., Willie, J. T., Fasano, R. E., Saindane, A. M., Soares, B. P., Pedersen, N. P., & Drane, D. L. (2018). Stereotactic laser amygdalohippocampotomy for mesial temporal lobe epilepsy. *Annals of Neurology*, *83*(3), 575–587. https://doi.org/10.1002/ana.25180

Gross, R. E., Willie, J. T., & Drane, D. L. (2016). The Role of Stereotactic Laser Amygdalohippocampotomy in Mesial Temporal Lobe Epilepsy. *Neurosurgery Clinics of North America*, *27*(1), 37–50.

Grouiller, F., Thornton, R. C., Groening, K., Spinelli, L., Duncan, J. S., Schaller, K., Siniatchkin, M., Lemieux, L., Seeck, M., Michel, C. M., & Vulliemoz, S. (2011). With or without spikes: localization of focal epileptic activity by simultaneous electroencephalography and functional magnetic resonance imaging. *Brain : A Journal of Neurology*, *134*(Pt 10), 2867–2886. https://doi.org/10.1093/brain/awr156

Guend, H., Widmar, M., Patel, S., Nash, G. M., Paty, P. B., Guillem, J. G., Temple, L. K., Garcia-Aguilar, J., & Weiser, M. R. (2016). Developing a robotic colorectal cancer surgery program: understanding institutional and individual learning curves. *Surgical Endoscopy*.

https://doi.org/10.1007/s00464-016-5292-0

Guo, T., Parrent, A. G., & Peters, T. M. (2007). Automatic target and trajectory identification for deep brain stimulation (DBS) procedures. *Medical Image Computing and Computer-Assisted Intervention : MICCAI ... International Conference on Medical Image Computing and Computer-Assisted Intervention*, *10*(Pt 1), 483–490.

Guo, Z., Leong, M. C. W., Su, H., Kwok, K. W., Chan, D. T. M., & Poon, W. S. (2018). Techniques for Stereotactic Neurosurgery: Beyond the Frame, Toward the Intraoperative Magnetic Resonance Imaging–Guided and Robot-Assisted Approaches. *World Neurosurgery*, *116*(Aug), 77–87. https://doi.org/10.1016/j.wneu.2018.04.155

Haneef, Z., Stern, J., Dewar, S., & Engel, J. J. (2010). Referral pattern for epilepsy surgery after evidence-based recommendations: a retrospective study. *Neurology*, *75*(8), 699–704. https://doi.org/10.1212/WNL.0b013e3181eee457

Harward, S. C., Chen, W. C., Rolston, J. D., Haglund, M. M., & Englot, D. J. (2018). Seizure outcomes in occipital lobe and posterior quadrant epilepsy surgery: A systematic review and meta-analysis. *Clinical Neurosurgery*, *82*(3), 350–358. https://doi.org/10.1093/neuros/nyx158

He, Y., & Evans, A. (2010). Graph theoretical modeling of brain connectivity. *Current Opinion in Neurology*, *23*(4), 341–350. https://doi.org/10.1097/WCO.0b013e32833aa567

Helmstaedter, C., Jockwitz, C., & Witt, J. A. (2015). Menstrual cycle corrupts reliable and valid assessment of language dominance: Consequences for presurgical evaluation of patients with epilepsy. *Seizure*, *28*, 26–31. https://doi.org/10.1016/j.seizure.2015.02.010

Helmstaedter, C., Richter, S., Roske, S., Oltmanns, F., Schramm, J., & Lehmann, T.-N. (2008). Differential effects of temporal pole resection with amygdalohippocampectomy versus selective amygdalohippocampectomy on material-specific memory in patients with mesial temporal lobe epilepsy. *Epilepsia*, *49*(1), 88–97. https://doi.org/10.1111/j.1528-1167.2007.01386.x

Hermann, B., Davies, K., Foley, K., & Bell, B. (1999). Visual confrontation naming outcome after standard left anterior temporal lobectomy with sparing versus resection of the superior temporal gyrus: a randomized prospective clinical trial. *Epilepsia*, *40*(8), 1070–1076.

Ho, A. L., Miller, K. J., Cartmell, S., Inoyama, K., Fisher, R. S., & Halpern, C. H. (2016). Stereotactic laser ablation of the splenium for intractable epilepsy. *Epilepsy and Behavior Case Reports*, *5*, 23–26. https://doi.org/10.1016/j.ebcr.2015.12.003

Hong, S.-J., Kim, H., Schrader, D., Bernasconi, N., Bernhardt, B. C., & Bernasconi, A. (2014). Automated detection of cortical dysplasia type II in MRI-negative epilepsy. *Neurology*, *83*(1), 48–55. https://doi.org/10.1212/WNL.0000000000000543

Hoppe, C., Elger, C. E., & Helmstaedter, C. (2007). Long-term memory impairment in patients with focal epilepsy. *Epilepsia*, *48*(SUPPL. 9), 26–29. https://doi.org/10.1111/j.1528-1167.2007.01397.x

Hoppe, C., Witt, J. A., Helmstaedter, C., Gasser, T., Vatter, H., & Elger, C. E. (2017). Laser interstitial thermotherapy (LiTT) in epilepsy surgery. *Seizure*, *48*, 45–52. https://doi.org/10.1016/j.seizure.2017.04.002

Hori, T., Tabuchi, S., Kurosaki, M., Kondo, S., Takenobu, A., & Watanabe, T. (1993). Subtemporal amygdalohippocampectomy for treating medically intractable temporal lobe epilepsy. *Neurosurgery*, *33*(1), 50–57.

Hori, T., Yamane, F., & Takenobu, A. (2002). Microanatomy of medial temporal area and subtemporal amygdalohippocampectomy. *Stereotactic and Functional Neurosurgery*, *77*(1–4), 208–212. https://doi.org/10.1159/000064594

Hou, Z., Chen, X., Shi, X., An, N., Yang, M., Yang, H., Zhang, D., & Liu, S. (2014). Comparison of neuronavigation and frame-based stereotactic system in implanting epileptic depth electrodes. *Turkish Neurosurgery*, *26*(16), 1–8. https://doi.org/10.5137/1019-5149.JTN.11400-14.2

Hu, W.-H., Zhang, C., Zhang, K., Shao, X.-Q., & Zhang, J.-G. (2016). Hemispheric surgery for refractory epilepsy: a systematic review and meta-analysis with emphasis on seizure predictors and outcomes. *Journal of Neurosurgery*, *124*(4), 952–961. https://doi.org/10.3171/2015.4.JNS14438

Huppertz, H.-J., Grimm, C., Fauser, S., Kassubek, J., Mader, I., Hochmuth, A., Spreer, J., & Schulze-Bonhage, A. (2005). Enhanced visualization of blurred gray-white matter junctions in focal cortical dysplasia by voxel-based 3D MRI analysis. *Epilepsy Research*, *67*(1–2), 35–50. https://doi.org/10.1016/j.eplepsyres.2005.07.009

International League Against Epilepsy. (1997). ILAE Commission Report Recommendations for Neuroimaging of Patients with Epilepsy. *Epilepsia*, *38*(11), 1255–1256.

Isnard, J., Taussig, D., Bartolomei, F., Bourdillon, P., Catenoix, H., Chassoux, F., Chipaux, M., Clémenceau, S., Colnat-Coulbois, S., Denuelle, M., Derrey, S., Devaux, B., Dorfmüller, G., Gilard, V., Guenot, M., Job-Chapron, A. S., Landré, E., Lebas, A., Maillard, L., … Sauleau, P.

(2018). French guidelines on stereoelectroencephalography (SEEG). *Neurophysiologie Clinique*, *48*(1), 5–13. https://doi.org/10.1016/j.neucli.2017.11.005

Jayne, D., Pigazzi, A., Marshall, H., Croft, J., Corrigan, N., Copeland, J., Quirke, P., West, N., Rautio, T., Thomassen, N., Tilney, H., Gudgeon, M., Bianchi, P. Pietro, Edlin, R., Hulme, C., & Brown, J. (2017). Effect of Robotic-Assisted vs Conventional Laparoscopic Surgery on Risk of Conversion to Open Laparotomy Among Patients Undergoing Resection for Rectal Cancer: The ROLARR Randomized Clinical Trial. *JAMA*, *318*(16), 1569–1580. https://doi.org/10.1001/jama.2017.7219

Jeanmonod, D., Werner, B., Morel, A., Michels, L., Zadicario, E., Schiff, G., & Martin, E. (2012). Transcranial magnetic resonance imaging-guided focused ultrasound: noninvasive central lateral thalamotomy for chronic neuropathic pain. *Neurosurgical Focus*, *32*(1), E1. https://doi.org/10.3171/2011.10.FOCUS11248

Jellison, B. J., Field, a. S., Medow, J., Lazar, M., Salamat, M. S., & Alexander, a. L. (2004a). Diffusion tensor imaging of cerebral white matter: a pictorial review of physics, fiber tract anatomy, and tumor imaging patterns. *Am J Neuroradiol*, *25*(3), 356—69. https://doi.org/10.1038/nrn2776

Jellison, B. J., Field, A. S., Medow, J., Lazar, M., Salamat, M. S., & Alexander, A. L. (2004b). Diffusion Tensor Imaging of Cerebral White Matter: A Pictorial Review of Physics, Fiber Tract Anatomy, and Tumor Imaging Patterns. *American Journal of Neuroradiology*, *25*(3), 356–369. https://doi.org/10.1038/nrn2776

Jenne, J. W. (2015). *Non-Invasive Transcranial Brain Ablation with High-Intensity Focused Ultrasound*. *36*, 94–105. https://doi.org/10.1159/000366241

Jermakowicz, W. J., Cajigas, I., Dan, L., Guerra, S., Sur, S., Haese, F. D., Kanner, A. M., & Jagid, J. R. (2018). Ablation dynamics during laser interstitial thermal therapy for mesiotemporal epilepsy. *PloS One*, 1–18.

Jermakowicz, W. J., Ivan, M. E., Cajigas, I., Ribot, R., Jusue-Torres, I., Desai, M. B., Ruiz, A., D'Haese, P. F., Kanner, A. M., & Jagid, J. R. (2017a). Visual deficit from laser interstitial thermal therapy for temporal lobe epilepsy: Anatomical considerations. *Operative Neurosurgery*, *13*(5), 627–633. https://doi.org/10.1093/ons/opx029

Jermakowicz, W. J., Kanner, A. M., Sur, S., Bermudez, C., D'Haese, P. F., Kolcun, J. P. G., Cajigas, I., Li, R., Millan, C., Ribot, R., Serrano, E. A., Velez, N., Lowe, M. R., Rey, G. J., & Jagid, J. R. (2017b). Laser thermal ablation for mesiotemporal epilepsy: Analysis of ablation volumes

and trajectories. *Epilepsia*, *58*(5), 801–810. https://doi.org/10.1111/epi.13715

Jeurissen, B., Tournier, J.-D., Dhollander, T., Connelly, A., & Sijbers, J. (2014). Multi-tissue constrained spherical deconvolution for improved analysis of multi-shell diffusion MRI data. *NeuroImage*, *103*, 411–426. https://doi.org/10.1016/j.neuroimage.2014.07.061

Jobst, B. C., & Cascino, G. D. (2015). Resective epilepsy surgery for drug-resistant focal epilepsy: A review. *JAMA - Journal of the American Medical Association*, *313*(3), 285–293. https://doi.org/10.1001/jama.2014.17426

Jolesz, F. A., Hynynen, K., McDannold, N., & Tempany, C. (2005). MR imaging-controlled focused ultrasound ablation: a noninvasive image-guided surgery. *Magnetic Resonance Imaging Clinics of North America*, *13*(3), 545–560. https://doi.org/10.1016/j.mric.2005.04.008

JonesGotman, M., Zatorre, R. J., Olivier, A., Andermann, F., Cendes, F., Staunton, H., McMackin, D., Siegel, A. M., & Wieser, H. G. (1997). Learning and retention of wards and designs following excision from medial or lateral temporal-lobe structures. *Neuropsychologia*, *35*(7), 963–973. https://doi.org/10.1016/S0028-3932(97)00024-9

Joo, E. Y., Han, H. J., Lee, E. K., Choi, S., Jin, J. H., Kim, J. H., Tae, W. S., Seo, D. W., Hong, S. C., Lee, M., & Hong, S. B. (2005). Resection extent versus postoperative outcomes of seizure and memory in mesial temporal lobe epilepsy. *Seizure*, *14*(8), 541–551. https://doi.org/10.1016/j.seizure.2005.08.011

Josephson, C. B., Dykeman, J., Fiest, K. M., Liu, X., Sadler, R. M., Jette, N., & Wiebe, S. (2013). Systematic review and meta-analysis of standard vs selective temporal lobe epilepsy surgery. *Neurology*, *80*(18), 1669–1676.

Kang, J. Y., Wu, C., Tracy, J., Lorenzo, M., Evans, J., Nei, M., Skidmore, C., Mintzer, S., Sharan, A. D., & Sperling, M. R. (2016). Laser interstitial thermal therapy for medically intractable mesial temporal lobe epilepsy. *Epilepsia*, *57*(2), 325–334. https://doi.org/10.1111/epi.13284

Kanner, A. M., Stagno, S., Kotagal, P., & Morris, H. H. (1996). Postictal psychiatric events during prolonged video-electroencephalographic monitoring studies. *Archives of Neurology*, *53*(3), 258–263. https://doi.org/10.1001/archneur.1996.00550030070024

Karsy, M., Patel, D. M., Halvorson, K., Mortimer, V., & Bollo, R. J. (2018). Anterior two-thirds corpus callosotomy via stereotactic laser ablation. *Neurosurgical Focus*, *44*(VideoSuppl2), V2. https://doi.org/10.3171/2018.4.focusvid.17721

Keihaninejad, S., Heckemann, R. A., Gousias, I. S., Hajnal, J. V., Duncan, J. S., Aljabar, P.,

Rueckert, D., & Hammers, A. (2012). Classification and lateralization of temporal lobe epilepsies with and without hippocampal atrophy based on whole-brain automatic mri segmentation. *PLoS ONE*, *7*(4), 1–12. https://doi.org/10.1371/journal.pone.0033096

Keller, S. S., Glenn, G. R., Weber, B., Kreilkamp, B. A. K., Jensen, J. H., Helpern, J. A., Wagner, J., Barker, G. J., Richardson, M. P., & Bonilha, L. (2017). Preoperative automated fibre quantification predicts postoperative seizure outcome in temporal lobe epilepsy. *Brain : A Journal of Neurology*, *140*(2016), 68–82. https://doi.org/10.1093/brain/aww280

Kim, H.-J., Lee, S. H., Chang, B.-S., Lee, C.-K., Lim, T. O., Hoo, L. P., Yi, J.-M., & Yeom, J. S. (2015). Monitoring the Quality of Robot-Assisted Pedicle Screw Fixation in the Lumbar Spine by Using a Cumulative Summation Test. *Spine*, *40*(2), 87–94. https://doi.org/10.1097/BRS.0000000000000680

Knake, S., Triantafyllou, C., Wald, L. L., Wiggins, G., Kirk, G. P., Larsson, P. G., Stufflebeam, S. M., Foley, M. T., Shiraishi, H., Dale, A. M., Halgren, E., & Grant, P. E. (2005). 3T phased array MRI improves the presurgical evaluation in focal epilepsies: A prospective study. *Neurology*, *65*(7), 1026–1031. https://doi.org/10.1212/01.wnl.0000179355.04481.3c

Kovac, S., Vakharia, V. N., Scott, C., & Diehl, B. (2016). Invasive epilepsy surgery evaluation. *Seizure*, *Jan*(44), 125–136. https://doi.org/10.1016/j.seizure.2016.10.016

Kovac, S., Vakharia, V. N. V. N., Scott, C., & Diehl, B. (2017). Invasive epilepsy surgery evaluation. *Seizure*, *44*, 125–136. https://doi.org/10.1016/j.seizure.2016.10.016

Kubicki, M., Westin, C.-F., Maier, S. E., Frumin, M., Nestor, P. G., Salisbury, D. F., Kikinis, R., Jolesz, F. A., McCarley, R. W., & Shenton, M. E. (2002). Uncinate fasciculus findings in schizophrenia: a magnetic resonance diffusion tensor imaging study. *The American Journal of Psychiatry*, *159*(5), 813–820. https://doi.org/10.1176/appi.ajp.159.5.813

Kupper, H., Groeschel, S., Alber, M., Klose, U., Schuhmann, M. U., & Wilke, M. (2015). Comparison of different tractography algorithms and validation by intraoperative stimulation in a child with a brain tumor. *Neuropediatrics*, *46*(1), 72–75. https://doi.org/10.1055/s-0034-1395346

Kwan, A., Ng, W. H., Otsubo, H., Ochi, A., Snead, O. C. 3rd, Tamber, M. S., & Rutka, J. T. (2010). Hemispherectomy for the control of intractable epilepsy in childhood: comparison of 2 surgical techniques in a single institution. *Neurosurgery*, *67*(2 Suppl Operative), 429–436. https://doi.org/10.1227/NEU.0b013e3181f743dc

Kwan, P., & Sperling, M. R. (2009). Refractory seizures: Try additional antiepileptic drugs (after

two have failed) or go directly to early surgery evaluation? *Epilepsia*, *50*(SUPPL. 8), 57–62. https://doi.org/10.1111/j.1528-1167.2009.02237.x

Kwoh, Y. S., Hou, J., Jonckheere, E. A., & Hayati, S. (1988). A robot with improved absolute positioning accuracy for CT guided stereotactic brain surgery. *IEEE Transactions on Bio-Medical Engineering*, *35*(2), 153–160. https://doi.org/10.1109/10.1354

la Fougère, C., Rominger, A., Förster, S., Geisler, J., & Bartenstein, P. (2009). PET and SPECT in epilepsy: A critical review. *Epilepsy and Behavior*, *15*(1), 50–55. https://doi.org/10.1016/j.yebeh.2009.02.025

Lagman, C., Chung, L. K., Pelargos, P. E., Ung, N., Bui, T. T., Lee, S. J., Voth, B. L., & Yang, I. (2017). Laser neurosurgery: A systematic analysis of magnetic resonance-guided laser interstitial thermal therapies. *Journal of Clinical Neuroscience*, *36*, 20–26. https://doi.org/10.1016/j.jocn.2016.10.019

Lancet, T. (2010). *Randomised trials in The Lancet : formatting guidelines*. *November*, 1–4.

Lancman, G., Virk, M., Shao, H., Mazumdar, M., Greenfield, J. P., Weinstein, S., & Schwartz, T. H. (2013). Vagus nerve stimulation vs. corpus callosotomy in the treatment of Lennox-Gastaut syndrome: a meta-analysis. *Seizure*, *22*(1), 3–8. https://doi.org/10.1016/j.seizure.2012.09.014

Landis, J. R., & Koch, G. G. (1977). An application of hierarchical kappa-type statistics in the assessment of majority agreement among multiple observers. *Biometrics*, *33*(2), 363–374.

Laoprasert, P., Ojemann, J. G., & Handler, M. H. (2017). Insular epilepsy surgery. *Epilepsia*, *58*, 35–45. https://doi.org/10.1111/epi.13682

Lee, S.-A., Yim, S. Bin, Lim, Y. M., Kang, J. K., & Lee, J. K. (2006). Factors predicting seizure outcome of anterior temporal lobectomy for patients with mesial temporal sclerosis. *Seizure*, *15*(6), 397–404. https://doi.org/10.1016/j.seizure.2006.05.003

Lee, T., Mackenzie, R. a, Walker, a J., Matheson, J. M., & Sachdev, P. (1997). Effects of left temporal lobectomy and amygdalohippocampectomy on memory. *Journal of Clinical Neuroscience : Official Journal of the Neurosurgical Society of Australasia*, *4*(3), 314–319. https://doi.org/10.1016/S0967-5868(97)90098-9

Lehner, K. R., Yeagle, E. M., Argyelan, M., Klimaj, Z., Du, V., Megevand, P., Hwang, S. T., & Mehta, A. D. (2018). Validation of corpus callosotomy after laser interstitial thermal therapy: a multimodal approach. *Journal of Neurosurgery*, 1–11. https://doi.org/10.3171/2018.4.JNS172588

Lewis, E. C., Weil, A. G., Duchowny, M., Bhatia, S., Ragheb, J., & Miller, I. (2015). MR-guided laser interstitial thermal therapy for pediatric drug-resistant lesional epilepsy. *Epilepsia*, *56*(10), 1590–1598. https://doi.org/10.1111/epi.13106

Li, K., Vakharia, V. N., Sparks, R., França, L. G. S., Granados, A., McEvoy, A. W., Miserocchi, A., Wang, M., Ourselin, S., & Duncan, J. S. (2019a). Optimizing Trajectories for Cranial Laser Interstitial Thermal Therapy Using Computer-Assisted Planning: A Machine Learning Approach. *Neurotherapeutics*, *Jan*(16(1)), 182:191. https://doi.org/10.1007/s13311-018-00693-1

Li, K., Vakharia, V. N., Sparks, R., Rodionov, R., Vos, S. B., McEvoy, A. W., Miserocchi, A., Wang, M., Ourselin, S., & Duncan, J. S. (2019b). Stereoelectroencephalography electrode placement: Detection of blood vessel conflicts. *Epilepsia*, *October 2018*, epi.16294. https://doi.org/10.1111/epi.16294

Liaw, A., & Wiener, M. (2002). Classification and Regression by randomForest. *R News*, *2*(3), 18–22.

Liberati, A., Altman, D. G., Tetzlaff, J., Mulrow, C., Gøtzsche, P. C., Ioannidis, J. P. A., Clarke, M., Devereaux, P. J., Kleijnen, J., & Moher, D. (2009). The PRISMA statement for reporting systematic reviews and meta-analyses of studies that evaluate health care interventions: explanation and elaboration. *Journal of Clinical Epidemiology*, *62*(10), e1-34. https://doi.org/10.1016/j.jclinepi.2009.06.006

Lipsman, N., Schwartz, M. L., Huang, Y., Lee, L., Sankar, T., Chapman, M., Hynynen, K., & Lozano, A. M. (2013). MR-guided focused ultrasound thalamotomy for essential tremor: a proof-of-concept study. *The Lancet. Neurology*, *12*(5), 462–468. https://doi.org/10.1016/S1474-4422(13)70048-6

Liu, Y., Konrad, P. E., Neimat, J. S., Tatter, S. B., Yu, H., Datteri, R. D., Landman, B. A., Noble, J. H., Pallavaram, S., Dawant, B. M., & D'Haese, P.-F. (2014). Multisurgeon, multisite validation of a trajectory planning algorithm for deep brain stimulation procedures. *IEEE Transactions on Bio-Medical Engineering*, *61*(9), 2479–2487. https://doi.org/10.1109/TBME.2014.2322776

Löscher, W., Klitgaard, H., Twyman, R. E., & Schmidt, D. (2013). New avenues for anti-epileptic drug discovery and development. *Nature Reviews Drug Discovery*, *12*(10), 757–776. https://doi.org/10.1038/nrd4126

Luders, H. O., Burgess, R., & Noachtar, S. (1993). Expanding the international classification of

seizures to provide localization information. *Neurology*, *43*(9), 1650–1655.

Lüders, H. O., Najm, I., Nair, D., Widdess-Walsh, P., & Bingman, W. (2006). The epileptogenic zone: General principles. *Epileptic Disorders*, *8*(SUPPL. 2), 1–9.

Lutz, M. T., Clusmann, H., Elger, C. E., Schramm, J., & Helmstaedter, C. (2004). Neuropsychological outcome after selective amygdalohippocampectomy with transsylvian versus transcortical approach: A randomized prospective clinical trial of surgery for temporal lobe epilepsy. *Epilepsia*, *45*(7), 809–816. https://doi.org/10.1111/j.0013-9580.2004.54003.x

Maier-Hein, K. H., Neher, P. F., Houde, J. C., Côté, M. A., Garyfallidis, E., Zhong, J., Chamberland, M., Yeh, F. C., Lin, Y. C., Ji, Q., Reddick, W. E., Glass, J. O., Chen, D. Q., Feng, Y., Gao, C., Wu, Y., Ma, J., Renjie, H., Li, Q., … Descoteaux, M. (2017). The challenge of mapping the human connectome based on diffusion tractography. *Nature Communications*, *8*(1). https://doi.org/10.1038/s41467-017-01285-x

Malak, R., Bouthillier, A., Carmant, L., Cossette, P., Giard, N., Saint-Hilaire, J.-M., Nguyen, D. B., & Nguyen, D. K. (2009). Microsurgery of epileptic foci in the insular region. *Journal of Neurosurgery*, *110*(6), 1153–1163. https://doi.org/10.3171/2009.1.JNS08807

Malikova, H., Kramska, L., Vojtech, Z., Liscak, R., Sroubek, J., Lukavsky, J., & Druga, R. (2014). Different surgical approaches for mesial temporal epilepsy: Resection extent, seizure, and neuropsychological outcomes. *Stereotactic and Functional Neurosurgery*, *92*(6), 372–380. https://doi.org/10.1159/000366003

Mancini, M., Vos, S. B., Vakharia, V. N., O'Keeffe, A. G., Trimmel, K., Barkhof, F., Dorfer, C., Soman, S., Winston, G. P., Wu, C., Duncan, J. S., Sparks, R., & Ourselin, S. (2019). Automated fiber tract reconstruction for surgery planning: Extensive validation in language-related white matter tracts. *NeuroImage: Clinical*, 101883. https://doi.org/https://doi.org/10.1016/j.nicl.2019.101883

Mandonnet, E., Nouet, A., Gatignol, P., Capelle, L., & Duffau, H. (2007). Does the left inferior longitudinal fasciculus play a role in language? A brain stimulation study. *Brain*, *130*(3), 623–629. https://doi.org/10.1093/brain/awl361

Marcus, H. J., Hughes-Hallett, A., Payne, C. J., Cundy, T. P., Nandi, D., Yang, G. Z., & Darzi, A. (2017). Trends in the diffusion of robotic surgery: A retrospective observational study. *International Journal of Medical Robotics and Computer Assisted Surgery*, *13*(4), 10–13. https://doi.org/10.1002/rcs.1870

Marcus, H. J., Payne, C. J., Hughes-Hallett, A., Marcus, A. P., Yang, G.-Z., Darzi, A., & Nandi, D. (2016). Regulatory approval of new medical devices: cross sectional study. *BMJ (Clinical Research Ed.)*, *353*, i2587. https://doi.org/10.1136/bmj.i2587

Marcus, H. J., Vakharia, V. N., Ourselin, S., Duncan, J., Tisdall, M., & Aquilina, K. (2018). Robot-assisted stereotactic brain biopsy: systematic review and bibliometric analysis. *Child's Nervous System*. https://doi.org/10.1007/s00381-018-3821-y

Marcus, H. J., Vakharia, V. N., Sparks, R., Rodionov, R., Kitchen, N., McEvoy, A. W., Miserocchi, A., Thorne, L., Ourselin, S. S., & Duncan, J. S. (2019). Computer-assisted versus manual planning for stereotactic brain biopsy: a retrospective comparative pilot study. *Operative Neurosurgery*, *ONS-D-18-00919R1*. https://doi.org/10.1093/ons/opz177

Marras, C. E., Granata, T., Franzini, A., Freri, E., Villani, F., Casazza, M., De Curtis, M., Ragona, F., Ferroli, P., D'Incerti, L., Pincherle, A., Spreafico, R., & Broggi, G. (2010). Hemispherotomy and functional hemispherectomy: Indications and outcome. *Epilepsy Research*, *89*(1), 104–112. https://doi.org/10.1016/j.eplepsyres.2009.09.006

Marsh, L., & Rao, V. (2002). Psychiatric complications in patients with epilepsy: a review. *Epilepsy Research*, *49*(1), 11–33. https://doi.org/10.1016/s0920-1211(02)00008-6

Marson, A. G., Al-kharusi, A. M., Alwaidh, M., Appleton, R., Baker, G. A., Chadwick, D. W., Cramp, C., Cockerell, O. C., Cooper, P. N., Doughty, J., Eaton, B., Gamble, C., Goulding, P. J., Howell, S. J. L., Hughes, A., Jackson, M., Jacoby, A., Kellett, M., Lawson, G. R., … Infi, V. (2007). *The SANAD study*. *369*(9566), 1000–1015. https://doi.org/10.1016/S0140-6736(07)60460-7.The

McClure, P., Rho, N., Lee, J. A., Kaczmarzyk, J. R., Zheng, C. Y., Ghosh, S. S., Nielson, D. M., Thomas, A. G., Bandettini, P., & Pereira, F. (2019). Knowing What You Know in Brain Segmentation Using Bayesian Deep Neural Networks . In *Frontiers in Neuroinformatics* (Vol. 13, p. 67). https://www.frontiersin.org/article/10.3389/fninf.2019.00067

McCormick, C., Quraan, M., Cohn, M., Valiante, T. A., & McAndrews, M. P. (2013). Default mode network connectivity indicates episodic memory capacity in mesial temporal lobe epilepsy. *Epilepsia*, *54*(5), 809–818. https://doi.org/10.1111/epi.12098

McCulloch, P., Cook, J. A., Altman, D. G., Heneghan, C., Diener, M. K., & IDEAL Group. (2013). IDEAL framework for surgical innovation 1: the idea and development stages. In *BMJ (Clinical research ed.)* (Vol. 346). https://doi.org/10.1136/bmj.f3012

McGonigal, A., Sahgal, A., De Salles, A., Hayashi, M., Levivier, M., Ma, L., Martinez, R., Paddick, I.,

Ryu, S., Slotman, B. J., & Régis, J. (2017). Radiosurgery for epilepsy: Systematic review and International Stereotactic Radiosurgery Society (ISRS) practice guideline. *Epilepsy Research*, *137*(August), 123–131. https://doi.org/10.1016/j.eplepsyres.2017.08.016

Mehta, A. D., Labar, D., Dean, A., Harden, C., Hosain, S., Pak, J., Marks, D., & Schwartz, T. H. (2005). Frameless stereotactic placement of depth electrodes in epilepsy surgery. *Journal of Neurosurgery*, *102*(6), 1040–1045. https://doi.org/10.3171/jns.2005.102.6.1040

Meng, F., Ding, H., & Wang, G. (2014). A stereotaxic image-guided surgical robotic system for depth electrode insertion. *Conference Proceedings : ... Annual International Conference of the IEEE Engineering in Medicine and Biology Society. IEEE Engineering in Medicine and Biology Society. Annual Conference*, *2014*, 6167–6170. https://doi.org/10.1109/EMBC.2014.6945037

Minchev, G., Kronreif, G., Martínez-Moreno, M., Dorfer, C., Micko, A., Mert, A., Kiesel, B., Widhalm, G., Knosp, E., & Wolfsberger, S. (2017). A novel miniature robotic guidance device for stereotactic neurosurgical interventions: preliminary experience with the iSYS1 robot. *Journal of Neurosurgery*, *126*(3), 985–996. https://doi.org/10.3171/2016.1.JNS152005

Modat, M., Cash, D. M., Winston, G. P., & Duncan, J. S. (2014). Global image registration using a symmetric block-matching approach. *Journal of Medical Imaging*, *1*(2), 1–7. https://doi.org/10.1117/1.JMI.1.2.024003

Monteith, S., Sheehan, J., Medel, R., Wintermark, M., Eames, M., Snell, J., Kassell, N. F., & Elias, W. J. (2013). Potential intracranial applications of magnetic resonance-guided focused ultrasound surgery. *Journal of Neurosurgery*, *118*(2), 215–221. https://doi.org/10.3171/2012.10.JNS12449

Morino, M., Uda, T., Naito, K., Yoshimura, M., Ishibashi, K., Goto, T., Ohata, K., & Hara, M. (2006). Comparison of neuropsychological outcomes after selective amygdalohippocampectomy versus anterior temporal lobectomy. *Epilepsy and Behavior*, *9*(1), 95–100. https://doi.org/10.1016/j.yebeh.2006.04.017

Morrell, M. J. (2011). Responsive cortical stimulation for the treatment of medically intractable partial epilepsy. *Neurology*, *77*(13), 1295–1304. https://doi.org/10.1212/WNL.0b013e3182302056

Mukherjee, P., Berman, J. I., Chung, S. W., Hess, C. P., & Henry, R. G. (2008). Diffusion tensor MR imaging and fiber tractography: Theoretic underpinnings. *American Journal of*

Neuroradiology, *29*(4), 632–641. https://doi.org/10.3174/ajnr.A1051

Mullin, J. P., Shriver, M., Alomar, S., Najm, I., Bulacio, J., Chauvel, P., & Gonzalez-Martinez, J. (2016a). Is SEEG safe? A systematic review and meta-analysis of stereo-electroencephalography-related complications. *Epilepsia*, *57*(3), 386–401. https://doi.org/10.1111/epi.13298

Mullin, J. P., Smithason, S., & Gonzalez-Martinez, J. (2016b). Stereo-Electro-Encephalo-Graphy (SEEG) With Robotic Assistance in the Presurgical Evaluation of Medical Refractory Epilepsy: A Technical Note. *Journal of Visualized Experiments : JoVE*, *112*. https://doi.org/10.3791/53206

Narvaez-Martinez, Y., Garcia, S., Roldan, P., Torales, J., & Rumia, J. (2016). [Stereoelectroencephalography by using O-Arm(R) and Vertek(R) passive articulated arm: Technical note and experience of an epilepsy referral centre]. *Neurocirugia (Asturias, Spain)*. https://doi.org/10.1016/j.neucir.2016.05.002

National Institute for Health and Clinical Excellence, & Excellence, N. I. for H. and C. (2012). The Epilepsies: The diagnosis and management of the epilepsies in adults and children in primary and secondary care. *Chapter 4: Guidance*, 57–83.

Navkar, N. V, Tsekos, N. V, Stafford, J. R., Weinberg, J. S., & Deng, Z. (2010). *Visualization and Planning of Neurosurgical Interventions with Straight Access BT - Information Processing in Computer-Assisted Interventions* (N. Navab & P. Jannin (eds.); pp. 1–11). Springer Berlin Heidelberg.

Neudorfer, C., Hunsche, S., Hellmich, M., El Majdoub, F., & Maarouf, M. (2018). Comparative Study of Robot-Assisted versus Conventional Frame-Based Deep Brain Stimulation Stereotactic Neurosurgery. *Stereotactic and Functional Neurosurgery*, *96*(5), 327–334. https://doi.org/10.1159/000494736

Neuwirth, E. (2014). *RColorBrewer: ColorBrewer Palettes*.

Niemeyer, P. (1958). The transventricular amygdalo-hippocampectomy in temporal lobe epilepsy. *Baldwin M, Bailey P, Eds. Temporal Lobe Epilepsy, Springfi Eld, IL, CC Thomas;*, 461–482.

NIH Clinical Trials.gov NCT02820740. (2016). *Feasibility Study on LITT for Medical Refractory Epilepsy NCT02820740*. https://clinicaltrials.gov/ct2/show/NCT02820740

NIH Clinical Trials.gov NCT02844465. (2016). *Stereotactic Laser Ablation for Temporal Lobe Epilepsy (SLATE) NCT02844465*. https://clinicaltrials.gov/ct2/show/NCT02844465

Nilsson, D., Malmgren, K., Rydenhag, B., & Frisen, L. (2004). Visual field defects after temporal lobectomy -- comparing methods and analysing resection size. *Acta Neurologica Scandinavica*, *110*(5), 301–307. https://doi.org/10.1111/j.1600-0404.2004.00331.x

Novara, G., Catto, J. W. F., Wilson, T., Annerstedt, M., Chan, K., Murphy, D. G., Motttrie, A., Peabody, J. O., Skinner, E. C., Wiklund, P. N., Guru, K. A., & Yuh, B. (2015). Systematic review and cumulative analysis of perioperative outcomes and complications after robot-assisted radical cystectomy. *European Urology*, *67*(3), 376–401. https://doi.org/10.1016/j.eururo.2014.12.007

Nowell, M., Rodionov, R., Diehl, B., Wehner, T., Zombori, G., Kinghorn, J., Ourselin, S., Duncan, J., Miserocchi, A., & McEvoy, A. (2014). A novel method for implementation of frameless StereoEEG in epilepsy surgery. *Clinical Neurosurgery*, *10*(4), 525–533. https://doi.org/10.1227/NEU.0000000000000544

Nowell, M., Rodionov, R., Zombori, G., Sparks, R., Rizzi, M., Ourselin, S., Miserocchi, A., McEvoy, A., & Duncan, J. (2016a). A Pipeline for 3D Multimodality Image Integration and Computer-assisted Planning in Epilepsy Surgery. *Journal of Visualized Experiments : JoVE*, *111*. https://doi.org/10.3791/53450

Nowell, M., Rodionov, R., Zombori, G., Sparks, R., Winston, G., Kinghorn, J., Diehl, B., Wehner, T., Miserocchi, A., McEvoy, A. W., Ourselin, S., & Duncan, J. (2015a). Utility of 3D multimodality imaging in the implantation of intracranial electrodes in epilepsy. *Epilepsia*, *56*(3), 403–413. https://doi.org/10.1111/epi.12924

Nowell, M., Sparks, R., Zombori, G., Miserocchi, A., Rodionov, R., Diehl, B., Wehner, T., Baio, G., Trevisi, G., Tisdall, M., Ourselin, S., McEvoy, A. W., & Duncan, J. (2016b). Comparison of computer-assisted planning and manual planning for depth electrode implantations in epilepsy. *Journal of Neurosurgery*, *124*(6), 1820–1828. https://doi.org/10.3171/2015.6.JNS15487

Nowell, M., Sparks, R., Zombori, G., Miserocchi, A., Rodionov, R., Diehl, B., Wehner, T., White, M., Ourselin, S., McEvoy, A., & Duncan, J. (2017). Resection planning in extratemporal epilepsy surgery using 3D multimodality imaging and intraoperative MRI. *British Journal of Neurosurgery*, *31*(4), 468–470. https://doi.org/10.1080/02688697.2016.1265086

Nowell, M., Vos, S. B., Sidhu, M., Wilcoxen, K., Sargsyan, N., Ourselin, S., & Duncan, J. S. (2015b). Meyer's loop asymmetry and language lateralisation in epilepsy. *Journal of Neurology, Neurosurgery & Psychiatry*, jnnp-2015-311161. https://doi.org/10.1136/jnnp-2015-311161

Nowinski, W. L., Yang, G. L., & Yeo, T. T. (2000). Computer-aided stereotactic functional neurosurgery enhanced by the use of the multiple brain atlas database. In *IEEE transactions on medical imaging* (Vol. 19, Issue 1, pp. 62–69). https://doi.org/10.1109/42.832961

Nowinski, W. L., Yeo, T. T., & Thirunavuukarasuu, A. (1998). Microelectrode-guided functional neurosurgery assisted by Electronic Clinical Brain Atlas CD-ROM. *Computer Aided Surgery : Official Journal of the International Society for Computer Aided Surgery*, *3*(3), 115–122. https://doi.org/10.1002/(SICI)1097-0150(1998)3:3<115::AID-IGS3>3.0.CO;2-Y

O'Keeffe, A. G., Ambler, G., & Barber, J. A. (2017). Sample size calculations based on a difference in medians for positively skewed outcomes in health care studies. *BMC Medical Research Methodology*, *17*(1), 157. https://doi.org/10.1186/s12874-017-0426-1

O'Sullivan., D., Fraccaro, P., E., C., & Weller, P. (2014). Decision time for clinical decision support systems. *Clinical Medicine, Journal of the Royal College of Physicians of London*, *14*(4), 338–341. https://doi.org/10.7861/clinmedicine.14-4-338

Olivier, A. (2000). Transcortical selective amygdalohippocampectomy in temporal lobe epilepsy. *The Canadian Journal of Neurological Sciences. Le Journal Canadien Des Sciences Neurologiques*, *27 Suppl 1*, S68-76; discussion S92-6.

Olson, I. R., Von Der Heide, R. J., Alm, K. H., & Vyas, G. (2015). Development of the uncinate fasciculus: Implications for theory and developmental disorders. *Developmental Cognitive Neuroscience*, *14*, 50–61. https://doi.org/10.1016/j.dcn.2015.06.003

Ortler, M., Sohm, F., Eisner, W., Bauer, R., Dobesberger, J., Trinka, E., Widmann, G., & Bale, R. (2011). Frame-based vs frameless placement of intrahippocampal depth electrodes in patients with refractory epilepsy: A comparative in vivo (application) study. *Neurosurgery*, *68*(4), 881–887. https://doi.org/10.1227/NEU.0b013e3182098e31

Otsuki, T., Jokura, H., Takahashi, K., Ishikawa, S., Yoshimoto, T., Kimura, M., Yoshida, R., & Miyazawa, T. (1994). Stereotactic γ-Thalamotomy with a Computerized Brain Atlas: Technical Case Report. *Neurosurgery*, *35*(4), 764–768. https://doi.org/10.1227/00006123-199410000-00029

Paglioli, E., Martins, W. A., Azambuja, N., Portuguez, M., Frigeri, T. M., Pinos, L., Saute, R., Salles, C., Hoefel, J. R., Soder, R. B., da Costa, J. C., Hemb, M., Theys, T., Palmini, A., & Costa, J. (2016). Selective posterior callosotomy for drop attacks A new approach sparing prefrontal connectivity. *Neurology*, *87*(19), 1–8. https://doi.org/10.1212/WNL.0000000000003307

Paldino, M. J., Yang, E., Jones, J. Y., Mahmood, N., Sher, A., Zhang, W., Hayatghaibi, S., Krishnamurthy, R., & Seghers, V. (2017). Comparison of the diagnostic accuracy of PET/MRI to PET/CT-acquired FDG brain exams for seizure focus detection: a prospective study. *Pediatric Radiology*, *47*(11), 1500–1507. https://doi.org/10.1007/s00247-017-3888-8

Palma, A. E., Wicks, R. T., Popli, G., & Couture, D. E. (2018). Corpus callosotomy via laser interstitial thermal therapy: a case series. *Journal of Neurosurgery: Pediatrics PED*, *23*(3), 303–307. https://doi.org/10.3171/2018.10.PEDS18368

Panov, F., Li, Y., Chang, E. F., Knowlton, R., & Cornes, S. B. (2016). Epilepsy with temporal encephalocele: Characteristics of electrocorticography and surgical outcome. *Epilepsia*, *57*(2), e33–e38. https://doi.org/10.1111/epi.13271

Parker, C. S., Clayden, J. D., Cardoso, M. J., Rodionov, R., Duncan, J. S., Scott, C., Diehl, B., & Ourselin, S. (2018). Structural and effective connectivity in focal epilepsy. *NeuroImage: Clinical*, *17*(December 2017), 943–952. https://doi.org/10.1016/j.nicl.2017.12.020

Parrent, A. G., & Blume, W. T. (1999). Stereotactic amygdalohippocampotomy for the treatment of medial temporal lobe epilepsy. *Epilepsia*, *40*(10), 1408–1416. https://doi.org/10.1111/j.1528-1157.1999.tb02013.x

Pathak-Ray, V., Ray, a, Walters, R., & Hatfield, R. (2002). Detection of visual field defects in patients after anterior temporal lobectomy for mesial temporal sclerosis-establishing eligibility to drive. *Eye (London, England)*, *16*(6), 744–748. https://doi.org/10.1038/sj.eye.6700152

Pendl, G., Eder, H. G., Schroettner, O., & Leber, K. A. (1999). Corpus callosotomy with radiosurgery. *Neurosurgery*, *45*(2), 303–308.

Perry, M. S., Bailey, L., Freedman, D., Donahue, D., Malik, S., Head, H., Keator, C., & Hernandez, A. (2017). Coregistration of multimodal imaging is associated with favourable two-year seizure outcome after paediatric epilepsy surgery. *Epileptic Disorders*, *19*(1), 40–48. https://doi.org/10.1684/epd.2017.0902

Petito, G. T., Wharen, R. E., Feyissa, A. M., Grewal, S. S., Lucas, J. A., & Tatum, W. O. (2018). The impact of stereotactic laser ablation at a typical epilepsy center. *Epilepsy and Behavior*, *78*. https://doi.org/10.1016/j.yebeh.2017.10.041

Pruitt, R., Gamble, A., Black, K., Schulder, M., & Mehta, A. D. (2017). Complication avoidance in laser interstitial thermal therapy: lessons learned. *Journal of Neurosurgery JNS*, *126*(4),

1238–1245. https://doi.org/10.3171/2016.3.JNS152147

R Core Team. (2018). *R: A Language and Environment for Statistical Computing*.

Rasmussen, T. (1973). Postoperative superficial hemosiderosis of the brain, its diagnosis, treatment and prevention. *Transactions of the American Neurological Association*, *98*, 133–137.

Rathore, C., Abraham, M., Rao, R. M., George, A., Sankara Sarma, P., & Radhakrishnan, K. (2007). Outcome after corpus callosotomy in children with injurious drop attacks and severe mental retardation. *Brain & Development*, *29*(9), 577–585. https://doi.org/10.1016/j.braindev.2007.03.008

Regis, J., Lagmari, M., Carron, R., Hayashi, M., McGonigal, A., Daquin, G., Villeneuve, N., Laguitton, V., Bartolomei, F., & Chauvel, P. (2017). Safety and efficacy of Gamma Knife radiosurgery in hypothalamic hamartomas with severe epilepsies: A prospective trial in 48 patients and review of the literature. *Epilepsia*, *58 Suppl 2*, 60–71. https://doi.org/10.1111/epi.13754

Reif, P. S., Strzelczyk, A., & Rosenow, F. (2016). The history of invasive EEG evaluation in epilepsy patients. *Seizure*, *41*, 191–195. https://doi.org/10.1016/j.seizure.2016.04.006

Ring, H. A., Moriarty, J., & Trimble, M. R. (1998). A prospective study of the early postsurgical psychiatric associations of epilepsy surgery. *Journal of Neurology, Neurosurgery, and Psychiatry*, *64*(5), 601–604. https://doi.org/10.1136/jnnp.64.5.601

Rodionov, R., Bartlett, P. A., He, C., Vos, S. B., Focke, N. K., Ourselin, S. G., & Duncan, J. S. (2015). T2 mapping outperforms normalised FLAIR in identifying hippocampal sclerosis. *NeuroImage: Clinical*, *7*, 788–791. https://doi.org/10.1016/j.nicl.2015.03.004

Rodionov, R., O'Keeffe, A., Nowell, M., Rizzi, M., Vakharia, V. N., Wykes, V., Eriksson, S. H., Miserocchi, A., McEvoy, A. W., Ourselin, S., & Duncan, J. S. (2019). Increasing the accuracy of 3D EEG implantations. *Journal of Neurosurgery*, *May 17*, 1–8. https://doi.org/10.3171/2019.2.JNS183313

Rodionov, R., Vollmar, C., Nowell, M., Miserocchi, A., Wehner, T., Micallef, C., Zombori, G., Ourselin, S., Diehl, B., McEvoy, A. W., & Duncan, J. S. (2013). Feasibility of multimodal 3D neuroimaging to guide implantation of intracranial EEG electrodes. *Epilepsy Research*, *107*(1–2), 91–100. https://doi.org/10.1016/j.eplepsyres.2013.08.002

Roessler, K., Sommer, B., Merkel, A., Rampp, S., Gollwitzer, S., Hamer, H. M., & Buchfelder, M. (2016). A frameless stereotactic implantation technique for depth electrodes in refractory

epilepsy utilizing intraoperative MR imaging. *World Neurosurgery*. https://doi.org/10.1016/j.wneu.2016.06.114

Rolston, J. D., Quigg, M., & Barbaro, N. M. (2011). Gamma knife radiosurgery for mesial temporal lobe epilepsy. *Epilepsy Research and Treatment*, *2011*, 840616. https://doi.org/10.1155/2011/840616

Rubinov, M., & Sporns, O. (2010). Complex network measures of brain connectivity: Uses and interpretations. *NeuroImage*. https://doi.org/10.1016/j.neuroimage.2009.10.003

Salanova, V. (2012). Parietal lobe epilepsy. *Journal of Clinical Neurophysiology : Official Publication of the American Electroencephalographic Society*, *29*(5), 392–396. https://doi.org/10.1097/WNP.0b013e31826c9ebc

Salanova, V., Andermann, F., Olivier, A., Rasmussen, T., & Quesney, L. F. (1992). Occipital lobe epilepsy: electroclinical manifestations, electrocorticography, cortical stimulation and outcome in 42 patients treated between 1930 and 1991. Surgery of occipital lobe epilepsy. *Brain : A Journal of Neurology*, *115 (Pt 6*, 1655–1680.

Sarkis, R. A., Jehi, L., Najm, I. M., Kotagal, P., & Bingaman, W. E. (2012). Seizure outcomes following multilobar epilepsy surgery. *Epilepsia*, *53*(1), 44–50. https://doi.org/10.1111/j.1528-1167.2011.03274.x

Schmeiser, B., Wagner, K., Schulze-Bonhage, A., Mader, I., Wendling, A.-S., Steinhoff, B. J., Prinz, M., Scheiwe, C., Weyerbrock, A., & Zentner, J. (2017). Surgical Treatment of Mesiotemporal Lobe Epilepsy: Which Approach is Favorable? *Neurosurgery*. https://doi.org/10.1093/neuros/nyx138

Schmidt, D., & Schachter, S. C. (2014). Drug treatment of epilepsy in adults. *BMJ (Clinical Research Ed.)*, *348*, g254. https://doi.org/10.1136/bmj.g254

Schmidt, R. F., Wu, C., Lang, M. J., Soni, P., Williams, K. A., Boorman, D. W., Evans, J. J., Sperling, M. R., & Sharan, A. D. (2016). Complications of subdural and depth electrodes in 269 patients undergoing 317 procedures for invasive monitoring in epilepsy. *Epilepsia*, *57*(10), 1697–1708. https://doi.org/10.1111/epi.13503

Schramm, J. (2002). Hemispherectomy techniques. *Neurosurgery Clinics of North America*, *13*(1), 113–134, ix.

Schramm, J., Kral, T., & Clusmann, H. (2001). Transsylvian keyhole functional hemispherectomy. *Neurosurgery*, *49*(4), 891.

Schramm, J., Lehmann, T. N., Zentner, J., Mueller, C. A., Scorzin, J., Fimmers, R., Meencke, H. J.,

Schulze-Bonhage, A., & Elger, C. E. (2011a). Randomized controlled trial of 2.5-cm versus 3.5-cm mesial temporal resection - Part 2: Volumetric resection extent and subgroup analyses. *Acta Neurochirurgica*, *153*(2), 221–228. https://doi.org/10.1007/s00701-010-0901-5

Schramm, J., Lehmann, T. N., Zentner, J., Mueller, C. A., Scorzin, J., Fimmers, R., Meencke, H. J., Schulze-Bonhage, A., & Elger, C. E. (2011b). Randomized controlled trial of 2.5-cm versus 3.5-cm mesial temporal resection--Part 2: volumetric resection extent and subgroup analyses. *Acta Neurochirurgica*, *153*(2), 221–228. https://doi.org/10.1007/s00701-010-0901-5

Scorza, D., Amoroso, G., Cortes, C., Artetxe, A., Bertelsen, A., Rizzi, M., Castana, L., De Momi, E., Cardinale, F., & Kabongo, L. (2018). Experience-based SEEG planning: from retrospective data to automated electrode trajectories suggestions. *Healthcare Technology Letters*, *5*(5), 167–171. https://doi.org/10.1049/htl.2018.5075

Scorza, D., De Momi, E., Plaino, L., Amoroso, G., Arnulfo, G., Narizzano, M., Kabongo, L., & Cardinale, F. (2017). Retrospective evaluation and SEEG trajectory analysis for interactive multi-trajectory planner assistant. *International Journal of Computer Assisted Radiology and Surgery*, *12*(10), 1727–1738. https://doi.org/10.1007/s11548-017-1641-2

Serletis, D., Bulacio, J., Bingaman, W., Najm, I., & González-Martínez, J. (2014). The stereotactic approach for mapping epileptic networks: a prospective study of 200 patients. *Journal of Neurosurgery*, *121*(5), 1239–1246. https://doi.org/10.3171/2014.7.JNS132306

Shah, P., Ashourvan, A., Mikhail, F., Pines, A., Kini, L., Oechsel, K., Das, S. R., Stein, J. M., Shinohara, R. T., Bassett, D. S., Litt, B., & Davis, K. A. (2019). Characterizing the role of the structural connectome in seizure dynamics. *Brain*, *142*(7), 1955–1972. https://doi.org/10.1093/brain/awz125

Shamir, R. R., Joskowicz, L., Tamir, I., Dabool, E., Pertman, L., Ben-Ami, A., & Shoshan, Y. (2012). Reduced risk trajectory planning in image-guided keyhole neurosurgery. *Medical Physics*, *39*(5), 2885–2895. https://doi.org/10.1118/1.4704643

Shamir, R. R., Tamir, I., Dabool, E., Joskowicz, L., & Shoshan, Y. (2010). A method for planning safe trajectories in image-guided keyhole neurosurgery. *Medical Image Computing and Computer-Assisted Intervention : MICCAI ... International Conference on Medical Image Computing and Computer-Assisted Intervention*, *13*(Pt 3), 457–464.

Shenai, M. B., Ross, D. A., & Sagher, O. (2007). The use of multiplanar trajectory planning in the

stereotactic placement of depth electrodes. *Neurosurgery*, *60*(4 Suppl 2), 272–276; discussion 276. https://doi.org/10.1227/01.NEU.0000255390.92785.A4

Sivaraman, A., Sanchez-Salas, R., Prapotnich, D., Yu, K., Olivier, F., Secin, F. P., Barret, E., Galiano, M., Rozet, F., & Cathelineau, X. (2017). Learning curve of minimally invasive radical prostatectomy: Comprehensive evaluation and cumulative summation analysis of oncological outcomes. *Urologic Oncology*. https://doi.org/10.1016/j.urolonc.2016.10.015

Skirrow, C., Cross, J. H., Harrison, S., Cormack, F., Harkness, W., Coleman, R., Meierotto, E., Gaiottino, J., Vargha-Khadem, F., & Baldeweg, T. (2015). Temporal lobe surgery in childhood and neuroanatomical predictors of long-term declarative memory outcome. *Brain : A Journal of Neurology*, *138*(Pt 1), 80–93. https://doi.org/10.1093/brain/awu313

Slim, K., Nini, E., Forestier, D., Kwiatkowski, F., Panis, Y., & Chipponi, J. (2003). Methodological index for non-randomized studies (Minors): Development and validation of a new instrument. *ANZ Journal of Surgery*, *73*(9), 712–716. https://doi.org/10.1046/j.1445-2197.2003.02748.x

Smith, R. E., Tournier, J.-D., Calamante, F., & Connelly, A. (2012). Anatomically-constrained tractography: improved diffusion MRI streamlines tractography through effective use of anatomical information. *NeuroImage*, *62*(3), 1924–1938. https://doi.org/10.1016/j.neuroimage.2012.06.005

Smyth, M. D., Vellimana, A. K., & Asano, E. (2017a). *Corpus callosotomy — Open and endoscopic surgical techniques*. 73–79. https://doi.org/10.1111/epi.13681

Smyth, M. D., Vellimana, A. K., Asano, E., & Sood, S. (2017b). Corpus callosotomy—Open and endoscopic surgical techniques. *Epilepsia*, *58*, 73–79. https://doi.org/10.1111/epi.13681

Sood, A., Ghani, K. R., Ahlawat, R., Modi, P., Abaza, R., Jeong, W., Sammon, J. D., Diaz, M., Kher, V., Menon, M., & Bhandari, M. (2014). Application of the statistical process control method for prospective patient safety monitoring during the learning phase: robotic kidney transplantation with regional hypothermia (IDEAL phase 2a-b). *European Urology*, *66*(2), 371–378. https://doi.org/10.1016/j.eururo.2014.02.055

Sparks, R., Vakharia, V., Rodionov, R., Vos, S. B. S. B., Diehl, B., Wehner, T., Miserocchi, A., McEvoy, A. W. A. W., Duncan, J. S. J. S., & Ourselin, S. (2017a). Anatomy-driven multiple trajectory planning (ADMTP) of intracranial electrodes for epilepsy surgery. *International Journal of Computer Assisted Radiology and Surgery*, *12*(8), 1245–1255. https://doi.org/10.1007/s11548-017-1628-z

Sparks, R., Zombori, G., Rodionov, R., Nowell, M., Vos, S. B., Zuluaga, M. A., Diehl, B., Wehner, T., Miserocchi, A., McEvoy, A. W., Duncan, J. S., & Ourselin, S. (2016). Automated multiple trajectory planning algorithm for the placement of stereo-electroencephalography (SEEG) electrodes in epilepsy treatment. *International Journal of Computer Assisted Radiology and Surgery*, 1–14. https://doi.org/10.1007/s11548-016-1452-x

Sparks, R., Zombori, G., Rodionov, R., Nowell, M., Vos, S. B., Zuluaga, M. A., Diehl, B., Wehner, T., Miserocchi, A., McEvoy, A. W., Duncan, J. S., & Ourselin, S. (2017b). Automated multiple trajectory planning algorithm for the placement of stereo-electroencephalography (SEEG) electrodes in epilepsy treatment. *International Journal of Computer Assisted Radiology and Surgery*, *12*(1), 123–136. https://doi.org/10.1007/s11548-016-1452-x

Spencer, D. D., Spencer, S. S., Mattson, R. H., Williamson, P. D., & Novelly, R. A. (1984a). Access to the posterior medial temporal lobe structures in the surgical treatment of temporal lobe epilepsy. *Neurosurgery*, *15*(5), 667–671.

Spencer, D. D., Spencer, S. S., Mattson, R. H., Williamson, P. D., & Novelly, R. A. (1984b). Access to the posterior medial temporal lobe structures in the surgical treatment of temporal lobe epilepsy. *Neurosurgery*, *15*(5), 667–671. https://doi.org/10.1227/00006123-198411000-00005

Sperling, M. R., Nei, M., Zangaladze, A., Sharan, A. D., Mintzer, S. E., Skidmore, C., Evans, J. G., Schilling, C. A., & Asadi-Pooya, A. A. (2008). Prognosis after late relapse following epilepsy surgery. *Epilepsy Research*, *78*(1), 77–81. https://doi.org/10.1016/j.eplepsyres.2007.10.011

Talairach, J., Bancaud, J., Bonis, A., Szikla, G., & Tournoux, P. (1962). Functional stereotaxic exploration of epilepsy. *Confinia Neurologica*, *22*, 328–331.

Tanriverdi, T., Olivier, A., Poulin, N., Andermann, F., & Dubeau, F. (2008). Long-term seizure outcome after mesial temporal lobe epilepsy surgery: corticalamygdalohippocampectomy versus selective amygdalohippocampectomy. *Journal of Neurosurgery*, *108*(3), 517–524. https://doi.org/10.3171/JNS/2008/108/3/0517

Tao, J. X., Issa, N. P., Wu, S., Rose, S., Collins, J., & Warnke, P. C. (2018). Interstitial Stereotactic Laser Anterior Corpus Callosotomy: A Report of 2 Cases with Operative Technique and Effectiveness. *Neurosurgery*. https://doi.org/10.1093/neuros/nyy273

Tao, J. X., Wu, S., Lacy, M., Rose, S., Issa, N. P., Yang, C. W., Dorociak, K. E., Bruzzone, M., Kim, J., Daif, A., Choi, J., Towle, V. L., & Warnke, P. C. (2017). Stereotactic EEG-guided laser

interstitial thermal therapy for mesial temporal lobe epilepsy. *Journal of Neurology, Neurosurgery, and Psychiatry*. https://doi.org/10.1136/jnnp-2017-316833

Téllez-Zenteno, J. F., Ronquillo, L. H., Moien-Afshari, F., & Wiebe, S. (2010). Surgical outcomes in lesional and non-lesional epilepsy: A systematic review and meta-analysis. *Epilepsy Research*, *89*(2–3), 310–318. https://doi.org/10.1016/j.eplepsyres.2010.02.007

Thornton, R., Vulliemoz, S., Rodionov, R., Carmichael, D. W., Chaudhary, U. J., Diehl, B., Laufs, H., Vollmar, C., McEvoy, A. W., Walker, M. C., Bartolomei, F., Guye, M., Chauvel, P., Duncan, J. S., & Lemieux, L. (2011). Epileptic networks in focal cortical dysplasia revealed using electroencephalography-functional magnetic resonance imaging. *Annals of Neurology*, *70*(5), 822–837. https://doi.org/10.1002/ana.22535

Tournier, J.-D., & , F. Calamante, and a. C. (2010). Improved probabilistic streamlines tractography by 2 nd order integration over fibre orientation distributions. *ISMRM*, *88*(2003), 2010.

Trope, M., Shamir, R. R., Joskowicz, L., Medress, Z., Rosenthal, G., Mayer, A., Levin, N., Bick, A., & Shoshan, Y. (2015). The role of automatic computer-aided surgical trajectory planning in improving the expected safety of stereotactic neurosurgery. *International Journal of Computer Assisted Radiology and Surgery*, *10*(7), 1127–1140. https://doi.org/10.1007/s11548-014-1126-5

Usami, K., Kawai, K., Koga, T., Shin, M., Kurita, H., Suzuki, I., & Saito, N. (2012). Delayed complication after Gamma Knife surgery for mesial temporal lobe epilepsy. *Journal of Neurosurgery*, *116*(6), 1221–1225. https://doi.org/10.3171/2012.2.JNS111296

Vaillant, M., Davatzikos, C., Taylor, R. H., & Bryan, R. N. (1997). A path-planning algorithm for image-guided neurosurgery. In J. Troccaz, E. Grimson, & R. Mösges (Eds.), *CVRMed-MRCAS'97: First Joint Conference Computer Vision, Virtual Reality and Robotics in Medicine and Medical Robotics and Computer-Assisted Surgery Grenoble, France, March 19--22, 1997 Proceedings* (pp. 467–476). Springer Berlin Heidelberg. https://doi.org/10.1007/BFb0029269

Vakharia, V., & Duncan, J. (2016a). *A Randomised Control Trial of SEEG Electrode Placement Methods*. ISRCTN Registry. https://doi.org/10.1186/ISRCTN17209025

Vakharia, V. N., Duncan, J. S., Sparks, R., & Ourselin, S. (2016b). *Accuracy of stereoencephalography (SEEG) electrode placement: a systematic review and meta-analysis PROSPERO CRD42016047839*.

www.crd.york.ac.uk/PROSPERO/display_record.asp?ID=CRD42016047839.

Vakharia, V. N., Duncan, J. S., Witt, J.-A. A., Elger, C. E., Staba, R., & Engel, J. J. (2018a). Getting the best outcomes from epilepsy surgery. *Annals of Neurology*, *83*(4), 676–690. https://doi.org/10.1002/ana.25205

Vakharia, V. N., McEvoy, A. W., Miserocchi, A., Rodionov, R., Ourselin, S., & Duncan, J. S. (2017a). Investigation of stereoencephalography electrode placement techniques in patients with refractory focal epilepsy: study protocol for a single-blinded randomised case control parallel group trial. *68th Annual Meeting of the German Society of Neurosurgery (DGNC) 7th Joint Meeting with the British Neurosurgical Society (SBNS)*. https://doi.org/doi: 10.3205/17dgnc394

Vakharia, V. N., Rodionov, R., McEvoy, A. W., Miserocchi, A., Sparks, R., O'Keeffe, A. G., Ourselin, S., Duncan, J. S., O'Keeffe, A. G., Ourselin, S., & Duncan, J. S. (2018b). Improving patient safety during introduction of novel medical devices through cumulative summation analysis. *Journal of Neurosurgery*, *130*(1), 213–219. https://doi.org/10.3171/2017.8.JNS17936

Vakharia, V. N., Sparks, R. E., Li, K., O'Keeffe, A. G., Pérez-García, F., França, L. G. S., Ko, A. L., Wu, C., Aronson, J. P., Youngerman, B. E., Sharan, A., McKhann, G., Ourselin, S., & Duncan, J. S. (2019a). Multicenter validation of automated trajectories for selective laser amygdalohippocampectomy. *Epilepsia*, *May*, epi.16307. https://doi.org/10.1111/epi.16307

Vakharia, V. N., Sparks, R. E., Vos, S. B., Bezchlibnyk, Y., Mehta, A. D., Willie, J. T., Wu, C., Sharan, A., Ourselin, S., & Duncan, J. S. (2020). Computer-assisted planning for minimally invasive anterior two-thirds laser corpus callosotomy: A feasibility study with probabilistic tractography validation: Automated laser callosotomy trajectory planning. *NeuroImage: Clinical*, *25*(December 2019), 102174. https://doi.org/10.1016/j.nicl.2020.102174

Vakharia, V. N., Sparks, R., Li, K., O'Keeffe, A. G., Miserocchi, A., McEvoy, A. W., Sperling, M. R., Sharan, A., Ourselin, S., Duncan, J. S., & Wu, C. (2018c). Automated trajectory planning for laser interstitial thermal therapy (LiTT) amygdalohippocampal complex ablation. *Epilepsia*, *59*(4), 814–824.

Vakharia, V. N., Sparks, R., Li, K., O'Keeffe, A. G., Miserocchi, A., McEvoy, A. W., Sperling, M. R., Sharan, A., Ourselin, S., Duncan, J. S., & Wu, C. (2018d). Automated trajectory planning for laser interstitial thermal therapy in mesial temporal lobe epilepsy. *Epilepsia*, *59*(4), 814–

824. https://doi.org/10.1111/epi.14034

Vakharia, V. N., Sparks, R., Miserocchi, A., Vos, S. B., O'Keeffe, A., Rodionov, R., McEvoy, A. W., Ourselin, S., & Duncan, J. S. (2019b). Computer-Assisted Planning for Stereoelectroencephalography (SEEG). *Neurotherapeutics*, *16*(4), 1183–1197. https://doi.org/10.1007/s13311-019-00774-9

Vakharia, V. N., Sparks, R., O'Keeffe, A. G., Rodionov, R., Miserocchi, A., McEvoy, A., Ourselin, S., & Duncan, J. (2017b). Accuracy of intracranial electrode placement for stereoencephalography: A systematic review and meta-analysis. *Epilepsia*, *58*(6), 1–12. https://doi.org/10.1111/epi.13713

Vakharia, V. N., Sparks, R., Rodionov, R., Vos, S. B., Dorfer, C., Miller, J., Nilsson, D., Tisdall, M., Wolfsberger, S., McEvoy, A. W., Miserocchi, A., Winston, G. P., O'Keeffe, A. G., Ourselin, S., & Duncan, J. S. (2018e). Computer-assisted planning for the insertion of stereoelectroencephalography electrodes for the investigation of drug-resistant focal epilepsy: an external validation study. *Journal of Neurosurgery*, *Apr*(1), 1–10. https://doi.org/10.3171/2017.10.JNS171826

Vakharia, V. N., Sparks, R., Vos, S. B., McEvoy, A. W., Miserocchi, A., Ourselin, S., & Duncan, J. S. (2019c). The Effect of Vascular Segmentation Methods on Stereotactic Trajectory Planning for Drug-Resistant Focal Epilepsy: A Retrospective Cohort Study. *World Neurosurgery: X*, *4*, 100057. https://doi.org/10.1016/J.WNSX.2019.100057

van Houdt, P. J., de Munck, J. C., Leijten, F. S. S., Huiskamp, G. J. M., Colon, A. J., Boon, P. A. J. M., & Ossenblok, P. P. W. (2013). EEG-fMRI correlation patterns in the presurgical evaluation of focal epilepsy: a comparison with electrocorticographic data and surgical outcome measures. *NeuroImage*, *75*, 238–248. https://doi.org/10.1016/j.neuroimage.2013.02.033

Van Roost, D., Solymosi, L., Schramm, J., van Oosterwyck, B., & Elger, C. E. (1998). Depth electrode implantation in the length axis of the hippocampus for the presurgical evaluation of medial temporal lobe epilepsy: a computed tomography-based stereotactic insertion technique and its accuracy. *Neurosurgery*, *43*(4), 817–819.

VAN WAGENEN, W. P., & HERREN, R. Y. (1940). SURGICAL DIVISION OF COMMISSURAL PATHWAYS IN THE CORPUS CALLOSUM: RELATION TO SPREAD OF AN EPILEPTIC ATTACK. *Archives of Neurology & Psychiatry*, *44*(4), 740–759. https://doi.org/10.1001/archneurpsyc.1940.02280100042004

Veersema, T. J., van Eijsden, P., Gosselaar, P. H., Hendrikse, J., Zwanenburg, J. J. M., Spliet, W. G. M., Aronica, E., Braun, K. P. J., & Ferrier, C. H. (2016). 7 tesla T2*-weighted MRI as a tool to improve detection of focal cortical dysplasia. *Epileptic Disorders : International Epilepsy Journal with Videotape*, *18*(3), 315–323. https://doi.org/10.1684/epd.2016.0838

Ventola, C. L. (2014). Epilepsy management: Newer agents, unmet needs, and future treatment strategies. *P and T*, *39*(11), 776–792.

Verburg, N., Baayen, J. C., Idema, S., Klitsie, M. A. J., Claus, S., De Jonge, C. S., Vandertop, W. P., & De Witt Hamer, P. C. (2016). In Vivo Accuracy of a Frameless Stereotactic Drilling Technique for Diagnostic Biopsies and Stereoelectroencephalography Depth Electrodes. *World Neurosurgery*, *87*, 392–398. https://doi.org/10.1016/j.wneu.2015.11.041

Von Der Heide, R. J., Skipper, L. M., Klobusicky, E., & Olson, I. R. (2013). Dissecting the uncinate fasciculus: Disorders, controversies and a hypothesis. *Brain*, *136*(6), 1692–1707. https://doi.org/10.1093/brain/awt094

von Oertzen, J. (2002). Standard magnetic resonance imaging is inadequate for patients with refractory focal epilepsy. *Journal of Neurology, Neurosurgery & Psychiatry*, *73*(6), 643–647.

von Rhein, B., Nelles, M., Urbach, H., Von Lehe, M., Schramm, J., & Helmstaedter, C. (2012). Neuropsychological outcome after selective amygdalohippocampectomy: subtemporal versus transsylvian approach. *Journal of Neurology, Neurosurgery, and Psychiatry*, *83*(9), 887–893. https://doi.org/10.1136/jnnp-2011-302025

Vos, S. B., Tax, C. M. W., Luijten, P. R., Ourselin, S., Leemans, A., & Froeling, M. (2017). The importance of correcting for signal drift in diffusion MRI. *Magnetic Resonance in Medicine*, *77*(1), 285–299. https://doi.org/10.1002/mrm.26124

Wagner, J., Weber, B., Urbach, H., Elger, C. E., & Huppertz, H.-J. (2011). Morphometric MRI analysis improves detection of focal cortical dysplasia type II. *Brain : A Journal of Neurology*, *134*(Pt 10), 2844–2854. https://doi.org/10.1093/brain/awr204

Wahlin, A., Ambarki, K., Hauksson, J., Birgander, R., Malm, J., & Eklund, A. (2012). Phase contrast MRI quantification of pulsatile volumes of brain arteries, veins, and cerebrospinal fluids compartments: repeatability and physiological interactions. *Journal of Magnetic Resonance Imaging : JMRI*, *35*(5), 1055–1062. https://doi.org/10.1002/jmri.23527

Wang, M., Meng, L., Cai, Y., Li, Y., Wang, X., Zhang, Z., & Peng, B. (2016). Learning Curve for Laparoscopic Pancreaticoduodenectomy: a CUSUM Analysis. *Journal of Gastrointestinal Surgery : Official Journal of the Society for Surgery of the Alimentary Tract*, *20*(5), 924–935.

https://doi.org/10.1007/s11605-016-3105-3

Wang, M. Y., Goto, T., Tessitore, E., & Veeravagu, A. (2017). Introduction. Robotics in neurosurgery. *Neurosurgical Focus*, *42*(5), E1. https://doi.org/10.3171/2017.2.focus1783

Wang, Z. I., Alexopoulos, A. V., Jones, S. E., Jaisani, Z., Najm, I. M., & Prayson, R. A. (2013). The pathology of magnetic-resonance-imaging-negative epilepsy. *Modern Pathology*, *26*(8), 1051–1058. https://doi.org/10.1038/modpathol.2013.52

Waseem, H., Vivas, A. C., & Vale, F. L. (2017). MRI-guided laser interstitial thermal therapy for treatment of medically refractory non-lesional mesial temporal lobe epilepsy: Outcomes, complications, and current limitations: A review. In *Journal of Clinical Neuroscience* (Vol. 38). https://doi.org/10.1016/j.jocn.2016.12.002

Watson, G. J., Byth, K., & da Cruz, M. (2015). Outcomes in Stapedotomy Surgery: The Learning Curve Redefined. *Otology & Neurotology : Official Publication of the American Otological Society, American Neurotology Society [and] European Academy of Otology and Neurotology*, *36*(10), 1601–1603. https://doi.org/10.1097/MAO.0000000000000887

WE, D. (1928). Removal of right cerebral hemisphere for certain tumors with hemiplegia: Preliminary report. *Journal of the American Medical Association*, *90*(11), 823–825.

Wellmer, J., Quesada, C. M., Rothe, L., Elger, C. E., Bien, C. G., & Urbach, H. (2013). Proposal for a magnetic resonance imaging protocol for the detection of epileptogenic lesions at early outpatient stages. *Epilepsia*, *54*(11), 1977–1987. https://doi.org/10.1111/epi.12375

Wendling, A. S., Hirsch, E., Wisniewski, I., Davanture, C., Ofer, I., Zentner, J., Bilic, S., Scholly, J., Staack, A. M., Valenti, M. P., Schulze-Bonhage, A., Kehrli, P., & Steinhoff, B. J. (2013). Selective amygdalohippocampectomy versus standard temporal lobectomy in patients with mesial temporal lobe epilepsy and unilateral hippocampal sclerosis. *Epilepsy Research*, *104*(1–2), 94–104. https://doi.org/10.1016/j.eplepsyres.2012.09.007

Wenzel, M., Hamm, J., Peterka, D., & Yuste, R. (2017). Reliable and elastic propagation of cortical seizures in vivo. *Cell Rep*, *19*(13), 2681–2693. https://doi.org/10.1016/j.celrep.2017.05.090

West, S., Nolan, S. J., Cotton, J., Gandhi, S., Weston, J., Sudan, A., Ramirez, R., & Newton, R. (2015a). Surgery for epilepsy. *The Cochrane Database of Systematic Reviews*, *7*(7), CD010541. https://doi.org/10.1002/14651858.CD010541.pub2

West, S., Sj, N., Cotton, J., Gandhi, S., Weston, J., Ramirez, R., & Newton, R. (2015b). Surgery for epilepsy (Review) SUMMARY OF FINDINGS FOR THE MAIN COMPARISON. *Cochrane*

Library, *7*. https://doi.org/10.1002/14651858.CD010541.pub2.www.cochranelibrary.com

Wickham, H. (2007). Reshaping Data with the {reshape} Package. *Journal of Statistical Software*, *21*(12), 1–20.

Wickham, H. (2009). *ggplot2: Elegant Graphics for Data Analysis*. Springer-Verlag New York.

Wickham, H. (2018). *stringr: Simple, Consistent Wrappers for Common String Operations*.

Wicks, R. T., Jermakowicz, W. J., Jagid, J. R., Couture, D. E., Willie, J. T., Laxton, A. W., & Gross, R. E. (2016). Laser Interstitial Thermal Therapy for Mesial Temporal Lobe Epilepsy. *Neurosurgery*, *79 Suppl 1*, S83–S91. https://doi.org/10.1227/NEU.0000000000001439

Wiebe, S., Blume, W. T., Girvin, J. P., Eliasziw, M., Warren, B. T., Girvon, J. T., & Eliasziw, M. (2001). A RANDOMIZED, CONTROLLED TRIAL OF SURGERY FOR TEMPORAL-LOBE EPILEPSY. *New England Journal of Medicine*, *345*(5), 311–318. https://doi.org/10.1056/NEJM200108023450501

Wieser, H. G., Blume, W. T., Fish, D., Goldensohn, E., Hufnagel, A., King, D., Sperling, M. R., Lüders, H., & Pedley, T. A. (2001). Proposal for a new classification of outcome with respect to epileptic seizures following epilepsy surgery. *Epilepsia*, *42*(2), 282–286. https://doi.org/10.1046/j.1528-1157.2001.35100.x

Wieser, H. G., & Yasargil, M. G. (1982). Selective amygdalohippocampectomy as a surgical treatment of mesiobasal limbic epilepsy. *Surgical Neurology*, *17*(6), 445–457.

Wilfong, A. A., & Curry, D. J. (2013). Hypothalamic hamartomas: Optimal approach to clinical evaluation and diagnosis. *Epilepsia*, *54*(SUPPL. 9), 109–114. https://doi.org/10.1111/epi.12454

Wilke, C. O. (2017). *cowplot: Streamlined Plot Theme and Plot Annotations for "ggplot2."*

Willats, L., Raffelt, D., Smith, R. E., Tournier, J.-D., Connelly, A., & Calamante, F. (2014). Quantification of track-weighted imaging (TWI): characterisation of within-subject reproducibility and between-subject variability. *NeuroImage*, *87*, 18–31. https://doi.org/10.1016/j.neuroimage.2013.11.016

Willie, J. T., Laxpati, N. G., Drane, D. L., Gowda, A., Appin, C., Hao, C., Brat, D. J., Helmers, S. L., Saindane, A., Nour, S. G., & Gross, R. E. (2014). Real-time magnetic resonance-guided stereotactic laser amygdalohippocampotomy for mesial temporal lobe epilepsy. *Neurosurgery*, *74*(6), 569–584. https://doi.org/10.1227/NEU.0000000000000343

Willmann, O., Wennberg, R., May, T., Woermann, F. G., & Pohlmann-Eden, B. (2007). The contribution of 18F-FDG PET in preoperative epilepsy surgery evaluation for patients with

temporal lobe epilepsy. A meta-analysis. *Seizure*, *16*(6), 509–520. https://doi.org/10.1016/j.seizure.2007.04.001

Winston, G. P., Daga, P., Stretton, J., Modat, M., Symms, M. R., McEvoy, A. W., Ourselin, S., & Duncan, J. S. (2012). Optic radiation tractography and vision in anterior temporal lobe resection. *Annals of Neurology*, *71*(3), 334–341. https://doi.org/10.1002/ana.22619

Winston, G. P., Daga, P., White, M. J., Micallef, C., Miserocchi, A., Mancini, L., Modat, M., Stretton, J., Sidhu, M. K., Symms, M. R., Lythgoe, D. J., Thornton, J., Yousry, T. A., Ourselin, S., Duncan, J. S., & McEvoy, A. W. (2014). Preventing visual field deficits from neurosurgery. *Neurology*, *83*(7), 604–611. https://doi.org/10.1212/WNL.0000000000000685

Wirsich, J., Perry, A., Ridley, B., Proix, T., Golos, M., Bénar, C., Ranjeva, J. P., Bartolomei, F., Breakspear, M., Jirsa, V., & Guye, M. (2016). Whole-brain analytic measures of network communication reveal increased structure-function correlation in right temporal lobe epilepsy. *NeuroImage: Clinical*, *11*, 707–718. https://doi.org/10.1016/j.nicl.2016.05.010

Woermann, F. G., Barker, G. J., Birnie, K. D., Meencke, H. J., & Duncan, J. S. (1998). Regional changes in hippocampal T2 relaxation and volume: a quantitative magnetic resonance imaging study of hippocampal sclerosis. *J Neurol Neurosurg Psychiatry*, *65*(5), 656–664. https://doi.org/10.1136/jnnp.65.5.656

Wu, C., Boorman, D. W., Gorniak, R. J., Farrell, C. J., Evans, J. J., & Sharan, A. D. (2015). The effects of anatomic variations on stereotactic laser amygdalohippocampectomy and a proposed protocol for trajectory planning. *Neurosurgery*, *11*(2). https://doi.org/10.1227/NEU.0000000000000767

Yasargil, M. G., von Ammon, K., Cavazos, E., Doczi, T., Reeves, J. D., & Roth, P. (1992). Tumours of the limbic and paralimbic systems. *Acta Neurochirurgica*, *118*(1–2), 40–52.

Yeni, S. N., Tanriover, N., Uyanik, Ö., Ulu, M. O., Özkara, Ç., Karaağaç, N., Ozyurt, E., & Uzan, M. (2008). Visual field defects in selective amygdalohippocampectomy for hippocampal sclerosis: The fate of meyers loop during the transsylvian approach to the temporal horn. *Neurosurgery*, *63*(3), 507–513. https://doi.org/10.1227/01.NEU.0000324895.19708.68

Young, A., Miller, J. P., & Azarow, K. (2005). Establishing learning curves for surgical residents using Cumulative Summation (CUSUM) Analysis. *Current Surgery*, *62*(3), 330–334. https://doi.org/10.1016/j.cursur.2004.09.016

Youngerman, B., Oh, J., Deepti, A., Santoshi, B., Casadei, C., Corrigan, E., Banks, G., Pack, A.,

Hyunmi, C., Bazil, C., Shraddha, S., Bateman, L., Schevon, C., Feldstein, N., Sheth, S., & McKhann, G. (2018). Laser ablation is effective for temporal lobe epilepsy with and without mesial temporal sclerosis if hippocampal seizure onsets are localized by stereoelectroencephalography. *Epilepsia*, *59*(3), 595–606. https://doi.org/10.1111/epi.14004

Zamorano, L., Jiang, Z., & Kadi, A. M. (1994). Computer-assisted neurosurgery system: Wayne State University hardware and software configuration. *Computerized Medical Imaging and Graphics : The Official Journal of the Computerized Medical Imaging Society*, *18*(4), 257–271.

Zelmann, R., Beriault, S., Marinho, M. M., Mok, K., Hall, J. A., Guizard, N., Haegelen, C., Olivier, A., Pike, G. B., & Collins, D. L. (2015). Improving recorded volume in mesial temporal lobe by optimizing stereotactic intracranial electrode implantation planning. *International Journal of Computer Assisted Radiology and Surgery*, *10*(10), 1599–1615. https://doi.org/10.1007/s11548-015-1165-6

Zhang, Z., Liao, W., Chen, H., Mantini, D., Ding, J. R., Xu, Q., Wang, Z., Yuan, C., Chen, G., Jiao, Q., & Lu, G. (2011). Altered functional-structural coupling of large-scale brain networks in idiopathic generalized epilepsy. *Brain*, *134*(10), 2912–2928. https://doi.org/10.1093/brain/awr223

Zola-Morgan, S., Squire, L. R., Amarel, D. G., & Suzuki, W. A. (1989). Lesions of perirhinal and parahippocampal cortex that spare the amygdala and hippocampal formation produce severe memory impairment. *Journal of Neuroscience*, *9*(12), 4355–4370. https://www.scopus.com/inward/record.uri?eid=2-s2.0-0024819854&partnerID=40&md5=b825f7f3a78400fda5d325b4a565642f

Zola-Morgan, S., Squire, L. R., & Ramus, S. J. (1994). Severity of memory impairment in monkeys as a function of locus and extent of damage within the medial temporal lobe memory system. *Hippocampus*, *4*(4), 483–495. https://doi.org/10.1002/hipo.450040410

Zombori, G., Rodionov, R., Nowell, M., Zuluaga, M. A., Clarkson, M. J., Micallef, C., Diehl, B., Wehner, T., Miserochi, A., McEvoy, A. W., Duncan, J. S., & Ourselin, S. (2011). A Computer Assisted Planning System for the Placement of sEEG Electrodes in the Treatment of Epilepsy. *Information Processing in Computer-Assisted Interventions*, 118–127.

Zombori, G., Rodionov, R., Nowell, M., Zuluaga, M. A., Clarkson, M. J., Micallef, C., Diehl, B., Wehner, T., Miserochi, A., McEvoy, A. W., Duncan, J. S., & Ourselin, S. (2014). A Computer

Assisted Planning System for the Placement of sEEG Electrodes in the Treatment of Epilepsy. In D. Stoyanov, D. L. Collins, I. Sakuma, P. Abolmaesumi, & P. Jannin (Eds.), *Information Processing in Computer-Assisted Interventions* (pp. 118–127). Springer International Publishing.

Zuckerman, S. L., Bhatia, R., Tsujiara, C., Baker, C. B., Szafran, A., Cushing, D., Aiken, J., Tracy, M., Mocco, J., & Ecker, R. D. (2015). Prospective series of two hours supine rest after 4fr sheath-based diagnostic cerebral angiography: Outcomes, productivity and cost. *Interventional Neuroradiology : Journal of Peritherapeutic Neuroradiology, Surgical Procedures and Related Neurosciences*, *21*(1), 114–119. https://doi.org/10.15274/INR-2014-10102

Zuluaga, M. A., Rodionov, R., Nowell, M., Achhala, S., Zombori, G., Mendelson, A. F., Cardoso, M. J., Miserocchi, A., McEvoy, A. W., Duncan, J. S., & Ourselin, S. (2015). Stability, structure and scale: improvements in multi-modal vessel extraction for SEEG trajectory planning. *International Journal of Computer Assisted Radiology and Surgery*, *10*(8), 1227–1237. https://doi.org/10.1007/s11548-015-1174-5